High-Magnetic-Field Study of the Heavy-Fermion System URu2Si2

Gernot Werner Scheerer

THÈSE

En vue de l'obtention du

DOCTORAT DE L'UNIVERSITÉ DE TOULOUSE

Délivré par : *l'Université Toulouse 3 Paul Sabatier (UT3 Paul Sabatier)*

Présentée et soutenue le *25 Novembre 2013* **par :**

GERNOT WERNER SCHEERER

Étude à Fort Champ Magnétique du Système à Fermions Lourds URu_2Si_2

-

High-Magnetic-Field Study of the Heavy Fermion System URu_2Si_2

JURY

SYLVAIN CAPPONI	Professeur (Université Toulouse III Paul Sabatier)	Président du Jury
RIKIO SETTAI	Professeur (Niigata University)	Rapporteur
SÉBASTIEN BURDIN	Maître de Conférence (Université de Bordeaux)	Rapporteur
ANNE DE VISSER	Associate Professor (University of Amsterdam)	Examinateur
GEORG KNEBEL	Chercheur (Commissariat à l'Energie Atomique de Grenoble)	Examinateur
WILLIAM KNAFO	Chercheur (Laboratoire National des Champs Magnétiques Intenses - Toulouse)	Directeur de Thèse

---

École doctorale et spécialité :
SDM : Physique de la matière - CO090
Unité de Recherche :
Laboratoire National des Champs Magnétiques Intenses (UPR 3228)
Directeur de Thèse :
William KNAFO
Rapporteurs :
Rikio SETTAI et *Sébastien BURDIN*

Étude à Fort Champ Magnétique du Système à Fermions Lourds URu_2Si_2

Résumé

Les composés à fermions lourds, qui sont à base de terres rares comme le cérium et l'ytterbium ou d'actinides comme l'uranium, sont connus pour leurs propriétés extraordinaires à basse température. Leur physique est gouvernée par l'hybridation des électrons f avec des électrons de conduction, ce qui mène à la formation de quasi-particules avec de très grandes masses effectives. URu_2Si_2 occupe une place particulière dans la famille des fermions lourds. Une transition de phase du second ordre à la température $T_0 = 17.5$ K a été observée par de nombreuses techniques expérimentales. Malgré des propositions théoriques multiples, aucun consensus n'existe concernant le paramètre d'ordre de la phase - dite à ordre caché - qui se développe sous T_0. Lorsqu'on le soumet à des champs magnétiques intenses, URu_2Si_2 a par ailleurs un comportement unique : une cascade de trois transitions du premier ordre entre 35 et 39 T mène le système de son état paramagnétique à un état polarisé paramagnétique à fort champ. Ce travail a consisté en l'investigation systématique des propriétés magnétiques et électroniques d'échantillons monocristallins de très haute qualité d'URu_2Si_2 dans des champs magnétiques intenses allant jusqu'à 80 T, et des températures descendant jusqu'à 100 mK. Des expériences d'aimantation et de magnétorésistivité ont été faites en champ magnétique pulsé non destructif au Laboratoire National des Champs Magnétiques Intenses de Toulouse (LNCMI-T). Le diagramme de phase champ magnétique-température de URu_2Si_2 a été étudié la première fois sur les gammes étendues de champs magnétiques $\mathbf{H} \parallel \mathbf{c}$ allant jusqu'à 60 T et de températures allant jusqu'à 80 K. Il indique que la domaine critique [35 T-39 T] est initié par la destabilisation d'un crossover, dont la température caractéristique atteint 40-50 K à champ nul. Il est démontré que ce crossover, qui résulte probablement des corrélations inter-site, est aussi un précurseur de la phase

à ordre caché. Une étude de la magnétorésistivité pour différentes orientations du champ magnétique dans les plans (**a**,**a**) and (**a**,**c**) a permis d'établir la dépendance en angle du diagramme de phase. Des mesures de l'aimantation du composé dopé en rhodium $U(Ru_{0.96}Rh_{0.04})_2Si_2$ révèlent un diagramme de phase simplifié, où la phase à ordre caché a disparu et le domaine critique a été remplace par une phase intermédiaire entre 26 et 37 T. La magnetoresistivité à très basse température se révèle être fortement dépendente de la qualité des échantillons et est la signature des propriétés orbitales d'URu_2Si_2. Une dépendance exceptionnellement intense de la magnétorésistivité en fonction de la température confirme que la surface de Fermi est reconstruite à T_0. Des anomalies dans la magnetoresistivité à fort champ magnétique $\mathbf{H} \parallel \mathbf{c}$ suggèrent que la surface de Fermi est modifiée à l'intérieur de la phase à ordre caché. Des oscillations quantiques - effet Shubnikov-de Haas - sont observées dans la magnétorésistivité à très basse température pour une multitude d'orientations des échantillons dans le champ magnétique. Elles confirment qu'un champ magnétique $\mathbf{H} \parallel \mathbf{c}$ induit des reconstructions de la surface de Fermi dans la phase à ordre caché. Dans un champ magnétique $\mathbf{H} \parallel \mathbf{a}$, des oscillations quantiques sont observées pour la première fois jusqu'à 80 T. Leur analyse a révélé une nouvelle branche de fréquence λ avec une faible masse effective. La dépendance en angle des fréquences Shubnikov-de Haas a été étudiée dans un champ magnétique allant jusqu'à 60 T, pour des champs appliqués dans les plans (**a**,**a**) et (**a**,**c**). Ce travail expérimental indique que le couplage entre le magnétisme des électrons f et les propriétés de la surface de Fermi joue un rôle important pour la physique du système à ordre caché URu_2Si_2.

High-Magnetic-Field Study of the Heavy Fermion System URu_2Si_2

Abstract

Heavy-fermion compounds, usually intermetallic compounds of rare-earth elements like Cerium and Ytterbium, or actinides like Uranium, are known for their extraordinary low-temperature physics. Their physics is governed by the hybridization of f- and conduction electrons, which gives rise to the formation of heavy quasiparticles with strongly-enhanced effective masses. URu_2Si_2 occupies a particular place in the heavy-fermion family. A second-order phase transition at the temperature $T_0 = 17.5$ K is reported by many experimental probes but, despite numerous propositions, no order parameter has been consensually associated to the phase below T_0, which is called the "hidden-order" phase. URu_2Si_2 shows a unique behavior when exposed to strong magnetic fields: a cascade of three first-order transitions between 35 and 39 T drives the system from the paramagnetic hidden-order phase to a high-field polarized paramagnetic state. This work presents a systematic investigation of the magnetic and electronic properties of high-purity URu_2Si_2 single crystals in intense magnetic fields up to 80 T and at temperatures down to 100 mK. The magnetization and magnetoresistivity experiments presented here have been done in non-destructive pulsed magnetic fields at the Laboratoire National des Champs Magnétiques Intenses of Toulouse (LNCMI-T). The magnetic field-temperature phase diagram of URu_2Si_2 was studied for the first time in both extended magnetic field $\mathbf{H} \parallel \mathbf{c}$ (up to 60 T) and temperature (up to 80 K) scales. It indicates that the critical area [35 T-39 T] is initiated by the vanishing of a crossover temperature, which reaches 40-50 K at zero-field. It is demonstrated that this crossover, which probably results from inter-site correlations, is a precursor of the hidden-order phase. An angle-dependent study of the magnetoresistivity, in a wide range of orientations of the magnetic field in the crystal planes (**a**,**a**) and (**a**,**c**), permitted to establish the angle-dependence of the phase diagram. Magneti-

zation measurements of the Rhodium-doped compound $U(Ru_{0.96}Rh_{0.04})_2Si_2$ revealed a simplified phase diagram, where the hidden-order phase has vanished and where the critical region has been replaced by one intermediate antiferromagnetic phase between 26 and 37 T. The magnetoresistivity is found to be strongly sample-quality dependent and reflects the peculiar electronic properties of URu_2Si_2. The temperature and field-dependencies of the exceptionally strong magnetoresistivity confirm that the Fermi surface is reconstructed below T_0. Crossover-like anomalies in the magnetoresistivity suggest that the Fermi surface is modified in a high-magnetic field $\mathbf{H} \parallel \mathbf{c}$ far below 35 T, i.e, in the hidden-order phase. Quantum oscillations have been observed in the magnetoresistivity for various orientations of the samples in the magnetic field. The Shubnikov-de Haas data confirm that a magnetic field applied along **c** induces Fermi surface reconstructions inside the hidden-order phase, as indicated by the anomalies observed in the non-oscillating magnetoresistivity. For a magnetic field applied along **a**, quantum oscillations are observed for the first time up to 80 T and their analysis shows a new frequency branch λ with a light effective mass. The angle-dependence of the observed Shubnikov-de Haas frequencies has been established at 1.5 K in high magnetic fields up to 60 T rotating in the (**a**,**a**) and (**a**,**c**)-planes. This experimental work emphasizes that the f-electron magnetic properties are intimately connected to the properties of the Fermi surface in the hidden-order material URu_2Si_2.

Remerciements

Ce travail a été réalisé au Laboratoire National des Champs Magnétiques Intenses de Toulouse (UPR 3228).
Je remercie le directeur de l'unité Geert Rikken, ainsi que le directeur adjoint Oliver Portugal, pour m'avoir accordé l'opportunité d'effectuer cette thése au sein du laboratoire.
Je suis trés reconnaissant envers l'ensemble des membres du jury qui m'ont fait l'honneur d'évaluer mon travail.
Je souhaite de remercier mon directeur de thèse William Knafo pour son soutien et la motivation qu'il a su me donner, aussi pour les expériences et les participations aux conférences.
Merci à Geraldine, Marc, Aziz et Alain qui ont beaucoup contribué à la réalisation de ce travail. Merci à l'ensemble du laboratoire et en particulier aux équipes Conducteurs et Aimants Quantiques, FFC, cryogénie, bobines, générateurs et installations techniques.
Un grand merci à nos collaborateurs, "les Grenoblois", Dai, Georg, Alexandre et Jacques.
Je remercie Hisatomo Harima, Frédéric Hardy, Daniel Braithwaite et Jean-Pascal Brison pour des discussions enrichissantes.
Enfin je ne veux pas oublier mes collègues thésards et post-docs: Sven, Xavier, David, Rebecca, Stéphane, Pierre-Yves, Fabrice, Agathe, Vladimir, Anaïs, Joanna et Anatolie.

Contents

1 Introduction **13**

2 Theory **17**

2.1 Magnetism 17
2.1.1 Magnetization of materials 18
2.1.2 Paramagnetism 19
2.1.3 Ferro- and antiferromagnetism 20
2.2 Fermi liquid theory 20
2.3 Heavy-fermion theory 22
2.3.1 Kondo effect 22
2.3.2 Kondo lattice and RKKY-interaction 24
2.3.3 Quantum criticality 25
2.4 Magnetoresistivity of metals 26
2.4.1 Resistivity at zero magnetic field 26
2.4.2 One-electron-band in a magnetic field 27
2.4.3 Electron-hole-band in a magnetic field 29
2.4.4 Kohler's rule 31
2.5 Quantum oscillations 33
2.5.1 Quantization of the electron motion in magnetic fields 33
2.5.2 The Lifshitz-Kosevich description of the de Haas-van Alphen effect 36
2.5.3 The Shubnikov-de Haas effect 38

3 Experimental Method and Setup **39**

3.1 Generation of pulsed magnetic fields 39
3.1.1 Introduction 39
3.1.2 The LNCMI-T pulsed-field facility 40
3.1.3 The LNCMI-T pulsed-field magnets 42
3.2 Cryogenics 43
3.2.1 ^{4}He-cryostat 44
3.2.2 ^{3}He-^{4}He-dilution cryostat 45
3.3 Magnetization 47

3.4 Electric transport 49
3.5 Samples and their characterization 51
3.5.1 Magnetic susceptibility 51
3.5.2 Resistivity 52
3.6 Gauging of the pickup 54
3.7 Analysis of the Shubnikov-de Haas data 55
3.8 Sample thermalization in pulsed magnetic fields 56
3.9 Reproducibility of the magnetoresistivity measurements 60

4 Introduction to URu_2Si_2 63
4.1 From a Kondo liquid to the hidden-order 63
4.2 Magnetic fluctuations and magnetic ordering 66
4.2.1 Hidden-order phase 66
4.2.2 Pressure-induced antiferromagnetic phase 66
4.3 Fermi surface 67
4.3.1 Transport properties 67
4.3.2 ARPES 68
4.3.3 Quantum oscillations 69
4.3.4 Band structure calculations 71
4.4 URu_2Si_2 in high-magnetic fields 72

5 High-Magnetic-Field properties of URu_2Si_2 in $\mathbf{H} \parallel \mathbf{c}$ 77
5.1 Magnetization 77
5.2 Magnetoresistivity 82
5.3 H-T phase diagram of URu_2Si_2 85
5.4 Comparison of the phase diagrams extracted using different techniques 88

6 H-T-phase diagram of $U(Ru_{0.96}Rh_{0.04})_2Si_2$ 91

7 Orbital Magnetoresistivity 97
7.1 Transverse and longitudinal magnetoresistivity in $\mathbf{H} \parallel \mathbf{c}$ 97
7.2 Transverse magnetoresistivity in $\mathbf{H} \parallel \mathbf{a}$ 99
7.3 Sample-dependent features in the magnetoresistivity 101
7.4 Analysis of the magnetoresistivity 104

8 Angle-Dependent Study of the High-Field Magnetoresistivity 111
8.1 Angle dependence of H_{c2} 111
8.2 H-T phase diagram for $(\mathbf{H}, \mathbf{c}) = 20°$ 112
8.3 Crossover and transition fields for $\mathbf{H}$ in the plane ($\mathbf{a}$,$\mathbf{c}$) 114
8.4 Magnetoresistivity in magnetic fields $\mathbf{H}$ in the plane ($\mathbf{a}$,$\mathbf{a}$) 117

9 Fermi Surface in High Magnetic Fields **119**

9.1 Low-field Fermi surface 119

9.2 Fermi surface modifications in high magnetic fields $\mathbf{H} \parallel \mathbf{c}$ 122

9.3 Fermi surface in high magnetic fields $\mathbf{H} \parallel \mathbf{a}$ 125

9.4 Fermi surface in high magnetic fields $\mathbf{H}$ in the ($\mathbf{a}$,$\mathbf{a}$) and ($\mathbf{a}$,$\mathbf{c}$)-planes 130

10 Conclusion **133**

1 Introduction

Heavy fermions are intermetallic compounds, known for their extraordinary low-temperature physics [Hewson 1993, Stewart 2001, Flouquet 2005]. Typically, heavy-fermion compounds contain rare earth elements like Cerium and Ytterbium, or actinides like Uranium, which have partially filled $4f$- or $5f$-electron shells. Heavy-fermion physics is governed by the Kondo effect [Kondo 1964], which is the scattering of the conduction electrons due to their interaction with the magnetic moments of the f-electrons. A hybridization of the f- and the conduction electrons, due to the closeness of the f-energy level to the Fermi energy, gives rise to the formation of heavy quasiparticles with strong enhanced effective masses, up to 1000 times the free electron mass. The Ruderman-Kittel-Kasuya-Yosida (RKKY) interaction is a magnetic exchange interaction between the f-electron moments mediated by the conduction electrons, which favors long-range magnetic ordering [Ruderman and Kittel 1954]. The phase diagram of heavy fermions is defined by the competition between Kondo and RKKY interactions, which both depend on the exchange interaction J between f- and conduction electrons and the density of states $D(\epsilon_F)$ at the Fermi level ϵ_F. Due to this competition, f-electron magnetic properties are very sensitive to pressure and chemical doping, which permit to tune a quantum phase transition between a paramagnetic regime and a (generally antiferro-) magnetic state [Doniach 1977].
URu_2Si_2 occupies a particular place in the heavy-fermion family [Mydosh and Oppeneer 2011]. A second-order phase transition at the temperature $T_0 = 17.5$ K is reported by many experimental probes but, despite numerous propositions, no order parameter has been consensually associated to the phase below T_0, which is called the "hidden-order" phase. The challenge is to experimentally identify the order parameter and/or to establish an order parameter theory, which would be consistent with the multitude of existing experimental results. An auspicious approach might be to identify the energy scales driving the system to the ordered phase.
Field-induced magnetic transitions are typical of heavy-fermion systems [Aoki 2013]. Either a paramagnetic or antiferromagnetic ground state can be suppressed by an applied magnetic field at a critical field value (at zero temperature) and the system is driven to a polarized paramagnetic regime at very high fields. Most of heavy-fermions systems show a strong magnetic anisotropy, which results in field-induced

first-order transitions. These transitions, called metamagnetic transitions, are characterized by a sudden step-like increase of the magnetization [Stryjewski 1977]. URu_2Si_2 shows an unique behavior when exposed to strong magnetic fields: a cascade of three first-order transitions between 35 and 39 T drives the system from the paramagnetic hidden order phase to a high-field polarized paramagnetic state [Sugiyama 1999, Kim 2003b].
During my Ph.D thesis I have performed a systematic investigation of the magnetic and electronic properties of high-purity URu_2Si_2 single crystals in intense magnetic fields up to 80 T and at temperatures down to 100 mK. These high magnetic fields were essential for the establishment of the temperature-magnetic field phase diagram and for the observation of high-field orbital effects, i.e., a strong magnetoresistivity and quantum oscillations. The magnetization and magnetoresistivity experiments presented in this work have been done in non-destructive pulsed magnetic fields at the Laboratoire National des Champs Magnétiques Intenses of Toulouse (LNCMI-T).
This work is organized as follows:

- Chapter 2 introduces the physical effects, interactions and theoretical models, which were relevant for this work.

- The experimental setups and procedures permitting to measure the magnetization and resistivity in extreme conditions (low temperature, high magnetic field) are presented in Chapter 3.

- Chapter 4 gives an introduction to the heavy-fermion system URu_2Si_2, based on a multitude of published experimental data and theoretical models.

- The high-field properties of URu_2Si_2 in a magnetic field applied along the **c**-axis are presented in Chapter 5. Its magnetic field-temperature (H,T) phase diagram, for $\mathbf{H} \parallel \mathbf{c}$, was studied for the first time in both extended temperature (up to 80 K) and magnetic field (up to 60 T) scales. It indicates that the critical area [35 - 39 T] is initiated by the vanishing of a crossover temperature, which reaches 40-50 K at zero-field. It is demonstrated that this crossover, which probably results from inter-site correlations, is a precursor of the hidden-order phase.

- Chapter 6 presents the magnetic field-temperature phase diagram of the Rhodium-doped compound $U(Ru_{0.96}Rh_{0.04})_2Si_2$ for $\mathbf{H} \parallel \mathbf{c}$. No hidden-order is observed for this system and its phase diagram is characterized by a low-field paramagnetic ground state, which is suppressed by a magnetic field of 26 T

applied along the **c**-axis. The magnetic field induces an intermediate antiferromagnetic state between 26 and 37 T and drives the system to a polarized paramagnetic state above 37 T.

- In Chapter 7, a comparison of the magnetoresistivity of URu_2Si_2 samples of different purities gives a new insight on the electronic transport properties inside the hidden-order phase. We observe an exceptionally strong orbital contribution to the magnetoresistivity, which indicates that the Fermi surface is modified at T_0, but also inside the hidden-order phase in a magnetic field applied along **c**.

- An angle-dependent study of the magnetoresistivity is presented in Chapter 8. A wide range of transverse and longitudinal configurations, for magnetic fields applied along the main crystal planes (**a**,**a**) and (**a**,**c**) permitted to establish the angle-dependence of the phase diagram. In particular for the hidden-order phase, f-electrons behavior is intimately connected to the properties of the Fermi surface.

- A study of the high-field Fermi surface of URu_2Si_2 by the Shubnikov-de Haas effect, observed for all orientations of the samples in the magnetic field, is presented in Chapter 9. Shubnikov-de Haas data confirm that a magnetic field applied along **c** induces Fermi surface reconstructions inside the hidden-order phase, as indicated by the anomalies observed in the non-oscillating magnetoresistivity. For a magnetic field applied along **a**, we observed quantum oscillations, whose analysis showed a new Fermi surface sheet with a light effective mass, for the first time up to 80 T. We established the angle-dependence of the observed Shubnikov-de Haas frequencies at 1.5 K in high magnetic fields up to 60 T rotating in the (**a**,**a**) and (**a**,**c**)-planes.

2 Theory

In this chapter I present the physical phenomena, principles, and models of low-temperature and solid state physics, which are relevant for this work, based on a selection of textbooks [Ashcroft and Mermin 1976, Shoenberg 1984, Pippard 1989, Hewson 1993, Grosso and Parravicini 2000, Enss and Hunklinger 2005]. Section 2.1 presents basic principles of magnetism. Notions of the Fermi liquid theory are found in Section 2.2. Section 2.3 gives a short introduction to heavy-fermion physics. The notion of orbital magnetoresistivity is developed in section 2.4. Section 2.5 presents the theory of quantum oscillations.

2.1 Magnetism

Usually, magnetism of materials is due to the non-zero total magnetic moment of electrons from uncomplete d- or f-orbitals, while the electrons from the s- and p-orbitals participate to the chemical bondings of insulators or are delocalized in the electron sea of metals (see [Grosso and Parravicini 2000] for a detailed review on magnetism theory).

Localized magnetism, which occurs mainly in insulating materials (EuO, Gd,..), usually can be described by the Heisenberg formalism. The Hamiltonian, within a localized picture, takes into account the interaction between two spin moments S_m and S_n localized at the lattice sites m and n, respectively:

$$H = -\sum\nolimits_{m \neq n} J_{m,n} S_m S_n, \tag{2.1}$$

where $J_{m,n}$ is the exchange interaction. The $4f$-orbitals of rare earth elements (Ce, Yb,...) show a local atomic-like character and the magnetism in rare earth compounds can often be described by a localized picture.

The $3d$-electrons of transition metals (Fe,Ni,..) are delocalized in the conduction band and can be described by a **itinerant magnetism** theory, as the Stoner-Hubbard model. In this model the conduction electrons, which participate in the magnetic state, are described by the Hamiltonian:

$$H = \sum\nolimits_{\mathbf{k},\sigma} E(\mathbf{k}) c^{\dagger}_{\mathbf{k}\sigma} c_{\mathbf{k}\sigma} + U \sum\nolimits_{\mathbf{r_m},\sigma} c^{\dagger}_{m\sigma} c_{m\sigma}, \tag{2.2}$$

where $\mathbf{k}$ is the wavevector, $E(\mathbf{k})$ is the $\mathbf{k}$-dependent conduction band energy, $c^{\dagger}_{\mathbf{k}\sigma}$ and $c_{\mathbf{k}\sigma}$ are creation and annihilation operators for conduction electrons of spin σ and wavevector $\mathbf{k}$, U is the Coulomb repulsion between two electrons of opposite spin at the same site, and $c^{\dagger}_{m\sigma}$ and $c_{m\sigma}$ are creation and annihilation operators for electrons of spin σ in the localized state of the lattice site m.

In heavy-fermion compounds, the electrons of the incomplete f-orbitals ($4f$- or $5f$-states) exhibit a behavior which is between that of itinerant $3d$-electrons and purely localized $4f$-electrons.

2.1.1 Magnetization of materials

The magnetization M is the reaction per unit of volume of matter to an external magnetic field H:

$$M = \chi H, \tag{2.3}$$

where χ is the magnetic susceptibility. A more general definition of the susceptibility can be given by:

$$\chi = \frac{\partial M}{\partial H}. \tag{2.4}$$

At finite temperature T and at a given magnetic field H, the relation between the magnetization $M(T,H)$ and the free energy $F(T,H)$ is given by:

$$M(T,H) = -\frac{1}{V}\frac{\partial F(T,H)}{\partial H}, \tag{2.5}$$

where V is the volume of the material. The magnetic susceptibility becomes:

$$\chi(T,H) = -\frac{1}{V}\frac{\partial^2 F(T,H)}{\partial H^2}. \tag{2.6}$$

The magnetic induction B (also called magnetic flux density) is the sum of the magnetization and the external magnetic field:

$$B = \mu_0(H + M) = \mu_0(H + \chi H) = \mu H, \tag{2.7}$$

where μ_0 is the magnetic constant of the vacuum and μ is the magnetic permeability of the material. The magnetic permeability of air is $\simeq \mu_0$. In the following, to simplify the notations, the magnetic induction B will be called "magnetic field", since there will be no risk of confusion with the actual magnetic field H.

2.1.2 Paramagnetism

The magnetic moment of an isolated ion (or atom) $\mathbf{m}_{ion}$ is given by

$$\mathbf{m}_{ion} = \mu_B(\mathbf{L} + \mathbf{S}) = g\mu_B\mathbf{J}, \tag{2.8}$$

where $\mathbf{L}$ is the total orbital angular momentum, $\mathbf{S}$ the total spin angular momentum, $\mathbf{J} = \mathbf{L} + \mathbf{S}$ the total angular momentum of the ion, g the Landé factor, and μ_B the Bohr magneton. The magnetization, the total magnetic moment per unit of volume, of a lattice of magnetic moments is given by:

$$\mathbf{M} = \sum_{i}^{N} \mathbf{m}_{ion}^{i}/V, \tag{2.9}$$

where N is the number of lattice sites, $\mathbf{m}_{ion}^{i}$ is the magnetic moment of the ion at the lattice site i, and V is the volume of the lattice.

A paramagnet is a magnetic material, whose magnetic moments are disordered. Paramagnets have a positive magnetic susceptibility $\chi > 0$. The paramagnetic susceptibility χ of a lattice of N non-interacting magnetic ions (localized picture) is given by the Curie law:

$$\chi = g^2 J(J+1)\frac{N}{V}\frac{\mu_B}{3k_BT} \equiv \frac{C}{T}, \tag{2.10}$$

where k_B the Boltzman constant, T the temperature, and C the Curie constant. A temperature dependence $\chi = C/T$ is found in many materials. However, many intermetallic compounds of rare-earth elements exhibits a Curie-Weiss law:

$$\chi = \frac{C}{T - \theta_p}, \tag{2.11}$$

where θ_p is the paramagnetic Curie-Weiss temperature. Usually, θ_p is related to intersite magnetic correlations, and a magnetically ordered state is often observed at low temperatures (cf. Subsect. 2.1.3).
The spin paramagnetism of a free-electron gas (itinerant picture), can be described by the Pauli susceptibility:

$$\chi_{Pauli} = \frac{3n\mu_B^2}{2k_BT_F}, \tag{2.12}$$

where T_F is the Fermi temperature and n is the density of electrons.

2.1.3 Ferro- and antiferromagnetism

Various magnetic compounds have ordered ground states, which means that the magnetic moments of the d- or f-electrons order spontaneously, when the temperature falls below a characteristic temperature. In a localized picture, the ordering is induced by intersite correlations between the localized magnetic moments, which become predominant compared to thermal fluctuations (supporting disorder) as the temperature falls below the characteristic temperature. In the case of a ferromagnetic material, all magnetic moments are ordered in one direction [↑↑↑↑] at temperatures below the Curie temperature T_C. The order in an antiferromagnetic material consists of two antiparallel ferromagnetic sub-lattices [↑↓↑↓↑↓] and occurs at temperatures below the Néel temperature T_N. More complex types of magnetic order are possible (for example ordering within commensurate, incommensurate, or multiple wavevectors, ferri- and antiferrimagnetic order,..).
Magnetic order is also possible in metals which can be described by an itinerant picture. For example, the Stoner model [Stoner 1938] describes itinerant ferromagnetism by an enhanced Pauli paramagnetism:

$$\chi_{Stoner} = \frac{\chi_{Pauli}}{1 - \alpha\chi_{Pauli}}, \tag{2.13}$$

where α is the Stoner factor determined within a molecular-mean-field approximation. Ferromagnetism appears, when the Stoner condition:

$$1 - \alpha\chi_{Pauli} < 0 \tag{2.14}$$

$$\Leftrightarrow 2\alpha\mu_B^2 D(\epsilon_F) > 1, \tag{2.15}$$

where $D(\epsilon_F)$ is the density of states at the Fermi level ϵ_F, is fulfilled. A review on models of itinerant ferro- and antiferromagnets developed within the mean-field theory can be found in [Moriya 1985].

2.2 Fermi liquid theory

Heavy-fermion low-temperature behavior can be generally described by the Landau theory of Fermi liquids [Landau 1957, Leggett 1975]. This theory (see [Enss and Hunklinger 2005] for a detailed review) allows to describe a system of strongly interacting particles onto a system of non-interacting particles with re-normalized parameters. The theory introduces quasi-particles with a re-normalized effective mass m^*, which is defined in terms of Landau parameters by:

$$m^* = m_0(1 + \frac{F_1^s}{3}), \tag{2.16}$$

where F_1^s is the symmetric Landau parameter and m_0 is the free electron mass. The density of states $D(\epsilon)$ of electrons at the Fermi level ϵ_F is also re-normalized:

$$D(\epsilon_F) = \frac{m^* k_F}{\pi^2 \hbar^2} = \frac{m_0 k_F}{\pi^2 \hbar^2}(1 + \frac{F_1^s}{3}), \tag{2.17}$$

where k_F is the wavevector at the Fermi level and $\hbar$ is the Planck constant reduced by 2π. The Pauli susceptibility χ_{Pauli} is given by:

$$\chi_{Pauli} = \frac{\mu_0 \mu_B m^* k_F}{\pi^2 \hbar^2} \frac{1}{1 + F_0^a}, \tag{2.18}$$

where F_0^a the asymmetric Landau parameter. The Sommerfeld coefficient γ, which is equal to the specific heat C_p over the temperature T in the limit of zero-temperature, is given by:

$$\gamma = \lim_{T \to 0} \frac{C_p}{T} = \frac{m^* k_F k_B^2}{3\hbar^2}. \tag{2.19}$$

The thermodynamic functions are enhanced due to the effective mass, which is itself enhanced due to the electronic interactions. In a non-interacting electron gas, the Wilson ratio R_W, relating the magnetic susceptibility to the electronic component of the specific heat is $R_W = 1$. The Wilson ratio of an interacting system becomes:

$$R_W = \frac{\chi}{\gamma} \frac{\pi^2 k_B^2}{3\mu_0 \mu_B} = \frac{1}{1 + F_0^a}. \tag{2.20}$$

In a Fermi liquid, the electronic resistivity ρ as function of the temperature T is given by

$$\rho(T) = \rho_0 + AT^2, \tag{2.21}$$

where $\rho_0 = \rho(T \to 0)$ is the residual resistivity and the term AT^2 is due to the electronic interactions. $\sqrt{A}$ is proportional to the density of states at the Fermi level and to the effective mass:

$$\sqrt{A} \propto D(\epsilon_F) \propto m^* \tag{2.22}$$

Kadowaki and Woods [Kadowaki and Woods 1986] emphasized the importance of the universal relationship between A and γ^2. The Kadowaki-Woods ratio:

$$R_{KW} = \frac{A}{\gamma^2} \tag{2.23}$$

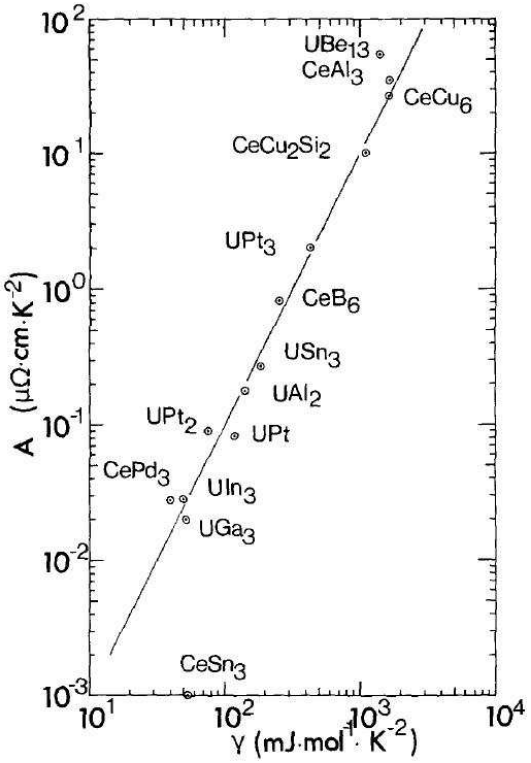

Figure 2.1: log-log-plot of the quadratic coefficient A in the resistivity versus the Sommerfeld coefficient for typical heavy-fermion systems. Figure taken from [Kadowaki and Woods 1986].

is constant within the families of transition metals and heavy-fermion compounds, as shown in Figure 2.1. The Kadowaki-Woods ratio of heavy-fermions is generally close to $1.0 \cdot 10^{-5}$ $\mu\Omega$.cm(mol.K/mJ)^2, which is about 25 times larger than that of transition metals [Kadowaki and Woods 1986].

2.3 Heavy-fermion theory

2.3.1 Kondo effect

In a metal alloy with dilute magnetic impurities (e.g., Fe-impurities in an Au-lattice), the electrons of the conduction band scatter off on the magnetic moments of the impurities, which are ions with non-zero magnetic moments from the d- or f-shells. This scattering mechanism, called the Kondo effect, induces an enhancement of the electric resistivity, when the temperature is reduced, as shown in Figure 2.2. To take this mechanism into account, Kondo [Kondo 1964] added the perturbation term H_K to the Hamiltonian:

$$H_K = -2J_K \mathbf{S} \cdot \mathbf{s}, \tag{2.24}$$

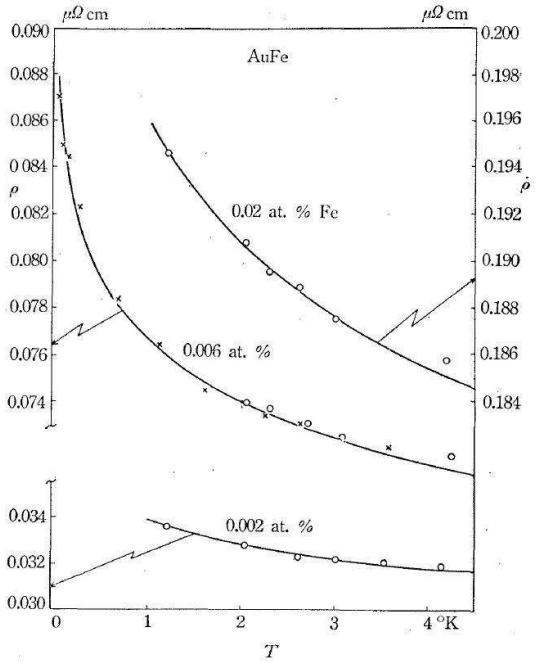

Figure 2.2: Electric resistivity versus the temperature of AuFe with different Fe concentrations. Lines are fits to the data using the Kondo model. Figure taken from [Kondo 1964].

where J_K is the Kondo exchange coupling, and where $\mathbf{S}$ and $\mathbf{s}$ are the spin moments of a localized and a conduction electron, respectively. The hybridization of the conduction electrons with the f-electrons due to the Kondo effect induces a peak in the density of states $D(\epsilon_F)$ at the Fermi enegry ϵ_F, with the characteristic energy:

$$k_B T_K \propto \exp\left(-\frac{1}{D(\epsilon_F) J_K}\right). \tag{2.25}$$

The contribution to the resistivity due to the Kondo effect developed by [Kondo 1964] is:

$$\rho_{Kondo} = \frac{3\pi m^* J^2 S(S+1)}{2e^2\hbar\epsilon_F}\left[1 - 4J_K D(\epsilon_F)\log\left(\frac{k_B T}{d}\right)\right], \tag{2.26}$$

where J and S are the total and spin momentum of the impurity, respectively, and d is a cut-off parameter. The total resistivity at low temperatures can be approximated by [Kondo 1964]:

$$\rho = a_{e-ph}T^5 + c_{Kondo}R_0 - c_{Kondo}R_1\log\left(\frac{k_B T}{d}\right), \tag{2.27}$$

where a_{e-ph}, c_{Kondo}, R_0, and R_1 are material constants. The term $a_{e-ph}T^5$ is due to electron-phonon scattering. Due to the Kondo effect, the resistivity exhibits a

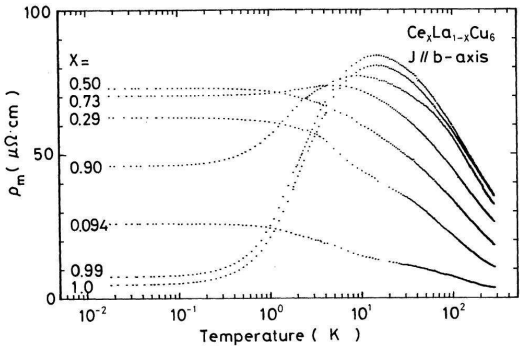

Figure 2.3: Temperature dependence of the magnetic resistivity in $Ce_xLa_{1-x}Cu_6$. Figure taken from [Sumiyama 1986].

minimum at:

$$T_{min} = \left(\frac{R_1}{5a_{e-ph}}\right)^{1/5} c_{Kondo}^{1/5}. \tag{2.28}$$

2.3.2 Kondo lattice and RKKY-interaction

The temperature-dependence of the resistivity described by Kondo [Kondo 1964] is valuable for metals with dilute magnetic impurities. A system with dense magnetic moments also behaves like diluted magnetic moments as long as the temperature is above the Kondo temperature T_K. For high impurity concentrations, the localized magnetic moments interact indirectly through the electron cloud of the conduction band, which is the RKKY-interaction (from Rudermann, Kittel, Kasuya, and Yosida), first described by Ruderman and Kittel [Ruderman and Kittel 1954] and then by Kasuya [Kasuya 1956] and Yosida [Yosida 1957]. This long-range interaction favors magnetic order. At low temperature, the electronic interactions lead to a coherent scattering of the conduction electrons and a strong reduction of the resistivity is observed as shown in Figure 2.3. A heavy-fermion material can be described as a Kondo lattice, where the magnetic moments are not randomly-distributed impurities, but situated on regular positions of the metallic lattice. Here, the RKKY-interaction tends to induce ordered ground states of the localized moments. The high effective masses of heavy-fermion systems are related to the scattering off of the conduction electrons on the dense magnetic moments of the Kondo lattice.
The characteristic energy of the RKKY-interaction is:

$$k_B T_{RKKY} = J_K^2 D(\epsilon_F) \frac{\cos(k_F r)}{k_F r}, \tag{2.29}$$

where r is the distance between two coupled f-sites. The strength of the Kondo effect and RKKY-interaction depends on the exchange energy J_K between the wave func-

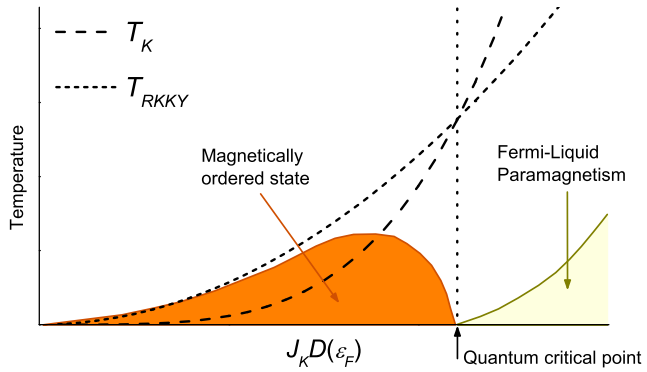

Figure 2.4: Doniach's phase diagram.

tion of the conduction electrons and that of the localized f-electrons. The ground state of the system is a direct consequence of the competition between the Kondo scattering and the RKKY-interaction, as illustrated by the Doniach's phase diagram [Doniach 1977] shown in Figure 2.4, and where T_K and T_{RKKY} are plotted as function of $J_K D(\epsilon_F)$. Experimentally, a quantum critical point can be reached using a tuning parameter, e.g. hydrostatic pressure or chemical pressure (doping), which drives a modification of $J_K D(\epsilon_F)$ and thus the quantum mechanic properties of the system. The transition between the magnetically-ordered state and the paramagnetic state occurs at the point, where $T_{RKKY} = T_K$ in the phase diagram, which is a quantum critical point, i.e., a transition between two quantum states occurring at zero temperature. Generally, heavy-fermion systems are located close to quantum critical points.

2.3.3 Quantum criticality

A quantum critical point is a singular feature in the phase diagram of matter at zero temperature [Sachdev 1999]. It occurs at the point of the phase diagram, where the transition temperature of an ordered phase is driven to zero by a tuning parameter, as pressure, chemical doping or an external magnetic field. Whereas thermal phase transitions occur at finite temperatures, where thermal fluctuations become critical, quantum phase transitions are driven by zero-temperature quantum fluctuations. The influence of a quantum critical point expands over a wide region of the phase diagram and effects of quantum criticality can be observed at finite temperatures above the quantum critical point. Quantum critical fluctuations can significantly transform the properties of a metal leading to unconventional behaviors such as that of non-fermi-liquids (cf. [Millis 1993, Lonzarich 1997]).

2.4 Magnetoresistivity of metals

The study of magnetic field effects on transport properties is a rich tool for the investigation of conducting materials [Pippard 1989]. For example, measurements of the Hall effect allow to determine the carrier concentrations and charge signs. The measurement of the resistivity in presence of an external magnetic field, i.e., the magnetoresistivity, shows a wide range of phenomena and can give insight to the Fermi surface topology. A detailed review on theory and experiment of magnetoresistivity is provided by Pippard [Pippard 1989]. The simplified development of the magnetoresistivity formalism shown here is based on [Grosso and Parravicini 2000].

2.4.1 Resistivity at zero magnetic field

The electric resistivity of metals at zero magnetic field can often be approximated by an isotrope one-band picture composed of the terms ρ_0, due to scattering off on lattice impurities and defaults, ρ_{e-ph}, due to electron-phonon scattering, and ρ_{e-e}, due to electron-electron interactions [Enss and Hunklinger 2005]:

$$\rho = \rho_0 + \rho_{e-ph} + \rho_{e-e}. \tag{2.30}$$

- ρ_0, the residual resistivity, is constant over all temperatures and depends on the sample quality only. ρ_0 is given by:

  $$\rho_0 = \frac{m^*}{ne\tau}, \tag{2.31}$$

  where n is the charge carrier density and τ the relaxation time, which corresponds to the mean value of the time between two consecutive electron-impurity collisions. The mean-free-path l between two consecutive collisions is given by:

  $$l = v_F\tau = \frac{\hbar k_F}{ne\rho_0}, \tag{2.32}$$

  where v_F is the charge carrier velocity at the Fermi surface.

- The phonon-term of the resistivity ρ_{e-ph} can be approximated by:

  $\rho_{e-ph}(T) \propto T^5$, for $T < T_D$,

  and $\rho_{e-ph}(T) \propto T$, for $T >> T_D$,

  where T_D is the Debye temperature.

- In a Fermi liquid, the electron-electron diffusion becomes dominant at low temperatures and can be approximated by:

$$\rho_{e-e} = AT^2, \tag{2.33}$$

  where $\sqrt{A} \propto m^*$ (cf. Sect. 2.2).

Considering only the electron-impurity diffusion, the electric conductivity at zero magnetic field is given by:

$$\sigma_0 = \frac{1}{\rho_0} = \frac{ne^2\tau}{m^*}, \tag{2.34}$$

and the mobility μ of the electrons can be defined by:

$$\mu = \frac{e\tau}{m^*}. \tag{2.35}$$

2.4.2 One-electron-band in a magnetic field

In this section, we consider an isotropic one-electron-band metal, and we assume that the scattering time, i.e, τ, is independent from the magnetic field. The zero-field conductivity and resistivity are controlled by the relaxation time τ:

$$\sigma_{x,x}(B=0) = 1/\rho_{x,x}(B=0) = \tau\frac{ne^2}{m^*}. \tag{2.36}$$

In a magnetic field $\mathbf{B} = B_z\mathbf{z}$, the particles with a charge q are deflected from their linear trajectories by the Lorentz force $F_L = q\mathbf{v} \times \mathbf{B}$. In a spherical one-electron band, the electrons follow orbital trajectories perpendicular to the magnetic field, with the cyclotron frequency:

$$\omega_c = \frac{eB}{m^*}. \tag{2.37}$$

From equations 2.35 and 2.37 we extract the mobility:

$$\mu = \frac{\omega_c\tau}{B}. \tag{2.38}$$

From equations 2.36 and 2.37 we extract:

$$\omega_c\tau = \frac{B\sigma_{x,x}(B=0)}{ne}, \tag{2.39}$$

which is also the mean angle between two consecutive electron-impurity collisions. No significant magnetoresistance is expected unless $\omega_c\tau > 1$. For a simple spherical

electron band in a magnetic field, considering only an electron-impurity scattering mechanism, the conductivity $\hat{\boldsymbol{\sigma}}$ and the resistivity $\hat{\boldsymbol{\rho}}$ tensors are given by:

$$\hat{\boldsymbol{\sigma}} = \frac{ne^2\tau}{m^*}\frac{1}{1+(\omega_c\tau)^2}\begin{pmatrix} 1 & \omega_c\tau & 0 \\ -\omega_c\tau & 1 & 0 \\ 0 & 0 & 1+(\omega_c\tau)^2 \end{pmatrix}, \tag{2.40}$$

$$\text{and} \quad \hat{\boldsymbol{\rho}} = \hat{\boldsymbol{\sigma}}^{-1} = \frac{m^*}{ne^2\tau}\begin{pmatrix} 1 & -\omega_c\tau & 0 \\ \omega_c\tau & 1 & 0 \\ 0 & 0 & 1 \end{pmatrix}. \tag{2.41}$$

The transverse resistivity, which is the first or the second diagonal component of the tensor in Equation 2.41 (i.e. $\rho_{x,x}$ or $\rho_{y,y}$), is given by:

$$\rho_{x,x}(B) = \rho_{y,y}(B) = 1/\sigma_{x,x}(B=0) = \frac{m^*}{ne^2\tau}. \tag{2.42}$$

Thus, in a spherical one-band metal with a constant relaxation time, the transverse resistivity $\rho_{x,x}$ turns out to be field-independent and the electric current density is equal to that at zero field. In fact, the Lorentz force induces a Hall voltage in the conductor perpendicularly to the current density and the magnetic field, and the forces due to the Hall and Lorentz effects on the electron compensate each other perfectly. The Hall resistivity is defined as one of the off-diagonal components (i.e. $\rho_{y,x}$ or $\rho_{x,y}$) of the tensor in Equation 2.41:

$$\rho_{y,x} = -\rho_{x,y} = \frac{-\omega_c\tau}{\sigma(B=0)} = \frac{-B}{ne}. \tag{2.43}$$

The tangent of the Hall angle, which is the angle between the electric field $\mathbf{E}$ and electric current density $\mathbf{J}$, is given by:

$$\tan\theta_H = \frac{\rho_{x,y}}{\rho_{x,x}} = \omega_c\tau, \tag{2.44}$$

and the Hall constant is defined as:

$$R_H = \frac{\rho_{y,x}}{B} = -\frac{1}{ne}. \tag{2.45}$$

In the case of an isotropic one-band metal, the Hall constant is independent of both the effective mass and the relaxation time, and it depends only on the carrier density n. A negative Hall constant indicates electron-type charge carriers (case considered here) and a positive Hall constant indicates hole-type charge carriers. In the case of a hole-band, the off-diagonal elements of the conductivity (Eq. 2.40) and resistivity (Eq. 2.41) tensors have opposite signs than that in the case of an electron-band.

2.4.3 Electron-hole-band in a magnetic field

In real metals, multiple bands with anisotropic Fermi surfaces have to be taken into account. The simplest case of multiple-band structure is the isotropic two-band model, within the approximation of a band structure made of two spherical bands, one of electron-type and one of hole-type, with the effective masses m_e^* and m_h^*, the constant relaxation times τ_e and τ_h, and the carrier densities n_e and n_h, respectively. The conductivity tensor of such a system is the sum of the electron and the hole conductivity tensors $\hat{\boldsymbol{\sigma}}_e$ and $\hat{\boldsymbol{\sigma}}_h$ (cf. Sect. 2.4.2), respectively:

$$\hat{\boldsymbol{\sigma}} = \hat{\boldsymbol{\sigma}}_e + \hat{\boldsymbol{\sigma}}_h, \tag{2.46}$$

and the electron and hole mobilities are given by:

$$\mu_e = \frac{e\tau_e}{m_e^*}, \tag{2.47}$$

$$\mu_h = \frac{e\tau_h}{m_h^*}, \tag{2.48}$$

$$\tag{2.49}$$

respectively. The field-induced variation of the transverse resistivity is given by:

$$\Delta\rho_{x,x}(B) = \rho_{x,x}(B) - \rho_{x,x}(B=0), \tag{2.50}$$

which can be reformulated as:

$$\frac{\Delta\rho_{x,x}(B)}{\rho_{x,x}(B=0)} = \frac{(\mu_e+\mu_h)^2\mu_e\mu_h n_e n_h B^2}{(n_e\mu_e+n_h\mu_h)^2+\mu_e^2\mu_h^2(n_e-n_h)^2B^2}, \tag{2.51}$$

and the Hall constant is given by:

$$R_H(B) = \frac{1}{e}\frac{n_h\mu_h^2 - n_e\mu_e^2 - \mu_e^2\mu_h^2(n_e-n_h)B^2}{(n_e\mu_e+n_h\mu_h)^2+\mu_e^2\mu_h^2(n_e-n_h)^2B^2}. \tag{2.52}$$

This case yields a field-dependent transverse resistivity $\Delta\rho_{x,x}(B)$ (often called transverse magnetoresistivity or orbital magnetoresistivity). The strength of the variation of $\Delta\rho_{x,x}$ with the magnetic field depends on the carrier mobility, thereby on the relaxation time τ, and on the effective mass m^*. In this simplified picture, three particular limits can be distinguished:

- In the low-field limit, i.e., $\omega_c\tau << 1$, the magnetoresistivity (Eq. 2.51) can be approximated by:

$$\Delta\rho_{x,x}(B) \propto B^2, \tag{2.53}$$

and the Hall constant (Eq. 2.52) by:

$$R_H(B) = \frac{1}{e}\frac{n_h\mu_h^2 - n_e\mu_e^2}{(n_e\mu_e + n_h\mu_h)^2}. \tag{2.54}$$

- In the high-field limit, i.e., for $\omega_c\tau >> 1$, the magnetoresistivity saturates and Equation 2.51 becomes:

$$\frac{\Delta\rho_{x,x}(B)}{\rho_{x,x}(B=0)} = \frac{(\mu_e + \mu_h)^2 n_e n_h}{\mu_e\mu_h(n_e - n_h)^2}, \tag{2.55}$$

and the Hall constant (Eq. 2.52) becomes:

$$R_H(B) = \frac{-1}{e(n_e - n_h)}, \tag{2.56}$$

which depends on the difference of the densities of electrons and holes only. Thus, the Hall constant in the high-field limit indicates the majority carrier type.

- In the particular case of a compensated metal, i.e., for $n_e = n_h = n$, no saturation of the magnetoresistivity occurs at high field and Equations 2.51 and 2.52 become:

$$\frac{\Delta\rho_{x,x}(B)}{\rho_{x,x}(B=0)} = \mu_e\mu_h B^2 = (\omega_c^e\tau_e)(\omega_c^h\tau_h), \tag{2.57}$$

and

$$R_H(B) = \frac{1}{ne}\frac{\mu_h - \mu_e}{\mu_h + \mu_e}, \tag{2.58}$$

respectively. For the case of a compensated metal, the sign of the Hall constant reflects which type of carriers has the highest mobility.

In compensated metals with closed Fermi surfaces, the magnetoresistivity increases quadratically by the magnetic field for any field orientation. In uncompensated metals with closed Fermi surfaces, the magnetoresistivity saturates at high fields for any orientation of the magnetic field. In metals with open Fermi surfaces, i.e., where a cyclotron orbit is open for a given field direction, the high-field magnetoresistivity depends on the current direction. It increases quadratically with the magnetic field

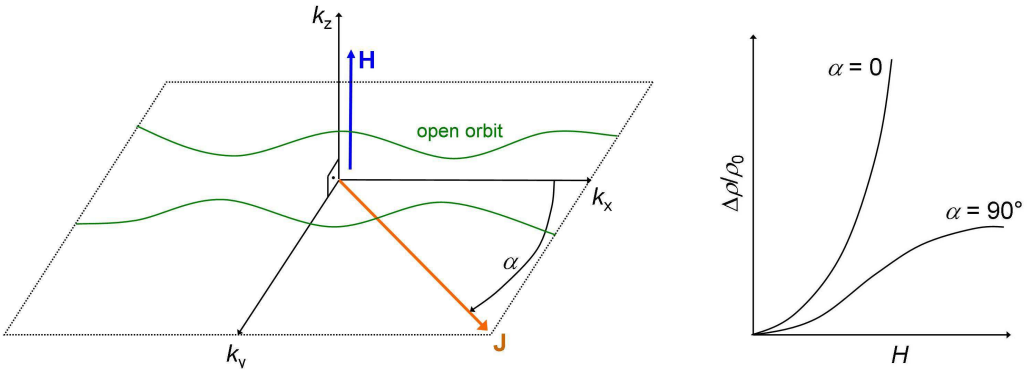

Figure 2.5: Projection of the $(\mathbf{k}_x,\mathbf{k}_y)$-plane of an open orbit perpendicular to the magnetic field and resulting transverse magnetoresistivity for different directions of the current in the plane.

when the current density is parallel to the open direction of the orbit but saturates at high fields when the current density is perpendicular to it (see Fig. 2.5).

2.4.4 Kohler's rule

The magnetoresistivity of many metals can be described by the Kohler's rule $\Delta\rho/\rho(B=0,T) = F_K[B/\rho(B=0,T)]$, where the function F_K depends on the Fermi surface and on the orientations of the magnetic field and measuring current [Kohler 1938]. The Kohler's rule implies that all $\Delta\rho/\rho(B=0,T)$ versus $B/\rho(B=0,T)$ plots of the magnetoresistivity data from samples of different qualities (same compound), or from the same sample at different temperatures, fall on the same curve. The Kohler's rule applies within the approximation of a unique relaxation time τ for all bands, which controls the sample- and temperature-dependencies of ρ.

• In the case of a multi-band metal, the conductivity is the sum of the conductivities of all bands. Assuming a unique relaxation time τ, the conductivity of a multi-band metal in $B=0$ (cf. Eq. 2.34 in the case of a single-electron-band) is given by:

$$\sigma_{x,x}(B=0) = \sum_i \sigma^i_{x,x}(B=0) = \tau \sum_i \frac{n_i q_i^2}{m_i^*}, \tag{2.59}$$

where $\sigma^i_{x,x}(B=0)$ and q_i are the zero-field conductivity and the charge, respectively, of band i, and the zero-field resistivity is given by:

$$\rho_{x,x}(B=0) = 1/\sigma_{x,x}(B=0) = \frac{1}{\tau}\left(\sum_i \frac{n_i q_i^2}{m_i^*}\right)^{-1}. \tag{2.60}$$

• In a magnetic field $B = B_z\mathbf{e}_z$, the conductivity tensor (cf. Eq. 2.40 in the case of

a single-electron-band) becomes:

$$\hat{\boldsymbol{\sigma}}(B) = \sum_i \hat{\boldsymbol{\sigma}}_i(B) = \sum_i \sigma^i_{x,x}(B=0)\hat{\mathbf{F}}(\omega^i_c\tau), \tag{2.61}$$

where $\hat{\boldsymbol{\sigma}}_i$ is the conductivity tensor of band i and $\hat{\mathbf{F}}$ is a tensor function. With $\sigma^i_{x,x}(B=0) = \tau n_i q_i^2/m_i^*$ (cf. Eq. 2.34) and $\omega^i_c = q_i B/m_i^*$ (cf. Eq. 2.37) follows:

$$\hat{\boldsymbol{\sigma}}(B) = \tau \sum_i \frac{q_i^2 n_i}{m_i^*}\hat{\mathbf{F}}(\frac{q_i^2}{m_i^*}\tau B) = \tau \sum_i \hat{\mathbf{F}}_i(\tau B), \tag{2.62}$$

where the tensor function $\hat{\mathbf{F}}_i$ is defined by $\hat{\mathbf{F}}_i(\tau B) = \frac{q_i^2 n_i}{m_i^*}\hat{\mathbf{F}}(\frac{q_i^2}{m_i^*}\tau B)$. By introducing the tensor function $\hat{\mathbf{F}}'(x) = \sum_i \hat{\mathbf{F}}_i(x)$ follows:

$$\hat{\boldsymbol{\sigma}}(B) = \tau\hat{\mathbf{F}}'(\tau B), \tag{2.63}$$

and the resistivity tensor is given by:

$$\hat{\boldsymbol{\rho}}(B) = \hat{\boldsymbol{\sigma}}^{-1}(B) = \frac{1}{\tau}\hat{\mathbf{F}}'^{-1}(\tau B). \tag{2.64}$$

From Equation (2.60) we finally extract the Kohler's rule:

$$\hat{\boldsymbol{\rho}}(B) = \rho_{x,x}(B=0)\hat{\mathbf{F}}_K\left[\frac{B}{\rho_{x,x}(B=0)}\right], \tag{2.65}$$

where $\hat{\mathbf{F}}_K(\frac{B}{\rho_{x,x}(B=0)}) = \frac{1}{\tau\rho_{x,x}(B=0)}\hat{\mathbf{F}}'^{-1}(\tau B)$.

• In the case of a compensated and isotrope two-band model with a unique relaxation time we can generalize Equation (2.57) to the case of a temperature-dependent resistivity:

$$\frac{\Delta\rho_{x,x}(B,T)}{\rho_{x,x}(B=0,T)} = \mu_e(T)\mu_h(T)B^2 = \frac{\tau(T)^2e^2}{m_e^*m_h^*}B^2 = c\left[\frac{B}{\rho_{x,x}(B=0,T)}\right]^2, \tag{2.66}$$

where $c = [e^2m_e^*m_h^*(n_e/m_e^* + n_h/m_h^*)^2]^{-1}$ is independent from the sample quality and the temperature. We will see in Chapter 7, that, for $\mathbf{H} \parallel \mathbf{c}$, the low-field magnetoresistivity of URu_2Si_2 exhibits a B^2-behavior and the approximated formula:

$$\frac{\Delta\rho_{x,x}(B,T)}{\rho_{x,x}(B=0,T)} = \mu(T)^2B^2, \tag{2.67}$$

will be used to extract the temperature- and sample-dependence of an "average" mobility $\mu = e\tau/m^*$ over all bands.

2.5 Quantum oscillations

Quantum oscillations of macroscopic quantities of materials are due to the quantization of the cyclotron movement of electrons in magnetic fields. First observed in the magnetization of bismuth by de Haas and van Alphen [de Haas and van Alphen 1930] and in its magnetoresistivity by Shubnikov and de Haas [Shubnikov and de Haas 1930], quantum oscillations have been predicted theoretically almost at the same time by Landau [Landau 1930]. Lifshitz and Kosevich [Lifshitz and Kosevich 1955] developed an exact theory of the de Haas-van Alphen effect. Quantum oscillations are powerful tool to probe the electronic properties of metals, as the Fermi surfaces, and their effective masses and Dingle temperatures.

2.5.1 Quantization of the electron motion in magnetic fields

The movement of an electron in a strong magnetic field is quantized in the manner that the surface, which is enclosed by the electron's orbit in the reciprocal space, can only have discrete values distant $2\pi eB/\hbar$ and the electron's energy can only have discrete values distant $\hbar\omega_c$. Quantization effects in magnetic fields are observed within the condition [Shoenberg 1984]:

$$\hbar\omega_c >> k_B T. \tag{2.68}$$

Otherwise thermal fluctuations cover quantization effects. The cyclotron frequency ω_c is given by (Eq. 2.37):

$$\omega_c = \frac{eB}{m_c^*}, \tag{2.69}$$

where m_c^* is the cyclotron effective mass of the quasi-particles (cf. Eq. 2.37). The cyclotron effective mass is given by:

$$m_c^* = \frac{\hbar^2}{2\pi}\left(\frac{\partial S_k}{\partial \epsilon}\right)_k, \tag{2.70}$$

where S_k is the area enclosed by the orbital trajectory in the k-space. In a semi-classical approach, the Bohr-Sommerfeld condition for the quantization of a periodic motion is:

$$\oint \mathbf{p}\cdot\mathbf{r} = 2\pi\hbar(n+\gamma), \tag{2.71}$$

where p is the impulsion, $n = 0, 1, -1, 2, -2, ...$, and γ is a phase constant ($\gamma = 1/2$ for electrons). The magnetic flux trough a surface S_r enclosed by a conductor loop in the real space is $\Phi = S_r B$, where B is the magnetic field at the center of the loop

generated by a current I through the conductor. The magnetic flux Φ through the surface S_r enclosed by the particle's trajectory in the real space is given by:

$$\oint \mathbf{p} \cdot \mathbf{r} = e\Phi \tag{2.72}$$

$$\Leftrightarrow \Phi = \frac{2\pi\hbar}{e}(n+\gamma). \tag{2.73}$$

Thus, the magnetic flux Φ through S_r is quantized in terms of universal quanta of flux $2\pi\hbar/e$. With $\Phi = S_r B$ follows from Equation(2.73) the Onsager condition [Onsager 1952] of the quantization of the surface S_k^n enclosed by the particle's trajectory in k-space:

$$S_k^n = \frac{2\pi e B}{\hbar}(n+\gamma) \tag{2.74}$$

The Hamiltonian of an electron in a magnetic field, without considering the Zeeman energy, is given by:

$$H = \frac{1}{2m_c^*}(\mathbf{p} + e\mathbf{A})^2, \tag{2.75}$$

where $\mathbf{A}$ is the vector potential of the magnetic field: $\mathbf{B} = \vec{\text{rot}}\mathbf{A}$. Solving the Schrödinger's equation leads to the Landau quantization in Landau levels of energies:

$$\epsilon_n = (n+\frac{1}{2})\hbar\omega_c + \frac{(\hbar k_z)^2}{2m_c^*}. \tag{2.76}$$

The permitted states lie on coaxial tubes in the k-space, called Landau tubes, whose cross-sections S_k^n perpendicular to $\mathbf{B}$ satisfy the Onsager condition (2.74). At zero temperature, only the states with an energy below the Fermi energy ϵ_F are occupied [see Fig. 2.6]. The number of occupied states on a Landau level decreases with increasing magnetic field and vanishes infinitely fast when the cross-section of this Landau tube approaches the extremal cross-section of the Fermi surface.

The Landau levels cross subsequently the Fermi surface with the periodicity given by:

$$T_{qo} = \Delta(1/B) = \frac{2\pi e}{\hbar S_{ext}}, \tag{2.77}$$

where S_{ext} is the extremal cross-section of the Fermi surface perpendicular to the magnetic field. The density of states $D(\epsilon)$ of free electrons in a magnetic field is given by:

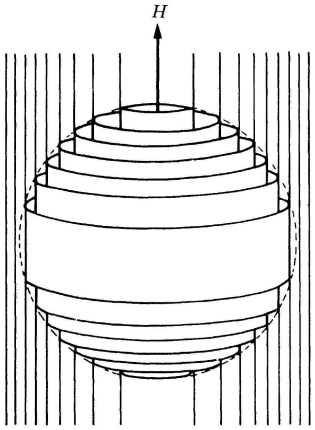

Figure 2.6: Scheme of Landau tubes in a magnetic field. The broken line indicates a spherical Fermi surface. At zero-temperature the occupied states lie within the Fermi surface. Figure taken from [Shoenberg 1984].

$$D(\epsilon) = \frac{V\omega_c\hbar}{4\pi^2}\left(\frac{2m_c^*}{\hbar}\right)^{3/2}\sum_{n=0}^{\infty}\left[\epsilon - \hbar\omega_c(n+\frac{1}{2})\right]^{1/2}, \tag{2.78}$$

and the density of states at the Fermi level $D(\epsilon_F)$ diverges when a Landau level crosses the Fermi surface, which results in a periodic variation of the free energy of the electronic system. This induces oscillatory modulations in the field-dependence of the macroscopic properties depending on $D(\epsilon_F)$, such as the magnetization, the resistivity, the heat capacity, and the ultrasonic velocity. From Equation (2.77), we obtain the relation between the extremal cross-section S_{ext} of the Fermi surface and the oscillation frequency $F = 1/T_{qo}$:

$$S_{ext} = \frac{2\pi e}{\hbar T_{qo}} = 2\pi eF/\hbar. \tag{2.79}$$

Quantum oscillations composed of several frequencies can result from multi-band structures. Also the warping of a Fermi surface sheet, with two or more extremal cross-sections perpendicular to the magnetic field, can lead to several frequencies. For example, Figure 2.7(a) shows the high-field quantum oscillations in the magnetization of the organic compound θ-$(ET)_4ZnBr_4(C_6H_4Cl_2)$ and Figure 2.7(b) shows the resulting Fourier spectra, where the frequency peaks correspond to the Fermi surface extremal cross-sections and to their harmonics and linear combinations [Béard 2012]. In a semiclassical picture, the p^{th} harmonic can be seen as the result of an electron making p turns in its Fermi surface orbit.

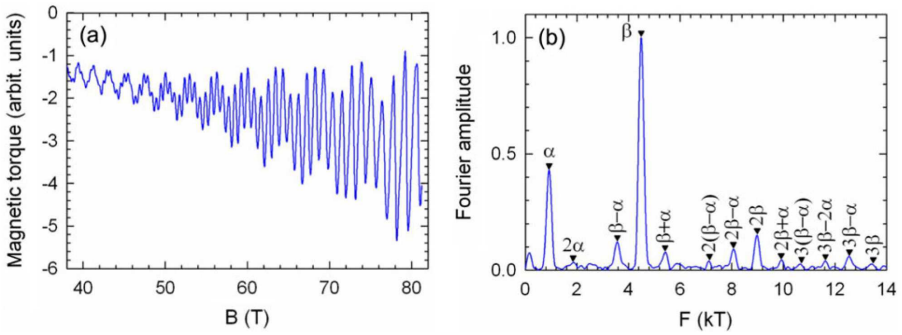

Figure 2.7: (a) De Haas-van Alphen effect in the magnetization of θ-$(ET)_4ZnBr_4(C_6H_4Cl_2)$ measured with the magnetic torque technique. (b) Resulting Fourier spectrum indicating the two fundamental frequency peaks from the Fermi surface sheets α and β and peaks from their harmonics and linear combinations. Data published in [Béard 2012].

2.5.2 The Lifshitz-Kosevich description of the de Haas-van Alphen effect

The oscillatory variation of the Gibbs thermodynamic potential by a magnetic field induces quantum oscillations in the magnetization of the material, which is called the de Haas-van Alphen effect. An exact description of the de Haas-van Alphen effect has been developed by Lifshitz and Kosevich ([Lifshitz and Kosevich 1955], see [Shoenberg 1984] for a detailed review of the theory). In this model, the oscillating part of the magnetization $\widetilde{M}$ as function of the magnetic field B and the temperature T is given by the magnetic field derivation of the oscillatory part $\widetilde{\Omega}$ of the Gibbs thermodynamic potential:

$$\widetilde{M}(B,T) = \frac{d\widetilde{\Omega}(B,T)}{dB} = \sum_i \sum_p \frac{1}{p^{3/2}} A_{i,p}(B,T) \sin\left(\frac{2\pi p F_i}{B} + \phi_i\right), \tag{2.80}$$

$$\text{where } A_{i,p}(B,T) \propto B^{1/2} \left|\frac{\partial^2 S^i_{ext}}{\partial k^2}\right|^{-1/2} R^i_T(p,B,T) R^i_D(p,B) R^i_S(p). \tag{2.81}$$

$\sum_i$ is the sum over all extremal Fermi-surface cross-sections S^i_{ext} perpendicular to B, F_i is the corresponding quantum oscillation frequency (see Eq. 2.79), and ϕ_i a phase constant. $\sum_p$ is the sum over all harmonics p and $R^i_T(p)$, $R^i_D(p)$, and $R^i_S(p)$ are damping factors due to finite temperature, electron-impurity scattering, and Zeeman splitting, respectively.
$\left|\frac{\partial^2 S^i_{ext}}{\partial k^2}\right|$ indicates the curvature of the Fermi surface in the B-direction at its extremal cross-section S^i_{ext}.

• The damping factor R_T, which is due to the smearing out of the Fermi-Dirac distribution at finite temperatures, is given by:

$$R_T^i(p,B,T) = \frac{2\pi^2 p k_B T(\hbar\omega_c^i)^{-1}}{\sinh(2\pi^2 p k_B T(\hbar\omega_c^i)^{-1})} = \frac{\alpha p m_c^{*i} T/B}{\sinh(\alpha p m_c^{*i} T/B)}, \tag{2.82}$$

where $\alpha = 2\pi^2 k_B/e\hbar$. The R_T-damping allows to extract the effective cyclotron mass m_c^{*i} of the Fermi surface branch i. To extract m_c^{*i} from the quantum oscillations in the field range $[B_1, B_2]$, one plots the amplitude $A_{p,i}$, obtained by a spectral analysis of the oscillations in the range $[B_1, B_2]$, versus the temperature T and applies a fit with the function:

$$A_{i,p}(B_{eff},T) = A_0(B_{eff})\frac{T/B_{eff}}{\sinh(\alpha p m_c^{*i} T/B_{eff})}, \tag{2.83}$$

where $B_{eff} = 2/(1/B_1 + 1/B_2)$ is the effective magnetic field and $A_0(B_{eff})$ is a fitting parameter.

• The R_D-damping factor is related to the broadening of the Landau levels due to the finite life time of the electron excitations. The life time is equivalent to the relaxation time τ, which is finite due to electron-impurity scattering in a real metal. In a perfect crystal the Landau levels would be infinitely sharp. The finite life time in real metals broadens the Landau levels according to Heisenberg's uncertainty principle, resulting in the damping factor:

$$R_D^i(p,B) = \exp\left(-\frac{\pi p}{\omega_c \tau^i}\right) = \exp\left(-\frac{\alpha p m_c^{*i} T_D^i}{B}\right), \tag{2.84}$$

where $T_D = \hbar/2\pi k_B \tau$ is the Dingle temperature. Knowing m_c^* one can extract the relaxation time τ and the Dingle temperature T_D by plotting $A_{i,p}$ versus B at a given temperature T, and fitting it with the function:

$$A_{i,p}(B) = A_0' \exp\left(-\frac{\alpha p m_c^{*i} T_D^i}{B}\right)\frac{TB^{-1/2}}{\sinh(\alpha p m_c^{*i} T/B)}, \tag{2.85}$$

where A_0' is a fitting parameter. Experimentally, one plotts $A_{i,p}$ obtained by the analysis of the oscillations over small field windows versus B_{eff}.

• The third damping factor R_S is due to the Zeeman spin splitting of a Landau level in two sub-bands with the energy difference $\Delta\epsilon = ge\hbar B/2m_0$, where g is the Landé factor:

$$R_S^i(p) = \cos\left(\frac{\pi p g m_c^{*i}}{2m_0}\right). \tag{2.86}$$

Usually, the effective mass and the Dingle temperature are extracted from the quantum oscillation data via the R_T and R_D terms. The R_S term is less frequently considered. Zeeman spin splitting of branches with different effective masses have been reported in some heavy-fermion systems (cf. [Aoki 2013]).

2.5.3 The Shubnikov-de Haas effect

It is more difficult to obtain an exact formula for the quantum oscillations in the magnetoresistivity, i.e., the Shubnikov-de Haas effect, than for that in the magnetization, i.e., the de Haas-van Alphen effect. Indeed, contrary to magnetization, magnetoresistivity is not a thermodynamic quantity and is difficult to model, due to the complex modifications of the scattering processes in an applied magnetic field. An approximative description of the Shubnikov-de Haas effect in terms of the Lifshitz-Kosevich theory can be obtained following Pippard's idea, i.e, that the scattering probability, which is the resistivity, is proportional to the number of states into which the electrons can be scattered, and thus to the density of states at the Fermi level $D(\epsilon_F)$ [Pippard 1989]. The latter depends on the magnetic field-derivative of the magnetization:

$$\widetilde{D}(\epsilon_F) \propto \left(\frac{m_c^* B}{S_{ext}}\right)^2 \frac{\partial \widetilde{M}}{\partial B}, \tag{2.87}$$

so that the oscillatory behavior of the Shubnikov-de Haas effect can be simply related to that of the de Haas-van Alphen effect. From Pippard's idea follows, for the oscillating part of the conductivity $\widetilde{\sigma}$:

$$\frac{\widetilde{\sigma}}{\sigma} \simeq \frac{\widetilde{D}}{D}, \tag{2.88}$$

where σ is the total conductivity, D the total density of states, and $\widetilde{D}$ the oscillating part of the density of states. For an isotropic case and when the amplitude of the Shubnikov-de Haas effect is small compared to the total resistivity, the relation between the oscillating conductivity $\widetilde{\sigma}$ and the oscillating resistivity $\widetilde{\rho}$ can be approximated by:

$$\frac{\widetilde{\sigma}}{\sigma} \simeq -\frac{\widetilde{\rho}}{\rho_0}, \tag{2.89}$$

where $\rho_0 = \rho(B) - \widetilde{\rho}(B)$ is the field-dependent non-oscillating background of the resistivity. Thus, within a good approximation, the amplitude $A_{i,p}(B,T)$ of the Shubnikov-de Haas oscillations is given by:

$$A_{i,p}(B,T) \propto B^{1/2} R_T^i(p,B,T) R_D^i(p,B) R_S^i(p), \tag{2.90}$$

and m_c^* and T_D can be extracted from the oscillations in the resistivity in a similar manner as that described above for the oscillations in the magnetization. In the case of an anisotropic band structure, one has to consider the conductivity and resistivity tensors $\hat{\boldsymbol{\sigma}}(B)$ and $\hat{\boldsymbol{\rho}}(B) = \hat{\boldsymbol{\sigma}}^{-1}(B)$, respectively, but usually the approximation of Equation 2.89 is sufficient for a consistent analysis.

3 Experimental Method and Setup

This chapter presents the experimental setups and procedures of the magnetization and resistivity measurements in high magnetic fields (up to 80 T) and at low temperatures (down to 100 mK). An introduction to the pulsed magnetic fields and a presentation of the LNCMI pulsed-field facility and magnets are given in Section 3.1. Section 3.2 is an introduction to the cryogenics used at the LNCMI-T. The measurements of magnetization and electric resistivity are presented in Sections 3.3 and 3.4, respectively. The characteristics of the samples studied here are presented in Section 3.5. Sections 3.6 - 3.9 give further details on the experimental techniques and problems encountered here.

3.1 Generation of pulsed magnetic fields

3.1.1 Introduction

The magnetic field $\mathbf{B}$ at position $\mathbf{r}$ generated by a current I in a conductor wire is given by the Biot-Savart law:

$$\mathbf{B} = \frac{\mu_0 I}{4\pi} \int \frac{d\mathbf{l} \times \mathbf{r}}{|\mathbf{r}|^2}, \tag{3.1}$$

where μ_0 is the vacuum permeability and $d\mathbf{l}$ the vector of an infinitesimal section of the wire. The magnetic field generated inside a long, thin conducting coil, where the length l is much greater than the diameter, can be considered as homogeneous and is given by:

$$B = \mu_0 NI/l, \tag{3.2}$$

where N is the number of turns of the coil. The magnetic flux Φ through the coil is given by:

$$\Phi = SB = \mu_0 NIS/l, \tag{3.3}$$

where S is the cross-section of the coil and the inductance L of the coil is defined as:

$$L = N\Phi/I = \mu_0 N^2 S/l. \tag{3.4}$$

The Lorentz force F_L on electrically charged particles moving in a magnetic field is induced perpendicular to the field and to the velocity of the charges. The resulting force on a conductor carring a current I in a magnetic field B is given by:

$$d\mathbf{F}_L = Id\mathbf{l} \times \mathbf{B}, \tag{3.5}$$

where dl is an infinitesimal section of the conductor. The Lorentz force induces a magnetic pressure in an electromagnet and limits the maximum field that can be generated in a magnet without damaging it.
The electromagnetic induction is the voltage induced in a conductor by a varying external magnetic field. In a uniform magnetic field, the induction generated on a conductor loop enclosing the surface S perpendicular to the field is given by:

$$U_{ind} = -\frac{d\Phi}{dt} = -S\frac{dB}{dt}. \tag{3.6}$$

To measure a magnetic field varying in time, we can use a pickup coil, generally made of a few turns of copper wire exposed to the field, and whose voltage is directly proportional to $d\Phi/dt$ (cf. Sect. 3.6).
Heating by the Joule effect in a resistive conductor is proportional to I^2. To generate the highest non-destructive magnetic fields, a strong current is sent through the magnet and is stopped before the magnet gets overheated. Pulsed magnetic fields allow in a viable, reproducible, and non-destructive manner to reach peak values of up to 80 T at the LNCMI-T (world-record: 100 T, NHMFL, USA). The pulses have a duration of several tens to hundreds of milliseconds and are generated by electric currents of several thousand amperes. Usually, the time variation of the magnetic field during such pulses is much slower than the characteristic timescales of the studied physical phenomena.

3.1.2 The LNCMI-T pulsed-field facility

Due to the high electric energy needed to be delivered during a very short duration in the pulsed magnets, the best technical solution is to store it using a capacitor bank. The capacitor banks of the main pulsed-field generator of the LNCMI-T [see Fig. 3.2(d)] have a total capacity of 48 mF and can charge a maximal voltage of 24 kV. The generator can store up to 14 MJ of electric energy and is powered by the local electricity supplier EDF. The generator is located in the basement of the LNCMI-T and controlled by an programmable logic controller (PLC), which is placed in the center of the experiment hall. For the 80-T dual-coil magnet (see

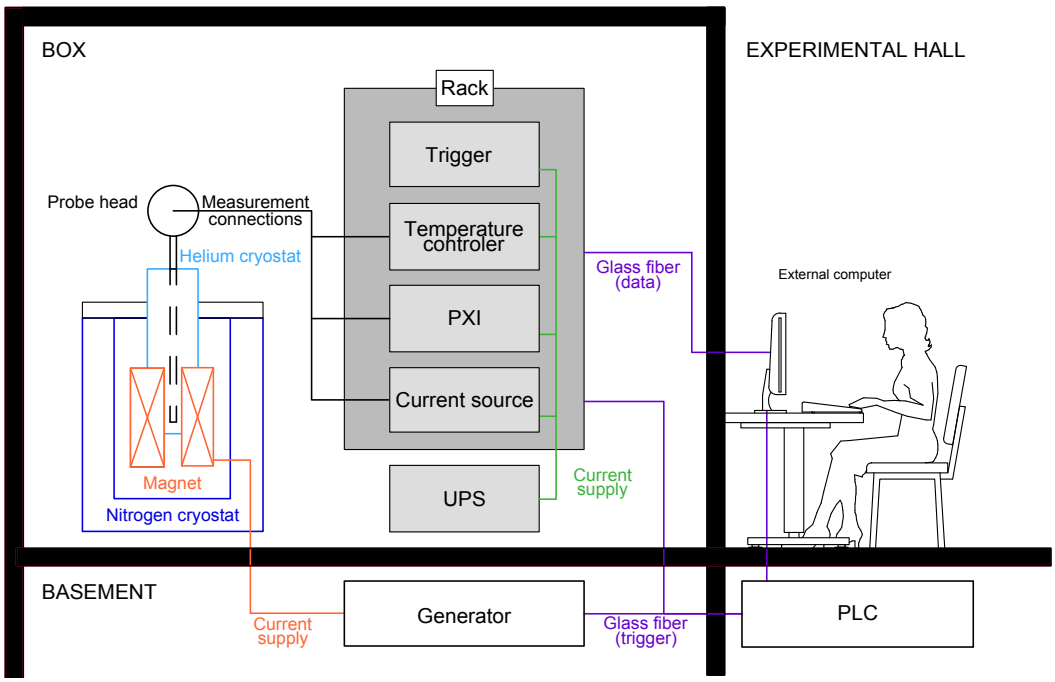

Figure 3.1: Scheme of a box with magnet, cryostats, instrumentation, generator, and experimentalist.

Sect. 3.1.3), which is made of an outer 30 T magnet and an inner 50 T magnet, a transportable 1-MJ-generator was used to provide current to the inner coil in addition of the 14-MJ-generator, which provided current to the external coil. The main generator circuit is shown in Figure 3.2(c). Computer-controlled thyristors are used to trigger the magnet pulses. The duration of the magnet pulse can be approximated as the period of the L-C-oscillation $T = 2\pi\sqrt{LC}$, where L is the inductance of the magnet and C the capacity the capacitor bank. The duration of the rise of a pulse can be approximated by $T/4 = 0.5\pi\sqrt{LC}$ and the field decreases exponentially with the time constant $\tau = L/R$, where R is the serial resistance of the crow-bar diodes and the magnet coil. At the LNCMI-T, experiments with non-destructive pulsed magnetic fields are performed in armored boxes. The setup inside a box consists of a magnet, high-voltage (24 kV) and high-current (65 kA) cables, cryogenics, an un-interruptible power supply (UPS), a measurement probe with the sample(s), and a rack containing the electric apparatus needed for the measurement. Figure 3.1 shows a scheme of such a box. The instruments inside the box and the generator in the basement are controlled via optical fibers from the experiment hall, to avoid electric contact between the inside and the outside of the box. During a measurement in a pulsed field, the box and the generator are galvanically isolated and the box is closed and interlocked, because of the high energies ($\sim 1 - 10$ MJ) and voltages (~ 10 kV) used for the field generation.

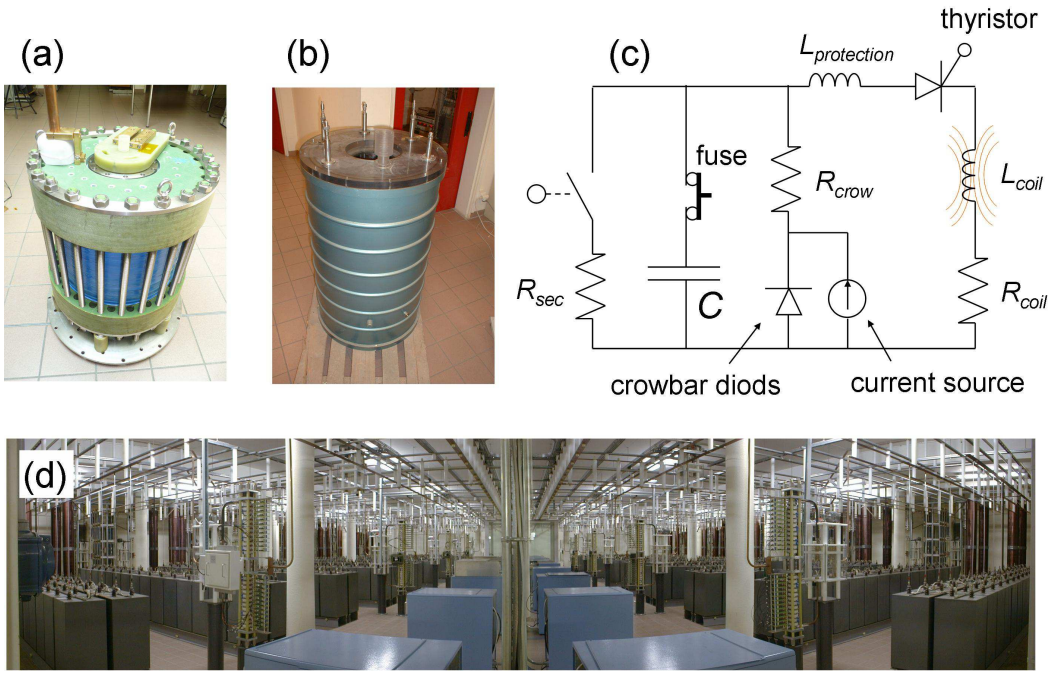

Figure 3.2: (a) 80 T magnet coil. (b) Nitrogen cryostat containing the magnet coil. (c) Electric circuit of the generator. (d) View on the capacitor bank.

3.1.3 The LNCMI-T pulsed-field magnets

The magnetization and the electric transport experiments of this work have been performed in magnetic fields up to 60 T and 80 T, respectively, generated by non-destructive pulsed field magnets of the Laboratoire National des Champs Magnétiques Intenses of Toulouse. Table 3.1 summarizes the characteristics of the magnets used here and Figure 3.3(a) shows their time profiles. The magnets are resistive conductor coils, which are immersed in a liquid Nitrogen bath in an outer cryostat [see Fig. 3.2(b)]. The magnetic pressure in the magnet during a pulse is compensated by the mechanical resistance of the coil and its reinforcement. A shot at the maximum field increases the coil temperature from 77 K (boiling point of liquid nitrogen) to $\sim$ 300 K due to the Joule effect. Temperatures higher than 300 K would strongly reduce the mechanical resistance of the materials and increase the risk of damages. With the temperature, the electrical resistance of the coil is also increased. The nitrogen bath cools down the magnet after a pulse, to reach again the temperature and resistance required for a new pulse. To increase the frequency of pulsed field shots, the cooling of the magnet is generally accelerated by pumping on the nitrogen bath (duration of cooling $\sim$ 1 h).
For the magnetization experiments, we used a (60-T, 12-mm)-coil of a copper-stainless steel alloy with a dense packing confined in a steel mantle. Here, the

Energy (MJ)	Max field (T)	inner bore diameter (mm)	diameter inside cryostat (mm)	coil type	total pulse duration [rise duration] (ms)
1.25	60	12	7	single	150 [25]
5	60	28	19/17 (^{4}He/dilution)	single	300 [55]
6	70	12	7	single	200 [32]
12 (coilex) / 1 (coilin)	80	12	7	dual coil	400 [90] (coilex) / 40 [16] coilin

Table 3.1: Characteristics of the magnets used here.

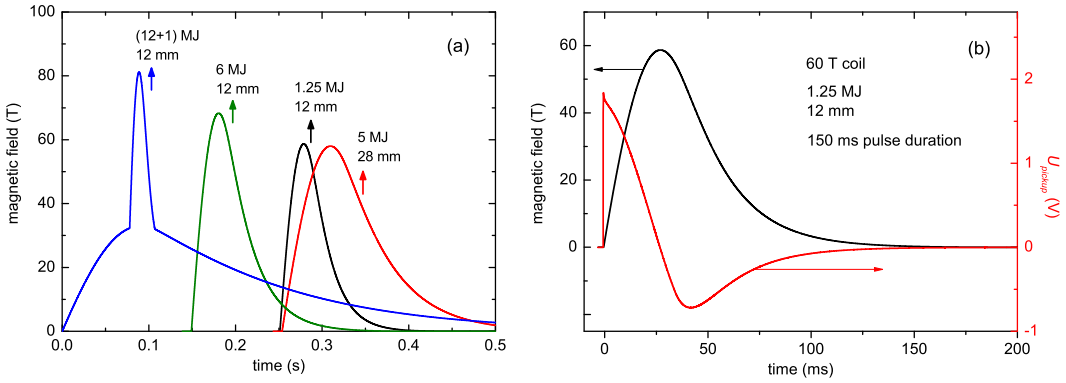

Figure 3.3: (a) Magnetic field versus time from the non-destructive pulsed field magnets of the LNCMI-T used here. (b) Magnetic field H and pickup voltage U_{pickup} versus time during a pulse from a 60 T, 12-mm inner bore magnet.

conductor itself provides a large part of the mechanical resistance. This construction results in a very low noise level in the magnetization measurements. The 60-, 70-, and 80-T magnets used for the resistivity experiments are coils of copper alloys, as Cu+Ag or Cu+Al_2O_3 (Glydcop), and are reinforced by layers of Zylon fiber, which are wound around every layer of copper wire. The 80-T magnet [see Fig. 3.2(a)] used for this work is a dual coil, made of an external coil generating a long background pulse up to 33 T and an inner coil producing a short pulse to reach a maximum of 81 T. This system allows a duration of 10.2 ms above 70 T, which is unique in the world and permits to investigate high-frequency quantum oscillations up to 80 T [Béard 2012].

3.2 Cryogenics

^{4}He fridges and a ^{3}He-^{4}He-dilution fridge, specially developed for the pulsed-field magnets of the LNCMI-T, have been used in this work to reach temperatures down to 1.4 K and 100 mK, in magnetic fields up to 80 T and 60 T, respectively. In this

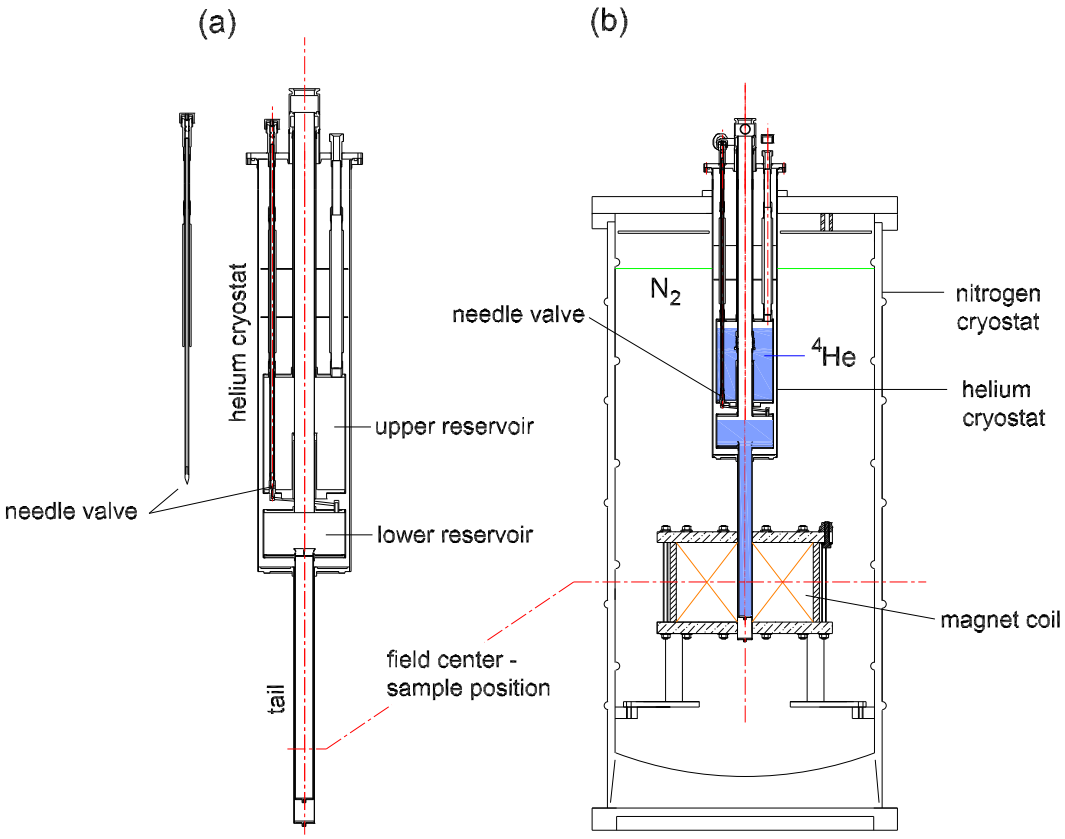

Figure 3.4: Technical drawings of (a) a helium cryostat, and (b) the ensemble of a nitrogen cryostat, a helium cryostat and a pulsed-field magnet [Nardone private com.]. The needle valve opens a capillary, which connects the upper and the lower reservoirs.

section, I present these two kinds of cryostats.

3.2.1 ^{4}He-cryostat

^{4}He fridges are provided for all types of non-destructive pulsed-field magnets of the LNCMI-T and cover temperatures from 1.4 to 300 K. Figure 3.4(a) shows a technical drawing of the nitrogen cryostat, magnet coil, and ^{4}He cryostat. The magnet and the helium cryostat are plunged in the nitrogen bath and the tail of the helium cryostat containing the sample chamber fits into the bore of the magnet. The temperature of the sample chamber is generally measured by a Cernox thermometer placed on the probe close to the samples, and is controlled by a Lakeshore 340. For measurements at temperatures above 4.2 K, the samples are in a ^{4}He atmosphere, the upper reservoir is filled with liquid helium ($T = 4.2$ K), and the needle valve is closed. The temperature T of the samples is then controlled by combining the cooling power provided by the upper reservoir and the heating power of a manganin resistance

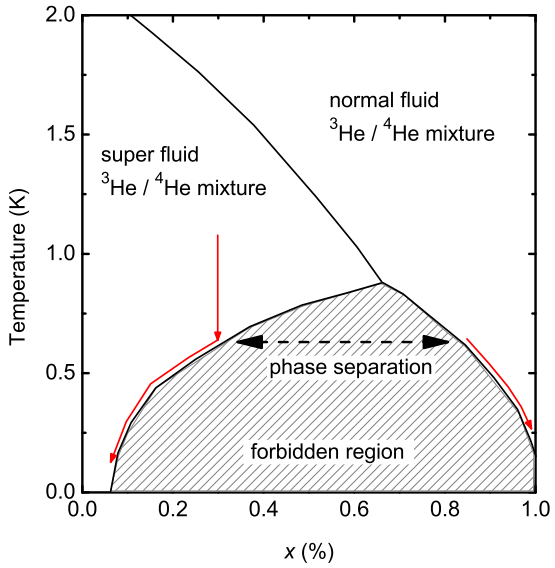

Figure 3.5: Phase diagram of the ^{3}He-^{4}He mixture, x is the ^{3}He concentration in %.

winded around the sample chamber of the cryostat. To reach $T = 4.2$ K, the lower reservoir is filled with liquid helium by opening the needle valve. Temperatures below 4.2 K and down to 1.4 K can be reached by pumping on the helium bath in the lower reservoir.

3.2.2 ^{3}He-^{4}He-dilution cryostat

The LNCMI-T is equipped with a home-made ^{3}He-^{4}He-dilution fridge, which has a non-metallic mixing chamber and can be used in a 60-T 28-mm bore pulsed magnet. The samples are immersed in the ^{3}He-^{4}He mixture and can be cooled down to 100 mK. The dilution technique is based on the cooling power generated by the heat absorption of the dilution of pure ^{3}He into a ^{3}He/^{4}He mixture.

Starting from an initial diluted concentration $x \sim 25\%$ of ^{3}He and temperature $T > 1$ K in the phase diagram of the ^{3}He-^{4}He mixture [see Fig 3.5], lowering the temperature leads to an abrupt phase separation at $T \sim 650$ mK, when reaching the boundary line of the forbidden region, inducing the formation of a concentrated phase ($x_c \sim 85\%$) and a diluted phase ($x_c \sim 25\%$). Further decreasing of the temperature reduces the ^{3}He concentration in the diluted phase and increases the ^{3}He concentration in the concentrated phase. Below $T \sim 100$ mK, the concentrated phase is almost a pure ^{3}He-phase and the diluted phase has an almost constant ^{3}He-concentration ($x \sim 0.06$) [Pobell 1992].

Figure 3.6(a) shows a technical drawing of the dilution fridge of the LNCMI-T and Figure 3.6(b) shows a scheme of its helium cycle [Nardone private com.]. A pump connected to the still separates the ^{3}He from the diluted phase, due to the higher

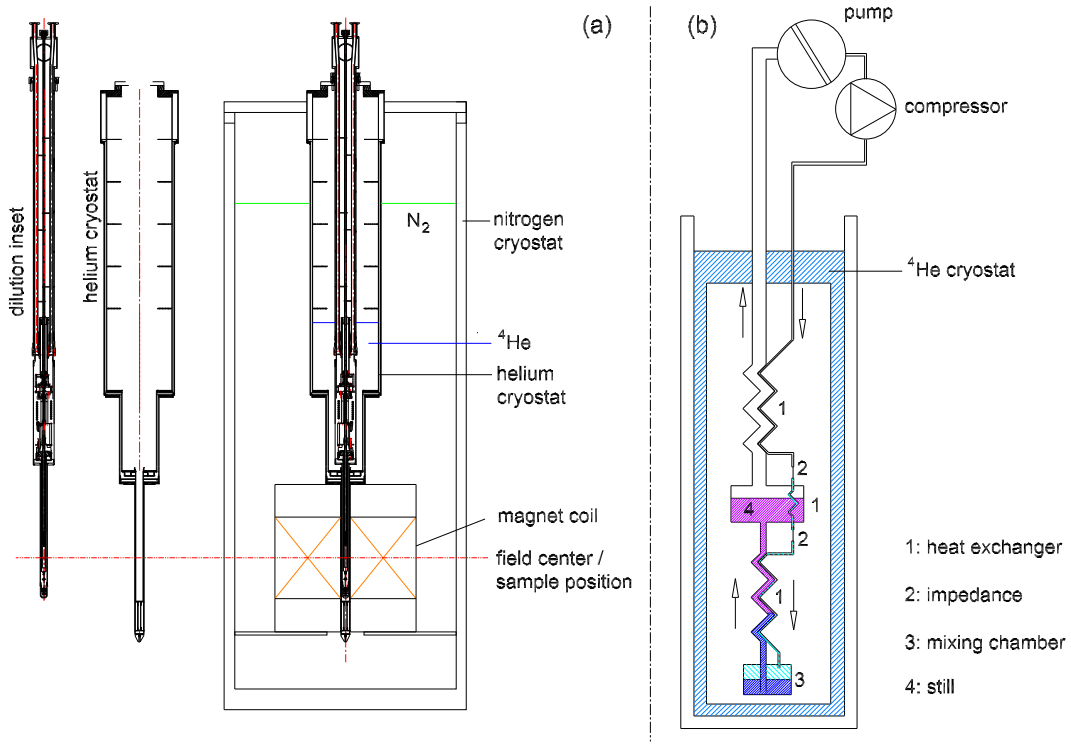

Figure 3.6: (a) Technical drawing of the LNCMI-T dilution cryostat and (b) scheme of the ^{3}He-cycle [Nardone private com.].

saturation vapor pressure of ^{3}He compared to that of ^{4}He. A compressor injects the ^{3}He gas back to the cryostat at a pressure of a few hundred millibars. The gas passes through three counterflow-heat-exchangers and two impedances before condensing in the mixing chamber, the region at the lowest temperature. The samples are in the mixing chamber, where the concentrated and the dilute phase are in equilibrium and separated by a phase boundary. In the mixing chamber, ^{3}He atoms move from the concentrated phase to the diluted phase. Since the enthalpy of the ^{3}He in the concentrated phase is smaller than that in the diluted phase, heat is absorbed at the phase boundary in the mixing chamber, allowing the chamber to reach temperatures below 100 mK [Pobell 1992]. A strong difference between the dilution cryostat developed for the pulsed magnetic fields at the LNCMI-T and most standard dilution cryostats is the absence of the 1-K-bath, which is normally used to liquefy the helium gas. Here, the instreaming helium gas is precooled and liquefied by a counterflow-heat-exchanger, which makes use of the enthalpy of the cold ^{3}He-gas pumped out of the still, and by subsequent Joule-Thomson expansion [Uhlig 1987].

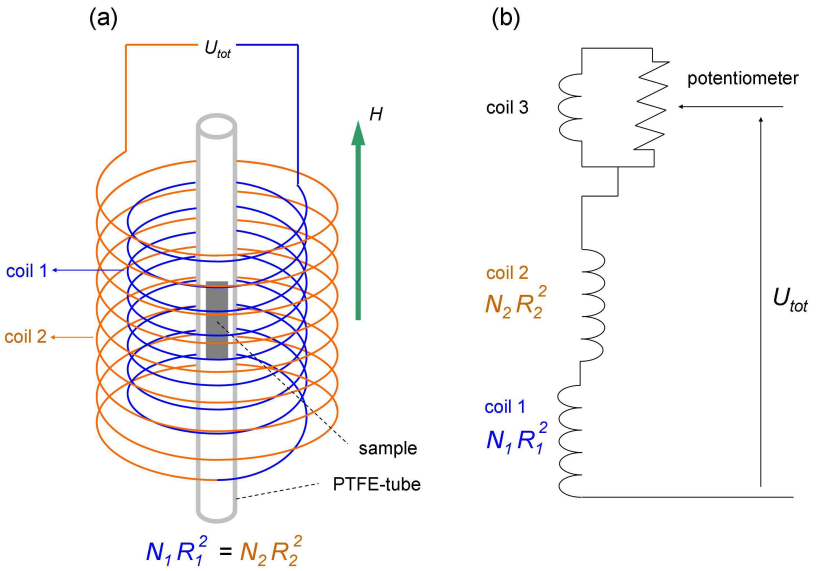

Figure 3.7: (a) Scheme and (b) electric circuit of the compensated-coils probe of the LNCMI-T.

3.3 Magnetization

The magnetization of URu_2Si_2 and $U(Ru_{0.96}Rh_{0.04})_2Si_2$ single-crystalline samples have been measured in pulsed fields using the compensated-coils technique. Additional magnetic torque experiments have been performed on a URu_2Si_2 single crystal using a piezo-resistive micro-cantilever (set-up of David Vignolles). The compensated-coils probe used for this work has been built by Geraldine Ballon. A detailed report about this probe can be found in [Höfner 2010]. The compensated-coils technique consists of the measurement of a voltage U_M, which is proportional to the time derivative of the magnetization dM/dt of the sample. Figure 3.7(a) shows a scheme of the magnetization probe, which consists of two concentric pickup coils 1 and 2 having their axes parallel to the external magnetic field H. The sample is placed at the center of the coils. The voltages U_1 and U_2 induced in the internal and external coils 1 and 2, respectively, are given by:

$$U_1 = -\pi\mu_0 N_1 R_1^2 \frac{d(H)}{dt} + \frac{d\Phi_1}{dt}, \tag{3.7}$$

$$\text{and} \qquad U_2 = \pi\mu_0 N_2 R_2^2 \frac{d(H)}{dt} + \frac{d\Phi_2}{dt}, \tag{3.8}$$

where, for $i = 1, 2$, N_i is the number of windings, R_i the radius of the coil i, and Φ_i is the magnetic flux through the coil i generated by the magnetization of the sample. Within the condition:

$$N_1 R_1^2 = N_2 R_2^2, \tag{3.9}$$

the total voltage induced in the probe is:

$$U_{tot} = U_1 + U_2 = -\frac{d\Phi_1}{dt} + \frac{d\Phi_2}{dt} = -\frac{d\Phi_{tot}}{dt}, \tag{3.10}$$

where $\Phi_{tot} = \Phi_1 - \Phi_2$ is the total flux generated by the magnetization of the sample seen by the coils 1 and 2. Figure 3.7(b) shows a scheme of the electric circuit of the magnetization probe. Due to a variation of the coils' resistance and dimensions (via thermal expansion) the compensation is not stable with the temperature. To regulate the compensation at a given temperature, the effective inductance of the circuit can be changed by a third coil connected in parallel to a potentiometer. A perfect compensation is not possible, thus the magnetic field always generates a parasitic voltage in the compensated coils. To eliminate this, two measurements are done for every magnetization curve: one with the sample at the "measurement" position and one with the sample at the "zero" position, i.e., outside of the compensated coils. At the "zero" position, only the background voltage U_{tot}^z of the external magnetic field is measured. The voltage U_M due to the magnetization of the sample only is the difference between the voltages U_{tot}^m and U_{tot}^z from the "measurement" and "zero" positions, respectively: $U_M = U_{tot}^m - U_{tot}^z$. The relation between the magnetization M and the voltage U_M is given by:

$$U_M = \frac{1}{c_M}\frac{dM}{dt}V \tag{3.11}$$

$$\Leftrightarrow M = \int c_M U_M / V dt, \tag{3.12}$$

where V is the volume of the sample and c_M is a calibration factor, which depends on the geometry and position of the sample. Figure 3.8(a) shows a plot of U_{tot}^z and U_{tot}^m versus time for measurements on URu_2Si_2 in a magnetic field $\mathbf{H} \parallel \mathbf{c}$ at $T = 1.5$ K and Figure 3.8(b) shows the resulting magnetization versus the magnetic field. In principle, knowing exactly the geometries of the compensated coils and the sample, one can calculate the calibration factor c_M (cf. [Höfner 2010]). However, the exact geometries can hardly be known (e.g. irregular shape of the sample) and a much easier way to determine c_M is to rescale the measured signals on existing low-field absolute magnetization data (see Sect. 3.5). For a measurement, the sample is slid into a PTFE-tube and fixed with vacuum grease. The tube is stuck on a long glass-fibre rod, which allows to bring the sample by top-loading directly from the room atmosphere in the center of the compensated coils in the probe chamber

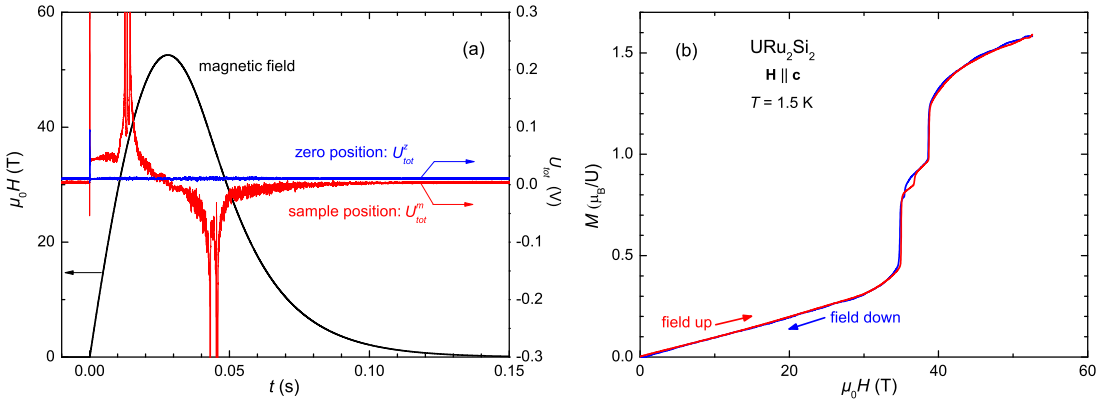

Figure 3.8: (a) Compensated coils voltage U_{tot} of the "zero" (blue) and the "measurement" position (red) versus time for measurements on URu_2Si_2 at $T = 1.5$ K in a magnetic field $\mathbf{H} \parallel \mathbf{c}$ and magnetic field $\mu_0 H$ (black) versus time. (b) Resulting magnetization M versus magnetic field $\mu_0 H$.

of the ^{4}He-cryostat. The rod also serves to shift the sample between the "zero" and "measurement" positions. Holes in the PTFE-tube allow an exchange of gas for a better thermalization of the sample. Since the voltage U_M induced in the magnetization probe is proportional to $dM/dt = d(\chi H)/dt$, U_M is enhanced when the time variation dH/dt of the external magnetic field is higher. For this reason, the noise level of the magnetization data is lower during the rise than during the fall of the pulsed field, the fall being slower than the rise. I will present mainly the data from the rise of the pulsed field in the following.

3.4 Electric transport

Resistivity measurements have been carried out in pulsed magnetic fields within the four-point technique. Due to the short duration of the magnet pulses, the field-dependent resistivity was measured using the lock-in technique at high excitation frequencies of about 20 - 70 kHz. At these high frequencies, very good electric contacts are essential to avoid signals from parasitic capacities. The excitation currents were provided by a standard lock-in amplifier (SR830 DSP, Stanford Research Systems). The voltage signals of excitation current and sample resistance are measured using fast acquisition cards (PXI 24-bit Digitalizer, National Instruments) at a rate of 500 kHz and the data were processed with two digital lock-in amplifiers developed in-house (by E. Haanappel and X. Fabrèges). The excitation currents were limited to 10 mA and 0.5 mA for the experiments in the ^{4}He fridge and in the dilution fridge, respectively. The resistivity signal measured during the fall of the pulsed field has a lower noise level than from its rise, which is due to longer duration of the fall. In this work, I will present mainly the resistivity data from the fall of the pulsed fields.

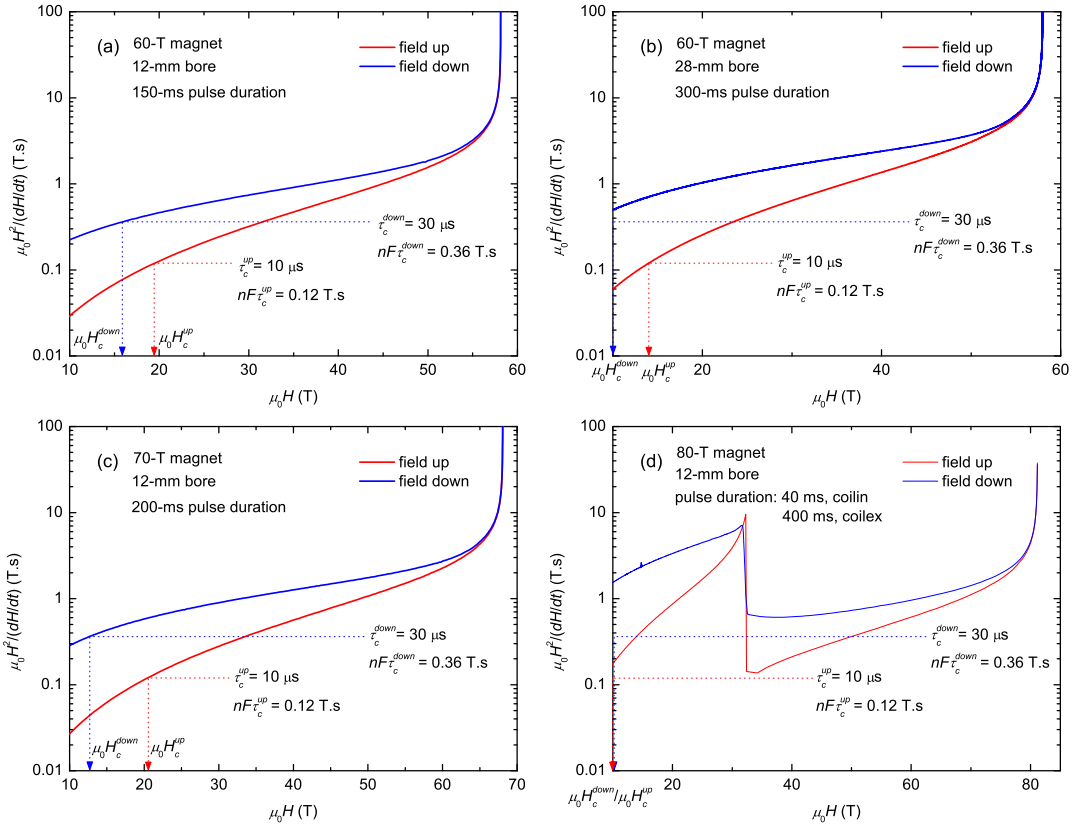

Figure 3.9: Field-dependence of the parameter $\mu_0 H^2/|dH/dt|$ (full lines, red: rise of the field, blue: fall of the field) for field pulses generated by magnets of the LNCMI-T. The horizontal dotted lines indicates the values of $nF\tau_c^{up} = 0.12$ T.s and $nF\tau_c^{down} = 0.36$ T.s with $\tau_c^{up} = 10$ μs and $\tau_c^{down} = 30$ μs, respectively, with $n = 8$ and $F = 1500$ T. The vertical arrows indicate the fields $\mu_0 H_c^{up}$ and $\mu_0 H_c^{down}$ above which the condition $\mu_0 H^2/|dH/dt| > nF\tau_c^{up}$ or $\mu_0 H^2/|dH/dt| > nF\tau_c^{down}$, respectively, is fulfilled.

The magnetoresistivity of three URu_2Si_2 samples have been studied here: samples #1 and #2 with $\mathbf{U}, \mathbf{I} \parallel \mathbf{a}$ and sample #3 with $\mathbf{U}, \mathbf{I} \parallel \mathbf{c}$, where U and I are the voltage and current, respectively. The transverse configurations ($\mathbf{H} \parallel \mathbf{c}$; $\mathbf{I}, \mathbf{U} \perp \mathbf{H}$) and ($\mathbf{H} \parallel \mathbf{a}$; $\mathbf{I}, \mathbf{U} \perp \mathbf{H}$) for samples #1 and #2 and the longitudinal configuration ($\mathbf{H} \parallel \mathbf{c}$; $\mathbf{U}, \mathbf{I} \parallel \mathbf{H}$) for sample #3 have been investigated using an electric transport probe with a static sample support. Configurations with the magnetic field applied along directions in the main crystal planes (**a**,**c**) and (**a**,**a**) have been investigated using a rotation transport probe. Additional resistivity measurements have been carried out at the Institut Nanosciences et Cryogénie of the CEA-Grenoble on sample #2 at subkelvin temperatures in transverse configurations in steady magnetic fields $\mu_0 H$ up to 13 T rotating in the (**a**,**c**)-plane, in collaboration with Georg Knebel, Alexandre Pourret, and Dai Aoki, using a conventional ^{3}He-^{4}He-dilution fridge in a superconductive magnet.

To achieve a suitable signal-over-noise ratio, the time constant τ_c of the low-band-pass filter of the digital lock-in has to be high-enough. On the other hand, τ_c has to be small compared to the timescales of the measured quantities. In the present work, a time constant $\tau_c = 150$ μs has been used as a good compromise to observe anomalies resulting from field-induced transitions and crossovers in the magnetoresistivity. However, a smaller time constant is necessary for the analysis of quantum oscillations [Béard 2012, Audouard private com.]: knowing that quantum oscillations are periodic in $1/(\mu_0 H)$ with a given frequency F, the time δt of one period can be approximated by $\delta t = \mu_0 H^2/(F\,|dH/dt|)$. Empirically, the condition $\tau_c < \delta t/n$ with $n = 8$, which is equivalent to $\mu_0 H^2/\,|dH/dt| > nF\tau_c$, assures that the amplitudes of the oscillations are not damped. For the analysis of quantum oscillations, I have used time constants $\tau_c^{up} = 10$ μs and $\tau_c^{down} = 30$ μs for the rise and fall of the pulsed field, respectively. Figure 3.9 shows the field-dependence of the parameter $\mu_0 H^2/\,|dH/dt|$ (full lines) for the magnetic field pulses generated by different magnets of the LNCMI-T (cf. Table 3.1 and Fig. 3.3). The horizontal dotted lines indicates the values of $nF\tau_c^{up} = 0.12$ T.s and $nF\tau_c^{down} = 0.36$ T.s with $\tau_c^{up} = 10$ μs and $\tau_c^{down} = 30$ μs, respectively, with $n = 8$ and $F = 1500$ T (the highest observed frequency, see Chapter 9). The vertical arrows indicate the fields $\mu_0 H_c^{up}$ and $\mu_0 H_c^{down}$ above which the condition $\mu_0 H^2/\,|dH/dt| > nF\tau_c^{up}$ or $\mu_0 H^2/\,|dH/dt| > nF\tau_c^{down}$, respectively, is fulfilled. Above $\mu_0 H_c^{up}$ and $\mu_0 H_c^{down}$, the signal from the quantum oscillation frequencies up to 1500 T is not smeared out by the lock-in analysis.

3.5 Samples and their characterization

The URu_2Si_2 and $U(Ru_{0.96}Rh_{0.04})_2Si_2$ single crystals studied here have been grown by the Czochralski method in a tetra-arc furnace by Dai Aoki at the Institut Nanosciences et Cryogénie of the CEA-Grenoble. The magnetization of a block-shaped URu_2Si_2 sample (mass $m = 40.5$ mg) and a block-shaped $U(Ru_{0.96}Rh_{0.04})_2Si_2$ sample (mass $m = 53.7$ mg) was measured within the compensated coils technique (cf. Sect. 3.3) and the magnetization of a very small URu_2Si_2 sample ($50\times100\times20$ μm^3) was measured within the magnetic torque technique. The resistivity of three URu_2Si_2 samples with irregular shapes ($\sim 0.5\times0.1\times0.03$ mm^3) has been measured with different transport probes (cf. Sect. 3.4).

3.5.1 Magnetic susceptibility

To obtain the calibration factor c_M from our magnetization experiments in pulsed fields (cf. Sect. 3.3), we rescaled the slope of our M versus H data obtained in pulsed

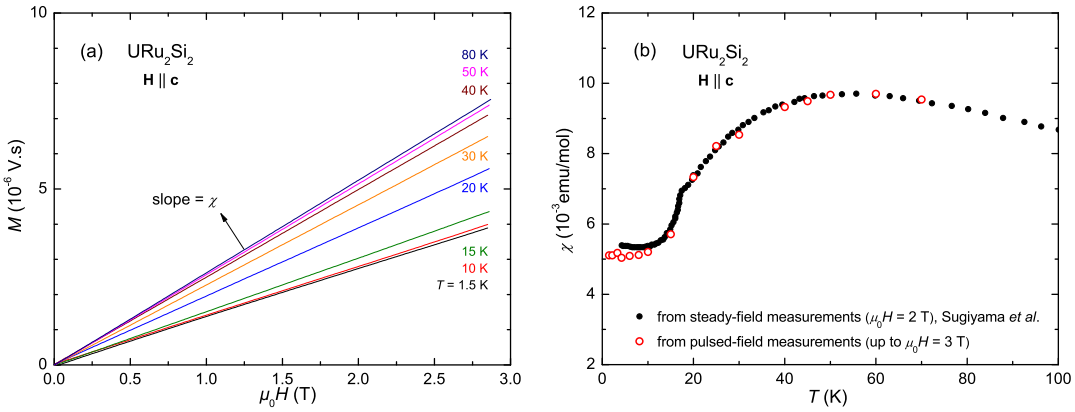

Figure 3.10: (a) Magnetization $M(H)$ in units V.s from 3 T-pulses at different temperatures. The slope of $M(H)$ is proportional to the susceptibility. (b) Zero-field susceptibility χ in units emu/mol from [Sugiyama 1999] and that resulting from the slope of the magnetization from the 3-T pulses rescaled by c_M.

fields up to 3 T at different temperatures [see Fig. 3.10(a)] on the susceptibility $\chi = M/H$ measured in steady fields. For URu_2Si_2, a comparison of χ measured at $\mu_0 H = 2$ T in [Sugiyama 1999] with the slope of the magnetization is given in Figure 3.10(b). For the $U(Ru_{0.96}Rh_{0.04})_2Si_2$ sample, we rescaled our data using a measurement of χ done at the CEA-Grenoble by Dai Aoki at $\mu_0 H = 1$ T.

3.5.2 Resistivity

The resistivity ρ of the samples studied here was measured as function of the temperature T at zero field using a standard lock-in amplifier (SR830 DSP, Stanford Research Systems) with excitation frequencies of ~ 150 Hz and excitation currents of 1 mA. In fact, the transport probe measures a voltage U proportional to the resistivity ρ:

$$U = I f_g \rho, \tag{3.13}$$

where I is the excitation current and f_g the geometric factor of the sample. The samples studied here had irregular shapes, thus the geometric factor could not be determined visually. To obtain f_g, we rescaled the resistance $R = U/I = f_g \rho$ of our samples on the resistivity of samples, for which the geometric factor is known, measured by Dai Aoki [see Fig. 3.11(a)]. Since the high-temperature resistivity is less sensitive to the sample qualities, we rescaled the data using the maximum of resistivity at around 70 K.

In simple metals, e.g. in the absence of magnetic impurities, the electric transport is perturbed only by the scattering off on lattice impurities and defects and by the electron-phonon scattering. At ambient temperature $T \sim 300$ K, the

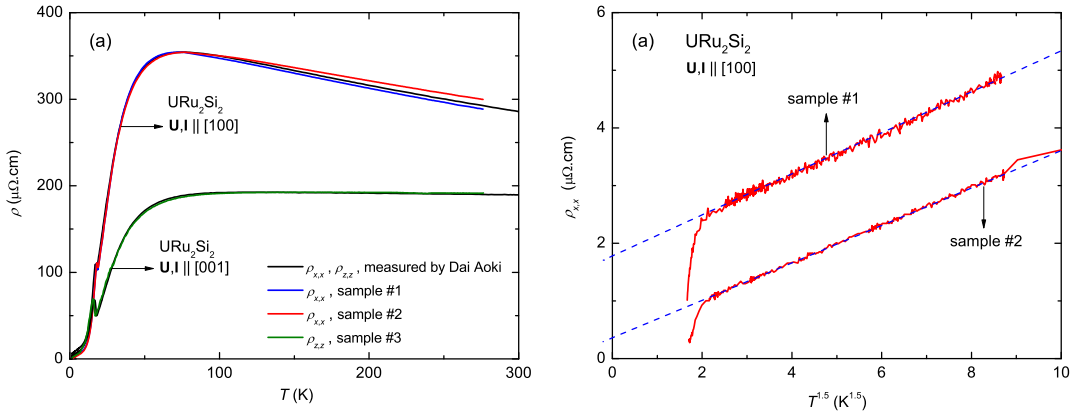

Figure 3.11: (a) $\rho_{x,x}$ ($\mathbf{U},\mathbf{I} \parallel \mathbf{a}$) of URu_2Si_2 samples #1, #2, and that of a sample measured by Dai Aoki and $\rho_{z,z}$ ($\mathbf{U},\mathbf{I} \parallel \mathbf{c}$) of URu_2Si_2 sample #3 and that of a sample measured by Dai Aoki versus the temperature T. (b) Resistivity $\rho_{x,x}$ of samples #1 and #2 versus $T^{1.5}$ up to 8 K. The scattered lines represent $\rho(T) = \rho_0 + aT^{1.5}$-fits to the data.

	$\rho(T = 2\,\mathrm{K})$ ($\mu\Omega$.cm)	ρ_0, from $T^{1.5}$-fit ($\mu\Omega$.cm)	RRR $= \rho^{300\,\mathrm{K}}/\rho^{2\,\mathrm{K}}$	RRR* $= \rho^{300\,\mathrm{K}}/\rho_0^n$
sample #1 $\mathbf{U},\mathbf{I} \parallel \mathbf{a}$	2.81	1.77	90	160
sample #2 $\mathbf{U},\mathbf{I} \parallel \mathbf{a}$	1.29	0.348	225	800
sample #3 $\mathbf{U},\mathbf{I} \parallel \mathbf{c}$	2.18	-	85	-

Table 3.2: Zero-field resistivity characteristics of samples #1, #2 and #3.

scattering mechanism is dominated by electron-phonon scattering and almost independent from the sample quality. The residual resistivity $\rho_0 = \rho(T \to 0)$ is due to the scattering off on lattice impurities and defects only. Thus, the residual resistivity ratio RRR $= \rho(300\,\mathrm{K})/\rho_0$ is a quantitative indicator of the sample quality. However, URu_2Si_2 samples are superconducting ($\rho = 0$) below $T_{SC} \sim 1.5$ K and it is common to define the RRR as $\rho(300\mathrm{K})/\rho(2\mathrm{K})$ (cf. [Matsuda 2011]). Samples #1 and #2 have residual resistivity ratios of RRR $= \rho_{x,x}(300\,\mathrm{K})/\rho_{x,x}(2\,\mathrm{K}) = 90$ and 225, respectively, while sample #3 has a residual resistivity ratio of RRR $= \rho_{z,z}(300\,\mathrm{K})/\rho_{z,z}(2\,\mathrm{K}) = 85$.

To obtain finite values of the resistivity for $T < T_{SC}$, that we need for the analysis of the transverse magnetoresistivity (cf. Chapter 7), we extrapolated the resistivity in the normal non-superconducting state to temperatures below T_{SC}. I will note $\rho^n_{x,x}$ the resistivity of the normal non-superconducting state (virtual normal state at temperatures below T_{SC}) and $\rho^n_0 = \rho^n_{x,x}(T \to 0)$. A detailed study by Matsuda *et al.* [Matsuda 2011] pointed out the difficulty to find a consistent model for the low-temperature resistivity of URu_2Si_2 because of its deviation from the T^2-dependence

of a Fermi liquid. For example, the extrapolation of $\rho_{x,x}(T)$ of our sample #2 with a T^2-fit gives a non-physical negative value of ρ_0. As proposed by Matsuda *et al.* [Matsuda 2011], we used the function $\rho(T) = \rho_0^n + aT^{1.5}$, where a is a constant parameter, to fit the resistivity of our samples between $T = 2$ K and 6 K [see Fig. 3.11(b)]. From this fit, we extrapolated $\rho_{x,x}^n(T \to 0)$ in the normal non-superconducting state, and we estimated the huge residual resistivity ratios $\mathrm{RRR}^* = \rho_{x,x}(300\ \mathrm{K})/\rho_{x,x}^n(T \to 0)$ of 160 and 800 for samples #1 and #2, respectively. This underlines the exceptional quality of our samples, in particular sample #2. Table 3.2 summarizes the characteristics of our transport samples.

3.6 Gauging of the pickup

The magnetic field H generated by a pulse can be measured by a pickup coil, made of a few tenths of turns of 50 μm copper wire. A pickup coil measures a voltage:

$$U_{pickup} = -\frac{d\Phi}{dt} = -S_{pickup}\frac{d(\mu_0 H)}{dt}, \tag{3.14}$$

where S_{pickup} is the cross-section of the coil perpendicular to the magnetic field. In the case of the magnetization probe, the pickup is exactly at the field center, whereas the pickup of a transport probe has a distance d to the field center/sample. Due to the profile of the magnetic field in z-direction, the pickup of the transport probes is exposed to lower fields than the sample. To calculate the field at the sample position from U_{pickup}, an effective cross-section S_{pickup}^{eff} is needed. The different types of magnets used here have different field profiles [see Fig. 3.12]. Thus, S_{pickup}^{eff} has to be determined for each magnet type and each distance d between the pickup and the sample. S_{pickup}^{eff} of a 6-mm-diameter transport probe was first estimated in a 12-mm-bore 60-T magnet with $d = 11.8$ mm using a calibrated Hall probe. For the experiments using the same probe in 70-T and 80-T magnets, we rescaled S_{pickup}^{eff} using the formula:

$$\left(S_{pickup}^{eff}\right)_{70/80-\mathrm{T\ magnet}} = \left(\frac{U_{pickup}}{U_{max}}\right)_{70/80-\mathrm{T\ magnet}} \cdot \left(S_{pickup}^{eff}\frac{U_{max}}{U_{pickup}}\right)_{60-\mathrm{T\ magnet}}, \tag{3.15}$$

where U_{max} and U_{pickup} are the pickup voltage at the sample and pickup positions, respectively, and were measured using a lockin amplifier (sending a voltage of 5 V at a frequency of 111.62 Hz to the magnet). A priori, the pickup technique is not adapted to measure the field of a dual coil, since it consists of an external coil and an inner coil, with different axial field profiles. Since the axial field profiles of

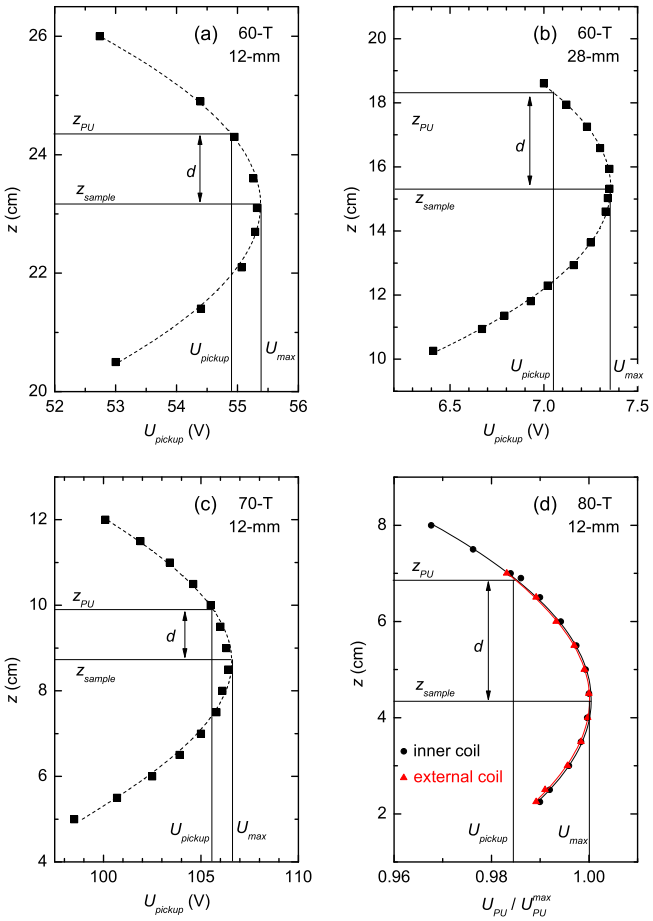

Figure 3.12: Field profiles in z-direction of the pulsed field magnets and corresponding positions of the pickup and the sample: (a) 60-T 12-mm-bore magnet, (b) 60-T 28-mm-bore magnet, (c) 70-T 12-mm-bore magnet, (d) rescaled profiles of the inner and external coil of the 80-T 12-mm-bore magnet.

external and inner coil of the 80-T magnet used here are very similar, as shown in Figure 3.12(d), we were able to define a unique effective cross-section S_{pickup}^{eff} for the ensemble.

3.7 Analysis of the Shubnikov-de Haas data

Shubnikov-de Haas oscillations have been observed in the magnetoresistivity $\rho_{x,x}$ of samples #1 and #2 and will be presented in Chapter 9. Here I present the procedure to analyze these quantum oscillation data. A non-oscillating background ρ_{BG}, as shown in Figure 3.13(a), was subtracted from the raw resistivity $\rho_{x,x}$ to obtain a purely oscillating signal $\rho_{x,x}^{osc}$, as shown in Figure 3.13(b). Since the oscillations are periodic in the inverse magnetic field, $\rho_{x,x}^{osc}$ versus $1/(\mu_0 H)$ was considered [see Fig. 3.13(c)]. I performed Discrete Fourier Transformations (DFT), which provide the

spectral amplitude A of the oscillations as function of the frequency F ($[F] = 1$ T):

$$A(F) = \left| \frac{1}{T\sqrt{2\pi}} \int_{x_1}^{x_2} [\exp(-i2\pi F x) y(x) w(x)]\, dx \right|, \tag{3.16}$$

where $x = 1/(\mu_0 H)$ is the inverse magnetic field, $x_1 = 1/(\mu_0 H_1)$ and $x_2 = 1/(\mu_0 H_2)$ are the lower and the upper limits, respectively, of the field range over which the data were analyzed, $T = |x_1 - x_2|$, $y(x)$ is the oscillating signal, and $w(x)$ is a window function. When applying the DFT without a window function, which is equivalent to the rectangular window [$w(x) = 1$, for $x_1 < x < x_2$, and $w(x) = 0$, elsewhere], the discontinuities of $y(x)$ at x_1 and x_2 induce strong parasitic peaks, called side lobes. To reduce these side-lobe effects, the oscillating signal can be multiplied by a smoothing-window function as the Blackman, Hamming, and Hann window [Damelin and Miller 2012]. A disadvantage of smoothing functions is the broadening of the frequency peaks. A good compromise between the peak width and the reduction of the side-lobe effects is to use the cosine window (also called Hann or Hanning window):

$$w(x) = 0.5[1 - \cos(2\pi(x - x_1)/T)]. \tag{3.17}$$

Figure 3.13 shows the Shubnikov-de Haas data measured on sample #2 in a steady field up to 13 T with an angle of 15° between **H** and **c** and at $T = 32$ mK (cf. Sect.9.1). Figure 3.13(d) shows the corresponding DFT extracted with the rectangular- (red) and the cosine-window (blue) functions from the oscillating signal $\rho_{x,x}^{osc}$ versus $1/(\mu_0 H)$ between $\mu_0 H = 6$ T and 13 T. Using the DFT to analyze the quantum oscillations, one has to respect the following constraints. The width of the frequency peaks depends on the number of oscillation periods contained between x_1 and x_2: the more periods are contained in $[x_1, x_2]$, the sharper are the peaks in the spectra. Empirically, a good analysis is obtained with at least seven periods. The maximal detectable frequency is limited by the sampling rate Δx, that is the distance in x, here in $1/(\mu_0 H)$, between two consecutive data points $y(x)$. Empirically, good results are obtained for $F < 7/\Delta x$. The minimal detectable frequency is limited by the analyzed field range T: $F >= [1/(\mu_0 H_2) - 1/(\mu_0 H_1)]$.

3.8 Sample thermalization in pulsed magnetic fields

A challenge of the measurements in pulsed magnetic fields is the thermalization of the samples. A pulsed field tends to heat metallic parts of the setup or metallic samples, as in the case of URu_2Si_2, due to eddy currents. Due to the non-metallic-nature of the sample support, the temperature gradient between the sample and the

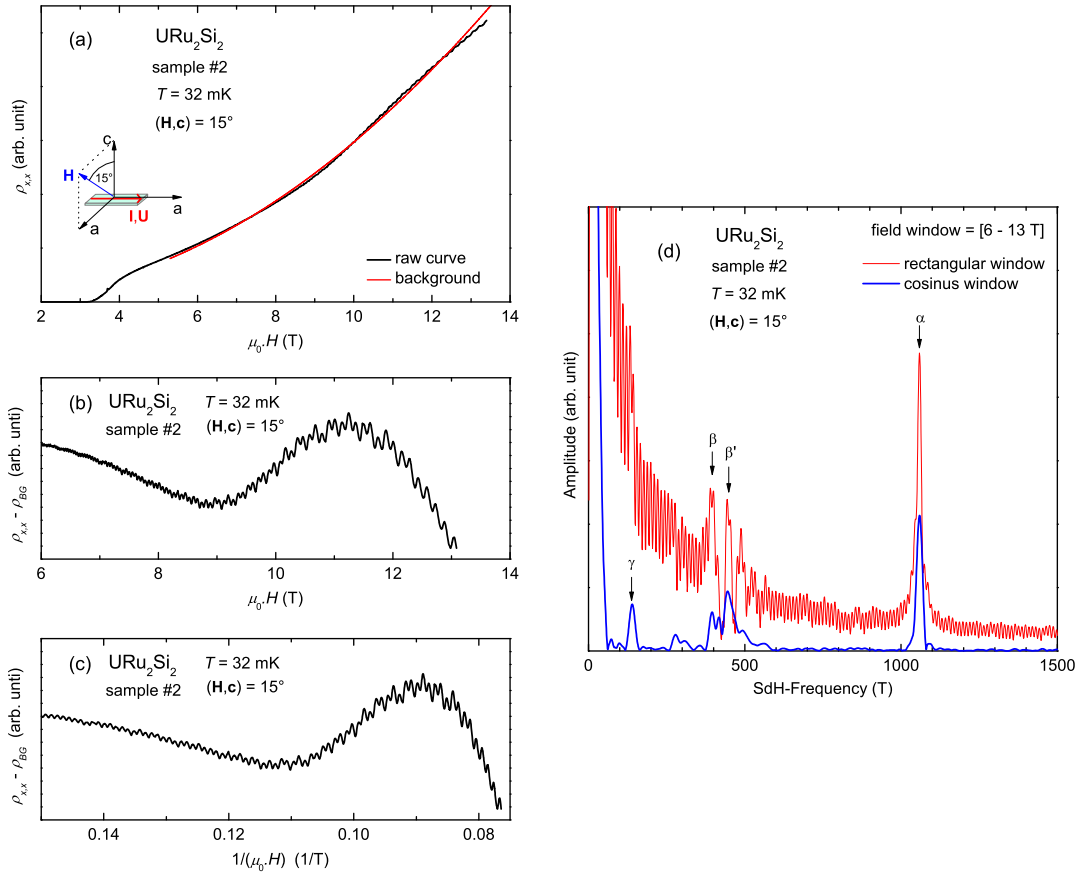

Figure 3.13: (a) Magnetoresistivity $\rho_{x,x}(H)$ of URu_2Si_2 sample #2 at $T = 32$ mK. The resistivity is modulated by Shubnikov-de Haas oscillations. The red line represents a non-oscillating polynomial background. (b) Oscillating signal $\rho^{osc}_{x,x}(H)$ extracted from the raw resistivity by subtracting a non-oscillating polynomial background. (c) $\rho^{osc}_{x,x}$ versus $1/(\mu_0 H)$. (d) Resulting Fourier spectra using the rectangular (red) and the cosine (blue) window functions.

thermometer can be important in a pulsed-field setup.

The compensated-coils probe of our magnetization-setup is a massive structure made of zircon and copper wire. It occupies most of the space available in the cryostat, i.e, there is very little space between the wall of the cryostat and the probe and between the PTFE-tube holding the sample and the inner diameter of the probe. Hence, the helium gas responsible for the thermal exchange can not flow easily. This resulted presumably in an important temperature gradient between the sample and the thermometer during the magnetization measurements of our URu_2Si_2 sample (see Sect. 5.4) and our $U(Ru_{0.96}Rh_{0.04})_2Si_2$ sample (see Chapt. 6). However, this was only observed for the high-pulsed-field magnetization, but not for the low-field susceptibility measurements on the same samples [cf. Sect. samples Fig. 3.10] or for the high-field magnetization measurements on other samples.

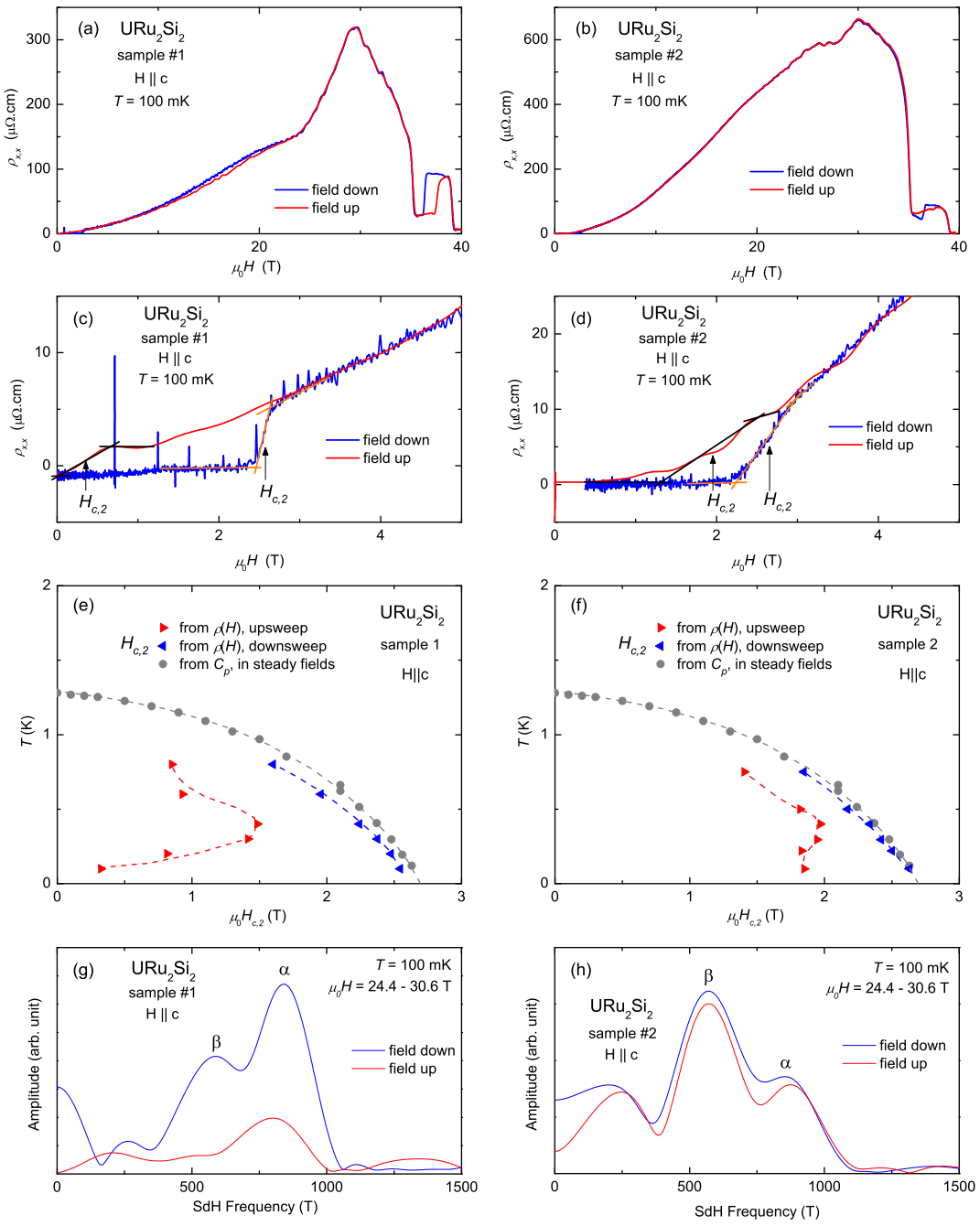

Figure 3.14: Resistivity data from URu_2Si_2 samples #1 (left) and #2 (right) measured at $T = 100$ mK with $\mathbf{H} \parallel \mathbf{c}$ in a 60 T magnet using the dilution fridge. (a,b) $\rho_{x,x}$ versus $\mu_0 H$. (c,d) Zoom on the superconducting critical field H_{c2} in $\rho_{x,x}(H)$. H_{c2} is defined at the middle of the resistivity step (see black lines) for the rise (red) and fall (blue) of the pulsed field. (e,f) Phase diagram of H_{c2} from specific heat data (grey dots, [Aoki, *private com.*]), rising- (red triangles), and falling-field (blue triangles) resistivity. (g,h) Shubnikov-de Haas spectra in the field window 24.4 T $< \mu_0 H <$ 30.6 T from rising- (red triangles), and falling-field (blue triangles).

In the case of the magnetoresistivity measurements on URu_2Si_2, we estimated the temperature gradient as follows. First, we checked if the resistivity curves from the rise and fall of the field pulse coincided, which was generally the case using ^{4}He-cryostats at temperatures above 1.4 K. As shown in Figure 3.14(a,b), the rising and falling resistivities, measured at $T = 100$ mK in a pulsed field $\mathbf{H} \parallel \mathbf{c}$ using the dilution fridge, coincide perfectly for sample #2 but not fully for sample #1 (clear deviation below 25 T). However, this method is not necessarily a good temperature indicator, since the resistivity may be temperature-independent. At temperatures below 1 K, the superconducting transition field $H_{c,2}$ can be used to estimate the temperature at the beginning and the end of the pulse [see Figs. 3.14(c-f)]. In the low-field regime $\mu_0 H < 3$ T, we observed that the rising and the falling-field resistivities do not coincide. This is a signature of strong eddy currents, which heat the samples at the beginning of the pulse where dH/dt is maximal, and result in an important hysteresis of the superconducting transition field H_{c2} [see Figs. 3.14(c,d)]. Moreover, we can estimate the temperature at the beginning and the end of the pulse by the value of $H_{c,2}$. The $H_{c,2}$-phase diagrams [here for $\mathbf{H} \parallel \mathbf{c}$, see Figs. 3.14(e,f)] show that samples #1 and #2 were well thermalized at the end of the pulse but were heated at the beginning of the pulse. For example, for $T_{thermometer} = 100$ mK, the temperature at the beginning of the pulse was ~ 1 K and ~ 800 mK for sample #1 and #2, respectively. At the end of the pulse, H_{c2} was close to that measured by specific heat in steady fields, i.e, the sample temperatures were close to that indicated by the thermometer. Quantum oscillations are a good indicator for the temperature of the sample during the pulse, i.e., at high fields. Figures 3.14(g) and (h) show the Shubnikov-de Haas spectra of samples #1 and #2, measured in the rise and fall of a magnetic field applied along $\mathbf{c}$ and at $T_{thermometer} = 100$ mK. For sample #1, the peak intensities of the frequencies α and β (see Chapter 9) measured during the rise are much smaller than that measured during the fall. The peak of frequency β, which has a high effective mass and therefore a strong temperature-dependence, has almost vanished from the spectra measured during the rise. For sample #2, the peak intensities of the rise and the fall are very similar, indicating that the temperature was fast recovered (before the rising field reached 20 T) and almost stable during the pulse. The heating by eddy currents, depending on the cross-section perpendicular to the pulsed field, was more important for sample #1 than for sample #2, which is probably due to their geometry: for $\mathbf{H} \parallel \mathbf{c}$, sample #1 had a large section exposed to the field, whereas the section of sample #2 exposed to the field was very small. In Chapter 9 we will present the Shubnikov-de Haas data from sample #2, for which the heating by eddy currents in the high-fields can

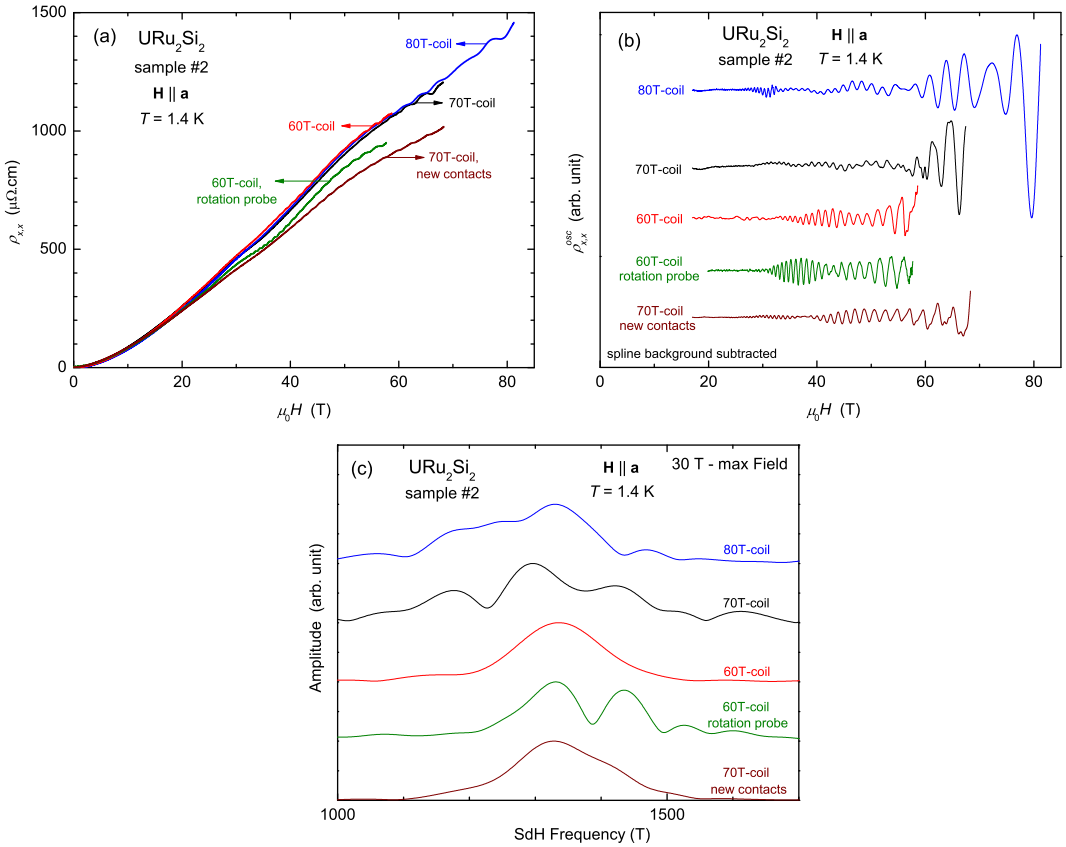

Figure 3.15: Comparison of resistivity data from measurements on URu_2Si_2 sample #2 in different cryostat-coil setups. (a) Transverse magnetoresistivity $\rho_{x,x}$ versus the magnetic field H applied along the **a**-axis at $T = 1.4$ K. (b) Corresponding oscillating signals $\rho^{osc}_{x,x}(H)$. (c) Resulting Fourier transforms.

be neglected. In Chapter 7, we consider the non-oscillating magnetoresistivity and data from both samples will be presented at low temperatures, assuming that i) for sample #2 there is no heating of the sample by eddy currents, and ii) for sample #1 in the fall of the field, the absolute value of $\rho_{x,x}$ is not affected by eddy currents (small temperature-dependence of $\rho_{x,x}$).

3.9 Reproducibility of the magnetoresistivity measurements

Slight differences have been observed in the resistivity data of sample #2 measured for $\mathbf{H} \parallel \mathbf{a}$ at $T = 1.4$ K using different setups of transport probe, cryostat, and magnet, as shown in Figure 3.15. The resistivity exhibits differences in the absolute variation by a magnetic field with a maximal deviation of $\sim 15\%$. The extracted quantum oscillations [Fig. 3.15(b)] differ in phase and amplitude and the resulting Shubnikov-de Haas spectra [Fig. 3.15(c)] show differences in the splitting of the frequency branch λ ($F \sim 1350$ T), which consists mainly of 2 or 3 satellites (see

Chapter 9). Reasons for this lack of reproducibility might be related to slight mis-orientations of the sample in the magnetic field, due to its irregular shape, but also to modified electrical contacts (after repair). This illustrates the high sensibility of the Fermi surface of URu_2Si_2 to slight variations of the field direction. In Chapter 8 we will see that the magnetoresistivity is very sensible to the a mis-orientation in a the magnetic field $\mathbf{H} \parallel \mathbf{a}$, but less sensible in $\mathbf{H} \parallel \mathbf{c}$, for which we observed a satisfying reproducibility.

4 Introduction to URu_2Si_2

In this chapter, I introduce the physical properties of URu_2Si_2, which occupies a particular place in the family of heavy-fermion systems and continues to be an unsolved issue after more than 20 years of investigations [Mydosh and Oppeneer 2011]. URu_2Si_2 exhibits a paramagnetic ordered state, the so-called "hidden-order" phase, below $T_0 = 17.5$ K [Palstra 1985, Maple 1986, Schablitz 1986, Ramirez 1992, Bourdarot 2003a], for which the order parameter has still not been identified. Also, the origin of unconventional superconductivity in URu_2Si_2 below $T_{SC} \sim 1.5$ K, which coexists with the hidden-order, remains unknown [Maple 1986, Schablitz 1986].
URu_2Si_2 is an intermetallic compound, which has a $ThCr_2Si_2$-type body centered tetragonal crystal structure with the space group 139, I4/mmm. The lattice parameters are $a = 4.124$ Å and $c = 9.82$ Å [see Fig. 4.1(a)]. The magnetic properties of URu_2Si_2, due to the magnetic moments of the Uranium sites, show a strong Ising-character, the **c**-axis being the magnetic easy axis. This results in strongly anisotropic bulk properties [Palstra 1985, Ramirez 1992, Dawson 1989, Ohkuni 1997]. The upper critical field H_{c2} related to the destruction of superconductivity is also strongly anisotropic [Kwok 1990, Ohkuni 1997].
Section 4.1 presents the temperature-dependent bulk properties of URu_2Si_2.
Section 4.2 presents the microscopic properties as seen by neutron scattering studies.
Section 4.3 presents the properties of the Fermi surface of URu_2Si_2 at low magnetic field. Section 4.4 presents the high-field properties of URu_2Si_2.

4.1 From a Kondo liquid to the hidden-order

Figure 4.2 shows the temperature-dependence of the magnetic susceptibility $\chi(T)$ of URu_2Si_2 in $\mathbf{H} \parallel \mathbf{a}$ and $\mathbf{H} \parallel \mathbf{c}$, whose strong anisotropy indicates Ising magnetic properties [Palstra 1985, Ramirez 1992, Dawson 1989]. The susceptibility along the magnetic easy axis **c** has a Curie-Weiss-like behavior at high temperatures with an effective magnetic moment of 3.51 μ_B/U-ion and a Curie-Weiss temperature $\theta_{CW} = -65$ K [de Visser 1987, Palstra 1985, Dawson 1989]. The susceptibility deviates from the Curie-Weiss behavior at $\sim$ 150 K due to the onset of the Kondo-screening. The maximum at 50 K indicates the onset of coherence effects of the Kondo lattice. The resistivity [Fig. 4.3(a)] shows a strong anisotropy

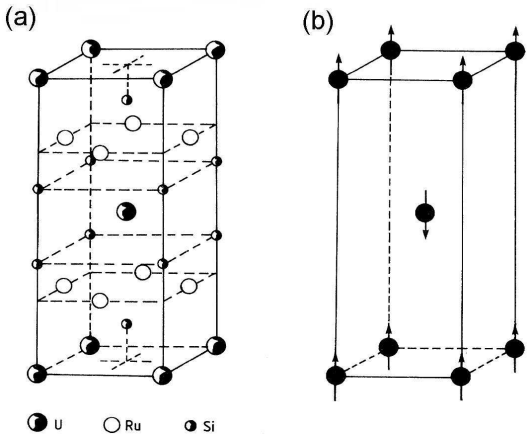

Figure 4.1: (a) Crystal structure of URu_2Si_2. (b) Antiferromagnetic structure of the Uranium ions below $T_0 = 17.5$ K. Figure taken from [Broholm 1991].

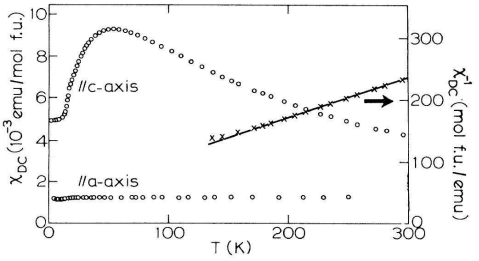

Figure 4.2: Dc-susceptibility (circles) of monocrystalline URu_2Si_2 for **H** along **a** and **c** ($\mu_0 H = 2$ T), and inverse susceptibility (crosses) for **H** $\parallel$ **c**. The solid line represents a Curie Weiss fit and yields $\theta_{CW} = -65$ K. Figure taken from [Palstra 1985].

too [Palstra 1986, Ohkuni 1997], being two times larger for a current along the **a**-axis than for the **c**-axis. The high-temperature behavior of the resistivity [see Fig. 4.3(a)] shows the characteristics of a single-impurity Kondo effect [Schoenes 1987]. The resistivity exhibits a large maximum at 70 K due to the onset of coherent scattering and decreases fast at lower temperatures [Schoenes 1987, Dawson 1989]. When the temperature is reduced below $\sim$ 100 K, the bulk properties indicate that a heavy-fermion liquid is created as the f-Uranium moments hybridize with the conduction band [Maple 1986, Schoenes 1987, Dawson 1989]. Early investigations of URu_2Si_2 by specific heat [Palstra 1985, Maple 1986, Schablitz 1986] [see Fig. 4.4], susceptibility [Palstra 1985, Dawson 1989] [see Fig. 4.2] and electric transport [Palstra 1986, Schoenes 1987, Dawson 1989] [see Fig. 4.3(b)] show large anomalies at $T_0 = 17.5$ and $T_{SC} \simeq 1$ K indicating the transitions to the hidden-order and superconducting phases, respectively. The specific heat [see Fig. 4.4] exhibits a Sommerfeld coefficient $\gamma = 180$ mJ/mol.K^2 and a Debye temperature $\theta_D = 312$ K [Palstra 1985]. The resistivity in the hidden-order phase [see Fig. 4.3(b)] can be

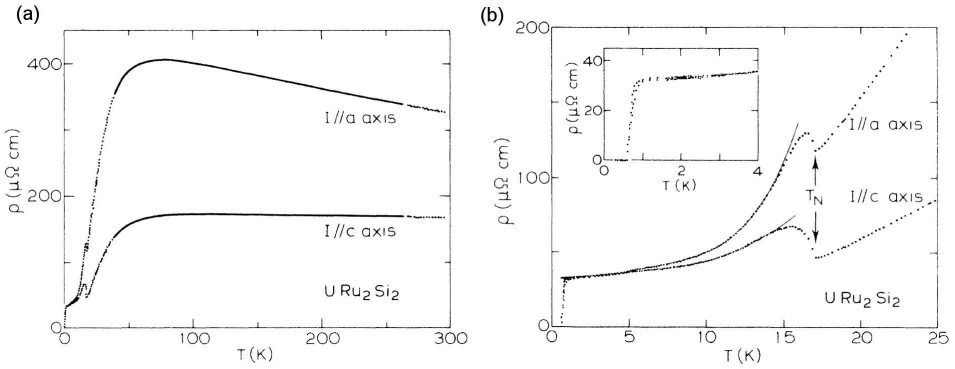

Figure 4.3: (a) Temperature dependence of the electrical resistivity of an URu_2Si_2 single crystal with I parallel to the **a** and **c** axes. (b) Low temperature resistivity of URu_2Si_2 showing the second-order transition at T_0 (noted here T_N) and the superconducting transition at T_{SC}. Figures taken from [Palstra 1986].

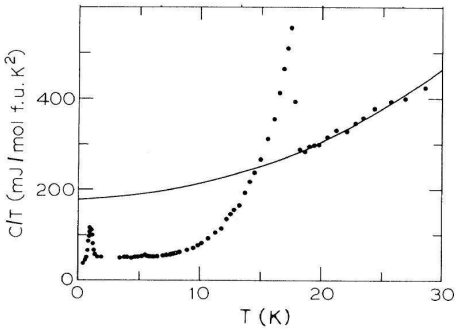

Figure 4.4: Specific heat C/T of polycrystalline URu_2Si_2. Figure taken from [Palstra 1985].

described in terms of a Fermi liquid, with an energy gap Δ [Palstra 1986]:

$$\rho = \rho_0 + AT^2 + bT(1 + 2T/\Delta)\exp(-\Delta/T). \tag{4.1}$$

The energy gap fitted by $\Delta \sim 80$ K [Palstra 1986, Matsuda 2011] can be related to gapped spin excitations as shown by inelastic neutron scattering [Wiebe 2007, Janik 2009]. Below T_{SC}, which varies from 0.8 to 1.5 K, depending on the sample quality, the resistivity drops to zero due to superconductivity, which coexists with the hidden-order [Broholm 1987].

Many theoretical models have been proposed for the hidden-order phase and will not be discussed in detail here. A multitude of possible orders have been proposed theoretically: incommensurate orbital antiferromagnetic order [Chandra 2002], spin density wave [Mineev 2005], octupolar order [Kiss 2005], helicity order [Varma 2006], charge density wave [Balatsky 2009], antiferromagnetic hexadecapolar order [Haule and Kotliar 2009, Kusunose and Harima 2011], fluctuating

dipolar order [Elgazzar 2009], antiferromagnetic quadrupolar order [Harima 2010], hybridization wave [Dubi 2011], modulated spin liquid [Pépin 2011], rank-5 multipole (dotriacontapole) order [Ikeda 2012], and hastatic order [Chandra 2013].

4.2 Magnetic fluctuations and magnetic ordering

4.2.1 Hidden-order phase

Despite a very clean transition in all thermodynamic properties [Palstra 1985, Maple 1986, Schablitz 1986] at $T_0 = 17.5$ K, no order parameter has yet been found for the so-called hidden-order phase developing below T_0. Initially, antiferromagnetic order with a small magnetic moment $m \simeq 0.03\ \mu_B$/U-ion at the wavevector $\mathbf{Q}_0 = (1, 0, 0)$ has been reported by neutron diffraction below T_0 [Broholm 1987, Mason 1990, Amitsuka 1999, Amitsuka 2007]. However, this small moment has later been shown, by neutron diffraction on samples of different qualities [Fak 1996] or under uniaxial pressure [Yokoyama 2005], and by ^{29}Si-NMR measurements [Matsuda 2001], to be extrinsic to the hidden-order phase, being related to spatial inhomogeneities (cf. also [Takagi 2007]). At temperatures above T_0, inelastic neutron scattering measurements revealed enhanced magnetic fluctuations with a large linewidth at the wavevector $\mathbf{Q}_1 = (0.6, 0, 0)$ [Broholm 1987, Broholm 1991]. A careful mapping of the low-temperature excitations in the reciprocal space was established by several inelastic neutron scattering studies [Broholm 1987, Broholm 1991, Fak 1996, Mason 1995, Bourdarot 2003a, Bourdarot 2010, Wiebe 2007, Janik 2009, Bourdarot 2010]. Below T_0, well defined strong peaks in the inelastic spectrum indicate magnetic fluctuations at the wavevectors $\mathbf{Q}_0 = (1, 0, 0)$ and $\mathbf{Q}_1 = (0.6, 0, 0)$ [see Fig. 4.5(a)]. Figure 4.5(b) shows the dispersion of the magnetic excitations [Broholm 1991]. The magnetic excitations at $\mathbf{Q}_0 = (1, 0, 0)$ are found to be a signature exclusively of the hidden-order phase [Bourdarot 2003b, Villaume 2008, Bourdarot 2010].

4.2.2 Pressure-induced antiferromagnetic phase

Figure 4.6 shows the pressure-temperature phase diagram of URu_2Si_2 obtained by resistivity and ac-calorimetry measurements [Hassinger 2008]. The application of hydrostatic pressure drives the superconducting transition temperature to zero at $P_x = 0.5$ GPa and drives the system to an antiferromagnetic ground state above P_x. The transition lines T_0 of the hidden-order phase and T_x of the antiferromagnetic state meet at the point ($P^* = 1.3$ GPa, $T_x = 20$ K) in the phase diagram. The antiferromagnetic order is stabilized within the wavevector $\mathbf{Q}_0 = (1, 0, 0)$ [Amitsuka 1999, Motoyama 2003, Amitsuka 2007, Villaume 2008]. The correspond-

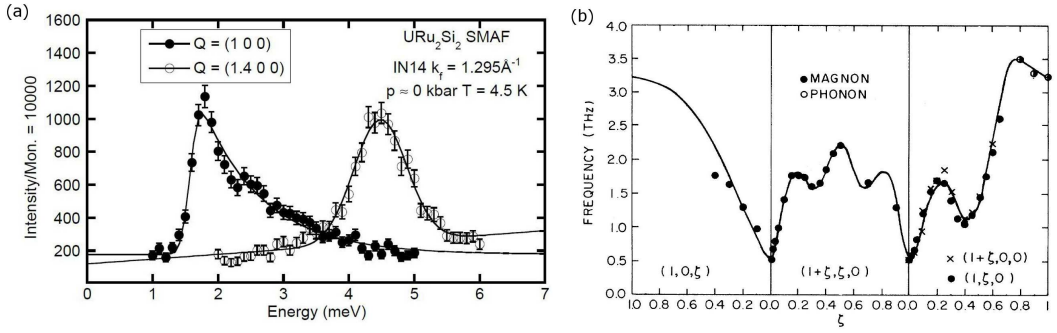

Figure 4.5: (a)Energy spectra at $\mathbf{Q}_0 = (1, 0, 0)$ and $\mathbf{Q}_1 = (0.6, 0, 0)$ [noted here (1.6,0,0)] in the hidden-order phase (noted here SMAF) at ambient pressure, at $T < 5$ K. Figure taken from [Bourdarot 2003b]. (b) Dispersion of the excitations in URu_2Si_2 along the $(1, 0, \xi)$, $(1 + \xi, \xi, 0,)$ and $(1 + \xi, 0, 0,)$ directions. Figure taken from [Broholm 1991].

ing ordered moment of 0.4 μ_B/U is accounted to the $5f$-U sites of the body-centered tetragonal structure and the moments are ordered ferromagnetically along the basal plane and antiferromagnetically along the **c**-direction, as shown in Figure 4.1(b). The antiferromagnetic transition changes the crystal structure from body centered tetragonal to simple tetragonal and the unit cell doubles within the ordering vector $\mathbf{Q}_0 = (1, 0, 0)$. At zero temperature, the magnetic fluctuations at the antiferromagnetic wave vector $\mathbf{Q}_0$, which are intrinsic to the hidden-order phase [Bourdarot 2003b, Villaume 2008, Bourdarot 2010], have vanished above P_x in the antiferromagentic phase, but re-appear at intermediate pressure $P_x < P < P^*$ and temperature $T_x < T < T_0$, indicating the restoration of the hidden-order phase [Bourdarot 2003b, Villaume 2008].

4.3 Fermi surface

4.3.1 Transport properties

In its hidden-order state, URu_2Si_2 is a compensated semi-metal, as indicated by a non-saturating quadratic magnetoresistance [Kasahara 2007, Levallois 2009] and a large Hall constant with a linear field-dependence (up to 10 T, [Kasahara 2007]) observed at temperatures below T_0. Optical conductivity measurements [Bonn 1988] indicate the opening of an energy gap as entering in the hidden-order phase at T_0. The gap opening at T_0 was related to a strong hybridization of the $5f$-electrons of the U-sites with the conduction band, from scanning tunneling microscopy experiments [Schmidt 2010]. At T_0, the charge carrier number is strongly reduced by $\sim$ 90%, as indicated by measurements of Hall effect [Schoenes 1987, Dawson 1989, Lerdawson 1989, Kasahara 2007], thermoelectric power [Bel 2004],

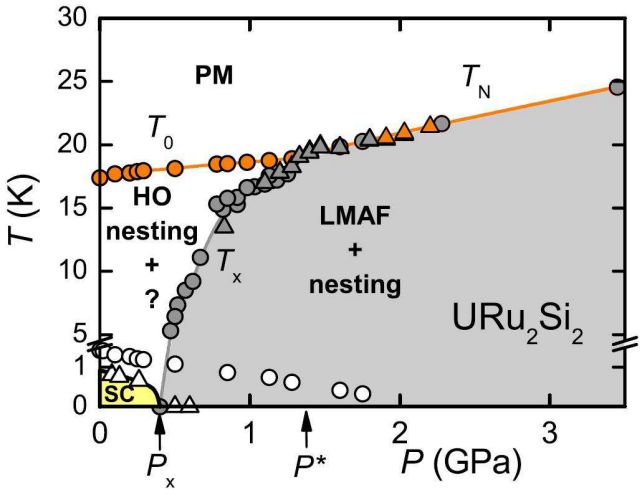

Figure 4.6: Pressure-temperature phase diagram of URu_2Si_2 obtained by resistivity (circles) and ac-calorimetry (triangles) measurements. Bulk superconductivity detected by ac calorimetry (open triangles) is suppressed when the antiferromagnetic state (noted here LMAF) appears. Open circles present the temperature of the onset of the superconducting transition in the electrical resistivity. Figure taken from [Hassinger 2008].

and heat capacity [Bel 2004]. The thermal conductivity is strongly enhanced at T_0 [Behnia 2005, Sharma 2006] indicating an enhanced relaxation time of the phonons and conducting electrons in the hidden-order phase. A giant Nernst signal has also been found in the hidden-order phase, indicating an enhanced electronic mobility [Bel 2004].

4.3.2 ARPES

Angle-resolved photoemission spectroscopy (ARPES) measurements revealed sudden changes of the Fermi surface as the system enters the hidden-order phase at T_0 [Santander 2009, Yoshida 2010]. Santander *et al.* [Santander 2009] observed the crossing of the Fermi level by a narrow band of low-energy quasiparticles band and the formation of a heavy-electron band, as the temperature is reduced below T_0. Another ARPES study [Yoshida 2010] revealed that a narrow hole-like band suddenly appears below ϵ_F as the temperature falls below T_0, which is interpreted as an evidence of the doubling of the unit cell along the **c**-axis in the hidden-order phase. By soft x-ray ARPES, Kawasaki *et al.* [Kawasaki 2011a] observed $5f$-U derived quasiparticles forming a large hole Fermi surface centered at the Z point and a large electron Fermi surface centered at the Γ point in the paramagnetic phase at temperatures just above T_0. They also identified nesting vectors fitting to that of the magnetic fluctuations observed by inelastic neutron scattering measurements [Broholm 1987, Bourdarot 2003a]. Kawasaki *et al.* [Kawasaki 2011b] performed soft

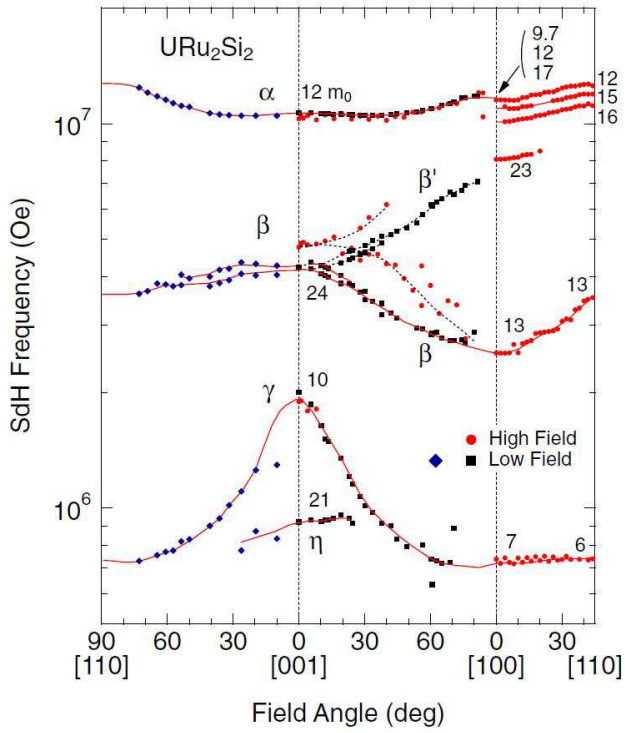

Figure 4.7: Angular dependence of the Shubnikov-de Haas frequencies in URu_2Si_2. The data are from high-field (red circles) and low-field (blue diamonds, black squares) measurements [Aoki 2012, Hassinger 2010]. The numbers indicate the cyclotron effective masses in terms of m_0 for $\mathbf{H} \parallel [001]$, [100], and [110]. Figure taken from [Aoki 2012].

x-ray ARPES on $U(Ru_{0.97}Rh_{0.03})_2Si_2$ and observed that the Fermi surface in the antiferromagnetic ground state of the doped compound is nearly identical to that of the hidden-order phase in the pure compound. ARPES measurements strongly support an itinerant nature of the $5f$-electrons due to their hybridization with the conduction bands at low temperatures [Santander 2009, Yoshida 2010, Kawasaki 2011a].

4.3.3 Quantum oscillations

The low-field Fermi surface of URu_2Si_2 was studied by quantum oscillation experiments, which have revealed four Fermi surface sheets α, β, γ, and η in the hidden-order phase [Bergemann 1997, Keller 1998, Ohkuni 1997, Ohkuni 1999, Hassinger 2010, Aoki 2012]. The associated frequencies for a magnetic field applied along the **c**-axis are $F_\eta \simeq 93$ T, $F_\gamma \simeq 200$ T, $F_\beta \simeq 425$ T, and $F_\alpha \simeq 1065$ T. The Fermi surface branches exhibit a wide range of heavy cyclotron effective masses ($m^*_\eta \simeq 21\ m_0$, $m^*_\gamma \simeq 10\ m_0$, $m^*_\beta \simeq 24\ m_0$, and $m^*_\alpha \simeq 12\ m_0$, for $\mathbf{H} \parallel \mathbf{c}$). The largest sheet α covers an area corresponding to less than 5% of the Brillouin zone [Keller 1998, Aoki 2010]. The Fermi surface is therefore very small,

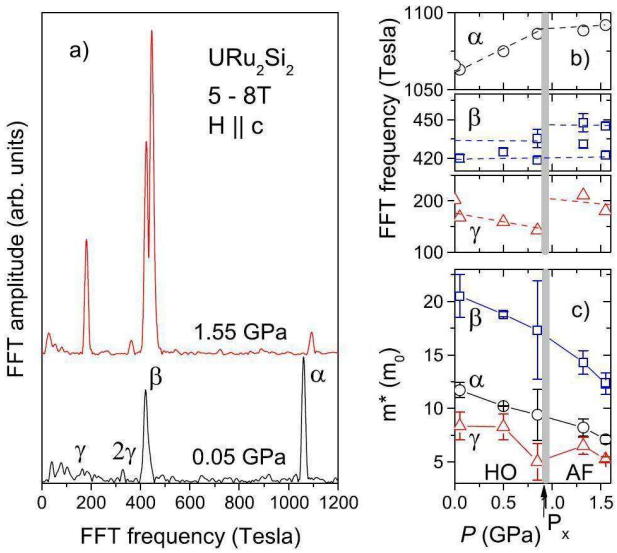

Figure 4.8: (a) Shubnikov-de Haas spectra in URu_2Si_2 for $\mathbf{H} \parallel \mathbf{c}$ at $T = 35$ mK for $p = 0.05$ GPa and at $T = 25$ mK for $p = 1.5$ GPa. (b) Pressure-dependence of the Shubnikov-de Haas frequencies. (c) Pressure-dependence of the effective masses. Figures taken from [Hassinger 2010].

in agreement with the low carrier density observed below T_0 by Hall effect measurements [Kasahara 2007]. The estimated Sommerfeld-coefficient calculated from these Fermi surfaces is $\gamma_{FS} \sim 40$ mJ/mol·K^2 [Aoki 2012], which represents 70% of the Sommerfeld-coefficient $\gamma_{Cp} \sim 55$ mJ/mol·K^2 extracted from the specific heat [Aoki 2010]. This indicates that part of the Fermi surface, presumably with a large effective cyclotron mass, is missing from the quantum oscillation experiments.

Figure 4.7 shows a detailed angular-dependence of the Shubnikov-de Haas frequencies in URu_2Si_2 [Aoki 2012]. The weak angle-dependence of the frequencies indicate that there are no open Fermi surface sheets [Keller 1998, Ohkuni 1999, Hassinger 2010, Aoki 2012]. The splitting of β into two branches may be due to the fact that the corresponding Fermi surface consists of different pockets with the same extremal cross-section for $\mathbf{H} \parallel \mathbf{c}$ and different cross-sections for $\mathbf{H} \parallel \mathbf{a}$ [Hassinger 2010, Aoki 2012]. The hypothesis of four noncentral pockets, which are flattened along the main axes of the Brillouin zone, is compatible with the proposition of the breaking of the four-fold symmetry from magnetic torque measurements [Okazaki 2011]. Shubnikov-de Haas data from measurements under pressure [Nakashima 2003, Hassinger 2010] show almost no modification of the frequencies and effective masses at the critical pressure P_x and in the pressure-induced antiferromagnetic phase, as shown in Figure 4.8. The Shubnikov-de Haas data indicate that the Fermi surface is essentially the same in the hidden-order and antiferromagnetic phases and that both phases exhibit the same unit cell doubling [Hassinger 2010].

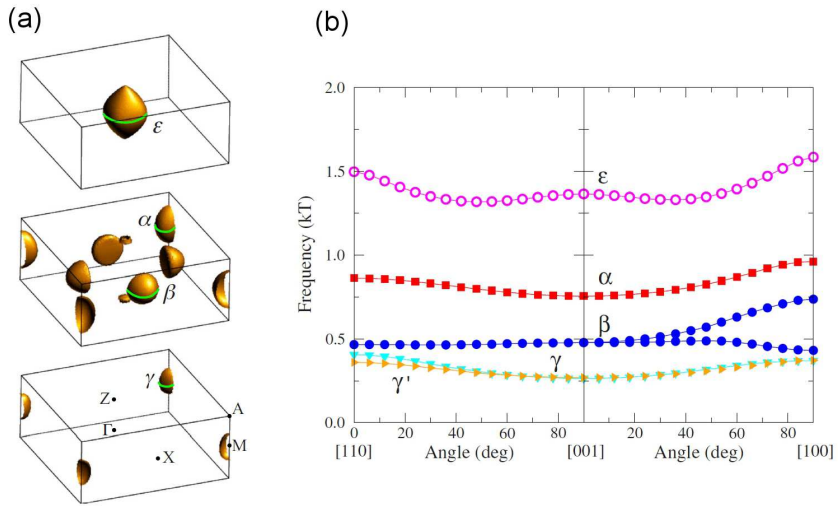

Figure 4.9: (a) Computed Fermi-surface sheets of URu_2Si_2 in the antiferromagnetic phase. The green lines indicate the extremal Fermi-surface orbits for a field along the **z**-axis. High-symmetry points are indicated in the bottom panel. (b) Calculated angular-dependence of the extremal Fermi surface cross-sections of URu_2Si_2. Figures taken from [Oppeneer 2010].

4.3.4 Band structure calculations

Oppeneer *et al.* [Elgazzar 2009, Oppeneer 2010] calculated the Fermi surface of the paramagnetic and the antiferromagnetic states by the local density approximation method [see Fig. 4.9(a)]. A possible nesting vector of the paramagnetic Fermi surface fits with the antiferromagnetic wave vector $\mathbf{Q}_0 = (1, 0, 0)$ of the magnetic fluctuations observed in the hidden-order phase [Broholm 1987, Bourdarot 2003a] and the ordering of the antiferromagnetic phase [Villaume 2008]. The incommensurate vector $\mathbf{Q}_1 = (0.6, 0, 0)$, where magnetic fluctuations are enhanced [Villaume 2008] in both the hidden-order and the antiferromagnetic phases, may also be related to a nesting vector of the antiferromagnetic phase. Figure 4.9(b) shows the calculated angular-dependence of the extremal Fermi surface cross-sections [Oppeneer 2010], which is in good agreement with that from quantum oscillations [Ohkuni 1999, Shishido 2009, Hassinger 2010, Aoki 2012].

Ikeda *et al.* [Ikeda 2012] performed density-functional theory calculations based on an itinerant $5f$-electron model. They found that the paramagnetic Fermi surface has the possible nesting vectors $\mathbf{Q}_0 = (1, 0, 0)$ and $\mathbf{Q}_1 = (0.6, 0, 0)$, which are related to the magnetic excitation gap observed at the same wavevectors in the hidden-order phase [Broholm 1987, Bourdarot 2003a]. Figure 4.10 shows the calculated Fermi surfaces of the hidden-order phase based on a dotriacontapole order and that of the antiferromagnetic phase. Both Fermi surfaces are similar, in agreement with Shubnikov-de Haas experiments under pressure [Nakashima 2003, Hassinger 2010].

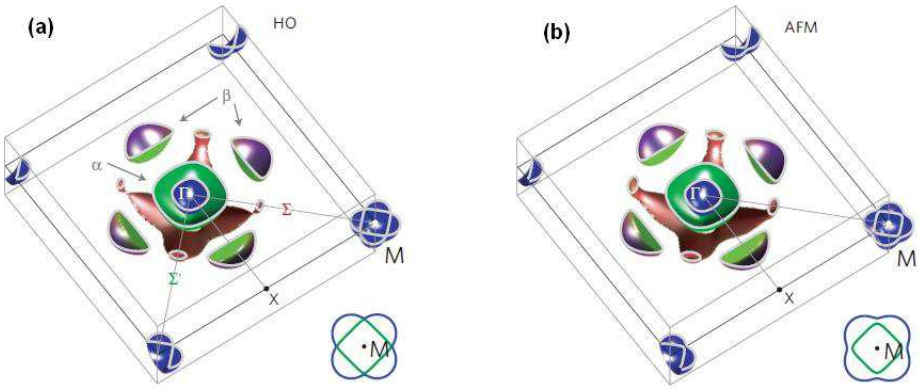

Figure 4.10: Cross-section of the Fermi surface in the (**a**,**a**)-plane including the Γ, X, and M points, from density-functional theory calculations for (a) a dotriacontapole order (HO) and (b) an antiferromagnetic order. Figures taken from [Ikeda 2012].

The band calculations of Oppeneer *et al.* [Oppeneer 2010] and Ikeda *et al.* [Ikeda 2012] both indicate a four-fold electron-Fermi surface β situated between the Γ and X points. The Fermi surface of the hidden-order phase differs between their calculations for the Γ and M points. The calculations of Oppeneer *et al.* [Oppeneer 2010] predict a small (γ) and a large (α) electron-Fermi surface at M and a large light hole-Fermi surface at Γ. Ikeda *et al.* [Ikeda 2012] predict a small electron-Fermi surface (γ) and a light hole-Fermi surface at Γ and a heavy electron-Fermi surface (κ) at M.
The calculations of Ikeda *et al.* [Ikeda 2012] are consistent with: i) ARPES measurements by Santander *et al.* [Santander 2009] observing a light hole-like and a heavy-electron-like band, ii) thermal transport measurements [Kasahara 2007] indicating a heavy-electron-Fermi surface with an effective mass of more than 30 m_0, and iii) a cyclotron resonance study by Tonegawa *et al.* [Tonegawa 2012] reporting a heavy electron-pocket (κ).

4.4 URu_2Si_2 in high-magnetic fields

Very early, URu_2Si_2 has been studied in high-magnetic field experiments [de Boer 1986, de Visser 1987, Sugiyama 1990]. Strong anomalies in the magnetization and resistivity have been observed in a magnetic field applied along the magnetic easy axis **c** [see Fig. 4.11]. Notably, sharp steps in the magnetization and magnetoresistivity have been observed at $\mu_0 H_1 \sim 35$ T, $\mu_0 H_2 \sim 37$ T, and $\mu_0 H_3 \sim 39$ T, where the transition at H_1 corresponds to the destruction of the hidden-order phase [Kim 2003a]. Sugiyama *et al.* [Sugiyama 1990] interpreted the

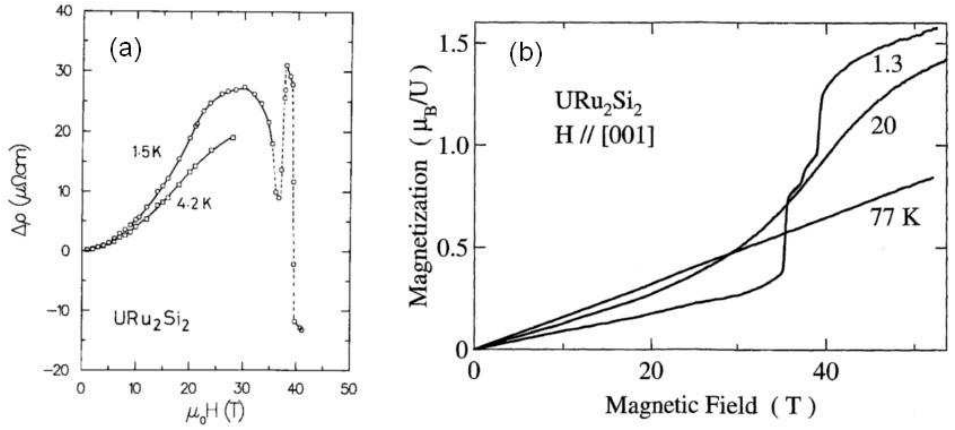

Figure 4.11: (a) Longitudinal magnetoresistivity of URu_2Si_2 measured in a magnetic field $\mathbf{H} \parallel \mathbf{I} \parallel \mathbf{c}$ at $T = 1.5$ and 4.2 K. Figure taken from [de Visser 1987]. (b) Magnetization of URu_2Si_2 measured in a magnetic field $\mathbf{H} \parallel \mathbf{c}$ at $T = 1.3$ K, 20 K, and 77 K. Figure taken from [Sugiyama 1999].

three transitions at H_1, H_2, and H_3 as metamagnetic transitions due to successive partial polarizations of the $5f$-electron moments and proposed that the intermediate phases between 35 and 39 T are canted antiferromagnetic states.

On the other hand, the hidden-order phase is very stable in a magnetic fields applied along the basal plane: the magnetic response to $\mathbf{H} \parallel \mathbf{a}$ is much weaker following the anisotropy of the magnetic susceptibility [Palstra 1985] and the magnetization versus the field is linear up to 50 T [de Boer 1986, Sugiyama 1990].

The magnetic field-temperature-phase diagram of URu_2Si_2 for $\mathbf{H} \parallel \mathbf{c}$ has been investigated using a wide range of experimental methods: magnetization [Sugiyama 1999, Harrison 2003], specific heat [Jaime 2002, Kim 2003a], ultrasound velocity [Suslov 2003, Yanagisawa 2013], resistivity [Jaime 2002, Kim 2003b], dilatometry [Correa 2012], and thermoelectricity [Malone 2011, Pourret 2013]. Figure 4.12 shows a precise H-T-phase diagram established from resistivity measurements [Kim 2003b].

Five different low-temperature phases are identified in the T-H-phase diagram:

- The paramagnetic hidden-order phase (I) below T_0, which is destabilized at ~ 35 T.
- Phase II is a intermediate magnetic phase between the first-order transitions at H_1 and H_2.
- Phase III is a intermediate magnetic phase between the first-order transitions at H_2 and H_3.
- Above H_3 the system is in a polarized paramagnetic state (IV). The polarized

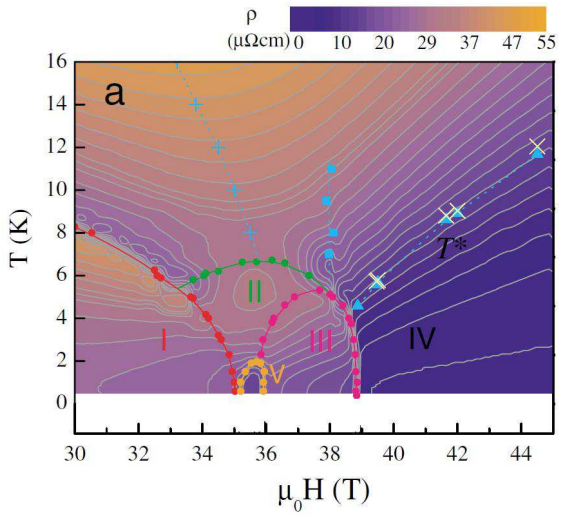

Figure 4.12: (a) High field-phase diagram of URu_2Si_2 obtained from ρ versus H, ρ versus T [Kim 2003b], and M versus H data [Harrison 2003]. Figure taken from [Kim 2003b].

magnetic moment reaches 1.5 μ_B/U at 45 T [Sugiyama 1999] and continues to increase at higher field, indicating remaining unquenched magnetic fluctuations.

- The small dome (V) is an intermediate phase, which appears between the phases II and III, when the temperature is reduced below $T \sim 2$ K.

Observations by Nernst, Hall [Levallois 2009] and Shubnikov-de Haas effect [Altarawneh 2011] indicate that successive Fermi surface reconstructions occur at the transition fields H_1, H_2 and H_3. Fermi surface modifications occur in fields applied along **c** smaller than $\mu_0 H_1 = 35$ T, i.e., inside the hidden-order phase. Shishido *et al.* [Shishido 2009] observed a step-like anomaly in the Hall resistivity at $\mu_0 H^* = 22.5$ T, which they identified as a signature of a field-induced Fermi surface reconstruction, in agreement with the observation of a new frequency $F_\epsilon \sim 1300$ T in their Shubnikov-de Haas data. Malone *et al.* [Malone 2011] observed anomalies in the thermoelectric power, a minimum at $\mu_0 H_m \simeq 11$ T and a maximum at $\mu_0 H^* \simeq 23$ T. They interpreted these anomalies as the signature of topological modifications of the band structure, i.e., Lifshitz transitions [Lifshitz 1960]. Kink-like anomalies in the resistivity were also observed at $\mu_0 H \sim 8$ T [Hassinger 2010], and at $\mu_0 H^* = 24$ T [Altarawneh 2011, Aoki 2012]. A change of the Fermi surface was also observed at the maximum of resistivity at ~ 30 T [Altarawneh 2011]. Recently, Pourret *et al.* [Pourret 2013] performed a detailed study of the thermoelectric power and Nernst effect on high-quality URu_2Si_2 single crystals in high-magnetic fields applied along the **c**-axis. They have confirmed a very rich H-T-phase diagram deep

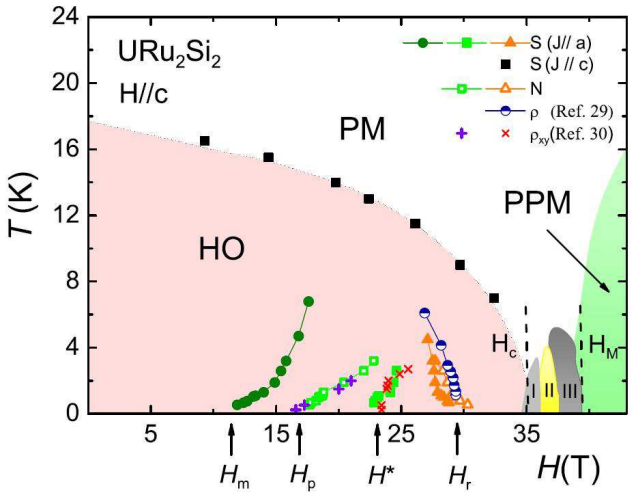

Figure 4.13: H-T-phase diagram of URu_2Si_2. Full symbols: anomalies in the thermoelectric power [Pourret 2013]. Open symbols: anomalies in the Nernst signal [Pourret 2013]. Pluses, crosses: anomalies in the Hall signal [Shishido 2009]. Half-filled circles: maximum in the resistivity (data from this work, see Sect. 5.2, [Scheerer 2012]). The field position of the changes in the Shubnikov-de Haas frequencies at H_m, H_p, H^*, and H_r [Aoki 2012] are indicated by vertical arrows. Figure taken from [Pourret 2013].

inside the hidden-order phase, with at least four field-induced anomalies below H_1 [see Fig. 4.13].

5 High-Magnetic-Field properties of URu_2Si_2 in $\mathbf{H} \parallel \mathbf{c}$

In this chapter, I present magnetization and transverse magnetoresistivity experiments performed on URu_2Si_2 in magnetic fields H applied along the easy axis **c**. Anomalies characteristic of magnetic phase transitions and magnetic crossovers are studied in detail. The associated transition and crossover lines are drawn in the magnetic field-temperature phase diagram. A comparison is made between the phase diagram obtained here and these published in the literature.

5.1 Magnetization

Figure 5.1(a) presents the magnetization M of URu_2Si_2, which has been measured with the compensated coils technique (cf. Sect. 3.3) versus the magnetic field H applied parallel to the **c**-axis at different temperatures from 1.5 to 60 K. At zero field and below $T_0 = 17.5$ K, the system is in the hidden-order phase. At $T = 1.5$ K and at low field, the magnetization increases almost linearly with H. Above ~ 30 T, the slope of $M(H)$ becomes non-linear and increases [see blue arrow in Fig. 5.1(a)]. At higher fields, three sharp steps occur in the magnetization at $\mu_0 H_1$, $\mu_0 H_2$, and $\mu_0 H_3$ between 35 and 39 T. The magnetization reaches 1.5 μ_B per Uranium-ion at $\mu_0 H \sim 45$ T and continues to increase significantly at higher field, showing that the polarization is not complete due to remaining unquenched magnetic fluctuations. The steps in the magnetization become less important at higher temperature and have vanished above 10 K. Figures 5.1(b) and 5.1(c) show the slope $\partial M/\partial H$ of the magnetization versus H at temperatures from 1.5 to 10 K and from 10 to 30 K, respectively. The transition fields H_1, H_2, and H_3 are defined at the local maxima of the slope. At $T = 15$ K, the sharp peaks of the transitions H_1, H_2, and H_3 have vanished and have been replaced by one broad peak at $H^{HT}_{\partial M/\partial H,max}$. This crossover-like peak is broadened at higher temperatures and we loose its trace above 30 K. Figures 5.1(d) and (e) show $\partial M/\partial H$, for the rise and the fall, respectively, of the pulsed field for $\mu_0 H = 34$ T - 40 T and at temperatures between 1.5 and 4.2 K. For the fall and at $T = 1.4$ K, I extract $\mu_0 H_1 = 34.9$ T and $\mu_0 H_3 = 38.7$ T. The sharpness of the peaks at H_1 and H_3 and their hysteresis indicate that they are signatures of

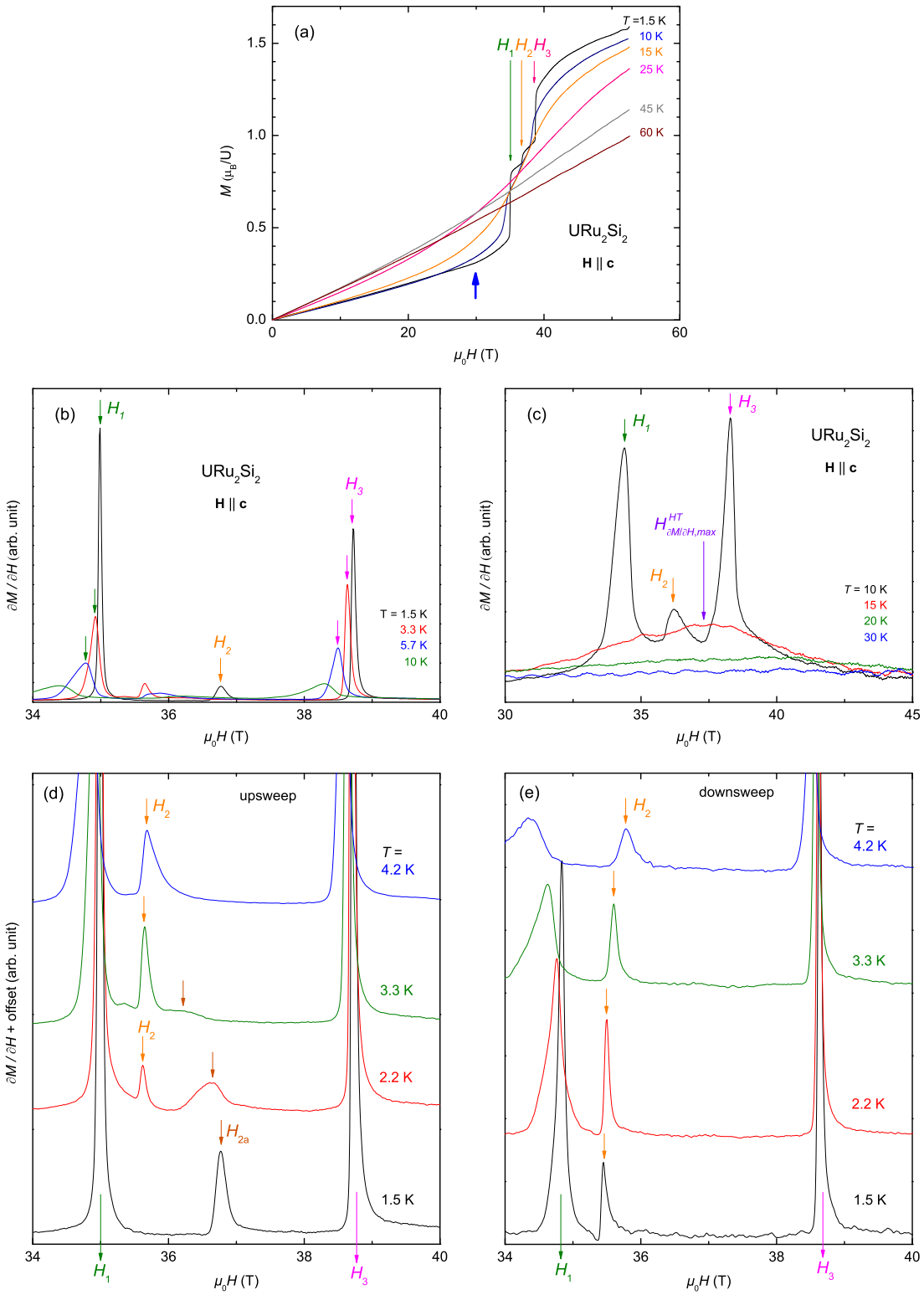

Figure 5.1: (a) Magnetization M versus the magnetic field H applied along c of URu_2Si_2 at temperatures between 1.5 K and 60 K. The inset shows $M(H)$ at 1.5 K for the rise and fall of the pulsed magnetic field. (b) $\partial M/\partial H$ versus H at temperatures between 1.5 K and 10 K. (c) $\partial M/\partial H$ versus H at temperatures between 10 K and 60 K. $\partial M/\partial H$ versus H between 34 and 40 T and at temperatures between 1.5 and 4.2 K, for (d) the rise and (e) the fall of the field, respectively.

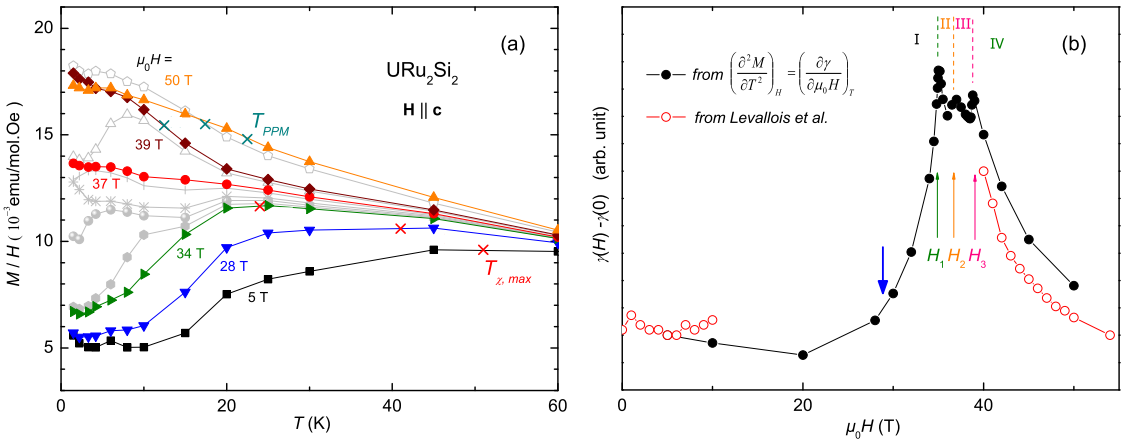

Figure 5.2: (a) M/H versus temperature T at different magnetic fields $\mathbf{H} \parallel \mathbf{c}$. (b) Comparison of the field-dependence of the Sommerfeld coefficient extracted from our magnetization data and the square root $\sqrt{A}$ of the quadratic coefficient of resistivity extracted by Levallois *et al.* [Levallois 2009]. The blue arrow indicates the onset of enhanced fluctuations.

first-order magnetic transitions. We observe less pronounced intermediate peaks at H_2 and H_{2a} with an unusual hysteresis: in an increasing magnetic field, at $T = 1.5\ K$, a transition-like peak occurs at $\mu_0 H_{2a} = 36.8$ T. For $T = 2.2$ K and 3.3 K, this peak is reduced and shifted to lower fields before vanishing above 3.3 K. For $T \geq 2.2$ K, a different transition induces a peak at $\mu_0 H_2 = 35.6$ T. In a decreasing magnetic field, we do not observe H_{2a}, but only one peak at $\mu_0 H_2$ at all temperatures below 10 K. At $T = 1.5$ K, this peak occurs at $\mu_0 H_2 = 35.45$ T and is slightly shifted to higher fields with increasing temperature.

Figure 5.2 (a) presents M/H versus T at different magnetic fields. These plots indicate that a change of behavior occurs in the critical regime of the magnetic transitions ($35 - 39$ T). The low-field regime, from 0 to 35 T, is characterized by a crossover associated with a broad maximum of the susceptibility $\chi(T)$ at the temperature $T_{\chi,max}$. $T_{\chi,max}$ equals $\simeq 50$ K at $\mu_0 H = 5$ T, decreases with increasing magnetic field and has vanished above 35 T. In the high-field regime, above 39 T, M/H decreases monotonically with T. Here, the system is polarized paramagnetically, having a strong field-induced magnetization. The characteristic temperature T_{PPM} of the polarized regime is defined at the inflection point of $M/H(T)$, indicating the onset of an enhanced magnetization. Between 35 and 39 T, the cascade of low-temperature transitions at H_1, H_2, and H_3 leads to complex features in the M/H versus T plots.

Figure 5.2(b) presents the field-dependence of the Sommerfeld coefficient $\gamma = C_p/T(T \to 0)$ of URu_2Si_2, where C_p is the specific heat, estimated using the Maxwell

relation:

$$\left(\frac{\partial\gamma}{\partial\mu_0 H}\right)_T = \left(\frac{\partial^2 M}{\partial T^2}\right)_H \tag{5.1}$$

and assuming that $M(T,H) = M(0,H) - \beta T^2$ is obeyed (cf. also [Paulsen 1990]). The variation of γ extracted here from $M(T)$ is only qualitative and expressed in arbitrary units. For the estimation of γ, the temperature of our magnetization experiments have been corrected thanks to additional torque experiments [see Fig. 5.9(a)]. γ is almost field-independent at low fields, but a strong enhancement of γ, and thus of the effective mass m^*, is found in a broad magnetic field window between 30 and 45 T. A comparison with the field-dependence of $\sqrt{A}$ from Levallois *et al.* [Levallois 2009], where A is the quadratic coefficient of the resistivity $\rho_{x,x}(T)$ at a given field, is added. As γ, $\sqrt{A}$ probes the effective mass m^* assuming the validity of a Fermi liquid picture in a frame where magnetic fluctuations dominate (see Sect. 2.2). γ and $\sqrt{A}$ are related by a Kadowaki-Woods ratio A/γ^2, which is almost constant in the heavy-fermion family [Kadowaki and Woods 1986] (see Sect. 2.2). γ starts to increase at $\mu_0 H \sim 30$ T [see blue arrow in see Fig. 5.2(b)], due to an enhancement of the magnetic fluctuations leading to a non-linear slope in $M(H)$ [see blue arrow in Fig. 5.1(a)]. This increase of γ occurs simultaneously with the maximum in $\rho_{x,x}(H)$ at $H^{LT}_{\rho,max}$, which will be associated in Chapters 7 and 9 to a Fermi surface reconstruction.

Figure 5.3(a) presents the H-T phase diagram of URu_2Si_2 constructed from the magnetization experiments in magnetic fields applied along **c**. At low temperature ($T \leq 10$ K), a cascade of magnetic transitions between 35 and 39 T leads from the hidden-order phase to a polarized regime. The first transition at H_1 corresponds to the field-induced destruction of the paramagnetic hidden-order state, labeled phase I. Above the third transition at H_3, the system is in the polarized paramagnetic state, labeled IV. The first-order phase transitions between $\mu_0 H = 35$ and 39 T have vanished at $T = 15$ K and the high-temperature regime ($T > 10$ K) is characterized by the crossover lines $T_{\chi,max}$, $H^{HT}_{\partial M/\partial H,max}$, and T_{PPM}. The energy scale $T_{\chi,max}$ in the low field-regime, which corresponds to a maximum in the zero-field susceptibility $\chi(T, H = 0)$ at 55 K, indicates a crossover line between a high-temperature weak-correlations regime and a low-temperature strong-correlations regime. The high-field scales $H^{HT}_{\partial M/\partial H,max}$ and T_{PPM}, defined at the extremal slopes of $M(H)$ and $M(T)$, respectively, correspond both to the onset of an enhanced magnetization. These scales are both the signatures of the same large crossover frontier between a low-polarization regime with strong magnetic fluctuations and a high-polarization regime with weak fluctuations. Figure 5.3(b) shows a zoom to the critical region of

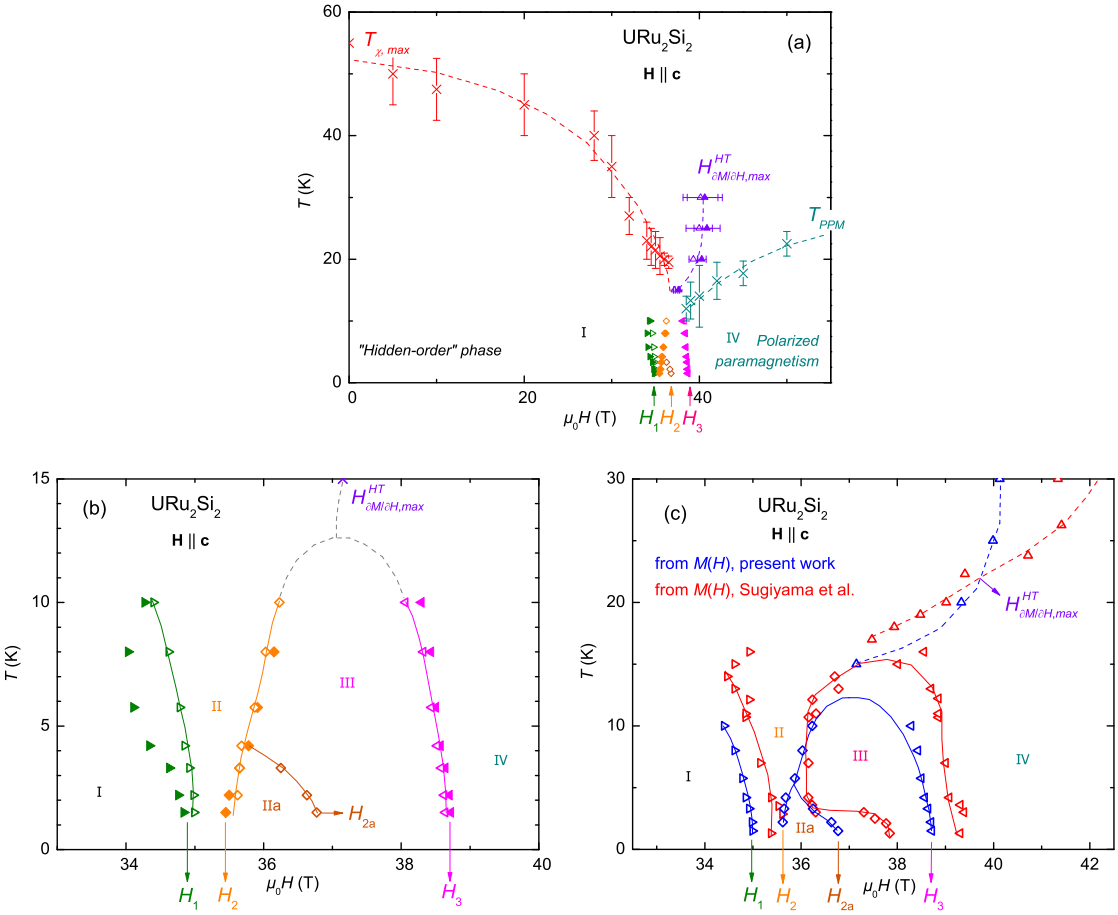

Figure 5.3: (a) H-T phase diagram constructed from our magnetization experiments for **H** ∥ **c**. Open symbols stand for the rise and full symbols for the fall of the pulsed magnetic field. (b) Zoom in the critical region of the transitions H_1, H_2, and H_3. (c) Comparison of the H-T phase diagram from the magnetization experiments (from the rise of the field only) of this work and from [Sugiyama 1999].

the phase diagram. For the rise (open symbols) and the fall (full symbols) of the pulsed field, two intermediate states, state II, between H_1 and H_2, and state III, between H_2 and H_3, are observed at temperatures below 15 K. For the rise of the field, an additional state IIa is observed between H_2 and H_{2a} at temperatures below 4.2 K.

Figure 5.3(c) shows the map of the critical region of the H-T phase diagram of URu_2Si_2 resulting from the rising-field magnetization measured here and measured by Sugiyama *et al.* [Sugiyama 1999]. The two sets of data are in good agreement, except for slight shifts of the transition lines over the field axis and a slight difference between the temperatures at which H_1, H_2, and H_3 have vanished. I note that the high-temperature crossover lines $T_{\chi,max}$ and T_{PPM} are new features of the present

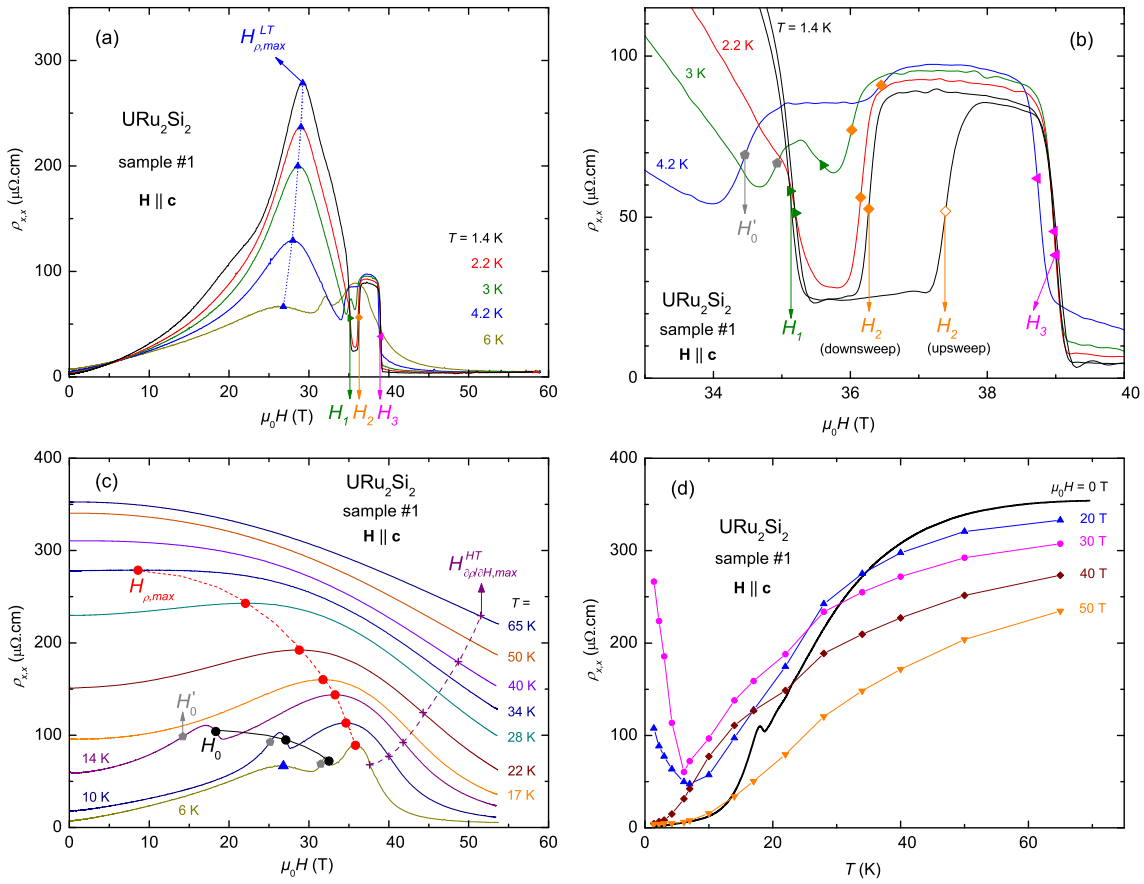

Figure 5.4: (a) Magnetoresistivity $\rho_{x,x}$ of URu_2Si_2 sample #1 versus the magnetic field H applied along **c** at temperatures between 1.4 K and 6 K. (b) $\rho_{x,x}(H)$ for the field range 33 - 40 T at temperatures between 1.4 K and 4.2 K. Rise and fall of the pulsed magnetic field for $T = 1.4$ K, fall only for the other temperatures. (c) $\rho_{x,x}$ versus H applied along **c** of sample #1 at temperatures between 6 K and 65 K. (d) $\rho_{x,x}$ versus T of sample #1 at magnetic fields $\mu_0 H = 0, 20, 30, 40$ and 50 T applied along **c**.

work. Sugiyama *et al.* [Sugiyama 1999] observed similar behaviors of the transitions at H_2 and H_{2a}: for rising fields, H_{2a} is shifted to lower fields with increasing temperature and vanishes at ~ 4 K and H_2 is not observed below 2 K. In both sets of data, the phase IIa between H_2 and H_{2a} is observed in rising but not in falling pulsed field. Sugiyama *et al.* [Sugiyama 1999] also observed a broad maximum in $\partial M/\partial H$ at $H^{HT}_{\partial M/\partial H,max}$, which is almost temperature-independent, up to 60 K.

5.2 Magnetoresistivity

Figure 5.4(a) presents the transverse magnetoresistivity $\rho_{x,x}$ of URu_2Si_2 versus the magnetic field H applied parallel to the **c**-axis at temperatures between 1.4 and 6 K (experiment performed on sample #1, RRR = 95, cf. Sects. 3.4 and 3.5).

At $T = 1.4$ K, the resistivity increases strongly with the magnetic field, up to a pronounced maximum at $\mu_0 H^{LT}_{\rho,max} \simeq 29$ T, and decreases fast from 29 to 35 T. $H^{LT}_{\rho,max}$ decreases slightly with increasing temperature, down to $\mu_0 H^{LT}_{\rho,max} \simeq 26.5$ T at $T = 6$ K. Inside the hidden-order phase, below $\mu_0 H = 35$ T, the magnetoresistivity exhibits a strong temperature-dependence. The maximum of $\rho_{x,x}$ at $\mu_0 H^{LT}_{\rho,max}$ is about four times higher at $T = 1.4$ K than at 6 K. Three sharp steps in the resistivity between 35 and 39 T are signatures of the first-order transitions at H_1, H_2, and H_3, which are also observed in the magnetization [see Fig. 5.1(a)]. The resistivity reaches $\simeq 25$ $\mu\Omega$.cm for $H_1 < H < H_2$ and $\simeq 90$ $\mu\Omega$.cm for $H_2 < H < H_3$. Above $\mu_0 H_3 = 39$ T, the resistivity has almost vanished.

Figure 5.4(b) shows a zoom on $\rho_{x,x}$ versus $\mu_0 \mathbf{H} \parallel \mathbf{c}$ from 30 to 40 T at temperatures between 1.4 K and 4.2 K, providing details on the critical region. H_1 is defined at the first abrupt decline of $\rho_{x,x}$. $\mu_0 H_1 = 35.1$ T at $T = 1.4$ K is shifted to 35.6 T at $T = 3$ K, and vanishes at $T = 4.2$ K. At $T = 3$ K, the resistivity shortly increases between $\simeq 34.7$ T and 35.3 T, which is associated with a maximum of slope of $\rho_{x,x}(H)$ at $\mu_0 H'_0 = 34.9$ T. At 4.2 K, $\mu_0 H'_0$ is shifted to 34.5 T. The transition field H_2 is defined at the abrupt rise of $\rho_{x,x}$. At $T = 1.4$, $\mu_0 H_2$ equals 36.3 T and 37.4 T for the fall and rise of the pulsed field, respectively. H_2 shifts to lower fields with increasing temperature up to 3 K and shifts to higher fields above 3 K ($\mu_0 H_2 = 36.5$ T at 4.2 K). The transition field H_3 is defined at the second abrupt decline of $\rho_{x,x}$. $\mu_0 H_3$ equals 39 T at $T = 1.4$ K and is slightly shifted to lower fields with increasing temperature ($\mu_0 H_3 = 38.7$ T at 4.2 K).

Figure 5.4(c) presents the transverse magnetoresistivity of sample #1 versus H applied along $\mathbf{c}$ at temperatures between 6 and 65 K. The low-temperature transitions at H_1, H_2, and H_3 vanish at $T = 6$ K and the low-temperature maximum at $\mu_0 H^{LT}_{\rho,max}$ vanishes at 10 K. Below $T_0 = 17.5$ K, the magnetoresistivity shows the signature of a transition at the magnetic field H_0, which corresponds to the boundary of the hidden-order phase ($H_0 \to 0$, when $T \to 17.5$ K). H_0 is defined at the second extremum in $\partial\rho_{x,x}/\partial H$ of a Z-shaped anomaly in $\rho_{xx}(H)$. H'_0 is defined at the first extremum in $\partial\rho_{x,x}/\partial H$ of the Z-shaped anomaly. As well as H_0, H'_0 is related to the field-induced destabilization of the hidden-order phase. The destruction of the hidden-order state at H_0 gives rise to a clear anomaly in $\rho_{x,x}(H)$, but no corresponding anomaly is observed in $M(H)$ [see Fig. 5.1(a)]. The magnetoresistivity exhibits a maximum at $H_{\rho,max}$, which is the signature of a "high-temperature" crossover. $\mu_0 H_{\rho,max}$ equals $\simeq 36$ T at $T = 6$ K, decreases with increasing temperature and has vanished at $T = 40$ K. The maximum at $H_{\rho,max}$ broadens strongly with increasing temperature. For $H > H_{\rho,max}$, the resistivity is continuously decreasing with H up to maximum field, due to the quenching of the scattering of conduction electrons

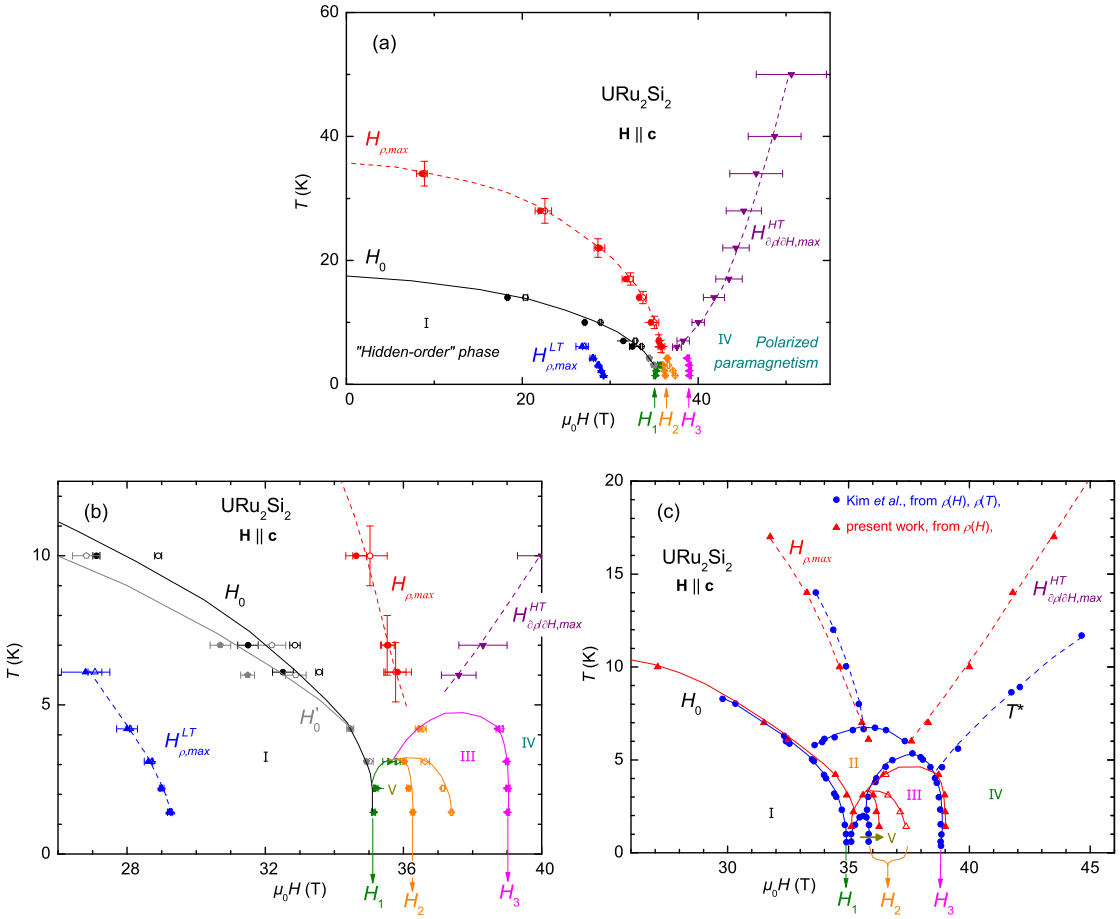

Figure 5.5: (a) H-T phase diagram constructed from our magnetoresistivity experiments for $\mathbf{H} \parallel \mathbf{c}$. Open symbols stand for the rise and full symbols for the fall of the pulsed magnetic field. (b) Zoom in the critical region of the transitions H_1, H_2, and H_3. (c) Comparison of the H-T phase diagram from the $\rho_{x,x}(H)$ data of this work and from the $\rho(H)$ and $\rho(T)$ data from [Kim 2003b].

on the f-electron moments, and a further "high-temperature" scale $H^{HT}_{\partial\rho/\partial H,max}$ can be defined at the extremum of $\partial\rho_{x,x}/\partial H$. $H^{HT}_{\partial\rho/\partial H,max}$ equals 37.6 T at $T = 6$ K and is shifted to higher fields with increasing temperature. Figure 5.4 (d) shows $\rho_{x,x}$ versus T of sample #1 at different magnetic fields. The plots show that, for $\mathbf{H} \parallel \mathbf{c}$, $\rho_{x,x}$ is strongly magnetic field-dependent over a large temperature range (at least up to 65 K). Furthermore the graph emphasizes that the maximum of $\rho_{x,x}$ at $H^{LT}_{\rho,max} \simeq 30$ T suddenly develops below 6 K.

Figure 5.5(a) presents the H-T phase diagram of URu_2Si_2 constructed from the magnetoresistivity experiments in magnetic fields applied along $\mathbf{c}$. The high temperatures are governed by the crossover lines $H_{\rho,max}$ and $H^{HT}_{\partial\rho/\partial H,max}$. The high-temperature crossover line $H_{\rho,max}$ decreases with T, which is equivalent in the H-T phase diagram to the decrease with H of a temperature scale $T_{\rho,max}$, which reaches

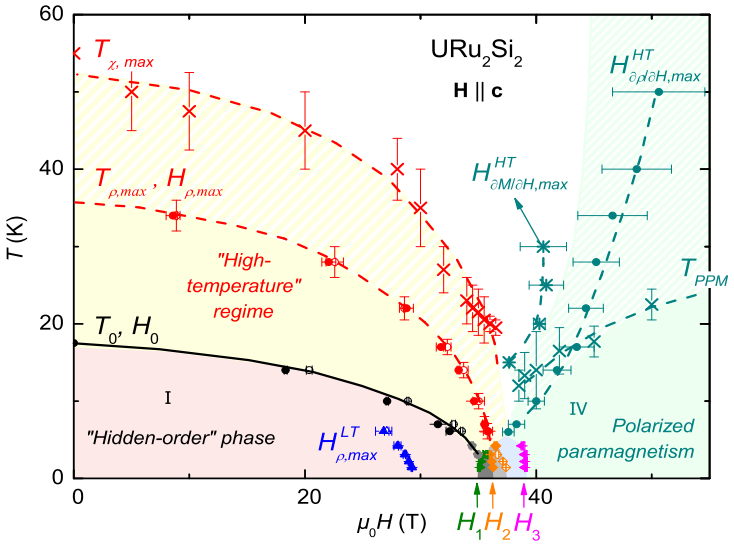

Figure 5.6: H-T phase diagram of URu_2Si_2 for $\mathbf{H} \parallel \mathbf{c}$.

40 K at zero-field and vanishes in the critical field area (35 to 39 T). The crossover line $\mu_0 H^{LT}_{\rho,max}$ occurs inside the hidden-order phase. The boundary line H_0 of the hidden-order phase is connected to the transition $T_0 = 17.5$ K at zero-field. Figure 5.5(b) shows a zoom to the critical region of the phase diagram. The transition lines H_1 and H_2 meet at ($\mu_0 H \sim 36$ T, $T \sim 3$ K) in the phase diagram, delimiting the intermediate phase V. The transition lines H_2 and H_3 delimit the intermediate phase III. The transition fields H_0 (or H_0') and H_1 correspond to the destruction of the hidden-order phase by a magnetic field applied along **c**, but are distinct transitions resulting in different anomalies in $\rho_{x,x}$, leading to different higher-field states. H_0 (or H_0') delimits the low-temperature hidden-order phase from the high-temperature regime, whereas H_1 leads from phase I to the metamagnetic state V.
Figure 5.5(c) compares the H-T phase diagrams constructed by the resistivity data $[\rho_{x,x}(H)]$ of this work and by the resistivity data $[\rho_{x,x}(H),\rho_{x,x}(T)]$ of Kim *et al.* [Kim 2003b]. Good agreement is found for the transition line H_0, the crossover line $H_{\rho,max}$ and for the phases V and III. Kim *et al.* [Kim 2003b] have defined an additional transition line thanks to their $\rho_{x,x}(T)$-data, which delimits phase II. Kim *et al.* [Kim 2003b] have also defined a crossover line T^*, below which a T^2-behavior of $\rho_{x,x}(T)$ is observed. Thus, T^* marks the onset of a high-field low-temperature Fermi liquid region, corresponding to phase IV.

5.3 H-T phase diagram of URu_2Si_2

Figure 5.6 presents the magnetic field-temperature phase diagram of URu_2Si_2 based on our resistivity and magnetization experiments. A singularity of URu_2Si_2 is that,

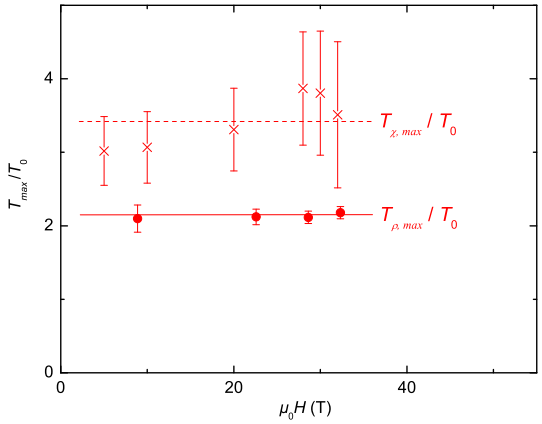

Figure 5.7: Magnetic field-dependence of the ratios $T_{\rho,max}/T_0$ and $T_{\chi,max}/T_0$, for **H** ∥ **c**.

instead of a unique second-order phase transition at a given critical field, the low-temperature phase diagram is made of a cascade, between 35 and 39 T, of three first-order transitions at H_1, H_2, and H_3, with an additional sharp crossover at $H^{LT}_{\rho,max} \simeq 30$ T within the hidden-order phase. As observed in the magnetization $M(H)$, successive partial polarizations of the $5f$-electron moments occur at H_1, H_2, and H_3. The phases II and III of the critical region of the phase diagram are presumably high-field-induced canted antiferromagnetic structures as proposed by Sugiyama *et al.* [Sugiyama 1990] for URu_2Si_2, and as observed in Rh-doped URu_2Si_2 by Kuwahara *et al.* [Kuwahara 2013] (see Chapter 6). The significant anomalies in the resistivity $\rho_{x,x}(H)$ at H_1, H_2, and H_3, and the fact that the metamagnetic transitions separate phases with very different resistivity behaviors, indicate that these transitions strongly change the electronic transport properties. In fact, observations by Nernst and Hall [Levallois 2009], and Shubnikov-de Haas effect [Altarawneh 2011] indicate Fermi surface reconstructions at H_1, H_2 and H_3.

In the high-temperature regime, two energy scales $T_{\chi,max}$ and $T_{\rho,max}$ show similar behaviors, both being suppressed by increasing magnetic field and vanishing in the critical area of the magnetic transitions between 35 and 39 T. Furthermore the ratios $T_{\chi,max}/T_0$ and $T_{\rho,max}/T_0$ are both constant up to 35 T as shown in Figure 5.8. At zero field, $T_{\chi,max}$ corresponds to the maximum in $\chi(T, H \to 0)$ at 55 K. A maximum in the zero-field resistivity is observed at $T = 70$ K, but not at 40 K. This can be explained by the fact that an electron-phonon scattering contribution $\rho^{e-ph}_{x,x}$ adds to the purely electronic term $\rho^{e-e}_{x,x}$ of the resistivity $\rho_{x,x}$. A difficulty is to estimate $\rho^{e-ph}_{x,x}(T)$. Assuming that, at $\mu_0 H = 50$ T, the magnetic polarization is accompanied by a quenching of almost all magnetic fluctuations and by a vanishing of the $\rho^{e-e}_{x,x}$ part in the resistivity, $\rho^{e-ph}_{x,x}$ can be approximated by $\rho_{x,x}(T, \mu_0 H = 50\text{T})$ [see Fig.5.8(a)]. Following this, we estimate the purely electronic term by

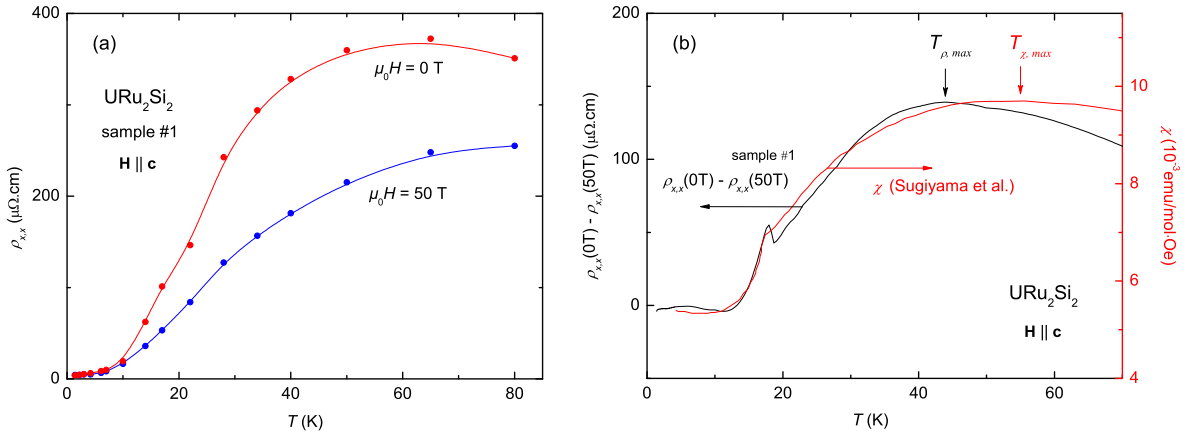

Figure 5.8: (a) $\rho_{x,x}$ versus T at $\mu_0 H = 0$ and 50 T for $\mathbf{H} \parallel \mathbf{c}$ (b) Comparison of $\rho_{x,x}(T, H = 0) - \rho_{x,x}(T, H = 50\,\mathrm{T})$ and $\chi(T)$ from [Sugiyama 1999] versus the temperature.

$\rho^{e-e}_{x,x}(T, H = 0) = \rho_{x,x}(T, H = 0) - \rho_{x,x}(T, \mu_0 H = 50\ \mathrm{T})$ [see Fig.5.8(b)]. The shift between the maximum observed in $\rho^{e-e}_{x,x}(T, H = 0)$ at 40 K and that observed in $\rho_{x,x}(T, H = 0)$ at 70 K is due to the additional electron-phonon contribution to the resistivity. The temperature scale of 40 K found in this estimation of $\rho^{e-e}_{x,x}(T, H = 0)$ coincides with $T_{\rho,max}$ extracted from the magnetoresistivity data, indicating that they correspond to the same phenomenon. Figure 5.8(b) compares the estimated electronic term in the resistivity $\rho^{e-e}_{x,x}(T, H = 0)$ with the magnetic susceptibility $\chi(T)$ from [Sugiyama 1999]. A striking similarity between the general shape of $\rho^{e-e}_{x,x}(T, H = 0)$ and that of the magnetic susceptibility $\chi(T)$ is found with the maxima of $\rho^{e-e}_{x,x}(T, H = 0)$ at $T_{\rho,max} \simeq 40$ K and that of $\chi(T)$ at $T_{\chi,max} \simeq 55$ K. Thus, both temperature-scales $T_{\chi,max}$ and $T_{\rho,max}$ are presumably related to the same physical phenomenon, i.e. a crossover frontier between a high-temperature independent-U-ions regime and a low-temperature interacting-U-ions regime. The offset between $T_{\chi,max}$ and $T_{\rho,max}$ in Figure 5.6 is due to the non-equivalence of their definitions and to the fact that the temperature or magnetic field of a crossover can not be defined precisely.

The field-induced suppression of the transition temperature T_0 of the hidden-order phase follows that of the high-temperature scale $T_{\chi,max}$ (or $T_{\rho,max}$). This and the constance of the ratios $T_{\chi,max}/T_0$ and $T_{\rho,max}/T_0$ [see Fig. 5.7] indicate that the vanishing of the higher-temperature crossover scale (either $T_{\chi,max}$ or $T_{\rho,max}$) controls that of T_0. In other words, the mechanism responsible for the crossover at $T_{\chi,max}$ or $T_{\rho,max}$ is a precursor of the hidden-order state since its destabilization leads to that of the hidden-order, and the high-temperature regime is a necessary condition for the development of the hidden-order state. The field-induced vanishing of the high-temperature crossover, which might be the mark of inter-site electronic correlations, governs thus both the critical area leading to a polarized

regime above 39 T and the destabilization of the hidden-order state at low temperature. The magnetic-field dependencies of $T_{\chi,max}$ and T_{PPM} recall strongly the case of the heavy-fermion paramagnet $CeRu_2Si_2$ [Paulsen 1990, Ishida 1998]. The phase diagram of $CeRu_2Si_2$ is characterized by a pseudo-metamagnetic transition to a polarized state at $\mu_0 H_m = 7.8$ T. As emphasized in [Aoki 2013], a correspondence 1 K $\leftrightarrow$ 1 T relates the maximum of susceptibility $T_{\chi,max}$ to the critical magnetic field H^* of several heavy-fermion paramagnets (including URu_2Si_2, for which $\mu_0 H^* = 35 - 39$ T, and $CeRu_2Si_2$, for which $\mu_0 H^* = \mu_0 H_m = 7.8$ T), suggesting that both $T_{\chi,max}$ and H^* are controlled by a single magnetic energy scale.
The crossover scales $H^{HT}_{\partial M/\partial H,max}$ and T_{PPM} from the magnetization data and $H^{HT}_{\partial \rho/\partial H,max}$ from the resistivity data are all signatures of the same crossover frontier between a low-polarization and a high-polarization regime.

5.4 Comparison of the phase diagrams extracted using different techniques

A stumbling difference between the resistivity experiments and the magnetization experiments performed here on URu_2Si_2 samples is that the transitions at H_1, H_2, and H_3 have vanished above $T = 4.2$ K in $\rho_{x,x}(H)$ but are observed up to 10 K in our $M(H)$, as shown in Figure 5.9(a). Contrary to the magnetization data of this work and that from Sugiyama *et al.* [Sugiyama 1999], Harrison *et al.* [Harrison 2003] obtained magnetization data, where the transitions H_1, H_2, and H_3 have already vanished at $T = 7$ K. Additional magnetic torque experiments have been performed in Toulouse on a URu_2Si_2 sample in the same experimental setup as the resistivity experiments, where a good thermalization is assured. The phase diagram extracted from the torque experiments, also shown in Figure 5.9(a), is in good agreement with that from the resistivity data of this work and from the magnetization data of Harrison *et al* [Harrison 2003]. Thus, the temperature difference between our resistivity and magnetization data might result from thermal gradients in our pulsed-field magnetization setup (as well as in the pulsed-field setup used by Sugiyama *et al* [Sugiyama 1999]).
Figure 5.9(b) compares the H-T phase diagrams obtained by ultrasonic velocity [Suslov 2003] and resistivity [Kim 2003b, Jo 2007] experiments. The three sets of data are in good agreement, all showing the phases I to V. Minor differences are small shifts over the H-axis of the transition lines and small differences in temperature. Strong variations are found for the transition line H_2, which delimits phase V: Kim *et al.* [Kim 2003b] observed $\mu_0 H_2$ at ~ 36 T, whereas Jo *et al.* [Jo 2007] and Suslov *et al.* [Suslov 2003] observed it at ~ 38 K. Comparing our data to that from the

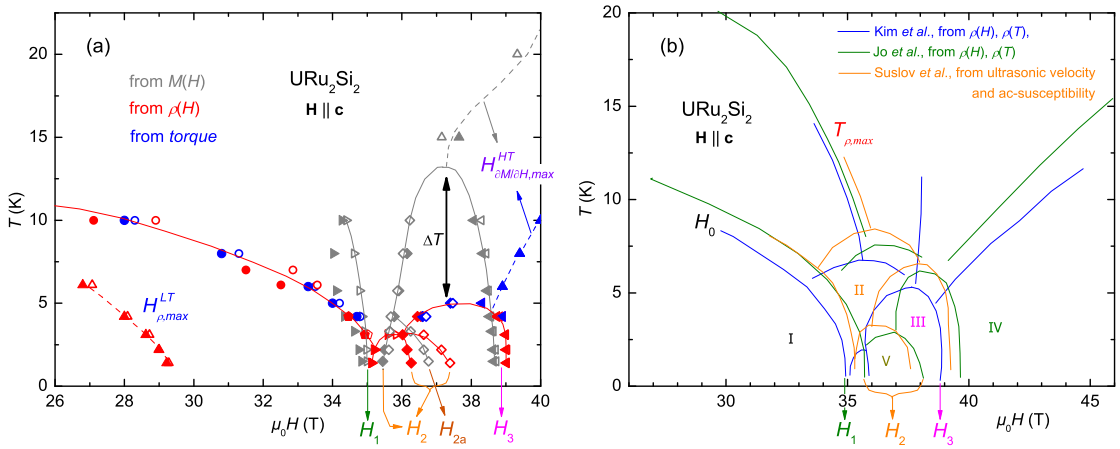

Figure 5.9: (a) Comparison of the H-T phase diagram of URu_2Si_2 from the magnetization, magnetoresistivity, and magnetic torque experiments from this work. Open symbols stand for the rise and full symbols for the fall of the pulsed magnetic field. (b) Comparison of H-T phase diagrams of URu_2Si_2 reported in the literature: from [Kim 2003b] and [Jo 2007] using magnetoresistivity, and from [Suslov 2003] using ultrasonic velocity and ac susceptibility.

literature, we note an ambiguity concerning the phase V: our resistivity data and that from Jo *et al.* [Jo 2007] suggest that, at $T = 0$, H_1 leads to phase V and H_2 leads to phase III, whereas the data from other experiments [Jaime 2002, Kim 2003b, Suslov 2003] suggest that, at $T = 0$ K, H_1 leads to phase II. Magnetization data reveal an unusual kind of hysteresis for the transition at H_{2a} and the phase IIa (see. Figs. 5.1(d) and (e) and [Sugiyama 1999]), which are observed in the rise but not in the fall of the pulsed field. Phase V observed by the resistivity and phase IIa observed by the magnetization seem to correspond roughly. The different behaviors of phase V or IIa are presumably due to different samples and/or due to different measurement techniques.

6 H-T-phase diagram of $U(Ru_{0.96}Rh_{0.04})_2Si_2$

Besides pressure and magnetic field, chemical doping is a rich tool to probe the ground states of heavy-fermion systems. As well as pressure, Rhodium doping leads to the destabilization of the hidden-order in URu_2Si_2. Yokoyama *et al.* [Yokoyama 2004] performed an elastic and inelastic neutron scattering study on Rhodium doped compounds $U(Ru_{1-x}Rh_x)_2Si_2$ with Rh-concentrations from $x = 0$ to 0.05. Figure 6.1(a) presents the resulting temperature-Rh-doping phase diagram. For $0.02 < x < 0.04$, the hidden-order is suppressed and an antiferromagnetic ground state is established below the Néel temperature T_M. Below T_M, the strongly enhanced Bragg reflection at the commensurable wave vector $\mathbf{Q}_0 = (1, 0, 0)$ indicates an antiferromagnetic order with the ordered moment $m_0 = 0.24\ \mu_B$/U (for $x = 0.02$) [see Fig. 6.1(b)]. For intermediate concentrations $0.02 \leq x < 0.03$, the hidden-order phase is restored in temperatures higher than T_M. Magnetic excitations at $\mathbf{Q}_0 = (1, 0, 0)$, which are intrinsic to the hidden-order phase [Bourdarot 2003b, Villaume 2008, Bourdarot 2010], vanish at temperatures below T_M and above T_0. The pressure [Hassinger 2008, Villaume 2008] and doping [Yokoyama 2004] phase diagrams show similarities, both containing a region of an intermediate tuning parameter (pressure P or Rh-doping x), where the ground state is antiferromagnetic (for $P > P_x$ or $x > 0.02$) and the hidden-order is restored for $T_N < T < T_0$ [$T_N = T_x$ in URu_2Si_2 or T_M in $U(Ru_{1-x}Rh_x)_2Si_2$] [Yokoyama 2004, Villaume 2008]. In both cases the magnetic excitations at $\mathbf{Q}_0 = (1, 0, 0)$ are enhanced for $T_M < T < T_0$ and are a signature the restoration of the hidden order. Figures 6.1(c-d) show the H-T-phase diagrams, for $\mathbf{H} \parallel \mathbf{c}$, of $U(Ru_{1-x}Rh_x)_2Si_2$ compounds with $x = 0.02$, 0.025, 0.03, and 0.04 obtained from magnetization and resistivity experiments by Kim *et al.* [Kim 2004]. With increasing concentration, the hidden-order phase and the intermediate phase III are destabilized, whereas the intermediate phase II is stabilized. Rh-doping strongly simplifies the high-field phase diagram of URu_2Si_2: for $x = 0.04$, the critical region between 35 and 39 T of the pure compound is reduced to a single field-induced phase between 26 to 37 T.

Here, I present magnetization measurements on a $U(Ru_{0.96}Rh_{0.04})_2Si_2$ monocrys-

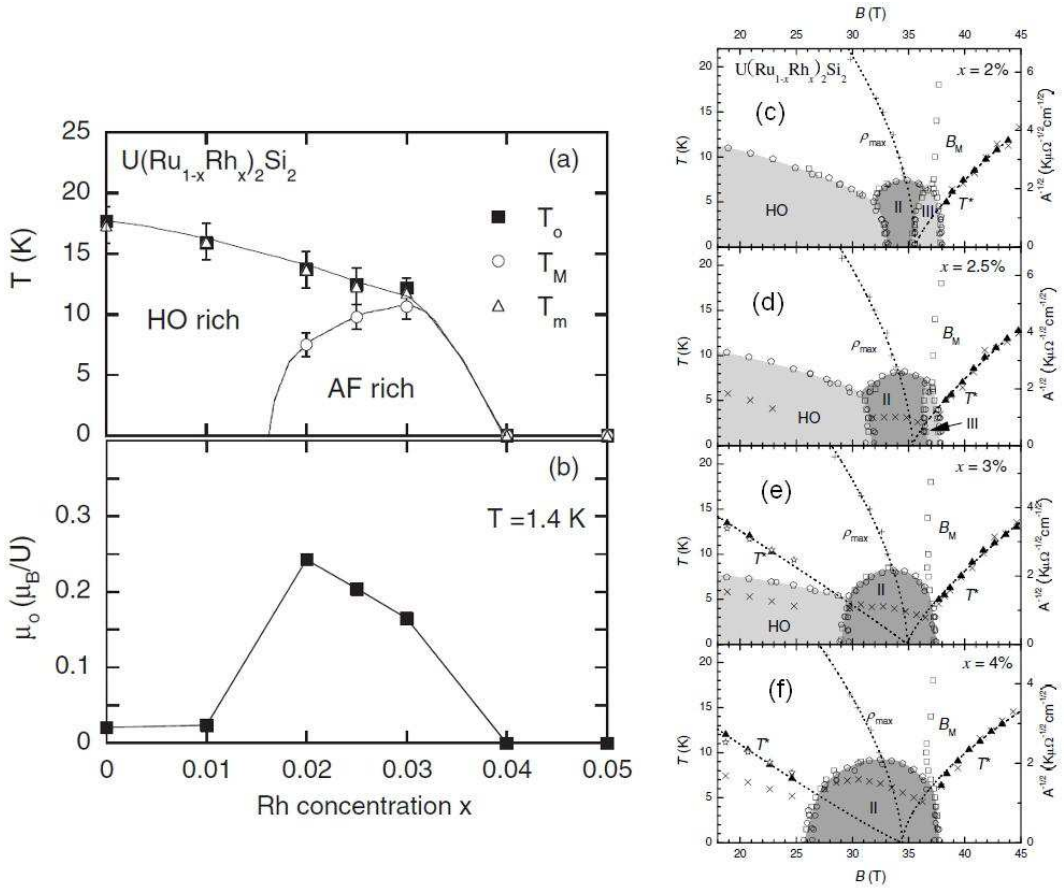

Figure 6.1: (a) Rhodium concentration-temperature phase diagram of $U(Ru_{1-x}Rh_x)_2Si_2$. (b) Staggered moment m_0 (noted here μ_0) of the antiferromagnetic order versus the Rh-concentration x. Figures taken from [Yokoyama 2004]. (c-d) H-T-phase diagrams of $U(Ru_{1-x}Rh_x)_2Si_2$ compounds for $x = 0.02$, 0.025, 0.03, and 0.04. Figures taken from [Kim 2004].

talline sample and the resulting H-T-phase diagram. This preliminary experiment was done before a neutron scattering study [Kuwahara 2013] of $U(Ru_{0.96}Rh_{0.04})_2Si_2$ under pulsed magnetic fields (to which I did not participate). Figure 6.2(a) shows the magnetization M of $U(Ru_{0.96}Rh_{0.04})_2Si_2$ versus the magnetic field H applied along **c** at temperatures between 1.5 and 60 K. At low fields, the magnetization increases linearly with the magnetic field. At $T = 1.5$ K, two sharp steps occur in the magnetization at $\mu_0 H_1 = 26.0$ T and $\mu_0 H_2 = 37.3$ T, indicating field-induced magnetic transitions. The sharpness of the steps in the magnetization at H_1 and H_2 and their hysteresis [see Fig. 6.4(a)] indicate first-order transitions. At high fields, the magnetization continues to increase, indicating that the polarization is not complete due to remaining unquenched magnetic fluctuations. Above H_2, the system is in the polarized paramagnetic phase. Figure 6.2(b) shows the slope $\partial M/\partial H$ of the magnetization versus $\mathbf{H} \parallel \mathbf{c}$ at $T = 1.5$, 10, 15, and 30 K. Above $T = 12.5$ K the

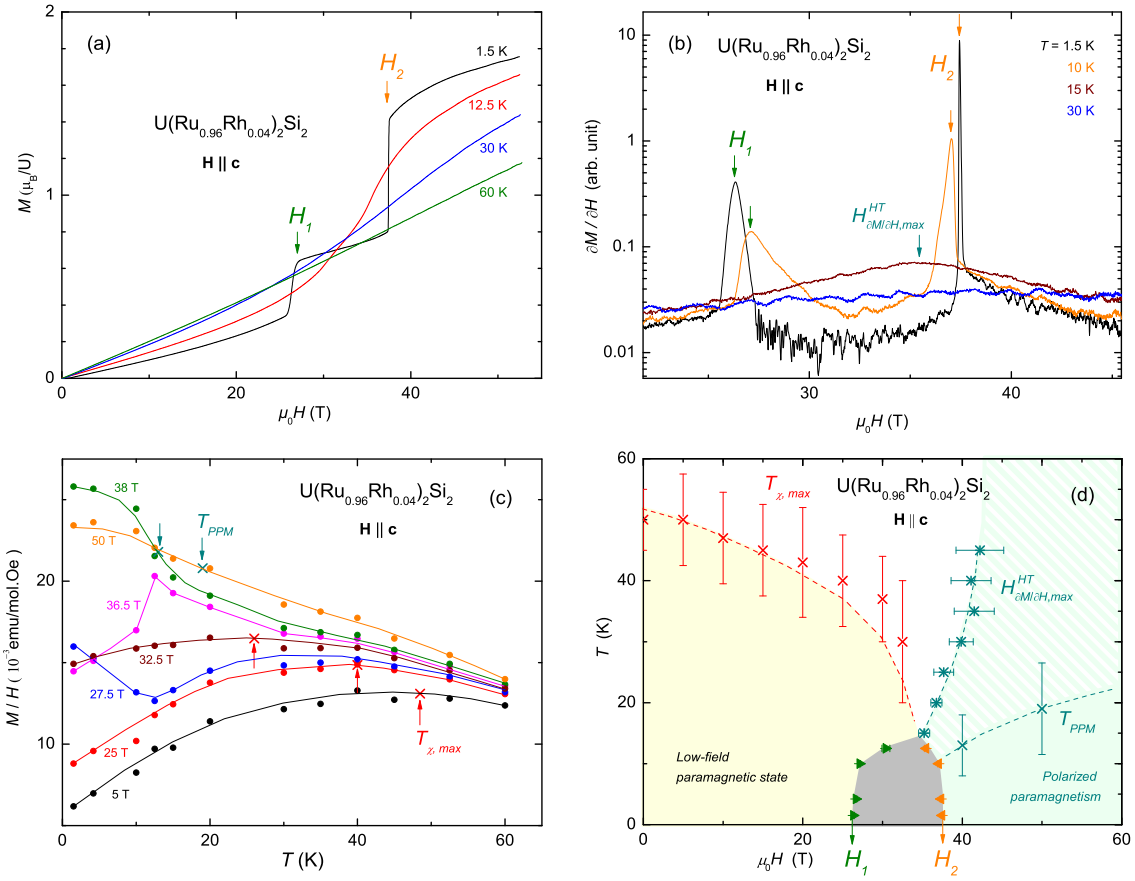

Figure 6.2: (a) Magnetization M of $U(Ru_{0.96}Rh_{0.04})_2Si_2$ versus the magnetic field H applied along **c**, at temperatures between 1.5 and 60 K. (b) $\partial M/\partial H$ versus $\mathbf{H} \parallel \mathbf{c}$ at temperatures between 1.5 and 30 K. (c) M/H versus T at different magnetic fields $\mathbf{H} \parallel \mathbf{c}$. (d) Resulting H-T phase diagram of $U(Ru_{0.96}Rh_{0.04})_2Si_2$.

magnetic transitions at H_1 and H_2 are replaced by a broad maximum in $\partial M/\partial H$ at $H^{HT}_{\partial M/\partial H,max}$. With increasing temperature, H_1 is shifted to higher field and H_2 to lower field, and the transitions lines of H_1 and H_2 meet at the point [$\mu_0 H \sim 34$ T, $T \sim 13$ K] in the phase diagram and delimit the intermediate phase II [Kim 2004]. Figure 6.2(c) shows M/H versus T of $U(Ru_{0.96}Rh_{0.04})_2Si_2$ at different magnetic fields $\mathbf{H} \parallel \mathbf{c}$. The temperature scale $T_{\chi,max}$ is defined at a broad maximum in the low-field regime, which corresponds to the maximum at 50 K in the zero-field susceptibility. The crossover temperature $T_{\chi,max}$ decreases with increasing magnetic field and is suppressed at ~ 33 T, leading to the critical region of the transitions at H_1 and H_2. The temperature scale T_{PPM} of the high-field polarized paramagnetic regime is defined at the inflection point of $M/H(T)$ and indicates the onset of an enhanced magnetization. The crossover lines $H^{HT}_{\partial M/\partial H,max}$ and T_{PPM}, both indicating the onset of an enhanced magnetization, form a large crossover frontier related the high-field polarized regime. Figure 6.2(d) presents the resulting H-T

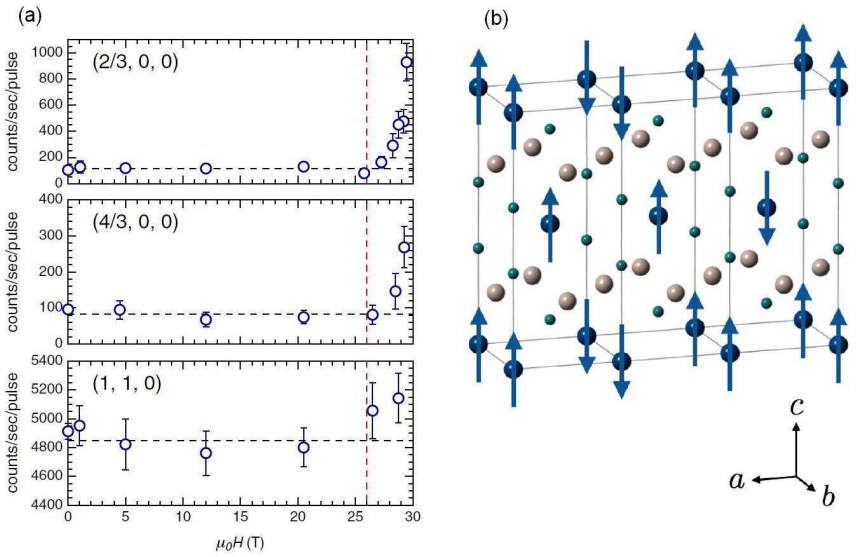

Figure 6.3: (a) Magnetic field-dependence of the intensity at the $(2/3, 0, 0)$, $(4/3, 0, 0)$, and $(1, 1, 0)$-Bragg peaks at $T = 1.7$ K. The vertical red dashed lines correspond to the critical field $\mu_0 H_1 = 26$ T. (b) Up-up-down magnetic structure of the field-induced phase II of $U(Ru_{0.96}Rh_{0.04})_2Si_2$. Figures taken from [Kuwahara 2013].

phase diagram of $U(Ru_{0.96}Rh_{0.04})_2Si_2$ for $\mathbf{H} \parallel \mathbf{c}$. For our magnetization data, the transitions at H_1 and H_2 vanish above $T = 12.5$ K, whereas they vanish above 9 K in the phase diagram reported by Kim *et al.* [Kim 2004] [see Fig. 6.1(f)]. This temperature difference is presumably due to a temperature gradient between the sample and the thermometer in our experimental set-up, as observed for the magnetization data of URu_2Si_2 (see Sect. 5.4). From neutron diffraction measurements on $U(Ru_{0.96}Rh_{0.04})_2Si_2$ under pulsed magnetic fields $\mu_0\mathbf{H} \parallel \mathbf{c}$ up to 30 T, Kuwahara *et al.* [Kuwahara 2013] have found an enhancement of the $(2/3, 0, 0)$ and $(4/3, 0, 0)$ magnetic Bragg peaks above $\mu_0 H_1 = 26$ T at $T = 1.7$ K [see Fig. 6.3(a)]. This indicates a magnetic ordering with the wave vector $\mathbf{q} = (2/3, 0, 0)$, i.e, a commensurate up-up-down magnetic structure with the magnetic moments parallel to the **c**-axis [see Fig. 6.3(b)]. One third of the associated ordered magnetic moment $m_{ord} = 0.6\ \mu_B$/U corresponds approximately to the jump in the magnetization at H_1, as expected from a up-up-down structure. Figure 6.4(a) compares $M(H)$ of

	T	$\Delta M(H_1)$	ΔM_{tot}	$\Delta M(H_1)/\Delta M_{tot}$
$U(Ru_{0.96}Rh_{0.04})_2Si_2$	1.5 K	0.29	0.95	0.31
URu_2Si_2	4.2 K	0.26	0.7	0.37
URu_2Si_2	1.5 K	0.35	0.76	0.46

Table 6.1: Steps in the magnetization $\Delta M(H_1)$ at H_1 and ΔM_{tot} between H_1 and H_2, and ratio $\Delta M(H_1)/\Delta M_{tot}$ for $U(Ru_{0.96}Rh_{0.04})_2Si_2$ at $T = 1.5$ K and URu_2Si_2 at $T = 1.5$ K and 4.2 K.

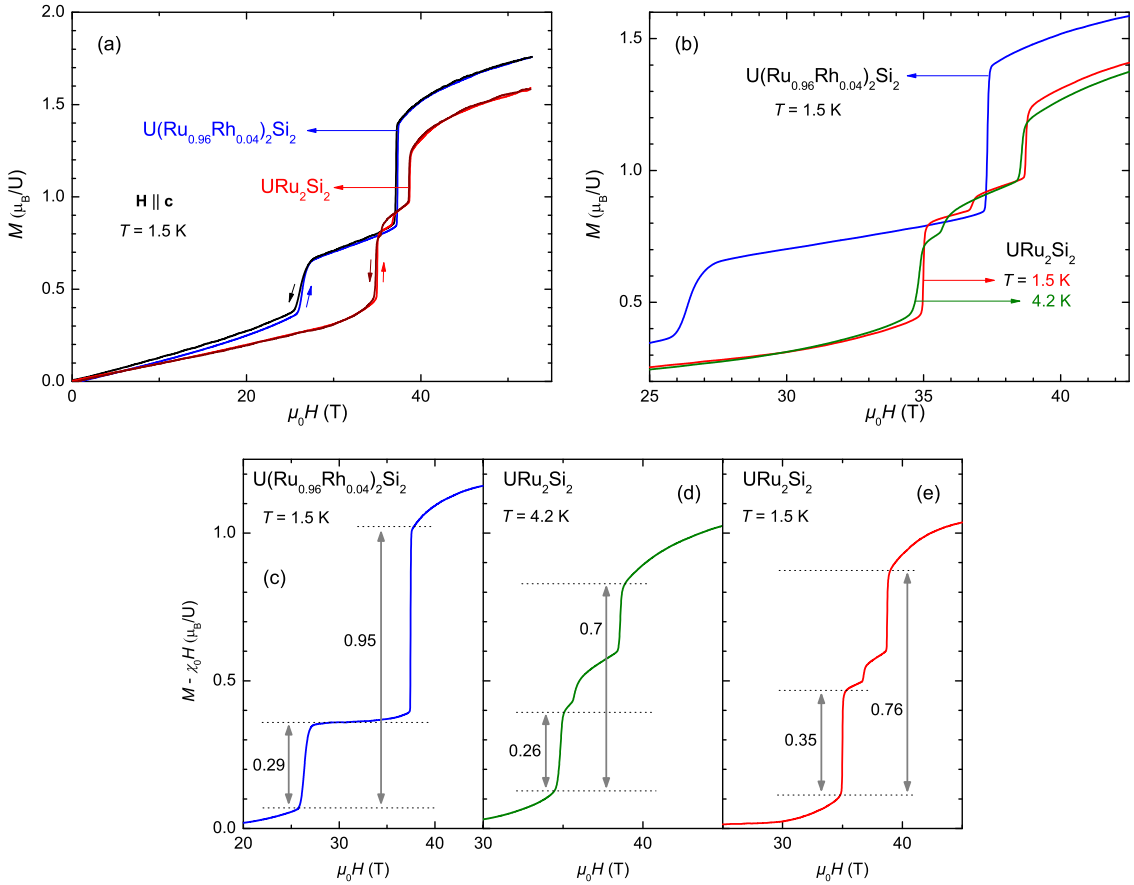

Figure 6.4: (a) $M(H)$ of $U(Ru_{0.96}Rh_{0.04})_2Si_2$ and URu_2Si_2 for rising and falling fields $\mathbf{H} \parallel \mathbf{c}$ at $T = 1.5$ K. (b) $M(H)$ of $U(Ru_{0.96}Rh_{0.04})_2Si_2$ at $T = 1.5$ K and of URu_2Si_2 at $T = 1.5$ K and 4.2 K, for rising fields. (c-f) $M - \chi_0 H$, where $\chi_0 \underset{H\to 0}{=} M/H$, for rising fields.

$U(Ru_{0.96}Rh_{0.04})_2Si_2$ and URu_2Si_2 for $\mathbf{H} \parallel \mathbf{c}$ at $T = 1.5$ K. The magnetization of $U(Ru_{0.96}Rh_{0.04})_2Si_2$ reaches 1.75 μ_B/U-ion at $\mu_0 H \sim 53$ T, which is 10 % higher than that of URu_2Si_2. Figures 6.4(c-e) show a plot of $M - \chi_0 H$, where $\chi_0 \underset{H\to 0}{=} M/H$ [cf. Sect. 3.5, Fig. 3.10], versus H of (c) $U(Ru_{0.96}Rh_{0.04})_2Si_2$ at $T = 1.5$ K, and URu_2Si_2 at (d) $T = 4.2$ K and (e) 1.5 K. From these plots we extract the steps in the magnetization $\Delta M(H_1)$ at H_1 and ΔM_{tot} between H_1 and H_2 (see Table 6.1). In a picture where H_1 is associated with the stabilization of an up-up-down structure, one expects to have $\Delta M(H_1)/\Delta M_{tot} \simeq 1/3$. This is indeed the case of $U(Ru_{0.96}Rh_{0.04})_2Si_2$ at 1.5 K, but also of URu_2Si_2 at 4.2 K, but not at 1.5 K. In the H-T-phase diagram of URu_2Si_2, H_1 leads to phase II at 4.2 K but not at 1.5 K, where phase IIa is established (see Sect. 5.1). From the values of the step of M at H_1, we conclude thus that phase II of URu_2Si_2 is compatible with an up-up-down structure, as in $U(Ru_{0.96}Rh_{0.04})_2Si_2$, but not its phase IIa. I note here that the idea

of an up-up-down structure for phase II was initially proposed by Sugiyama *et al.* [Sugiyama 1990, Sugiyama 1999].

7 Orbital Magnetoresistivity

In this Chapter, I present and discuss the strongly sample-dependent and exceptionally-high magnetoresistivity observed in the hidden-order phase of URu_2Si_2. For $\mathbf{H} \parallel \mathbf{c}$, anomalies in the magnetoresistivity are found to be related to field-induced Fermi surface modifications inside the hidden-order phase.

7.1 Transverse and longitudinal magnetoresistivity in $\mathbf{H} \parallel \mathbf{c}$

Figure 7.1(a) shows the transverse magnetoresistivity $\rho_{x,x}$ versus the magnetic field H measured for $\mathbf{H} \parallel \mathbf{c}$ and $\mathbf{U}, \mathbf{I} \parallel \mathbf{a}$ at $T = 1.4$ K on the URu_2Si_2 samples #1 and #2 studied for this work, and a third sample studied by Levallois *et al.* [Levallois 2009]. The third sample has been measured in a similar experimental setup than the samples of this work. The samples have different qualities as indicated by their RRR (see Sect. 3.5). The resistivity is almost sample-independent in the intermediate phases between H_1 and H_3. For all three samples, the resistivity equals $\simeq 25$ $\mu\Omega$.cm for $H_1 < H < H_2$ and $\simeq 90$ $\mu\Omega$.cm for $H_2 < H < H_3$. The strong maximum in the magnetoresistivity at $\mu_0 H^{LT}_{\rho,max} \simeq 29$ T is found to be strongly sample-dependent. At 29 T, the resistivity of the highest-quality sample #2 (RRR = 225) reaches $\simeq 510$ $\mu\Omega$.cm, that of sample #1 (RRR = 90) reaches $\simeq 280$ $\mu\Omega$.cm, and that of the third sample (RRR = 40) reaches $\simeq 120$ $\mu\Omega$.cm. The anomaly at $H^{LT}_{\rho,max}$ is two times bigger for sample #2 than for sample #1, where it is three times bigger than for the sample studied by Levallois *et al* [Levallois 2009]. This indicates a correlation between the intensity of the anomaly in $\rho_{x,x}(H)$ at 29 T and the sample quality. The higher is the sample quality, the stronger is the anomaly. The inset of Figure 7.1(a) shows $\rho_{x,x}(H)$ at $T = 6$ and 40 K. At higher temperatures, the magnetoresistivity becomes almost sample-independent. Figure 7.1(b) compares the transverse and longitudinal magnetoresistivities $\rho_{x,x}$ and $\rho_{z,z}$, respectively, measured at $T = 1.5$ K and in a field $\mathbf{H} \parallel \mathbf{c}$ on the URu_2Si_2 samples #1 and #3, which are of similar qualities [$\rho_{z,z}(300\text{ K})/\rho_{z,z}(2\text{ K}) = 85$ for sample #3]. The higher noise level in the resistivity of sample #3 is due to the smaller resistance. $\rho_{z,z}(H)$ of sample #3 presents similar anomalies as $\rho_{x,x}(H)$ at $H_{\rho,max}$, H_0, H_1, H_2, and H_3. The inset of Figure 7.1(b) shows that at high temperature, the difference between the absolute values of $\rho_{x,x}$ and $\rho_{z,z}$ versus H reflects the different behaviors of $\rho_{x,x}$ and $\rho_{z,z}$ versus T at zero-

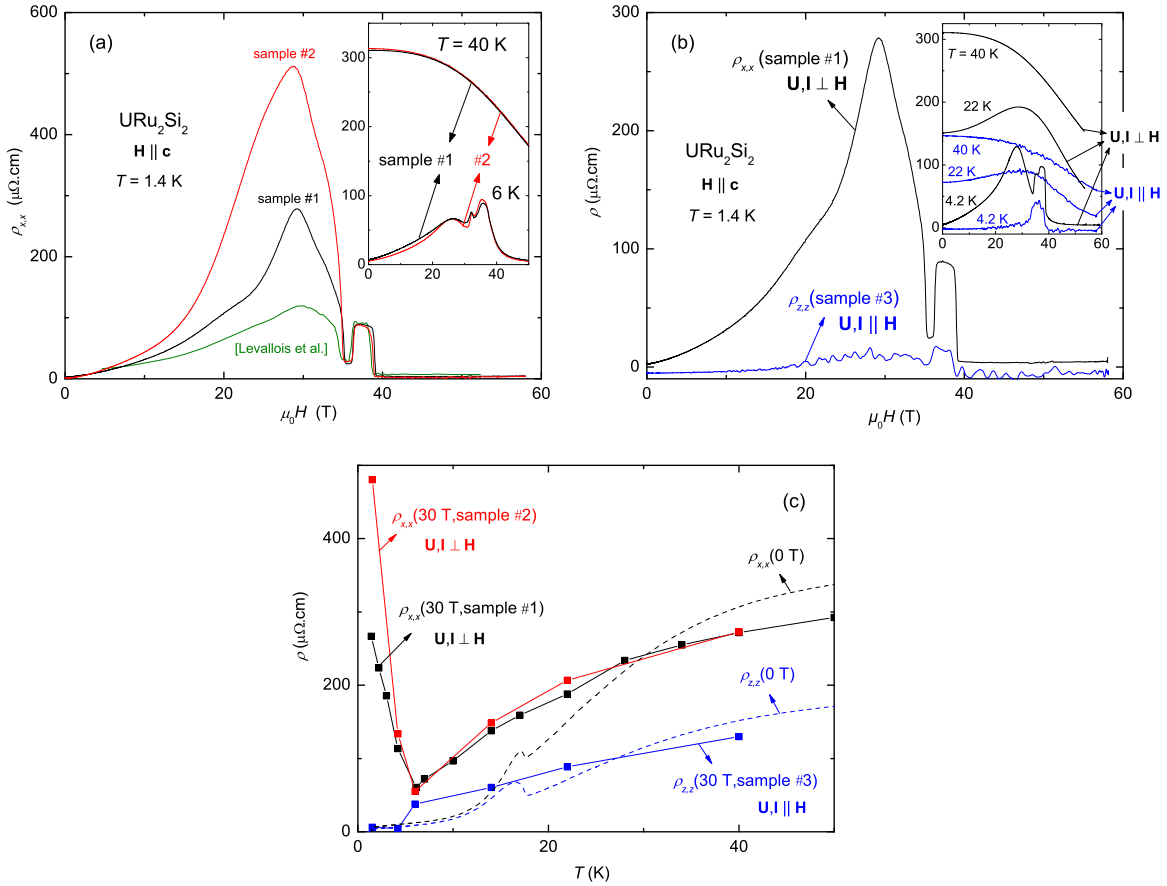

Figure 7.1: (a) Transverse magnetoresistivity $\rho_{x,x}$ versus the magnetic field H applied along **c** measured at $T = 1.5$ K on URu_2Si_2 samples #1 and #2 and on a third sample by [Levallois 2009]. The Inset shows $\rho_{x,x}(H)$ of samples #1 and #2 at $T = 6$ K and 40 K. (b) Comparison of the transverse magnetoresistivity $\rho_{x,x}$ and the longitudinal magnetoresistivity $\rho_{z,z}$ versus H of samples #1 and #3, respectively, for $\mathbf{H} \parallel \mathbf{c}$ at $T = 1.5$ K. The Inset shows $\rho_{x,x}(H)$ and $\rho_{z,z}(H)$ at $T = 4.2$ K, 22 K, and 40 K. (c) $\rho_{x,x}$ versus T of samples #1 and #2 and $\rho_{z,z}$ versus T of sample #3, at $\mu_0 H = 0$ and 30 T, for $\mathbf{H} \parallel \mathbf{c}$.

field, presented in Figure 7.1(c). At low temperature, the strong anomaly at ~ 30 T occurs in the transverse magnetoresistivity $\rho_{x,x}$, but not in the longitudinal configuration as shown in Figure 7.1(b). This is confirmed by the temperature-dependence of the resistivity, shown in Figure 7.1(c), where a sudden increase of the transverse resistivity $\rho_{x,x}$ of samples #1 and #2 occurs below $T = 6$ K at $\mu_0 H = 30$ T, while the longitudinal resistivity $\rho_{z,z}$ of sample #3 at $\mu_0 H = 30$ T vanishes below 6 K. I note here, that the point ($\mu_0 H = 30$ T,$T = 6$ K) in the phase diagram falls approximately on the transition line H_0/T_0 of the hidden-order phase. Thus, the sudden decrease below 6 K of the longitudinal resistivity $\rho_{z,z}$ measured at 30 T is related to T_0. Equivalently, the effect which is responsible for the strong increase of the transverse resistivity $\rho_{x,x}$ develops below T_0.

To summarize, the maximum of magnetoresistivity observed in a magnetic field of ∼ 30 T applied along the **c**-axis i) develops at low temperature, below $T = 6\text{K} \sim T_0$, ii) is present in the transverse configuration, but not in the longitudinal configuration, and iii) is enhanced when the sample quality, and thereby the electronic mean free path, are higher. This indicates that the magnetoresistivity inside the hidden-order phase is controlled by an orbital effect (cf. also [Kasahara 2007, Levallois 2009]). This effect is due to the field-induced cyclotron motion of the conduction electrons along their Fermi surface trajectories within the condition $\omega_c\tau > 1$, where ω_c is the cyclotron frequency and τ is the lifetime of the conduction electrons. A modification of the Fermi surface accompanied by a reduction of the carrier mobility $\mu = \omega_c\tau/\mu_0 H$ is a natural way to explain the decrease of the magnetoresistivity above $\mu_0 H \sim 30$ T.

7.2 Transverse magnetoresistivity in H ∥ a

Figure 7.2(a) presents the transverse magnetoresistivity $\rho_{x,x}$ of URu_2Si_2 samples #1 and #2 versus the magnetic field H applied parallel to the magnetic hard axis **a** at $T = 1.4$ K. The transverse magnetoresistivity increases monotonically with the magnetic field. $\rho_{x,x}$ at a given field is almost a factor two higher in sample #2 (RRR=225) than in sample #1 (RRR=90) due to a higher mean free path in sample #2. No anomalies due to field-induced transitions are observed up to maximal fields of 68 T and 81 T for samples #1 and #2, respectively, indicating that the system remains in the hidden-order phase. This is consistent with an ultrasonic velocity study performed by Yanagisawa *et al.* [Yanagisawa 2013], where, at $T = 1.5$ K, a monotonic elastic constant is observed up to 69 T for **H** ∥ **a**. On the other hand, a magnetic field applied along the **c**-axis destabilizes the hidden-order phase at $\mu_0 H_1 = 35$ T (see Chapt. 5). This reflects that the strong Ising-character of the magnetic properties is connected with the hidden-order parameter.

The resistivity of the high-quality sample #2 reaches 1455 $\mu\Omega$cm at $\mu_0 H = 81.3$ T, which is more than three orders of magnitude higher than the zero-field resistivity at 1.4 K. The fact that $\rho_{x,x}$ increases without saturating up to 80 T is an indication for a nearly perfect compensation of the electrons and holes in URu_2Si_2 (cf. also [Pippard 1989, Kasahara 2007, Levallois 2009]). Shubnikov-de Haas oscillations are observed for both samples and will be discussed in Chapter 9. Figures 7.2(b) and 7.2(c) show that the strong magnetic field-dependence of $\rho_{x,x}$ under **H** ∥ **a** is reduced when T is increased, which is the signature of the impurity-dependent orbital magnetoresistivity. A striking feature is the sudden suppression of the magnetic field-dependence of $\rho_{x,x}$ above the hidden-order transition temperature $T_0 = 17.5$ K. This result is compatible with a Fermi surface reconstruction occurring at T_0, with

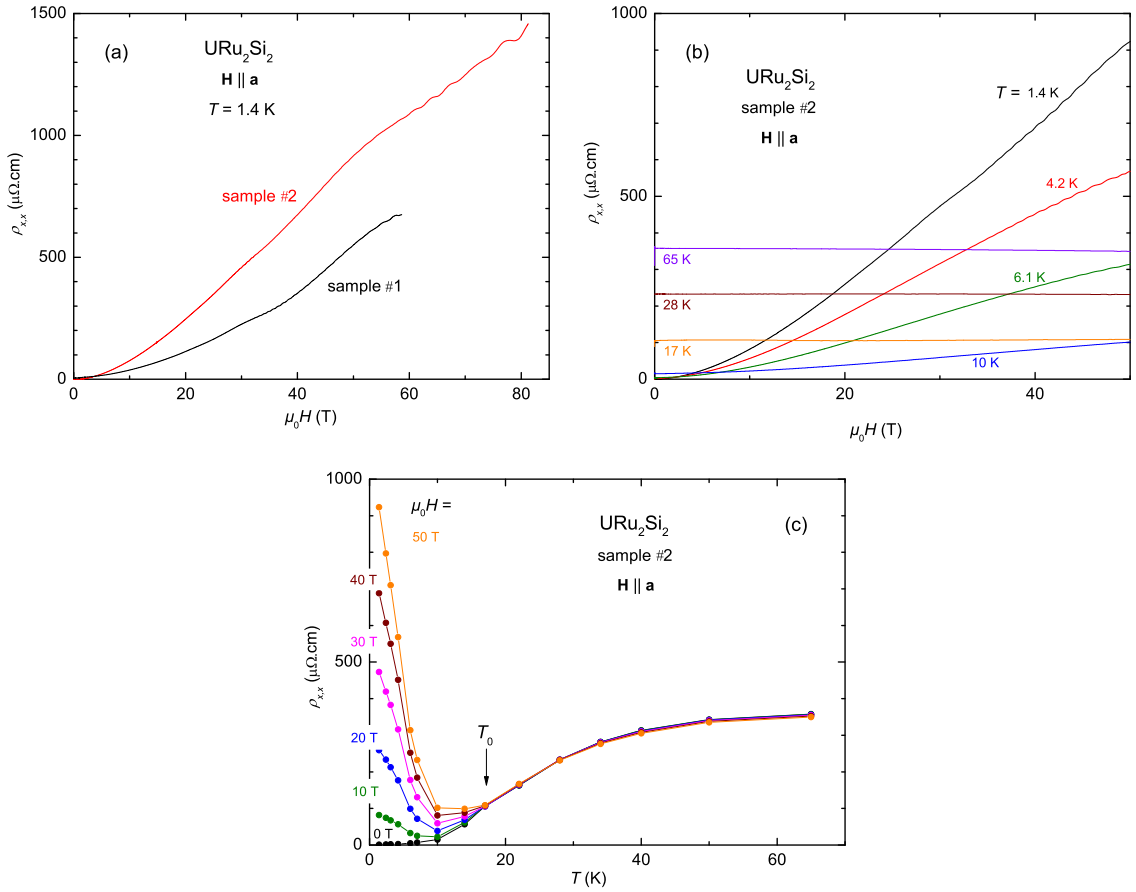

Figure 7.2: (a) Transverse magnetoresistivity $\rho_{x,x}$ of URu_2Si_2 samples #1 and #2 versus the magnetic field H applied along the **a**-axis at $T = 1.5$ K. (b) $\rho_{x,x}(H)$ of sample #2 for $\mathbf{H} \parallel \mathbf{a}$ at temperatures between 1.5 and 65 K. (c) $\rho_{x,x}(T)$ of sample #2 at constant fields $\mathbf{H} \parallel \mathbf{a}$.

a fundamental change of the electric transport properties. In fact, Hall effect measurements by Schoenes *et al.* [Schoenes 1987] and Dawson *et al.* [Dawson 1989] showed an abrupt increase of the Hall coefficient below $T_0 = 17.5$ K, which indicates a Fermi surface reconstruction resulting in a strong reduction ($\sim 90\%$) of the carrier density inside the hidden-order phase. This is confirmed by thermoelectricity experiments [Bel 2004] and thermal transport measurements indicating a reduction of the electron phonon-scattering and a drastic increase of the electronic mean free path below T_0 [Bel 2004, Behnia 2005, Sharma 2006].

The sudden change of the field-dependence of $\rho_{x,x}$ below T_0, due to the fundamental change of the electronic properties, is easily observed for $\mathbf{H} \parallel \mathbf{a}$ since there is no field-induced variation of the magnetic properties, which would result in an additional field-dependence of $\rho_{x,x}$. The situation is different for $\mathbf{H} \parallel \mathbf{c}$ [see Fig. 5.4(d)], where a significant variation with H of $\rho_{x,x}$ is observed at all temperatures (up to 65 K) due to a field-induced modification of the magnetic properties. This magnetic

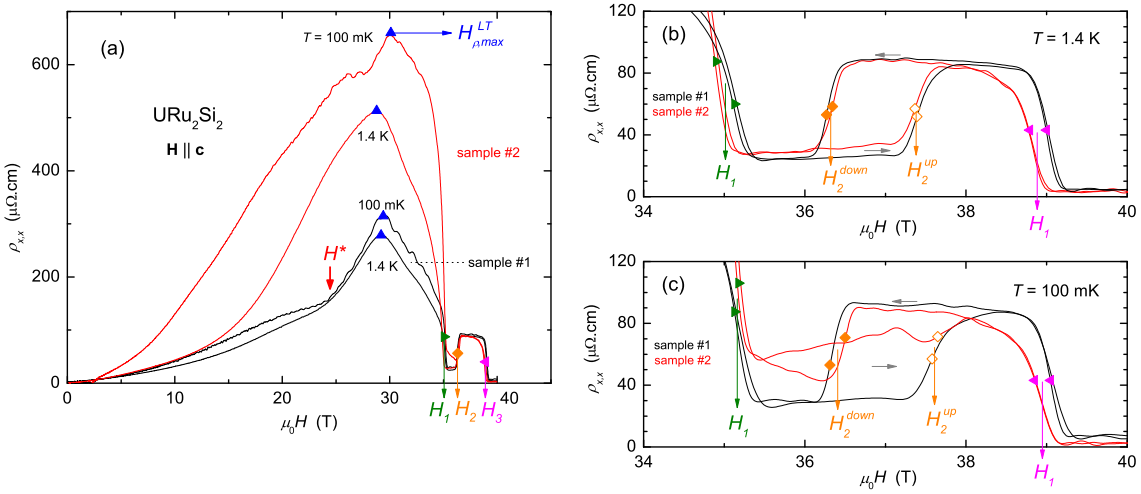

Figure 7.3: (a) Transverse magnetoresistivity $\rho_{x,x}$ of URu_2Si_2 samples #1 and #2 versus the magnetic field H applied along **c** at $T = 100$ mK and 1.4 K. Zoom on $\rho_{x,x}(H)$ of samples #1 and #2 for $\mu_0\mathbf{H} \parallel \mathbf{c}$ between 34 T and 40 T at (b) $T = 1.4$ K and (c) $T = 100$ mK. The grey arrows indicate the directions of the rise and fall of the pulsed field.

contribution adds to the orbital contribution to $\rho_{x,x}$, and the temperature below which the orbital contribution develops cannot be determined precisely. At high-temperatures ($T > T_{\chi,max}$), the magnetic field quenches the scattering of conduction electrons on f-electrons moments, which is indicated by a negative slope of the magnetoresistivity versus field. This effect is strong for **H** along the magnetic easy axis **c** [see Fig. 5.4(c)] and very small for **H** along the magnetic hard axis **a**.

7.3 Sample-dependent features in the magnetoresistivity

Figure 7.3(a) presents, at $T = 100$ mK and 1.4 K, the transverse magnetoresistivity $\rho_{x,x}$ of URu_2Si_2 samples #1 and #2 versus the magnetic field H applied along the **c**-axis. Superconductivity results in $\rho_{x,x} = 0$ in magnetic fields below the superconducting critical field $\mu_0 H_{c,2} \simeq 2.5$ T at $T = 100$ mK. Above $H_{c,2}$, the resistivity increases with increasing magnetic field, up to a maximum at $\mu_0 H^{LT}_{\rho,max} \sim 30$ T, and decreases from 30 T to 35 T. The characteristic field-induced anomalies at H_1, H_2, and H_3 are observed for both temperatures. At $T = 100$ mK the resistivity of samples #1 and #2 reach $\simeq 320$ $\mu\Omega$.cm and $\simeq 660$ $\mu\Omega$.cm, respectively, at the maximum at $H^{LT}_{\rho,max}$. The high-field resistivity inside the hidden-order phase increases with increasing sample quality and with decreasing temperature. Above $\mu_0 H_3 = 39.0$ T, the magnetic field drives the system into a polarized paramagnetic state, where the resistivity vanishes due to a strong enhancement of the carrier density, as shown by the Hall and Nernst effects measured in magnetic fields $\mathbf{H} \parallel \mathbf{c}$ up to 60 T by

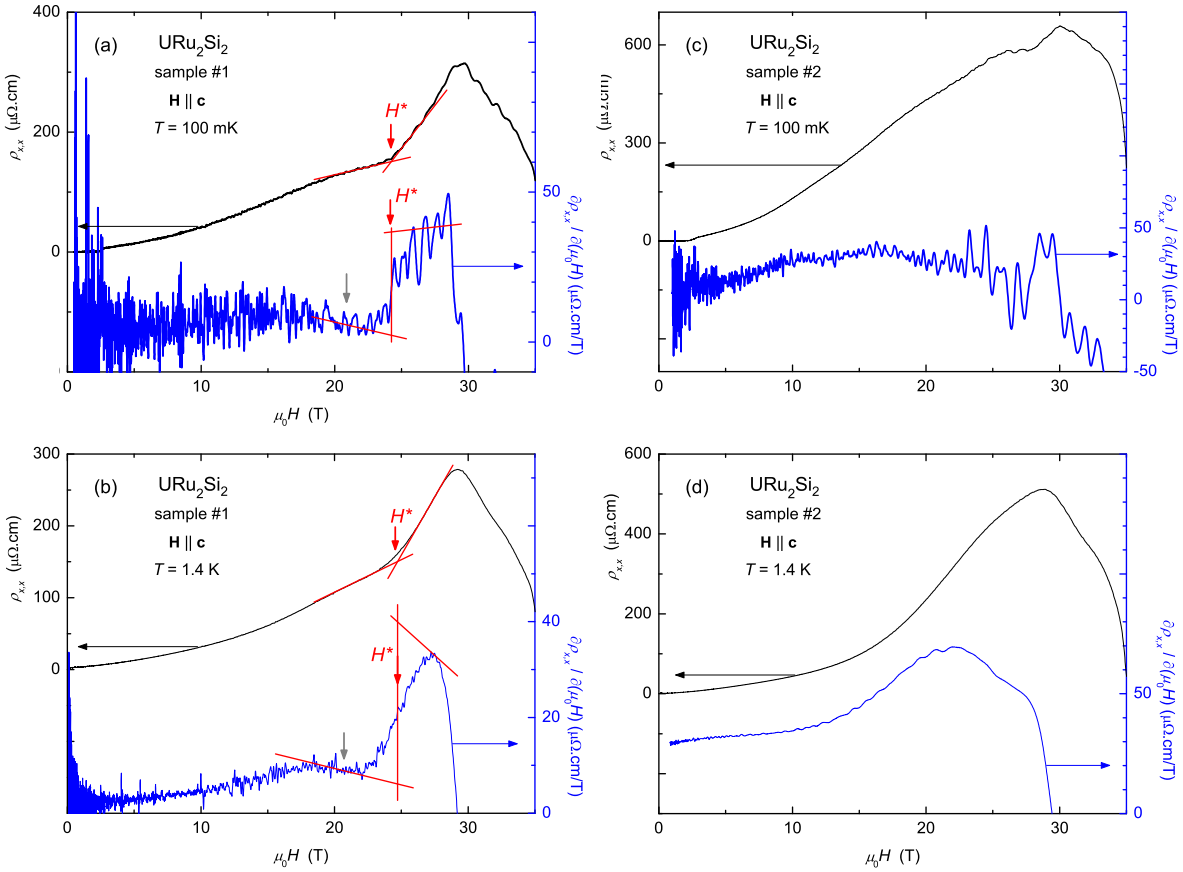

Figure 7.4: Resistivity $\rho_{x,x}$ and field derivative of the resistivity $\partial\rho_{x,x}/\partial(\mu_0 H)$ versus the magnetic field $\mathbf{H} \parallel \mathbf{c}$: (a) sample #1, $T = 100$ mK, (b) sample #1, $T = 1.4$ K, (c) sample #2, $T = 100$ mK, (d) sample #2, $T = 1.4$ K.

Levallois *et al.* [Levallois 2009]. At $T = 100$ mK, the magnetoresistivity of both samples exhibits Shubnikov-de Haas oscillations, which will be discussed in Chapter 9.

The magnetoresistivity of sample #1 shows an abrupt change of slope at $\mu_0 H^* \sim 25$ T for both temperatures $T = 100$ mK and 1.4 K, as indicated by the red arrow in Figure 7.3(a). This anomaly observed well below $H^{LT}_{\rho,max}$ corresponds presumably to a crossover related to an electronic instability. A shown in Figures 7.4(a) and (b) for $T = 100$ mK and 1.4 mK, respectively, H^* in sample #1 (indicated by red arrows) is defined at the kink in $\rho_{x,x}$, or equivalently at the step-like increase of $\partial\rho_{x,x}/\partial(\mu_0 H)$, which follows an inflection point at ~ 20 T in $\rho_{x,x}$ (indicated by a grey arrow). The anomaly occurs at $\mu_0 H^* = (24.3 \pm 0.8)$ T and (24.7 ± 0.5) T at $T = 100$ mK and $T = 1.4$ K, respectively. Figures 7.4(c) and (d) show that this anomaly at H^* is not observed in the resistivity of sample #2 for $\mathbf{H} \parallel \mathbf{c}$. We speculate that the H^*-anomaly in the resistivity of sample #2 is masked by an additional orbital contribution due to the higher sample quality. In fact, the study of

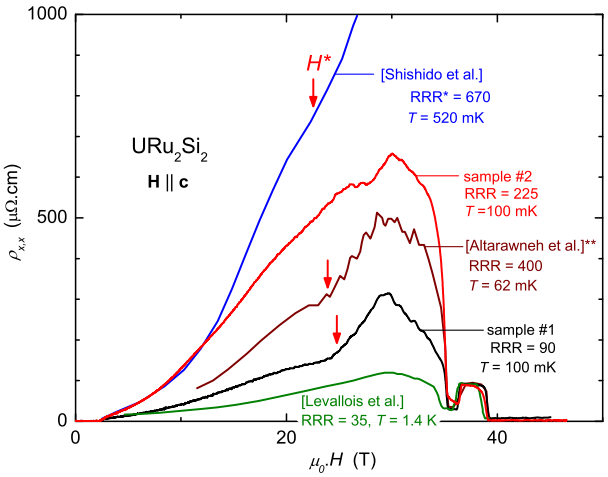

Figure 7.5: $\rho_{x,x}(H)$ for $\mathbf{H} \parallel \mathbf{c}$ measured on different samples from this work and from [Shishido 2009, Altarawneh 2011, Levallois 2009]. Here, RRR = $\rho_{x,x}(300\,\mathrm{K})/\rho_{x,x}(2\,\mathrm{K})$ and RRR* = $\rho_{x,x}(300\,\mathrm{K})/\rho^n_{x,x}(T \to 0)$. **The resistance data from Altarawneh *et al.* [Altarawneh 2011] has been rescaled to absolute units of resistivity by fixing the plateau between H_2 and H_3 to 90 $\mu\Omega$.cm.

the high-field magnetoresistivity with a rotating magnetic field, presented in Chapter 8, shows that H^* is observed for both samples when H rotates in the transverse (**a**,**c**)-plane. Thanks the rotation data, $\mu_0 H^*$ can be extrapolated for $\mathbf{H} \parallel \mathbf{c}$ to $\mu_0 H^* \simeq 20$ T in sample #2. Another "kink" occurs for sample #2 at around 27 T at $T = 100$ mK and is presumably not related to the same phenomenon as that observed at $\mu_0 H^* \simeq 25$ T in sample #1. This kink could be due to a low-frequency quantum oscillation. Similar kink-like anomalies following an inflection point in the resistivity for $\mathbf{H} \parallel \mathbf{c}$ were also observed for other samples at $\mu_0 H^* \sim 22.5$ T [Shishido 2009] and at 24 T [Altarawneh 2011, Aoki 2012], but not for the sample measured by Levallois *et al.* [Levallois 2009]. Anomalies in the Hall resistivity [Shishido 2009, Malone 2011] and thermoelectric power [Malone 2011, Pourret 2013] have been observed in the same field range, too, and local maxima in the thermoelectric power at $\mu_0 H \sim 24$ T and 30 T were understood as signatures of topological Fermi surface changes [Malone 2011, Pourret 2013]. The anomalies at H^* and $H^{LT}_{\rho,max}$ are both observed here in the orbital contribution to the magnetoresistivity, and thus are related to the Fermi surface. In fact, recent Shubnikov-de Haas experiments led to the conclusion that the anomalies at H^* and $H^{LT}_{\rho,max}$ are related to field-induced Fermi surface modifications inside the hidden-order phase [Jo 2007, Shishido 2009, Altarawneh 2011, Aoki 2012], as discussed in Chapter 9.

Figures 7.3(b) and 7.3(c) show $\rho_{x,x}(H)$ of samples #1 and #2 at $T = 1.4$ K and 100 mK, respectively, for $\mu_0 H$ between 34 and 40 T. At $T = 1.4$ K, the resistivity is almost sample-independent for $H > H_1$ and well-defined sharp steps in $\rho_{x,x}(H)$

are observed at H_1, H_2 and H_3. On the other hand, the resistivity becomes sample-dependent in these regimes at $T = 100$ mK. $\rho_{x,x}(H)$ of sample #1 has the same behavior at both temperatures $T = 100$ mK and 1.4 K. The behavior of $\rho_{x,x}(H)$ from sample #2 becomes different at $T = 100$ mK: the transition at H_2 induces a broader anomaly, in particular for increasing magnetic field. Knowing that sample #2 has the highest quality, this observation is intriguing. The change of behavior is probably due to an interplay between the cyclotron motion of the electrons and their scattering off on the localized magnetic moments.

Figure 7.5 shows the comparison of the transverse magnetoresistivity $\rho_{x,x}(H)$ measured for $\mathbf{H} \parallel \mathbf{c}$ on URu_2Si_2 samples of different qualities [Shishido 2009, Levallois 2009, Altarawneh 2011]. The graph emphasizes the strong sample dependence of the anomaly at $\sim$ 30 T, which results from an orbital contribution to the magnetoresistivity inside the hidden-order phase. The quality of the sample, for which $\mathrm{RRR}^* = \rho_{x,x}(300\ \mathrm{K})/\rho^n_{x,x}(T \to 0) = 670$, studied by Shishido *et al.* [Shishido 2009] is comparable with that of a sample, for which $\mathrm{RRR} = \rho_{x,x}(300\ \mathrm{K})/\rho_{x,x}(T = 2\ \mathrm{K}) = 270$, studied by Matsuda *et al.* [Matsuda 2011, Matsuda private com.]. The RRR of the sample of Altarawneh *et al.* [Altarawneh 2011] is higher than that of sample #2, but the resistivity maximum at 30 T is lower, which is in contradiction with the RRR-dependence of the magnetoresistivity observed for the other samples (see Sect. 7.4). However, this may be due to experimental conditions.

7.4 Analysis of the magnetoresistivity

We have shown that the transverse magnetoresistivity inside the hidden-order phase of URu_2Si_2 strongly depends on the sample quality. In fact, the orbital effect is enhanced when the mobility, proportional to the relaxation time (see Sect. 2.4), of the charge carriers is higher. The relaxation time τ increases with the purity of the samples and decreases with the temperature. An almost perfect compensation of electrons and holes in URu_2Si_2 is shown by the monotonously-increasing transverse magnetoresistivity in fields $\mu_0\mathbf{H} \parallel \mathbf{a}$ up to 80 T (see Fig. 7.2). Assuming that the electronic properties can be described by a unique relaxation time and an average mobility for all conduction bands, the magnetoresistivity $\Delta\rho_{x,x} = \rho_{x,x}(H) - \rho^n_{x,x}(H = 0)$ of a compensated metal with spherical Fermi surfaces is given by (see Sect. 2.4):

$$\frac{\Delta\rho_{x,x}}{\rho^n_{x,x}(H = 0)} = (\omega_c\tau)^2 = \mu^2(\mu_0 H)^2, \tag{7.1}$$

where $\rho^n_{x,x}$ is the zero-field resistivity estimated for the normal non-superconducting state (virtual normal state at temperatures below T_{SC}, see Sect. 3.5).

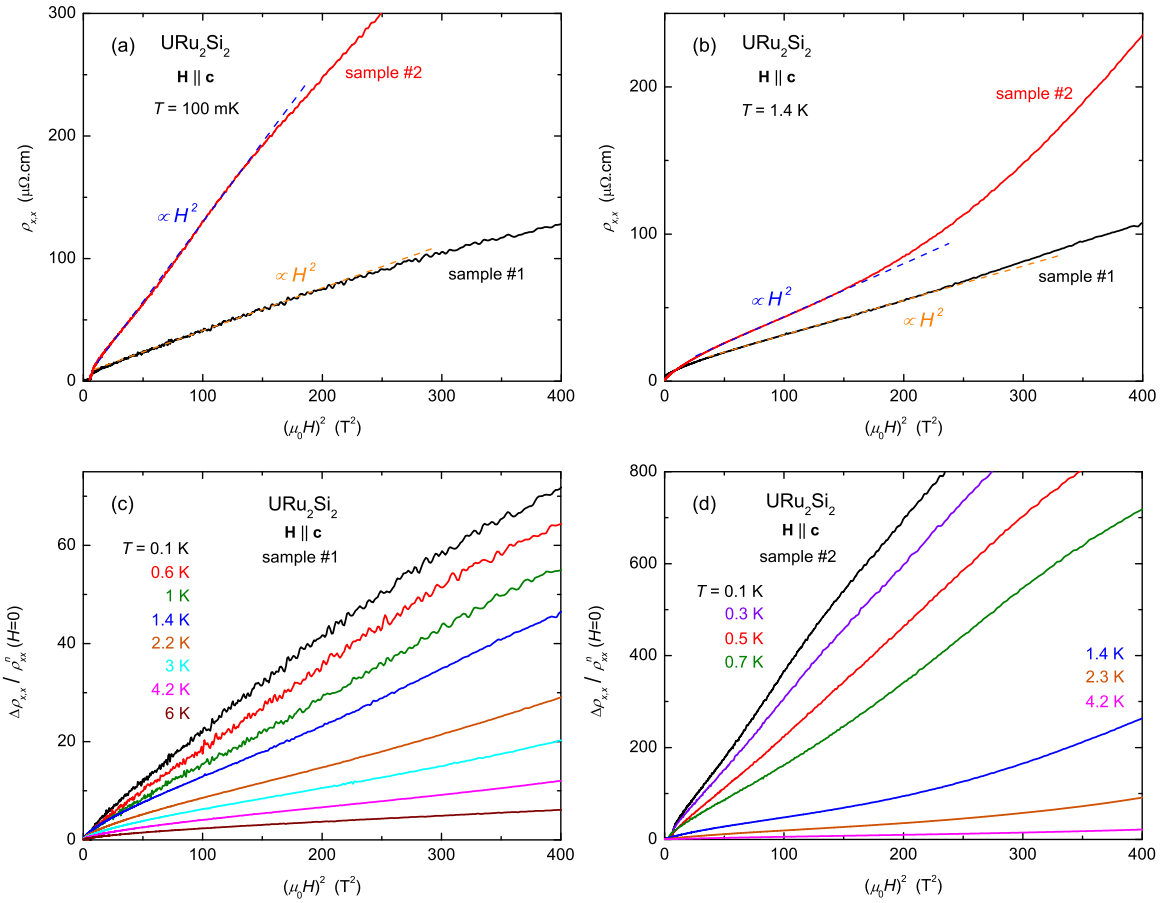

Figure 7.6: $\rho_{x,x}(H)$ of samples #1 and #2 versus $(\mu_0 H)^2$ in $\mu_0\mathbf{H} \parallel \mathbf{c}$ up to 20 T, at (a) $T = 100$ mK and (b) $T = 1.4$ K. The scattered lines represent H^2-dependencies. $\Delta\rho_{x,x}/\rho^n_{x,x}(H = 0)$ of samples (c) #1 and (d) #2 versus $(\mu_0 H)^2$ in $\mu_0\mathbf{H} \parallel \mathbf{c}$ up to 20 T, at temperatures from 100 mK to 6 K.

Kasahara *et al.* [Kasahara 2007] have found, for a high-quality sample [RRR* = $\rho_{x,x}(300\text{ K})/\rho_{x,x}(T \to 0) = 670$], a nearly perfect $\propto H^2$-dependence of $\Delta\rho_{x,x}$ in magnetic fields $\mu_0\mathbf{H} \parallel \mathbf{c}$ up to 10 T and Levallois *et al.* [Levallois 2009] have found for a sample of lower quality [RRR = $\rho_{x,x}(300\text{K})/\rho_{x,x}(2\text{K}) = 40$], a field-dependence of $\Delta\rho_{x,x}$ close to $\propto H^2$ in fields $\mathbf{H} \parallel c$ up to $\mu_0 H = 20$ T. The resistivity of our high-quality URu_2Si_2 sample #2 increases by more than two orders of magnitude in magnetic fields applied along **a** and **c**, as shown in Figures 7.2(a) and 7.3(a), respectively. This exceptionally-strong transverse magnetoresistivity is due to a very low carrier density [Levallois 2009] combined with the high sample-qualities [Kasahara 2007, Matsuda 2011].

Figure 7.6 shows plots of the magnetoresistivity of samples #1 and #2 versus H^2 for $\mu_0\mathbf{H} \parallel c$ up to 20 T at different temperatures from 100 mK to 6 K. The plots show a H^2-dependence of $\rho_{x,x}$ in low fields between ~ 3 and 13 T in agreement with

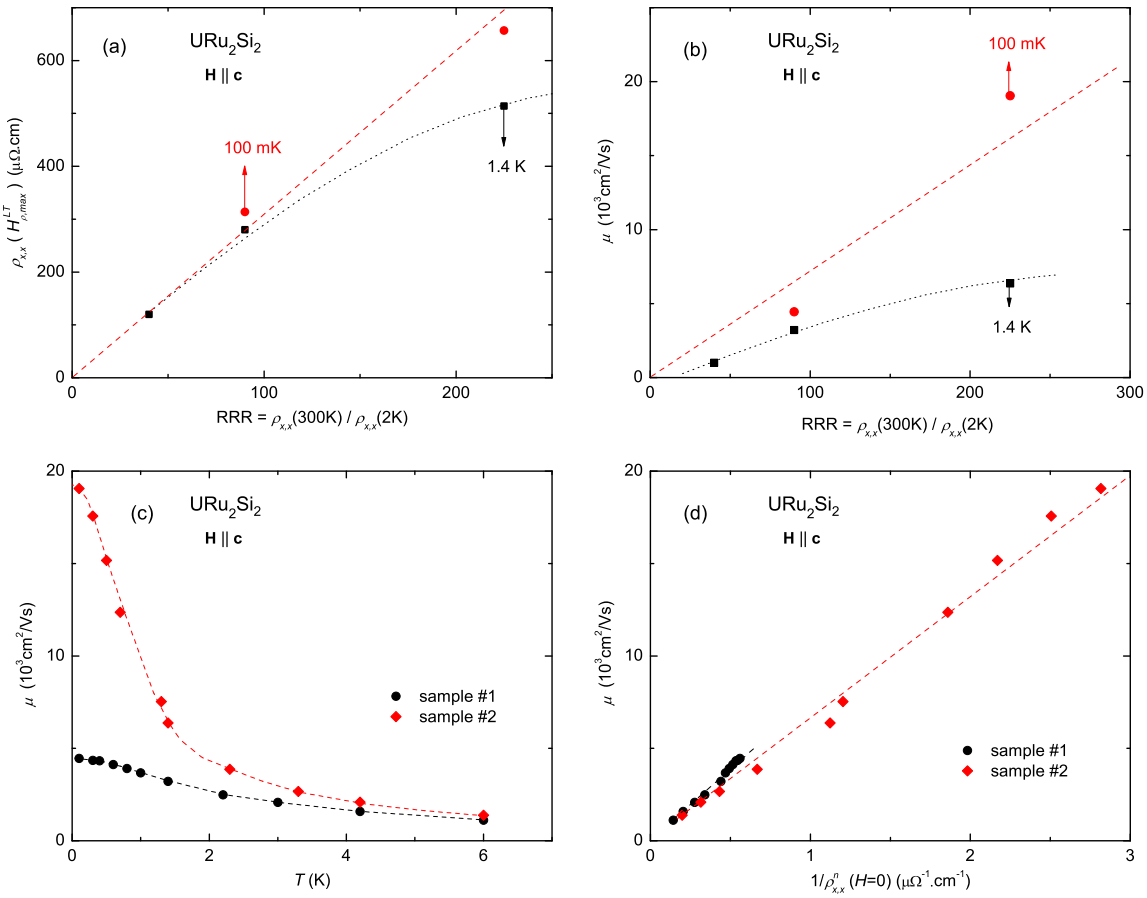

Figure 7.7: (a) Maximum of $\rho_{x,x}(H)$ at $H^{LT}_{\rho,max}$ in $\mathbf{H} \parallel \mathbf{c}$ and (b) mobility μ versus the RRR, from samples #1 (RRR = 90), #2 (RRR = 225) and that studied by Levallois *et al.* (RRR = 40) [Levallois 2009]. The mobilities were extracted from by the slope of $\rho(H)$ versus $(\mu_0 H)^2$ in $\mathbf{H} \parallel \mathbf{c}$ [see Fig. 7.6]. The dashed lines are guides to the eyes. Mobility μ of samples #1 and #2 versus (c) T and (d) $1/\rho^n_{x,x}(H = 0)$. The dashed lines are guides to the eyes.

the results of Kasahara *et al.* [Kasahara 2007] and Levallois *et al.* [Levallois 2009]. On the other hand, the behavior of the magnetoresistivity clearly deviates from the H^2-dependence at higher fields. As the maximum in the resistivity at ~ 30 T [see Fig. 7.3(a)], the slope of the low-field H^2-dependence is enhanced with the sample quality. I extracted a mobility μ averaged over all bands by fitting ρ_{xx} versus H^2, in the regime between 3 and 13 T, using Equation (7.1). I note here, that for temperatures below $T_{SC} = 1.5$ K, the zero-field resistivity $\rho^n_{x,x}(H = 0)$ of the normal non-superconducting state was obtained by the extrapolation via a fit $\rho_{x,x}(T) = \rho_0 + AT^{1.5}$ to the resistivity between 1.5 and 8 K (see Sect. 3.5 and [Matsuda 2011]). I found similar RRR-dependencies of the resistivity maximum at $H^{LT}_{\rho,max}$ [see Fig. 7.7(a)] and of the mobility [see Fig. 7.7(b)], both being strongly enhanced with a higher sample quality. Figure 7.7(c) shows the mobility μ versus

the temperature T extracted for samples #1 (RRR = 90) and #2 (RRR = 225) in $\mathbf{H} \parallel \mathbf{c}$. The mobility is enhanced as the temperature decreases and a saturation occurs due to a finite relaxation time in the limit of zero temperature (non-perfect crystals). Figure 7.7(d) shows that the mobilities μ of samples #1 and #2 increase approximately linearly with $1/\rho^n_{x,x}(H = 0)$, which is compatible with the picture of an isotrope metal with a unique relaxation time τ, where $\tau \propto 1/\rho^n_{x,x}(H = 0)$ (see Sect. 2.4).

The Kohler's rule [Kohler 1938] implies that all plots of $\Delta\rho_{x,x}(H)/\rho^n_{x,x}(H = 0)$ versus $[\mu_0 H/\rho^n_{x,x}(H = 0)]^2$ fall on a unique curve, which is independent of the sample quality and the temperature (see Sect. 2.4.4). Levallois *et al.* [Levallois 2009] have shown that the Kohler plots from the resistivity of their sample (RRR = 40) at temperatures between 1.5 and 17 K in fields $\mu_0\mathbf{H} \parallel \mathbf{c}$ up to 20 T fall on a same $[\mu_0 H/\rho^n_{x,x}(H = 0)]^2$-line. Figures 7.8(a) and (b) show the Kohler plots of the resistivities of our samples #1 and #2, respectively, in fields $\mu_0\mathbf{H} \parallel \mathbf{c}$ up to 20 T, at temperatures from 100 mK to 6 K. For sample #1, the plots coincide almost up to 20 T and a H^2-dependence is clearly observed. For sample #2, the plots coincide in a smaller field window (up to $\sim$ 10 T) and deviate faster in higher fields from the H^2-dependence than for sample #1. Figures 7.8(c) and (d) show the same plots for $\mu_0 H$ up to 40 T in a double-logarithmic scale. These plots emphasize that the magnetoresistivity behavior changes drastically at low fields in the proximity of H_{c2} and at the field-induced crossovers H^* and $H^{LT}_{\rho,max}$. The deviation from the H^2-dependence at low fields is due to the combination of the proximity of H_{c2} and a parasitic off-set in the raw resistivity data. Figures 7.8(e) and (f) compare the Kohler plots of the resistivities of samples #1 and #2 and that from the sample studied by Levallois *et al.* [Levallois 2009] in a double-logarithmic scale, at $T = 100$ mK and $T = 1.4$ K, respectively. The plots of the different samples are close but do not coincide in the low-field regime.

To summarize, the low-field magnetoresistivity exhibits a H^2-behavior, as predicted for a metal with a compensated spherical Fermi surface (cf. also [Pippard 1989, Kasahara 2007, Levallois 2009]). The extracted mobility depends on the sample quality and the temperature. On the other hand, the high-field magnetoresistivity $\Delta\rho(H)/\rho(H = 0)$ deviates strongly from the H^2-behavior, namely, when field-induced crossover-like anomalies in the magnetoresistivity occur at $\mu_0 H^* \sim 20-25$ T and $\mu_0 H^{LT}_{\rho,max} \sim 30$ T. In fact, URu_2Si_2 has a complex multi-band structure (see Sect. 9.1) and field-induced Fermi surface modifications have been observed in magnetic fields far below the destruction of the hidden-order phase at $\mu_0 H_1 = 35$ T (see Sect. 9.2). For $\mathbf{H} \parallel \mathbf{a}$, I could not analyze the magnetoresistivity, as done for $\mathbf{H} \parallel \mathbf{c}$, because of a lack of reproducibility between the different sets of data (cf. Sect 3.9).

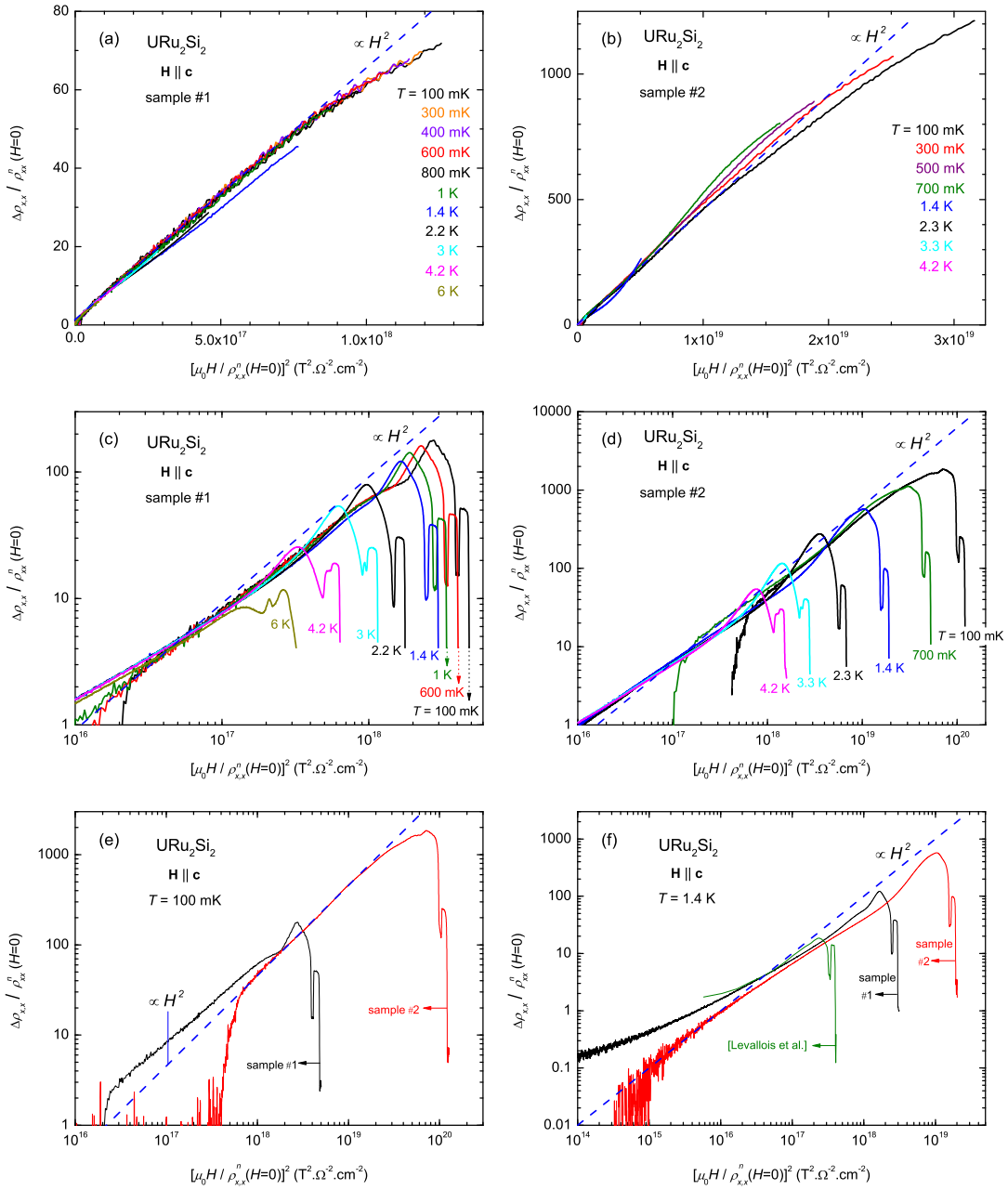

Figure 7.8: $\Delta\rho_{x,x}(H)/\rho^n_{x,x}(H=0)$ of samples (a) #1 and (b) #2 versus $[\mu_0 H/\rho^n_{x,x}(H=0)]^2$ for $\mu_0\mathbf{H} \parallel \mathbf{c}$ up to 20 T, at temperatures from 100 mK to 6 K. $\Delta\rho_{x,x}(H)/\rho^n_{x,x}(H=0)$ of samples (c) #1 and (d) #2 versus $[\mu_0 H/\rho^n_{x,x}(H=0)]^2$ in $\mu_0\mathbf{H} \parallel \mathbf{c}$ up to 40 T, at temperatures from 100 mK to 6 K, in a double-logarithmic scale. (e) $\Delta\rho_{x,x}(H)/\rho^n_{x,x}(H=0)$ of samples #1 and #2 versus $[\mu_0 H/\rho^n_{x,x}(H=0)]^2$ in $\mathbf{H} \parallel \mathbf{c}$, at $T = 100$ mK, in a double-logarithmic scale. (f) $\Delta\rho_{x,x}(H)/\rho^n_{x,x}(H=0)$ of samples #1, #2, and of that studied by Levallois *et al.* [Levallois 2009] $[\mu_0 H/\rho^n_{x,x}(H=0)]^2$ in $\mathbf{H} \parallel \mathbf{c}$, at $T = 1.4$ mK, in a double-logarithmic scale. The scattered lines represent H^2-dependencies.

For $\mathbf{H} \parallel \mathbf{a}$, the slope of the low-field magnetoresistivity is stronger and indicates a mobility higher than for $\mathbf{H} \parallel \mathbf{c}$ [see also Chapt. 8, Fig. 8.4(b)]. Since the mobility is inversely proportional to the cyclotron effective mass (see Sect. 2.4), a higher mobility for $\mathbf{H} \parallel \mathbf{a}$ than for $\mathbf{H} \parallel \mathbf{c}$ is compatible with the anisotropy of the cyclotron effective masses extracted by Shubnikov-de Haas experiments [Aoki 2012].

8 Angle-Dependent Study of the High-Field Magnetoresistivity

URu_2Si_2 exhibits strongly anisotropic bulk properties due to the Ising-character of its magnetic properties. The magnetic easy axis is the **c**-axis of the body-centered tetragonal lattice. This results in strongly anisotropic resistivity [Palstra 1986, Ohkuni 1997] and magnetic susceptibility [Palstra 1985, Dawson 1989, Ramirez 1992]. The upper critical field H_{c2} related to the destruction of superconductivity is also strongly anisotropic [Kwok 1990, Brison 1994, Ohkuni 1997]. Magnetization [Sugiyama 1990] and magnetoresistivity [Jo 2007] measurements have shown that the low-temperature critical fields H_1, H_2, and H_3 follow a simple $1/\cos\theta$-law, at least up to $\theta = 30°$, where θ is the angle between the magnetic field and the **c**-axis. Furthermore, Aoki *et al.* [Aoki 2012] observed that the crossover field H^* in the magnetoresistivity also follows a $1/\cos\theta$-law, at least up to $\theta = 30°$. In this chapter, I present magnetoresistivity experiments performed on the URu_2Si_2 monocrystalline samples #1 and #2 in a rotation probe, which permitted to measure the magnetoresistivity versus a magnetic field up to 60 T applied along different orientations of the crystal. The basic crystal planes (**a**,**c**) and (**a**,**c**) of the tetragonal structure have been investigated. These experiments extended the angle-dependence of the transition fields H_1, H_2, and H_3 and the crossover fields H^* and $H^{LT}_{\rho,max}$ up to $\theta = 60°$.

8.1 Angle dependence of H_{c2}

Figure 8.1(a) presents the transverse magnetoresistivity $\rho_{x,x}$ of our sample #2 of URu_2Si_2 versus the magnetic field H applied parallel to the (**a**,**c**)-plane, for different angles θ between the magnetic field and the **c**-axis at $T = 32$ mK. The resistivity equals zero below the superconducting critical field H_{c2} and increases monotonically above H_{c2}. The critical field $\mu_0 H_{c2}$ equals 3.1 T for $\theta = 5°$ and increases with θ, reaching 7.1 T for $\theta = 67°$. In the normal conducting state, $\rho_{x,x}(H)$ exhibits an oscillatory modulation due to the Shubnikov-de Haas effect, which will be analyzed in Chapter 9. The θ-dependence of H_{c2} obtained by our resistivity experiments on sample #2 is plotted in Figure 8.1(b). H_{c2} exhibits a pronounced anisotropy in the

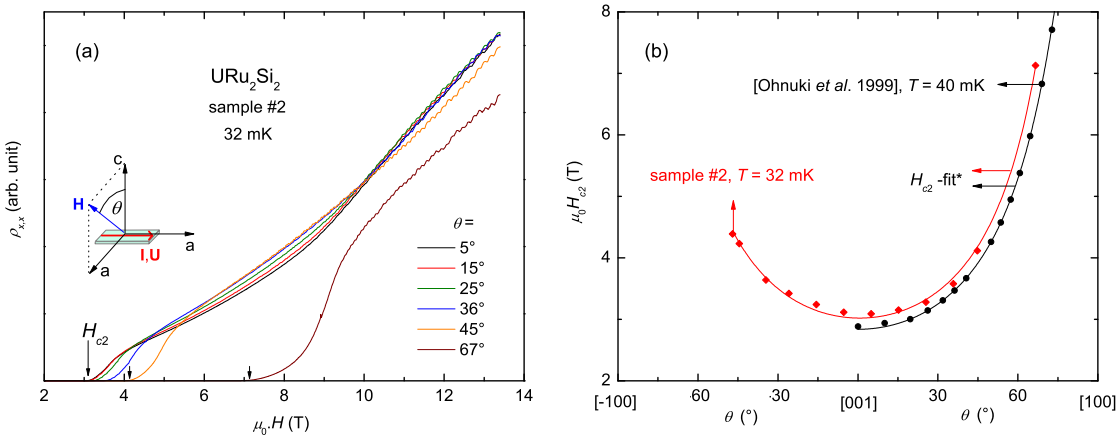

Figure 8.1: (a) Magnetoresistivity $\rho_{x,x}$ of URu_2Si_2 sample #2 versus the magnetic field H for different angles θ between **H** and **c** at $T = 32$ mK. (b) Angle-dependence of H_{c2} for **H** in the plane (**a**,**c**) from our resistivity data of sample #2 and from resistivity data from [Ohkuni 1999]. *The solid lines represent fits to the data with the function (8.1).

(**a**,**c**)-plane. The angle dependence of $H_{c,2}$ obtained by Ohkuni *et al.* [Ohkuni 1999] on another sample, also plotted in Fig. 8.1(b), is in good agreement with that from our data. The data of Ohkuni *et al.* [Ohkuni 1999] show that, at $T = 30$ mK, $\mu_0 H_{c2}$ reaches $\simeq 13$ T for $\mathbf{H} \parallel \mathbf{a}$ ($\theta = 90°$). The angle dependence of $H_{c,2}$ was first established by Brison *et al.* [Brison 1994] from specific heat measurements. They proposed a theoretical model for the anisotropy of H_{c2}, based on the Pauli paramagnetic limit:

$$H_{c2}(\theta) = \frac{H_{c2}(\mathbf{H} \parallel \mathbf{c})}{\sqrt{\cos^2(\theta) + \epsilon^2 \sin^2(\theta)}}, \tag{8.1}$$

where $\epsilon = H_{c2}(\mathbf{H} \parallel \mathbf{c})/H_{c2}(\mathbf{H} \parallel \mathbf{a})$, and found that this model fits well to their data at $T = 10$ mK. The angle-dependencies of $H_{c,2}$ established by Ohkuni *et al.* [Ohkuni 1999] and in this work are well described by this model, too [see Fig. 8.1(b)].

8.2 H-T phase diagram for $(\mathbf{H}, \mathbf{c}) = 20°$

Figure 8.2(a) presents the resistivity ρ_{xx} of sample #1 as a function of the magnetic field **H** applied parallel to **c** for different temperatures T between 1.4 and 40 K. A detailed description of the field-induced anomalies in the magnetoresistivity in a field $\mathbf{H} \parallel \mathbf{c}$ is given in Chapter 5. Figure 8.2(c) presents the resistivity ρ_{xx} of sample #1 as a function of the magnetic field H, for an angle $\theta = 20°$ between **H** and **c**, at different temperatures T between 1.4 and 40 K. The general form of the magnetoresistivity is similar to that obtained for $\mathbf{H} \parallel \mathbf{c}$, with the same field-induced transitions and crossovers. The difference is that for $\theta = 20°$, the resistivity curves, and thereby the

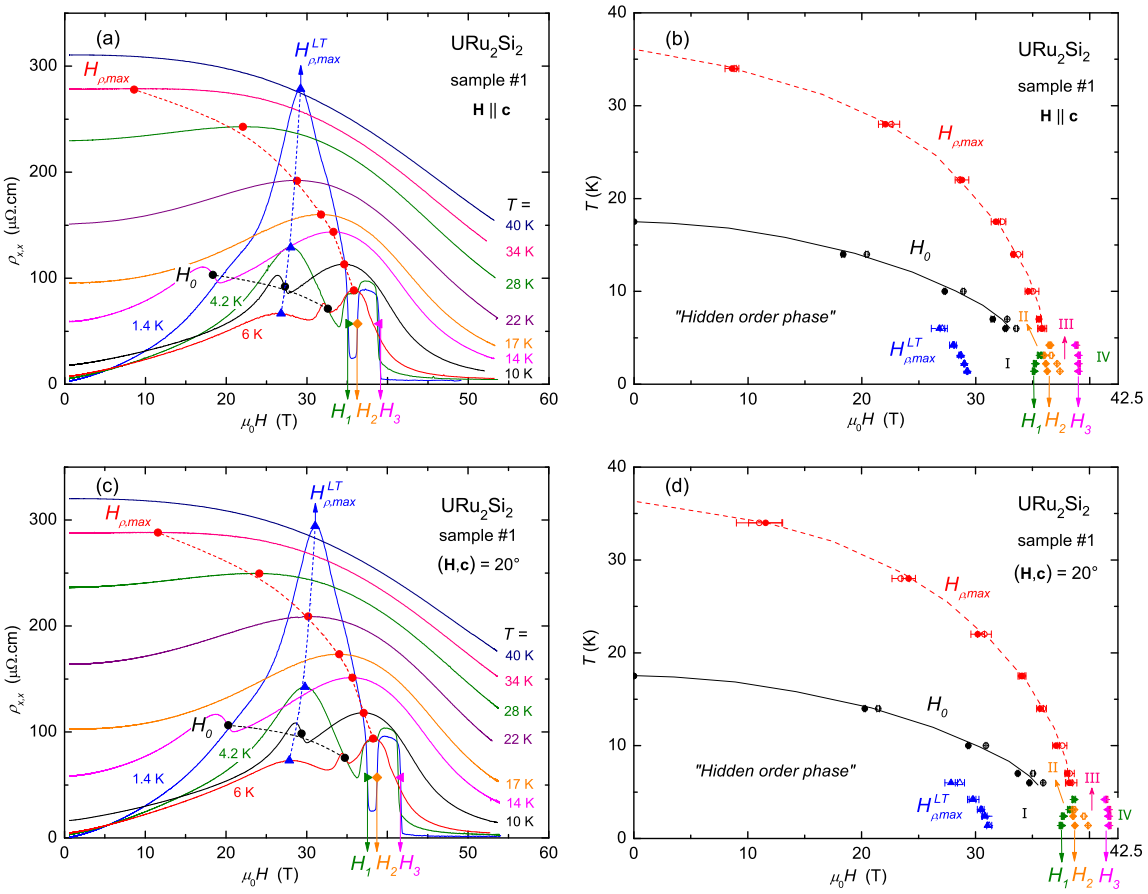

Figure 8.2: (a) Resistivity ρ_{xx} of URu_2Si_2 sample #1 versus the magnetic field H applied parallel to **c**, at temperatures from 1.4 K to 40 K. (b) H-T-phase diagram of URu_2Si_2 resulting from $\rho_{xx}(H)$ for $\mathbf{H} \parallel \mathbf{c}$. (c) Resistivity ρ_{xx} of URu_2Si_2 sample #1 versus the magnetic field H for $(\mathbf{H}, \mathbf{c}) = 20°$, at temperatures from 1.4 K to 40 K. (d) H-T-phase diagram of URu_2Si_2 from $\rho_{xx}(H)$ for $(\mathbf{H}, \mathbf{c}) = 20°$.

transition and crossover fields, are shifted to higher field values. For example the transition field H_1, which is related to the destruction of the hidden-order phase, is shifted from $\mu_0 H_1 = 35.1$ T to 37.6 T. Figures 8.2(b) and 8.2(d) present the resulting H-T-phase diagrams for $\theta = 0$ and $\theta = 20°$, respectively, obtained from the magnetoresistivity data shown in Figures 8.2(a) and 8.2(c), respectively. As shown in Figure 8.3, the phase diagram obtained for (**H**,**c**) = 20° is re-scalable on that obtained for $\mathbf{H} \parallel \mathbf{c}$. The scaling factor of 0.94 corresponds approximately to $\cos\theta$, with $\theta = 20°$. This indicates that the physics of the whole H-T-phase diagram is governed by the projection of the magnetic field along the magnetic easy axis **c**. In Section 8.3, we extend the study of the angle-dependence of the high-field resistivity to a large set of angles up to 90°.

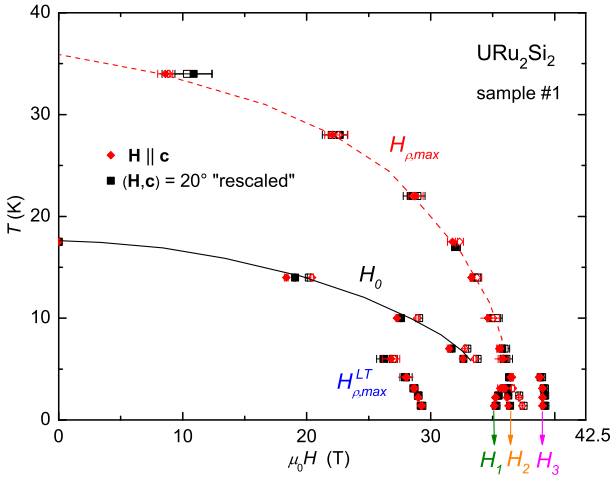

Figure 8.3: H-T-phase diagram of URu_2Si_2 sample #1 resulting from the resistivity data for $\mathbf{H} \parallel \mathbf{c}$ superimposed with that resulting from the resistivity data for $(\mathbf{H}, \mathbf{c}) = 20°$ rescaled by a factor $0.94 = \cos(20°)$.

8.3 Crossover and transition fields for H in the plane (a,c)

Figure 8.4(a) presents the magnetoresistivity $\rho_{x,x}$ of URu_2Si_2 sample #2 versus the magnetic field H at $T = 1.5$ K for different angles θ_1 between the magnetic field and the **c**-axis. The magnetic field is turning from the transverse ($\mathbf{H} \parallel \mathbf{c}$; $\mathbf{H} \perp \mathbf{I}, \mathbf{U}$; $\theta_1 = 0°$) to the longitudinal ($\mathbf{H} \parallel \mathbf{a}$; $\mathbf{H} \parallel \mathbf{I}, \mathbf{U}$; $\theta_1 = 90°$) configurations. Contrary to sample #1 (presented in Sect. 8.2, RRR = 90), sample #2 (RRR = 225) does not show an anomaly at H^* for $\mathbf{H} \parallel \mathbf{c}$, as seen in Section 7.3. When θ_1 increases, the general form of the magnetoresistivity remains unchanged, but the anomalies from the metamagnetic transitions at H_1, H_2, and H_3 and from the crossover at $H^{LT}_{\rho,max}$ are shifted to higher field values. For $\theta_1 > 50°$, the anomalies are shifted out of the field range (60 T) and the resistivity increases monotonically. The value of $\rho_{x,x}$ at the maximum at $H^{LT}_{\rho,max}$ is also slightly increasing with θ_1, which may be due to a small misalignment of the sample. The θ_1-dependencies of the transition fields H_1, H_2, and H_3 and the crossover field $H^{LT}_{\rho,max}$ are presented in Figure 8.6(a).

Figure 8.4(b) presents the magnetoresistivity $\rho_{x,x}$ of sample #2 versus the magnetic field H at $T = 1.6$ K for different angles θ_2 between the magnetic field and the **c**-axis. θ_2 is the angle between **c** and **H**, which lies in the (**a**,**c**)-plane and is perpendicular to the electric current. Hence the magnetic field is turning from the transverse ($\mathbf{H} \parallel \mathbf{c}$; $\mathbf{H} \perp \mathbf{I}, \mathbf{U}$) to the transverse ($\mathbf{H} \parallel \mathbf{a}$; $\mathbf{H} \perp \mathbf{I}, \mathbf{U}$) configurations. At small angles, we observe that the same field-induced anomalies as that observed for sample #1 in Chapter 5. With increasing angle θ_2, the transition fields H_1, H_2, and H_3 and the crossover field $H^{LT}_{\rho,max}$ shift to higher field values and are shifted out of the field range (upper limit: 60 T) for $\theta_2 \geq 65°$. The angle-dependence of H_1, H_2, H_3, and

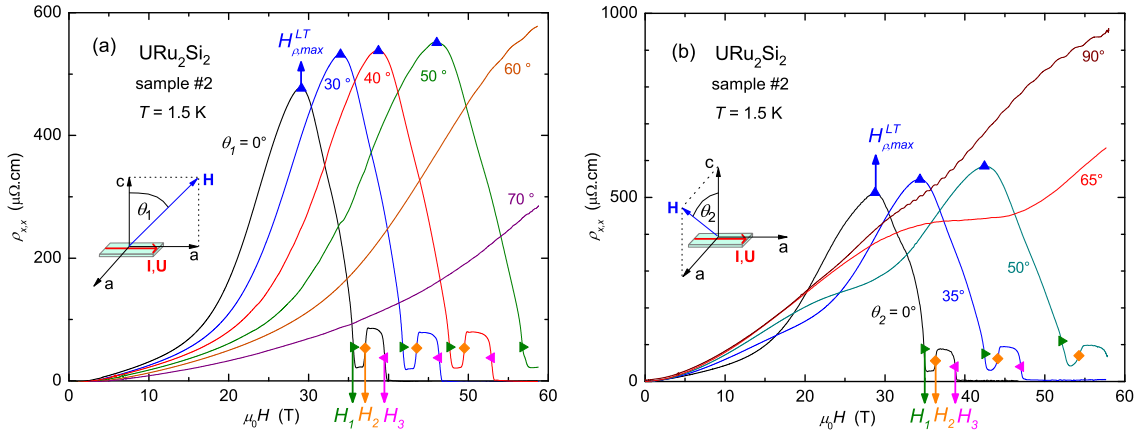

Figure 8.4: (a) Magnetoresistivity $\rho_{x,x}$ of sample #2 versus the magnetic field H at $T = 1.5$ K for different angles θ_1 between **H** and **c**. The field is turning in the (**a**,**c**)-plane from the transverse ($\theta_1 = 0°$) to the longitudinal ($\theta_1 = 90°$) configurations. (b) Magnetoresistivity $\rho_{x,x}$ of sample #2 versus H at $T = 1.6$ K for different angles θ_2 between the magnetic field and the **c**-axis. The magnetic field is turning in the transverse (**a**,**c**)-plane.

$H^{LT}_{\rho,max}$ is presented in Figure 8.6(b). In this second configuration, the magnetic field remains transverse for all angles θ_2 and the general form of the magnetoresistivity evolves differently than in the first configuration. For $\theta_2 = 90°$, i.e., when **H** $\parallel$ **a**, the transverse magnetoresistivity increases continuously up to the maximal field and no field-induced anomalies are observed. The oscillatory modulation of $\rho_{x,x}(H)$ for $\theta_2 = 90°$ is due to the Shubnikov-de Haas effect and will be analyzed in Chapter 9. Remarkably, the heights of the plateaus of phase V between H_1 and H_2 and phase III between H_2 and H_3 are independent of the orientation of the magnetic field relatively to the **c**-axis or to the current, as seen in Figures 8.4(a) and 8.4(b). Above H_1, the magnetoresistivity is also sample-independent, as shown in Chapter 7, and has thus no observable orbital contribution. We conclude that the resistivity in phases III and V is dominated by the scattering of the charge carriers on the magnetic moments of the localized $5f$-electrons. Within this picture, the scattering off of the f-electrons is sample-independent, since it corresponds to a scattering of the conduction electrons by the static or fluctuating magnetic moments from each $5f$ U-ion site, the distance - between two ions - involved in this process being smaller than the distance between two impurities.

A pronounced inflection point in $\rho_{x,x}(H)$ of sample #2 develops at a field well below $H^{LT}_{\rho,max}$ for $\theta_2 \geq 35°$. This is the same anomaly as that observed in the resistivity of sample #1 for **H** $\parallel$ **c** at H^*, which is defined at the kink just after an inflection point [see Chapter 7], and corresponds to a Fermi surface-related crossover. Figures 8.5(a) and (b) present for both samples the evolution, with an increasing angle θ_2,

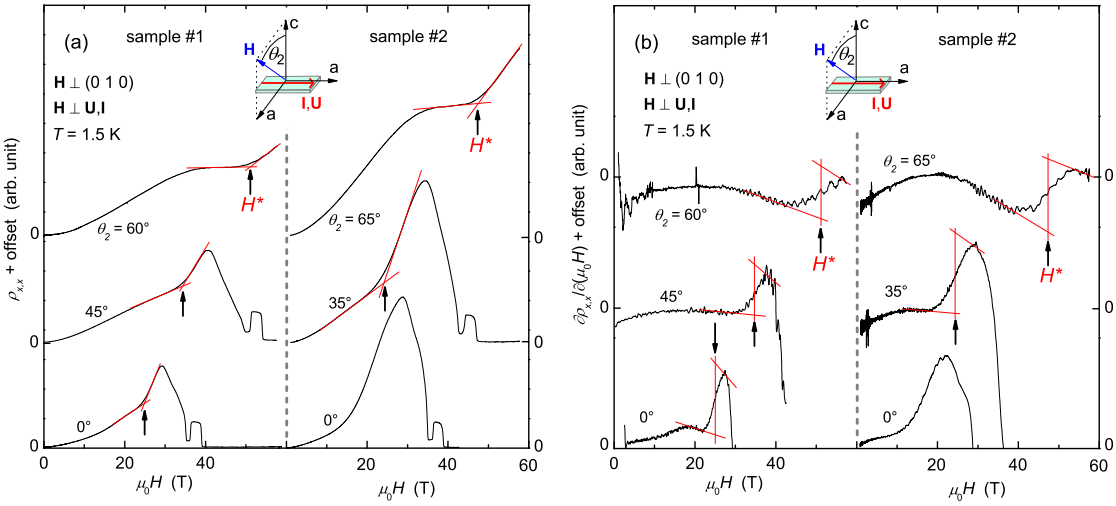

Figure 8.5: (a) Definition of the anomaly at H^* in the magnetoresistivity of samples #1 and #2 for different orientations of the magnetic field in the transverse (**a**,**c**)-plane. (b) Equivalent definition of H^* in the field-derivative of the resistivity.

of the kink-like anomaly in the resistivity and in the associated step-like anomaly in the field-derivative of the resistivity, respectively. Even if this anomaly at H^* is not observed for sample #2 for $\mathbf{H} \parallel \mathbf{c}$, the figures 8.5(a) and (b) clearly shows that both samples exhibits a similar anomaly at H^* for $\theta_2 \geq 35°$. Figure 8.6 shows the angle-dependence of the transition fields H_1, H_2, and H_3, and the crossover fields $H^{LT}_{\rho,max}$ and H^* in angles up to 60°. All of these transition and crossover fields can be fitted with $1/\cos\theta$-functions ($\theta = \theta_1$,θ_2). The angle-dependence of the low-temperature critical fields H_1, H_2, and H_3 established by the resistivity measurements of this work is consistent with results from previous magnetization experiments for θ up to 15° [Sugiyama 1990] and resistivity experiments for θ up to 30° [Jo 2007]. The angle dependence of the crossover field $H^{LT}_{\rho,max}$ defined at the maximum of the resistivity is a new feature of the present work. The $1/\cos\theta$-dependence indicates that the physics of these transitions and crossovers only depend on the projection of the magnetic field on the **c**-axis, at least up to $\theta = 60°$ ($\theta = \theta_1$, θ_2). The $1/\cos\theta$-dependence of H^* observed here is consistent with results from previous resistivity experiments for θ up to 40° [Shishido 2009, Aoki 2012]. The resistivity of our sample #2 does not show an anomaly at H^* for $\theta = 0$ but an extrapolation of the $1/\cos\theta$-law leads to $\mu_0 H^* \to 20$ T, when $\theta_2 \to 0$, which is much lower than $\mu_0 H^* \simeq 25$ T in sample #1 or the values of 22.5 and 24 T reported in the literature [Shishido 2009, Altarawneh 2011, Aoki 2012]. Sample #2 has the highest quality and the anomaly at H^* in its magnetoresistivity may be hidden, for $\mathbf{H} \parallel \mathbf{c}$, by an additional orbital contribution, whose intensity decreases at high angles θ_2, while the intensity of the anomaly at H^* increases at high θ_2.

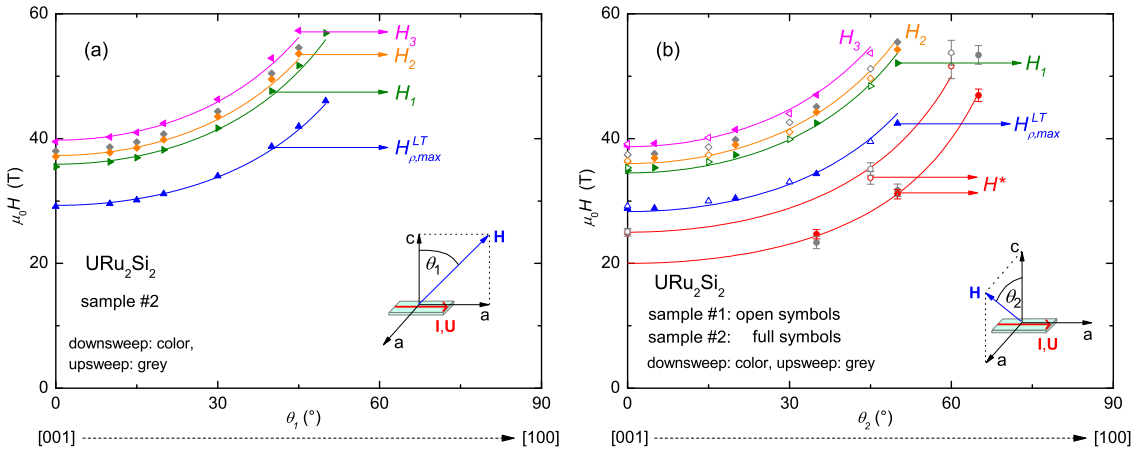

Figure 8.6: Angle dependence of the transition fields H_1, H_2, and H_3 and crossover fields $H^{LT}_{\rho,max}$ and H^* of sample #1 (open symbols) and sample #2 (closed symbols) (rising field - colored, falling field - grey). The solid lines represent $1/\cos\theta$-fits to the data.

The transition fields H_1, H_2 and H_3 are related to the f-electron magnetic properties, and their angle-dependence is a consequence of the strong Ising-character of the magnetic properties of URu_2Si_2. I have shown in Chapter 7 that the anomalies at H^* and $H^{LT}_{\rho,max}$ occur in the orbital contribution to the magnetoresistivity, thus are related to Fermi surface modifications. H^* and $H^{LT}_{\rho,max}$ show $1/\cos\theta$-dependencies, similarly to the magnetic transitions H_1, H_2, and H_3. This indicates that only the projection of the magnetic field along the **c**-axis affects the Fermi surface, and confirms a strong correlation between the magnetic properties of the $5f$-electrons and that of the Fermi surface in URu_2Si_2. This underlines the dual localized-itinerant nature of the $5f$ electrons.

8.4 Magnetoresistivity in magnetic fields H in the plane (a,a)

Figure 8.7 shows the magnetoresistivity $\rho_{x,x}$ of sample #2 versus the magnetic field H at $T = 1.4$ K for different directions of **H** in the (**a**,**a**)-plane. The field has been turned from the transverse ($\phi = 0°$) to the longitudinal ($\phi = 90°$) configurations, ϕ being the angle between **H** and **a**. For all values of ϕ, the magnetoresistivity increases continuously with the field and no anomalies due to field-induced transitions are observed, the system remaining in the hidden-order phase at least up to 60 T. $\rho_{x,x}(H)$ is modulated by Shubnikov-de Haas oscillations, which will be analyzed in Chapter 9. The field-dependence of the magnetoresistivity decreases with increasing angle ϕ and $\rho_{x,x}$ has almost vanished at $\phi = 90°$. The fact that the magnetoresistivity

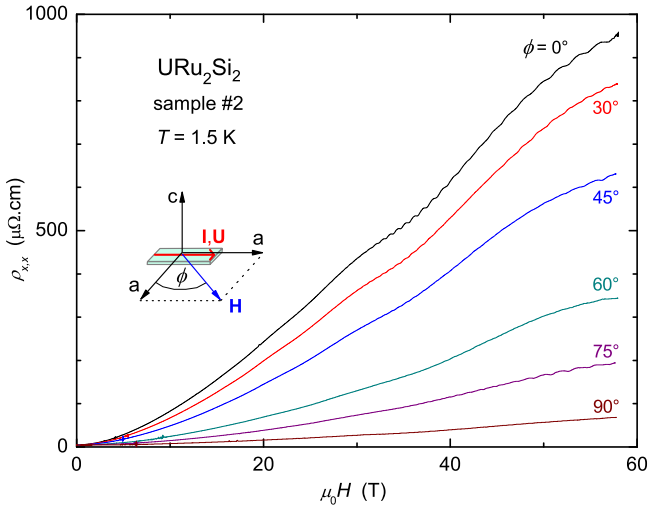

Figure 8.7: Magnetoresistivity $\rho_{x,x}$ of URu_2Si_2 sample #2 versus H at $T = 1.5$ K for different angles ϕ between **H** and **a**. The field is turning in the (**a**,**a**)-plane from the transverse ($\phi = 0°$) to the longitudinal ($\phi = 90°$) configurations.

vanishes, when the magnetic field is turning from the transverse to the longitudinal configurations, is a signature of the orbital effect, which dominates the transverse magnetoresistivity of URu_2Si_2 in its hidden-order phase. Figures 8.4(b) and 8.7 emphasize the strong dependence of the magnetoresistivity on the orientation of the sample in a magnetic field for small angles between **H** and **a**. This is one of the reasons for the limited reproducibility of our magnetoresistivity measurements in **H** ∥ **a** (cf Sect. 3.9).

9 Fermi Surface in High Magnetic Fields

In this Chapter, I present a study of the Fermi surface of URu_2Si_2 in high magnetic fields via the Shubnikov-de Haas effect observed on our highest-quality URu_2Si_2 sample #2. Section 9.1 presents a preliminary study of the low-field Fermi surface in steady magnetic fields up to 13 T. Section 9.2 shows that magnetic-field-induced Fermi surface modifications occur in intense magnetic fields below 35 T applied along the **c**-axis, i.e., inside the hidden-order phase. In Section 9.3, quantum oscillations are observed for the first time in magnetic fields $\mu_0\mathbf{H} \parallel \mathbf{a}$ up to 81 T. A new Fermi surface branch λ, with a small effective mass $m^* = (1 \pm 0.5)\ m_0$ and the frequency $F_\lambda \sim 1350$ T, is extracted. An angle-dependence of the observed high-field Shubnikov-de Haas frequencies is established in Section 9.4.

9.1 Low-field Fermi surface

The low-magnetic-field Fermi surface of URu_2Si_2 is well-known from quantum oscillation experiments in steady magnetic fields performed by Ohkuni *et al.* [Ohkuni 1999] and Hassinger *et al.* [Hassinger 2010]. The low-field Shubnikov-de Haas experiments presented here were performed on our sample #2 in steady magnetic fields up to 13 T at the Institut Nanosciences et Cryogénie of the CEA-Grenoble, in collaboration with Georg Knebel, Alexandre Pourret, and Dai Aoki. Figure 9.1 presents the Shubnikov-de Haas data resulting from resistivity measurements at $T = 32$ mK in a magnetic field applied along different directions in the transverse (**a**,**c**)-plane. In this graph, θ indicates the angle between **H** and **c**. Figure 9.1(a) shows the oscillating signals $\rho^{osc}_{x,x} = \rho_{x,x} - \rho_{BG}$ versus H obtained by subtracting non-oscillating polynomial backgrounds ρ_{BG} from the raw resistivity (shown in Sect. 8.1, Fig. 8.1). Figure 9.1(b) shows the Shubnikov-de Haas spectra obtained via Fourier transforms of the oscillating signals $\rho^{osc}_{x,x}/\rho_{BG}$ versus the inverse magnetic field $(\mu_0 H)^{-1}$, and Figure 9.1(c) focuses on the example of the Shubnikov-de Haas spectrum for $\theta = 5°$. This spectrum exhibits peaks at the frequencies $F_\eta \simeq 95$ T, $F_\gamma \simeq 185$ T, $F_\beta \simeq 435$ T, $F_{\beta'} \simeq 500$ T, and $F_\alpha \simeq 1063$ T. Furthermore, peaks due to the harmonics of γ, β, and α, and a peak due to the combination of α and β are observed. The angle dependencies of the Fermi surface branches α, β and γ are shown in Figure 9.1(d). F_α is almost angle-independent in the (**a**,**c**)-plane ($F_\alpha \sim 1060$ T).

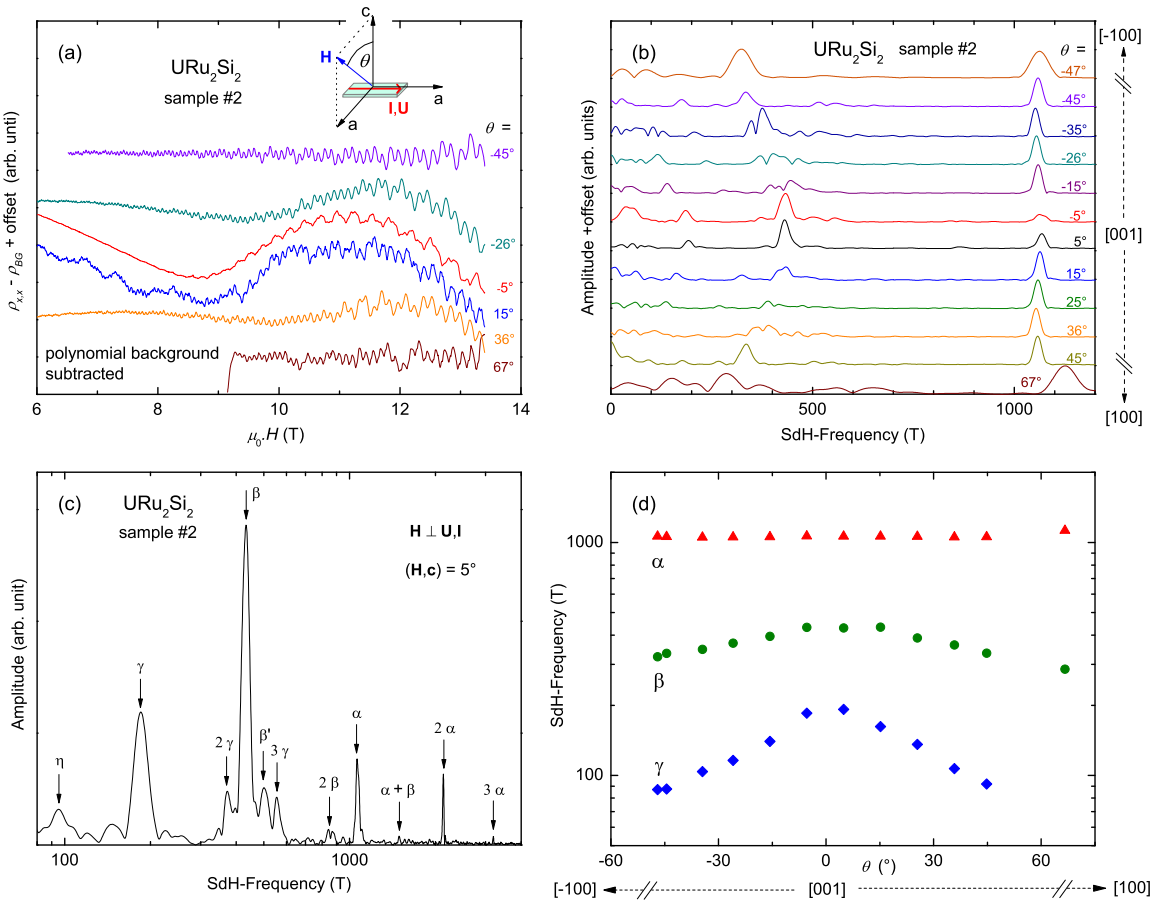

Figure 9.1: Shubnikov-de Haas data of URu_2Si_2 sample #2 at $T = 32$ mK and in a magnetic field up to 13 T, applied along different directions in the (**a**,**c**)-plane with an angle θ between **H** and **c**. Data extracted from that shown in Sect. 8.1, Fig. 8.1. (a) Oscillating signals $\rho^{osc}_{x,x} = \rho_{x,x} - \rho_{BG}$ versus H, where ρ_{BG} is a non-oscillating polynomial background. (b) Resulting Fourier spectra. (c) Exemple of the fourier spectrum for $\theta = 5°$. (d) Angle-dependence of the low-field Shubnikov-de Haas frequencies γ, β, and α.

F_β decreases with increasing θ from ~ 430 T at $\theta = 0°$ to ~ 330 T at $\theta = 45°$. F_γ exhibits the strongest angle-dependence and decreases from ~ 190 T at $\theta = 0°$ to ~ 85 T at $\theta = 45°$.

Figure 9.2 presents the Shubnikov-de Haas data of sample #2 from measurements at temperatures between 32 and 250 mK for an angle $\theta = 15°$ between **H** and **c**. Figure 9.2(a) shows the resistivity $\rho_{x,x}(H)$ and Figure 9.2(b) shows the extracted oscillating signal $\rho^{osc}_{x,x}(H)$. The amplitude of the oscillations decreases with increasing temperature due to the R_T-damping (Sect. 2.5, Eq. 2.82). Figure 9.2(c) presents the resulting Shubnikov-de Haas spectra. For $\theta = 15°$, I have extracted the fundamental frequencies $F_\alpha \simeq 1060$ T, $F_\beta \simeq 395$ T, $F_{\beta'} \simeq 445$ T, $F_\gamma \simeq 140$ T, and $F_\eta \simeq 100$ T. The cyclotron effective masses $m^*_\alpha = (11.7 \pm 2)\ m_0$, $m^*_\beta = (21.7 \pm 6.5)\ m_0$, $m^*_{\beta'} =$

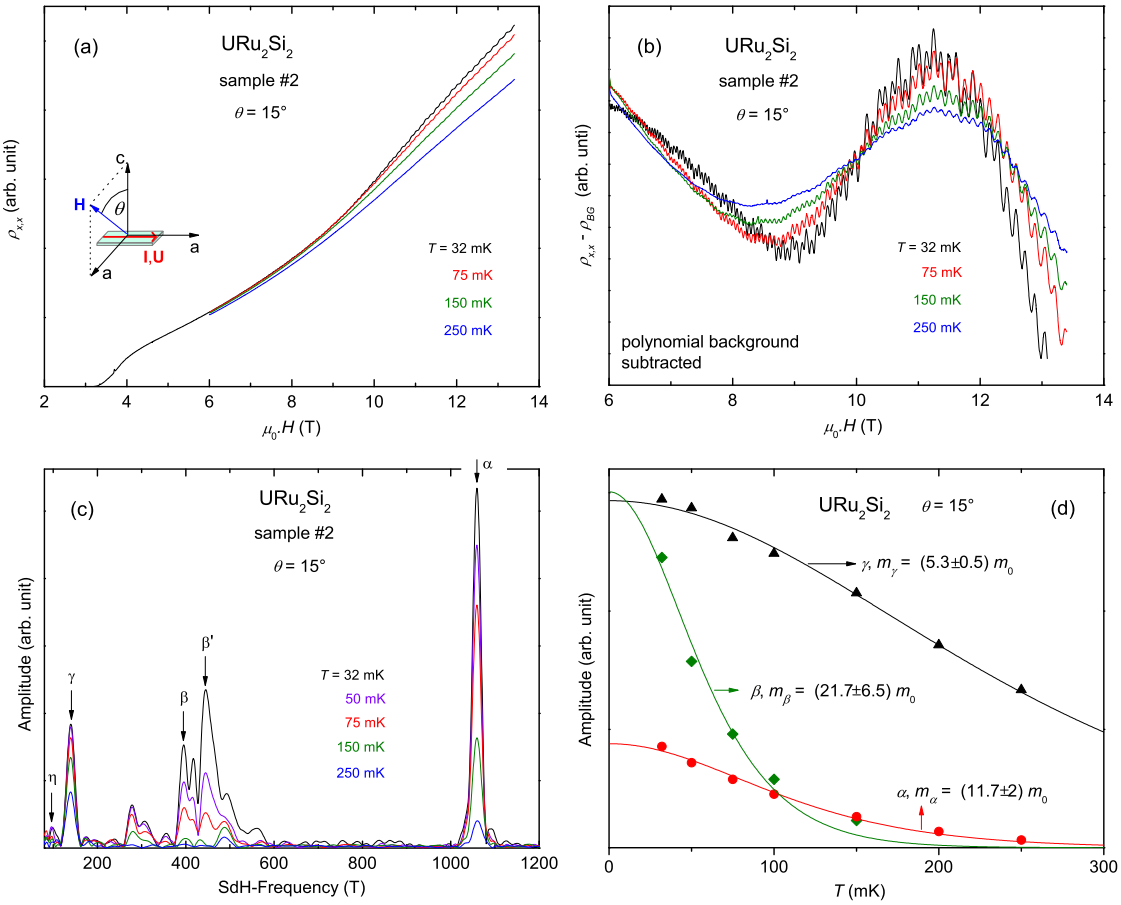

Figure 9.2: (a) $\rho_{x,x}(H)$ of URu_2Si_2 sample #2 for $\theta = 15°$ at temperatures from 32 to 250 mK. (b) Oscillating signal $\rho^{osc}_{x,x} = \rho_{x,x} - \rho_{BG}$ versus H, where ρ_{BG} is a non-oscillating polynomial background. (c) Fourier spectra of the Shubnikov-de Haas oscillations observed in magnetic fields up to 13 T, for $\theta = 15°$. (d) Mass-plots of the frequencies γ, β, and α, for $\theta = 15°$. The solid lines represent fits with the R_T-damping function.

(32.4±10) m_0, and $m^*_\gamma = (5.3\pm0.5)\ m_0$ are obtained by fitting the peak amplitude of the Fermi surface branches α, β, β', and γ, respectively, versus the temperature with the R_T-damping function (Sect. 2.5, Eq. 2.83), as shown in Figure 9.2(d). I was not able to extract the mass of γ because to its weak amplitude. The spectra, the angle-dependencies, and the cyclotron effective masses of the Fermi surface sheets α, β, and γ are in good agreement with the data reported by Hassinger *et al.* [Hassinger 2010] and Ohkuni *et al.* [Ohkuni 1999] (see Fig. 9.3).

The steady-field experiments on our highest-quality URu_2Si_2 sample (RRR = 225) show Shubnikov-de Haas data consistent with recent studies, when measured in similar experimental conditions (steady fields, subkelvin temperatures). Keeping this in mind, the Shubnikov-de Haas data obtained in pulsed-high-field experiments will be presented in the following, where i) new features are observed in high fields

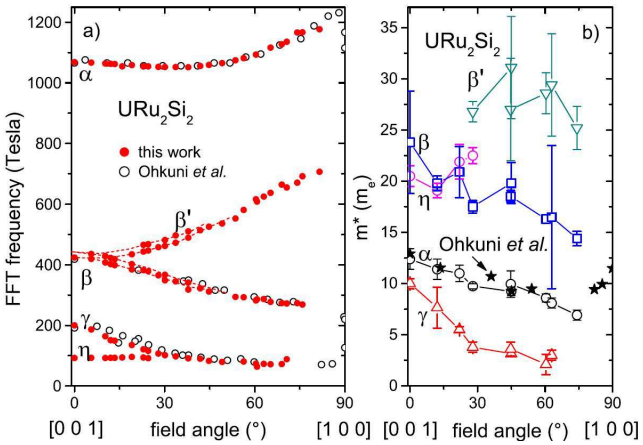

Figure 9.3: Angle-dependence of (a) the Shubnikov-de Haas frequencies and (b) the corresponding effective masses of URu_2Si_2. Figures taken from [Hassinger 2010].

(above ~ 20 T) and ii) a higher noise level is due to the pulsed fields.

9.2 Fermi surface modifications in high magnetic fields H ∥ c

We have seen in Chapter 7 that a magnetic field applied along the **c**-axis induces anomalies in the orbital contribution to the magnetoresistivity of URu_2Si_2, namely a the sample-dependent field $\mu_0 H^* \sim 20 - 25$ T and a maximum of $\rho_{x,x}(H)$ at $\mu_0 H^{LT}_{\rho,max} = 31.5$ T, i.e., well below the destruction of the hidden-order phase at $\mu_0 H_1 = 35$ T (cf. also [Shishido 2009, Altarawneh 2011, Aoki 2012]).
Figure 9.4(a) shows the magnetoresistivity $\rho_{x,x}(H)$ of our sample #2 at $T = 100$ mK in a magnetic field H applied parallel to the magnetic easy axis **c**. The magnetoresistivity exhibits Shubnikov-de Haas oscillations in a field range from ~ 15 T to 35 T. Figure 9.4(b) shows the oscillating signal extracted by subtracting a non-oscillating spline background from the raw resistivity. Figure 9.5(a) presents the resulting Shubnikov-de Haas spectra obtained via Fourier transforms of the quantum oscillations for different field-windows between 13.6 and 34.7 T. Figure 9.5(b) presents the extracted Shubnikov-de Haas frequencies as function of the magnetic field applied along **c**. The spectra exhibit the frequencies of the α and β Fermi surface sheets, which have been observed in the low magnetic fields (see Sect 9.1). The frequency F_α (~ 1000 T at low field) is observed up to 35 T, while the frequency F_β (~ 400 T at low fields) is observed up to 32.5 T. Approaching 35 T, the frequency peaks become much broader due to the limited number of periods in the $1/H$-range. F_α decreases from 1020 T at $\mu_0 H = 15$ T to 830 T at $\mu_0 H = 30$ T, while F_β increases from 420 T at $\mu_0 H = 15$ T to 590 T at $\mu_0 H = 30$ T. Abrupt changes in the spectra occur at

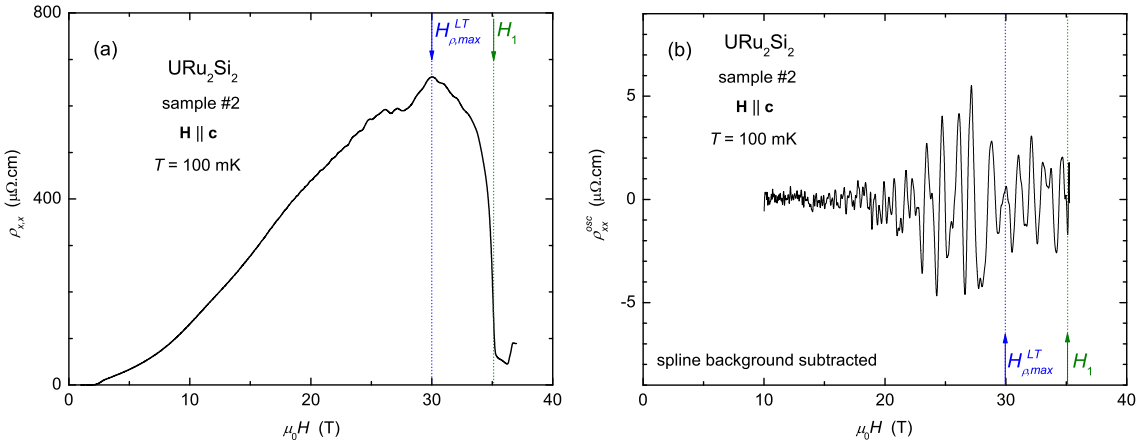

Figure 9.4: (a) $\rho_{x,x}(H)$ of URu_2Si_2 sample #2 at $T = 100$ mK, for $\mu_0\mathbf{H} \parallel \mathbf{c}$ up to 40 T. (b) Oscillating signal $\rho^{osc}_{x,x}(H)$ extracted with a spline background from $\rho_{x,x}(H)$.

$\mu_0 H \sim 30$ T: in the field-window $31.5 - 34.7$ T, F_β has vanished and a new distinct frequency peak appears at $F_\delta = 1300$ T.

For comparison, the results of recent Shubnikov-de Haas experiments performed in steady magnetic fields [Jo 2007, Shishido 2009, Altarawneh 2011, Aoki 2012] are also plotted in Figure 9.5(b). An excellent agreement is found with the data of Aoki *et al.* [Aoki 2012], where a similar analysis as here, i.e., with a high number of small field windows, was performed. A striking feature of the Shubnikov-de Haas data of Aoki *et al.* [Aoki 2012] is that a new frequency labeled F_ω with a large cyclotron mass ($m^*_\omega \sim 25\ m_0$) appears at $\mu_0 H \sim 20$ T. F_ω increases strongly with the magnetic field from 240 T at $\mu_0 H = 21$ T to 640 T at $\mu_0 H = 29$ T. The data of the present work are also in good agreement with studies where the quantum oscillations were analyzed on fewer field windows [Jo 2007, Shishido 2009, Altarawneh 2011]. The frequencies F_α, F_β, and F_δ have been observed in all sets of data [Jo 2007, Shishido 2009, Altarawneh 2011, Aoki 2012]. However, from the magnetoresistivity data reported here, we can not observe all of the frequencies reported by the steady-field experiments, due to the intrinsic noise of the pulsed field experiments. Particularly, the field-dependencies of the low frequencies η, γ, and ω have not been established here. Surprisingly we were able to follow the frequency β from 22 to 25 T, where Aoki *et al.* [Aoki 2012] did not observe it. Further differences are as follows: i) at 20 T, a high frequency of 1500 T was observed by Altarawneh *et al.* [Altarawneh 2011], but neither in the present work nor in that of Aoki *et al.* [Aoki 2012], ii) as well, no trace of the frequency at ~ 1300 T observed by Shishido *et al.* [Shishido 2009] above $\mu_0 H = 17\ T$ is found here, iii) Altarawneh *et al.* [Altarawneh 2011] and Jo *et al.* [Jo 2007] observed a frequency of 230 T at $\mu_0 H \sim 27$ T, which is not observed here or by Aoki *et al.* [Aoki 2012], iv) at $\mu_0 H \sim 33$ T, Altarawneh *et al.*

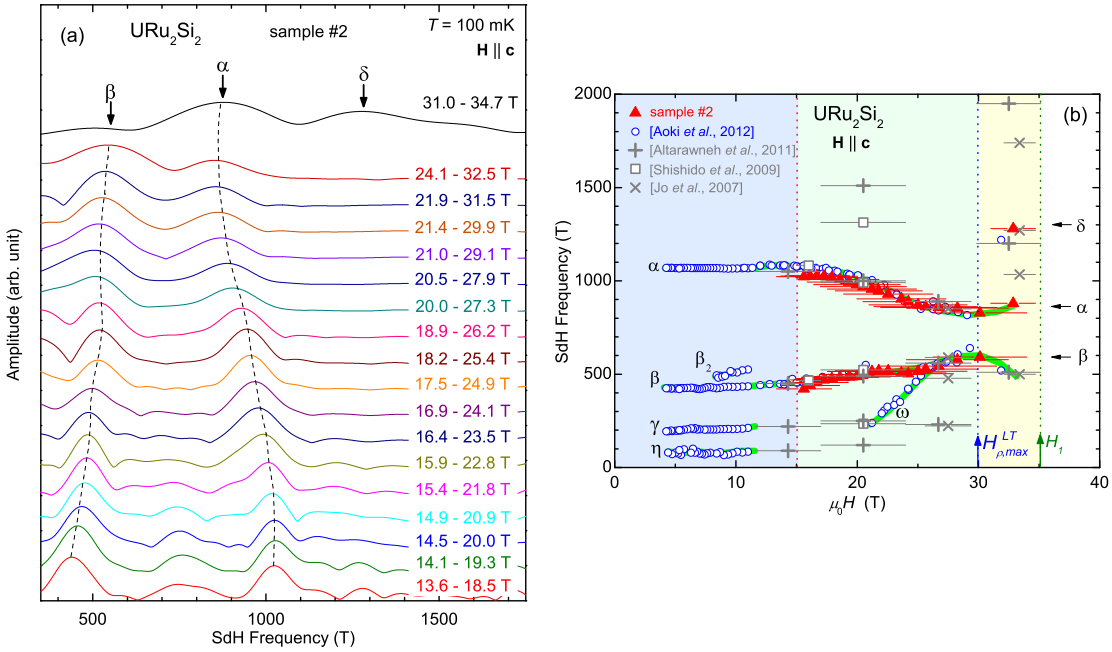

Figure 9.5: (a) Fourier spectra of the quantum oscillations of sample #2, for $\mathbf{H} \parallel \mathbf{c}$ and at $T = 100$ mK, for small field windows between 13.6 and 34.7 T. The dashed lines are guides to the eyes. (b) Field-dependence of the Shubnikov-de Haas frequencies for $\mathbf{H} \parallel \mathbf{c}$. The horizontal bars indicate the analyzed field windows. Data from steady-field measurements [Jo 2007, Shishido 2009, Altarawneh 2011, Aoki 2012] are added for comparison.

[Altarawneh 2011] and Jo *et al.* [Jo 2007] observed a high frequency of ~ 1700 T, which is not observed here or by Aoki *et al.* [Aoki 2012]. The differences between the presented Shubnikov-de Haas data is due the limited number of oscillation periods in the analysed field windows.

The low-field Shubnikov-de Haas experiments show that URu_2Si_2 is a multi-band metal with at least four Fermi surface sheets α,β, γ, and η [Bergemann 1997, Keller 1998, Ohkuni 1999, Hassinger 2010, Aoki 2012]. α, β, and γ are closed Fermi surface pockets and no open Fermi surface is observed from quantum oscillation experiments [Ohkuni 1999, Aoki 2012]. Effective masses up to $\sim 30\ m_0$ indicate that URu_2Si_2 is well a heavy-fermion compound, in agreement with measurements of bulk properties [Palstra 1985, Maple 1986, Schoenes 1987]. The specificity of URu_2Si_2 is that the Fermi surface reconstruction at T_0 (cf. Sect. 7.2) leads to different Fermi surface bands whose characteristic band filling energies $\Delta\epsilon = \hbar eF/m_c^* \sim 1-10$ meV are rather low, due to the combined effects of low-carrier densities [Schoenes 1987, Dawson 1989, Kasahara 2007] and high effective masses. Since $\Delta\epsilon$ is of the same order than the Zeeman energy $\epsilon_Z = \frac{1}{2} g \mu_B \mu_0 H$ ($\simeq 1.2$ meV at $\mu_0 H = 20$ T, for $g \simeq 2$), applying a magnetic field of 20 T or more may permit to

decouple the minority and majority spin bands. Considering the complex band structure of URu_2Si_2, exotic phenomena such as the cascade of Fermi surface reconstructions observed here and in [Jo 2007, Shishido 2009, Altarawneh 2011, Aoki 2012] could be thus related to the Zeeman effect.

To summarize, as observed here and in previous studies [Jo 2007, Shishido 2009, Altarawneh 2011, Aoki 2012], the evolution of the Shubnikov-de Haas spectrum clearly indicates that a magnetic field applied along **c** induces important modifications of the Fermi surface of URu_2Si_2, in magnetic fields far below $\mu_0 H_1 = 35$ T, i.e., inside the hidden-order phase. Abrupt modifications of the Fermi surface occur in the proximity of the strong maximum in the resistivity at $\mu_0 H^{LT}_{\rho,max} = 30$ T, whereas progressive frequency changes are observed in a large field range from 15 to 30 T, in which the kink-like anomaly in the magnetoresistivity at $\mu_0 H^* \sim 20 - 25$ T was observed. The Fermi surface reconstructions are presumably due to successive polarizations of the different Fermi surface pockets. Remarkably, the low-temperature magnetization does not show signatures of anomalies in the thermodynamic properties in the field range 0 to 35 T (see Sect. 5.1). Furthermore, the anomalies detected in the hidden-order phase are smeared out by increasing temperature, which indicates that they are not conventional phase transitions. Thus, the observed anomalies in the transport properties are due to purely electronic instabilities, possibly Lifshitz-transitions [Lifshitz 1960] (cf. also [Malone 2011, Pourret 2013]). It is worthwhile to remark that an enhancement of the critical magnetic fluctuations, as indicated by the field-dependence of the Sommerfeld coefficient is also observed above 30 T [see Sect. 5.1, Fig. 5.2(b)]. We underline the strong interplay between the magnetic polarization and the field-induced evolution of the Fermi surface in URu_2Si_2.

9.3 Fermi surface in high magnetic fields H ∥ a

Figure 9.6(a) presents the transverse magnetoresistivity $\rho_{x,x}$ of our URu_2Si_2 sample #2 measured in a magnetic field applied along the magnetic hard axis **a**, at temperatures from 500 mK to 4.2 K. At $T = 500$ mK, the sample is in the superconducting phase, which is destabilized at $\mu_0 H_{c,2} \sim 8$ T, and the magnetoresistivity increases significantly with increasing magnetic field, from 57 $\mu\Omega$cm at $\mu_0 H = 10$ T to 1150 $\mu\Omega$cm at $\mu_0 H = 55$ T. No field-induced transition is observed up to $\mu_0 H = 57$ T at $T = 500$ mK and up to $\mu_0 H = 81$ T at $T = 1.4$ K, respectively, indicating that the system remains in the hidden-order phase. Quantum oscillations due to the Shubnikov-de Haas effect are visible over large field ranges, e.g., up to 81 T at $T = 1.4$ K. We distinguish slow and fast oscillations in the raw resistivity. At $T = 500$ K, the non-oscillating part of the magnetoresistivity is almost linear above

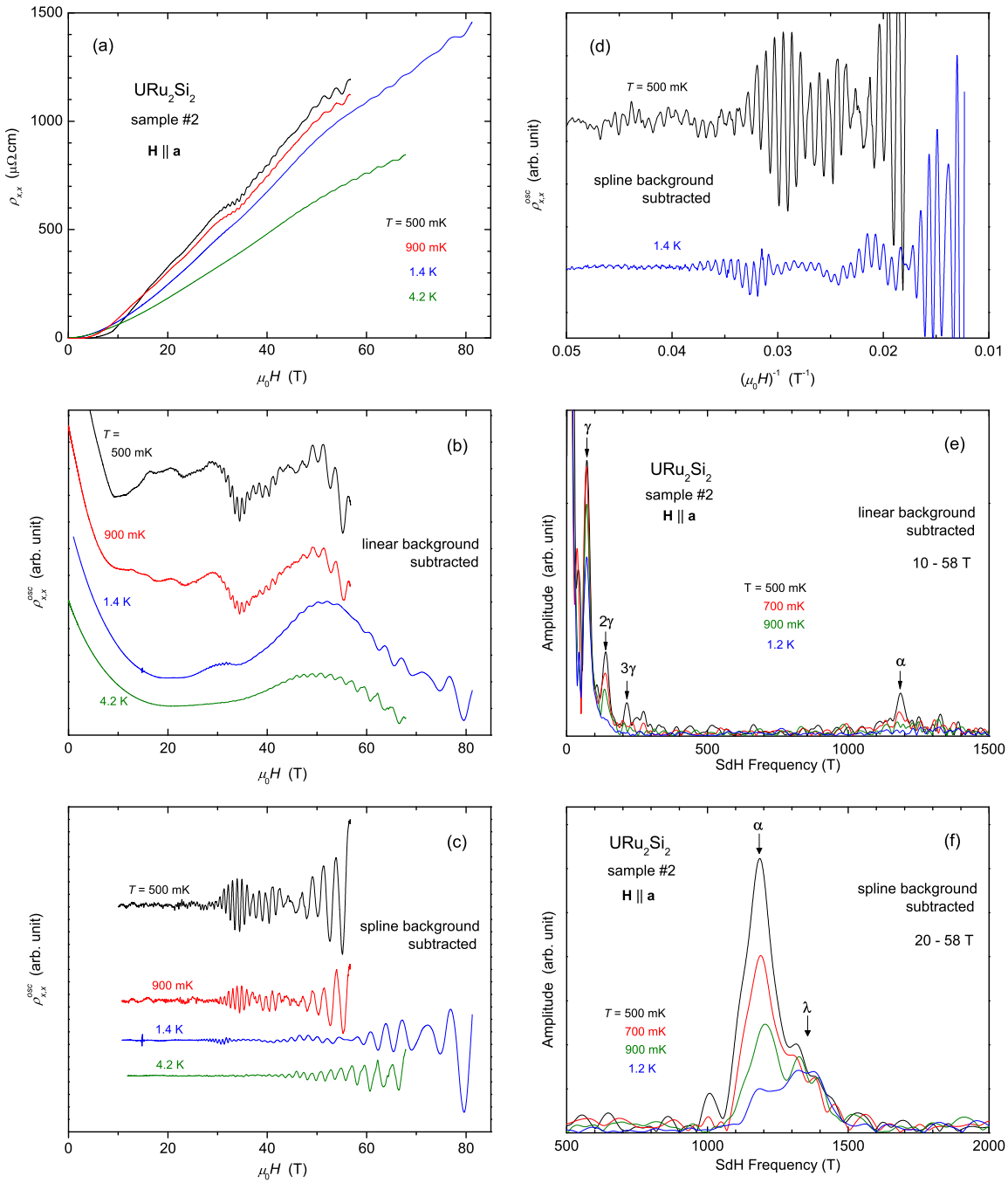

Figure 9.6: (a) Transverse magnetoresistivity $\rho_{x,x}$ of URu_2Si_2 sample #2 versus the magnetic field H applied along the **a**-axis at temperatures from 500 mK to 4.2 K. (b) Oscillating signal $\rho^{osc}_{x,x}$ versus H extracted by subtracting linear backgrounds from $\rho_{x,x}$. (c) Fast oscillating signals extracted by subtracting spline backgrounds from $\rho_{x,x}$. (d) Fast oscillating signals $\rho^{osc}_{x,x}$ versus the inverse magnetic field $(\mu_0 H)^{-1}$. (e) Fourier spectra of the oscillations of sample #2 extracted by subtracting linear backgrounds for $\mathbf{H} \parallel \mathbf{a}$, at temperatures from 500 mK to 1.2 K. (f) Fourier spectra of the fast oscillations extracted by subtracting spline backgrounds for $\mathbf{H} \parallel \mathbf{a}$ at temperatures from 500 mK to 1.2 K.

$H_{c,2}$, which deviates significantly from the $\rho_{x,x} \propto H^2$ behavior discussed in Section 7.4. Non-oscillating backgrounds have been subtracted from the raw resistivity curves to obtain the oscillating signals $\rho_{x,x}^{osc}$. Figure 9.6(b) shows the oscillating signals $\rho_{x,x}^{osc}(H)$ extracted by subtracting linear backgrounds from $\rho_{x,x}(H)$ and Figure 9.6(c) shows the fast oscillating signals extracted by subtracting spline backgrounds. Using a linear background assures that the complete frequency range is preserved in the oscillating signal, especially the low frequencies, but risks that a high parasitic signal from a remaining monotonic background appears in the low frequency regime of the spectra. A manually defined spline background easily eliminates the non-oscillating part of $\rho_{x,x}(H)$ but may cut off slow oscillations, too. Subtracting a spline background permits to obtain a higher resolution in the high-frequency range of the spectra than subtracting a linear background, since the spline background reduces the discontinuities at the limits of the analyzed field range. Figure 9.6(d) shows the fast oscillating signal $\rho_{x,x}^{osc}$ versus the inverse magnetic field $(\mu_0 H)^{-1}$ at $T = 500$ mK and 1.4 K and illustrates that the oscillations are periodic in $1/H$. The fast oscillating signals clearly show beatings, indicating a splitted frequency branch. Figure 9.6(e) shows the Fourier spectra of the Shubnikov-de Haas oscillations extracted with linear backgrounds. The spectra exhibit frequency peaks at $F = 70$ T, 140 T, 210 T and 1185 T. The low frequency $F_\gamma = 70$ T corresponds to the small elliptic Fermi surface pocket γ and the high frequency $F_\alpha = 1185$ T corresponds to the large spherical Fermi surface sheet α (cf. Section 9.1, [Ohkuni 1999, Aoki 2012]). The spectra also show harmonics of γ at $2F_\gamma = 140$ T and $3F_\gamma = 210$ T. Figure 9.6(f) shows the Fourier spectra of the fast oscillations extracted with spline backgrounds. At $T = 500$ mK, a main peak is observed at the frequency $F_\alpha = 1185$ T, corresponding to the α-branch, and a shoulder to this peak is observed at around 1350 T. The peak at $F_\alpha = 1185$ T decreases fast with increasing temperature, because of a rather high effective mass $m_\alpha^* = 9.7\ m_0$ [Aoki 2012]. At $T = 1.2$ K, the intensity of F_α is strongly reduced, whereas the peak at ~ 1350 T is almost unchanged. The latter corresponds to a newly-observed Fermi surface branch, labeled λ, which has to be distinguished from the close branch α.

Thanks to higher excitation currents in the resistivity measurements, the Shubnikov-de Haas data obtained in the ^{4}He-cryostat ($T \geq 1.4$ K) have a better resolution than those obtained in the dilution cryostat ($T \leq 1.2$ K), which allows a more precise observation of the λ-branch . Figure 9.7(a) presents the transverse magnetoresistivity $\rho_{x,x}(H)$ of sample #2 measured in a magnetic field $\mathbf{H} \parallel \mathbf{a}$ and at temperatures from 1.4 to 10 K. Figure 9.7(b) shows the fast oscillating signal $\rho_{x,x}^{osc}/\rho_{BG}$ extracted with spline backgrounds and Figures 9.7(c) and (d) show the resulting Fourier spectra, up to $F = 2000$ T and 6000 T, respectively. The spectra exhibit frequency peaks at

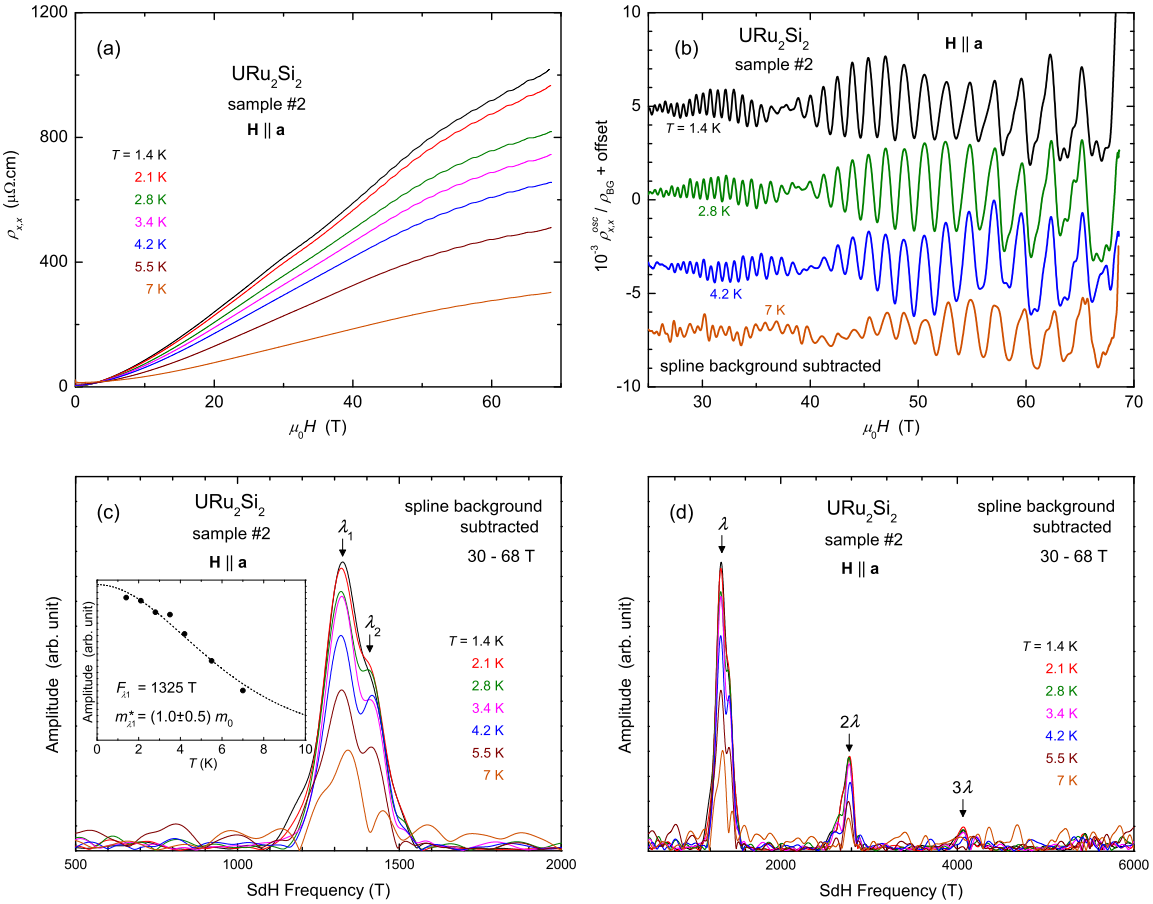

Figure 9.7: (a) Transverse magnetoresistivity $\rho_{x,x}$ of URu_2Si_2 sample #2 versus the magnetic field H applied along the **a**-axis at temperatures from 1.4 K to 10 K. (b) Fast oscillating signals $\rho^{osc}_{x,x}/\rho_{BG}$ extracted by subtracting spline backgrounds from $\rho_{x,x}$. (c,d) Resulting Fourier spectra. Inset: mass-plot for the λ_1-branch.

$F_{\lambda 1} = 1325$ T and $F_{\lambda 2} = 1415$ T, which survive up to $T = 7$ K. We observe also the second and third harmonics of λ at $2F_\lambda \sim 2275$ T and $3F_\lambda \sim 4065$ T, which indicates the high resolution of the experiments in pulsed magnetic fields. The inset of Figure 9.7(c) shows the Fourier amplitude of the λ_1-peak versus the temperature T. The cyclotron effective mass of λ_1 obtained by a fit with the R_T-damping function (Sect. 2.5, Eq. 2.83) equals $m^*_{\lambda 1} = (1.0 \pm 0.5)\ m_0$. Due to the closeness of $F_{\lambda 1}$ and $F_{\lambda 2}$, we were not able to determine the effective mass of λ_2 precisely.

Figures 9.8(a) and (b) show, at $T = 500$ mK and 1.4 K, respectively, an Onsager plot of the fast oscillations, i.e., a plot of the number of the oscillation extrema (#1 for the first maximum, #2 for the first minimum, #3 for the second maximum,...) versus their corresponding position in $(\mu_0 H)^{-1}$. Assuming that the oscillations are governed by a single frequency, the slope of the Onsager-plot is equal to this frequency. Here, the slopes of the Onsager plots are linear up to the maximum

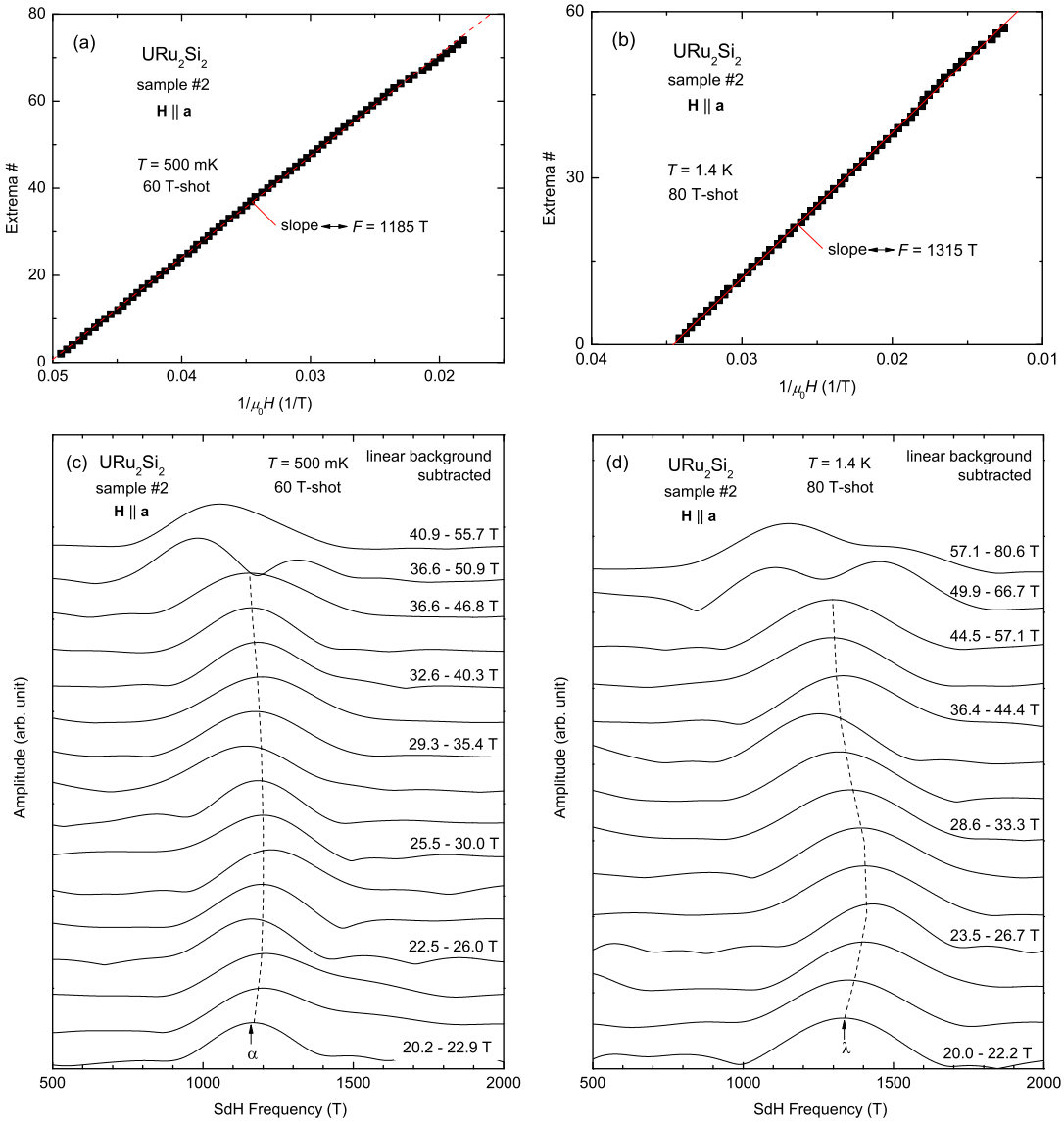

Figure 9.8: Onsager-plot of the dominant frequency of the fast quantum oscillations for **H** ∥ **a**, at (a) $T = 500$ mK and (b) $T = 1.4$ K. Fourier spectra over small field windows of the fast oscillations for **H** ∥ **a**, at (c) $T = 500$ mK and (d) $T = 1.4$ K.

field and correspond to the frequencies $F_\alpha = 1185$ T and $F_\lambda = 1315$ T observed in the Shubnikov-de Haas spectra at 500 mK and 1.4 mK, respectively. These plots indicate that, for $\mathbf{H} \parallel \mathbf{a}$, the dominant frequencies F_α and F_λ are independent of the magnetic field at least up to 57 T and 81 T, respectively. This is confirmed by the Shubnikov-de Haas spectra resulting from Fourier transforms over small field windows, shown in Figures 9.8(c) and (d) at 500 mK and 1.4 K, respectively. The spectra are almost unchanged by the field up to $\mu_0 H = 36$ T at $T = 500$ mK and up to $\mu_0 H = 50$ T at 1.4 K. Modifications of the spectra at higher fields are artefacts related to the beatings in the raw oscillationg signal, due to of the small field-windows used for the Fourier transformation. The fact that the frequencies of the α and λ-sheets are field-independent is consistent with the continuous increase of the non-oscillating-background resistivity and indicates that the Fermi surface is not affected by a magnetic field applied along **a**.

To summarize, we observed for the first time the quantum oscillations of the Fermi surface sheets α and γ in magnetic fields $\mathbf{H} \parallel \mathbf{a}$ up to 60 T and of a new branch λ in magnetic fields up to 81 T. λ is a splitted branch and is associated with a light effective cyclotron mass $m^*_\lambda = (1 \pm 0.5)\ m_0$. The cyclotron mass of the λ-branch is much smaller than that of the α-branch, ($m^*_\alpha = 9.7\ m_0$ [Aoki 2012]). Indeed, λ survives up to 7 K, whereas α already vanishes at $T = 1.4$ K. The Shubnikov-de Haas frequencies of the splitted λ-branch ($F_\lambda \sim 1350$ T), observed for the first time in the present work, are close to the frequencies of the splitted α-branch. The light cyclotron mass of the λ-branch excludes that the frequency λ is a harmonic or a combination of other Fermi surface branches of heavier cyclotron masses.

9.4 Fermi surface in high magnetic fields H in the (a,a) and (a,c)-planes

Figure 9.9 presents Shubnikov-de Haas data of our URu_2Si_2 sample #2 measured with a rotation probe in magnetic fields up to 60 T applied along directions in the (**a**,**a**) and (**a**,**c**)-planes, at $T = 1.5$ K (raw data presented in Sects. 8.3 and 8.4). Here, θ_2 corresponds to the angle between **H** and **c**, the system being in the transverse configuration for all θ_2, and ϕ corresponds to the angle between **H** and **a**, the system turning form the transversal to the longitudinal configurations. The oscillating signals $\rho^{osc}_{x,x}(H)$ extracted with linear backgrounds exhibit slow and fast quantum oscillations [see Fig. 9.9(a)]. The slow oscillations correspond to the frequency $F_\gamma = 70$ T of the γ-branch. The fast oscillating signals extracted with spline backgrounds show beatings, which indicate close frequencies [see Fig. 9.9(b)]. The amplitude of the oscillations decreases with increasing angle [ϕ or $(90° - \theta)$]

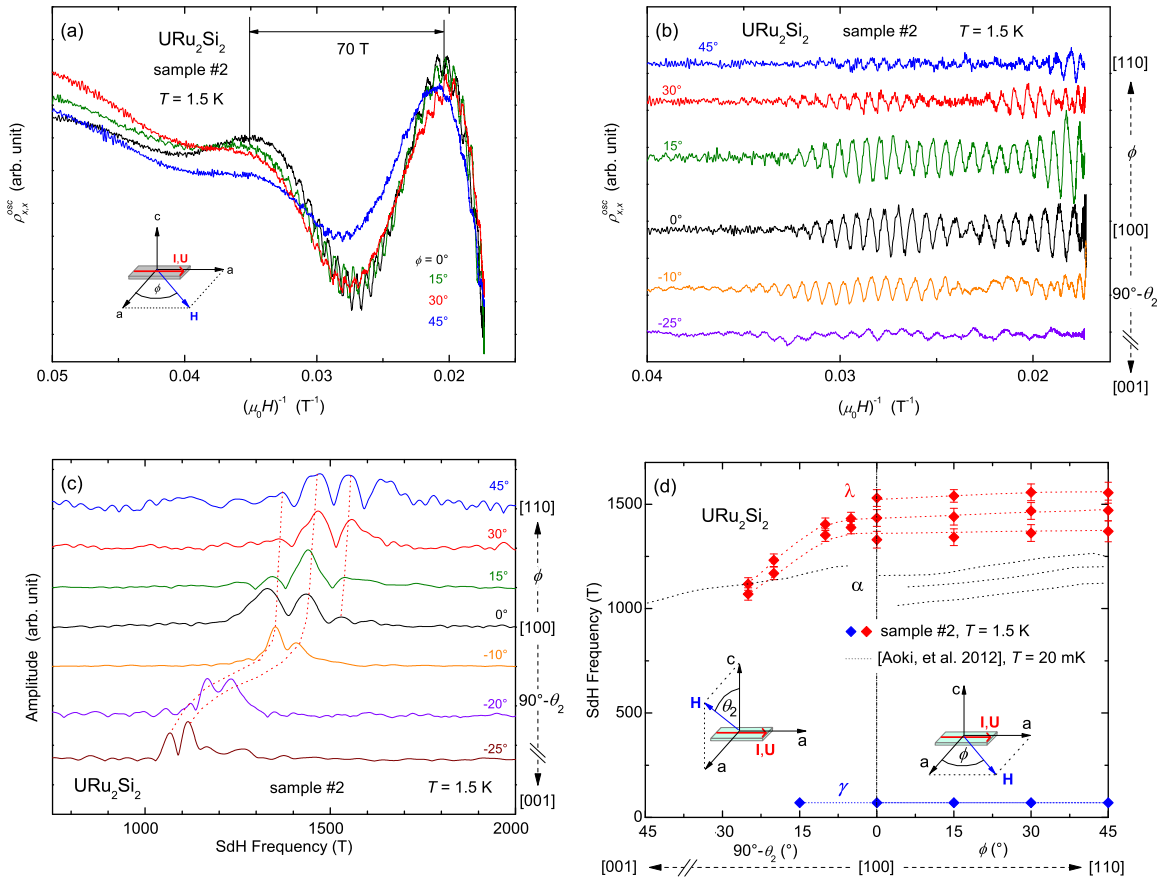

Figure 9.9: (a) Quantum oscillations $\rho_{x,x}^{osc}$ versus $1/(\mu_0 H)$ extracted by subtracting linear backgrounds from $\rho_{x,x}$ of URu_2Si_2 sample #2 measured in magnetic fields up to 60 T, with different angles between the magnetic field and the **a**-axis. (b) Fast oscillating signal $\rho_{x,x}^{osc}$ versus $1/(\mu_0 H)$ extracted by subtracting spline backgrounds. (c) Fourier spectra of the fast oscillations for different angles between the magnetic field and the **a**-axis. The dotted lines are guides to the eyes. (d) Angle-dependence of the Shubnikov-de Haas frequencies of the λ and γ branches of the Fermi surface, observed here at $T = 1.5$ K, and of the α branch observed by Aoki *et al.* [Aoki 2012] at $T = 20$ mK.

between **H** and **a**. Figure 9.9(c) shows the Fourier spectra of the fast Shubnikov-de Haas oscillations for various directions of **H** in the (**a**,**a**) and (**a**,**c**)-planes. The spectra show the frequencies of the splitted light-mass branch λ. We observe two frequency satellites of λ, when **H** is applied along directions in the (**a**,**c**)-plane and three satellites when **H** is applied along **a**. The threefold splitting of λ remains when the magnetic field is rotating in the (**a**,**a**)-plane. In Chapter 3 (Sect. 3.9), I have shown the extreme sensibility of the Fermi surface to slight mis-orientations of the sample in the magnetic field. The fact that λ has three satellites here for **H** $\parallel$ **a**, while only two satellites were reported in Section 9.3, also for **H** $\parallel$ **a**, illustrates the limit of reproducibility of our different sets of experiments. Figure 9.9(d) presents the

angle-dependence of the Shubnikov-de Haas frequencies of the γ and the λ-branches extracted here. A slight increase by $\sim$ 50 T of the λ-frequencies is observed as the field-direction moves from [100] ($\phi = 0°$) to [110] ($\phi = 45°$), similarly to the close α-frequencies (also shown in Fig. 9.9, [Aoki 2012]). The λ-branch has thus a nearly circular cross-section in the basal plane. When the field rotates from [100] ($\phi_2 = 90°$) to [110] ($\phi_2 = 0°$), the frequencies decrease more significantly from $F_\lambda \sim 1400$ T at $\theta_2 = 90°$ to $F_\lambda \sim 1100$ T at $\theta_2 = 60°$. In agreement with Aoki *et al.* [Aoki 2012], no variation of the γ frequency is observed in the (**a**,**a**)-plane. The angle-dependence of F_γ presented here and in Section 9.1 indicate that γ is a small disc-shaped Fermi surface with a circular cross-section in the basal plane and a flattening in the direction of the **c**-axis. The angle-dependence of the λ-frequencies indicates a similar geometry as that of the α-branch, i.e., a large almost spherical Fermi surface.

10 Conclusion

I have performed a systematic investigation per magnetoresistivity and magnetization of high-quality URu_2Si_2 single crystals in pulsed magnetic fields up to 80 T and temperatures down to 100 mK.

I have established the magnetic-field-temperature phase diagram of the system for $\mathbf{H} \parallel \mathbf{c}$, in extended scales up to 60 T and 60 K. Instead of a unique phase transition at a given critical field, the low-temperature phase diagram of URu_2Si_2 is made of a cascade of three first-order transitions between 35 and 39 T. A polarized paramagnetic regime is induced above 39 T. A high-temperature crossover probed by magnetoresistivity at $T_{\rho,max} \simeq 40$ K and by magnetization at $T_{\chi,max} \simeq 55$ K (in the zero-field limit), probably related to the onset of intersite electronic correlations, is found to be a precursor of the "hidden-order" phase (which develops below $T_0 = 17.5$ K at $H = 0$). In $\mathbf{H} \parallel \mathbf{c}$, the vanishing of the crossover temperatures $T_{\rho,max}$ and $T_{\chi,max}$ is responsible i) for the critical area developing at [35 T-39 T] and ii) for the destabilization of the hidden-order state, a polarized regime being reached above 39 T. The effective mass is enhanced in a wide regime between 30 and 45 T, indicating enhanced and thus critical magnetic fluctuations.

Magnetoresistivity measurements on high-quality single crystals were performed in magnetic fields applied along the hard axis **a** and the easy axis **c**, for both transverse and longitudinal configurations. A sample-dependent magnetoresistivity confirmed that a Fermi surface reconstruction occurs at the hidden-order temperature T_0. A remarkably strong transverse magnetoresistivity develops inside the hidden-order phase, which is dominated by the orbital effect, as shown by the sample- and angle-dependencies of the magnetoresistivity. The transverse magnetoresistivity of our purest sample increases by three orders of magnitude in a magnetic field up to 80 T applied along the **a**-axis, indicating a nearly perfect electron-hole compensation. High sample qualities, low carrier densities (~ 0.05 carrier/U-site [Levallois 2009]), and high mobilities $\mu \sim 20 \cdot 10^3$ cm^2/Vs (cf. also [Kasahara 2007]) are responsible for this exceptionally-large signal. An angle-dependent study of the magnetoresistivity showed that the magnetic transitions and the anomalies related to Fermi surface changes exhibit similar angle-dependencies in $1/\cos\theta$, where θ is the angle between **H** and **c**, indicating a strong correlation between the Fermi surface and the magnetic properties in URu_2Si_2. A magnetic field applied along the **c**-axis destabi-

lizes the hidden-order phase at $\mu_0 H_1 = 35$ T, but no anomalies are induced when a magnetic field up to 81 T is applied along the **a**-axis, reflecting that the strong Ising-character of the magnetic properties is connected with the hidden-order parameter. Above H_1, the magnetoresistivity is neither sample- nor angle-dependent, and has no observable orbital contribution, indicating that the resistivity is then dominated by the scattering of the charge carriers on the magnetic moments of the localized $5f$-electrons.

The specificity of URu_2Si_2 is that its Fermi surface reconstruction at T_0 leads to different Fermi surface bands whose characteristic band energies are rather low, due to the combined effects of low-carrier densities and high effective masses. A magnetic field applied along the **c**-axis induces anomalies in the orbital contribution to the magnetoresistivity, well below the destruction of the hidden-order phase at $\mu_0 H_1 = 35$ T. These signatures of crossovers are related to Fermi surface modifications observed by Shubnikov-de Haas oscillations. A progressive change of the Fermi surface occurs in a large field window of 15 - 30 T and a Fermi surface reconstruction occurs at $\mu_0 H \sim 30$ T. For $\mathbf{H} \parallel \mathbf{a}$, quantum oscillations corresponding to the Fermi surface sheets γ and α and, for the first time, the branch λ with the frequency $F_\lambda \sim 1400$ T and the light effective mass $m^*_\lambda = (1 \pm 0.5)\ m_0$, are observed .

The work presented here is a step forward in the understanding of URu_2Si_2 and emphasizes the interplay between the magnetic properties, the Fermi surface, and the hidden-order, as well as the necessity to use a dual "localized-itinerant" description of the f-electrons for a future understanding of the hidden-order in URu_2Si_2. Experiments in high magnetic fields have been decisive to reach this conclusion.

Bibliography

[Audouard private com.] A. Audouard, private communication.

[Alers and Webber 1953] P. B. Alers and R. T. Webber, Phys. Rev. **91**, 1060 (1953).

[Altarawneh 2011] M. M. Altarawneh, N. Harrison, S. E. Sebastian, L. Balicas, P. H. Tobash, J. D. Thompson, F. Ronning, and E. D. Bauer, Phys. Rev. Lett. **106**, 146403 (2011).

[Amitsuka 1999] H. Amitsuka, M. Sato, N. Metoki, M. Yokoyama, K. Kuwahara, T. Sakakibara, H. Morimoto, S. Kawarazaki, Y. Miyako, and J. A. Mydosh, Phys. Rev. Lett. **83**, 5114 (1999).

[Amitsuka 2007] H. Amitsuka, K. Matsuda, I. Kawasaki, K. Tenya, M. Yokoyama, C. Sekine, N. Tateiwa, T. C. Kobayashi, S. Kawarazaki, and H. Yoshizawa, J. Magn. Magn. Mater. **310**, 214 (2007).

[Aoki 2010] D. Aoki, F. Bourdarot, E. Hassinger, G. Knebel, A. Miyake, S. Raymond, V. Taufour, and J. Flouquet, J. Phys.: Condens. Matter **22**, 164205 (2010).

[Aoki 2012] D. Aoki, G. Knebel, I. Sheikin, E. Hassinger, L. Malone, D. Matsuda, and J. Flouquet, J. Phys. Soc. Jpn. **81**, 074715 (2012).

[Aoki 2013] D. Aoki, W. Knafo, and I. Sheikin, C. R. Phys. **14** 1, 53 (2013).

[Ashcroft and Mermin 1976] N. W. Ashcroft and N. D. Mermin, *Solid state physics* (Saunders College, Philadelphia, USA, 1976).

[Balatsky 2009] A. V. Balatsky, A. Chantis, H. P. Dahal, D. Parker, and J. X. Zhu, Phys. Rev. B **79**, 214413 (2009).

[Béard 2012] J. Béard, J. Billette, M. Suleiman, P. Frings, W. Knafo, G. W. Scheerer, F. Duc, D. Vignolles, M. Nardone, A. Zitouni, P. Delescluse, J.-M. Lagarrigue, F. Giquel, B. Griffe, N. Bruyant, J.-P. Nicolin, G. L. J. A. Rikken, R. B. Lyubovskii, G. V. Shilov, E. I. Zhilyaeva, R. N. Lyubovskaya, and A. Audouard, Eur. Phys. J. Appl. Phys. **59**, 30201 (2012).

[Behnia 2005] K. Behnia, R. Bel, Y. Kasahara, Y. Nakajima, H. Jin, H. Aubin, K. Izawa, Y. Matsuda, J. Flouquet, Y. Haga, Y. Ōnuki, and P. Lejay, Phys. Rev. Lett. **94**, 156405 (2005).

[Bel 2004] R. Bel, H. Jin, K. Behnia, J. Flouquet, and P. Lejay, Phys. Rev. B **70**, 220501(R) (2004).

[Bergemann 1997] C. Bergemann, S. R. Julian, G. J. McMullan, B. K. Howard, G. G. Lonzarich, P. Lejay, J. P. Brison, and J. Flouquet, Physica B **230-232**, 348 (1997).

[Bonn 1988] D. A. Bonn, J. D. Garrett, and T. Timusk, Phys. Rev. Lett. **61** (11), 1305 (1988).

[Bourdarot 2003a] F. Bourdarot, B. Fak, K. Habicht, and K. Prokes, Phys. Rev. Lett. **90**, 067203 (2003).

[Bourdarot 2003b] F. Bourdarot, B. Fak, V.P. Mineev, M.E. Zhitomirsky, N. Kernavanois, S. Raymond, P. Burlet, F. Lapierre, P. Lejay, and J. Flouquet, arXiv0312206 (2003).

[Bourdarot 2010] F. Bourdarot, E. Hassinger, S. Raymond, D. Aoki, V. Taufour, L. P. Regnault, and J. Flouquet, J. Phys. Soc. Jpn. **79**, 064719 (2010).

[Brison 1994] J.P. Brison, N. Keller, P. Lejay, A. Huxley, L. Schmidt, A. Buzdin, N.R. Bernhoeft, I. Mineev, A.N. Stepanov, J. Flouquet, D. Jaccard, S.R. Julian, G.G. Lonzarich, Physica B **199-200**, 70 (1994).

[Broholm 1987] C. Broholm, J. K. Kjems, W. J. L. Buyers, P. Matthews, T. T. M. Palstra, A. A. Menovsky, and J. A. Mydosh, Phys. Rev. Lett. **58**, 14671470 (1987).

[Broholm 1991] C. Broholm, H. Lin, P. T. Matthews, T. E. Mason, W. J. L. Buyers, M. F. Collins, A. A. Menovsky, J. A. Mydosh, and J. K. Kjems, Phys. Rev. B **43** (16), 12809 (1991).

[Chandra 2002] P. Chandra, P. Coleman, and J. A. Mydosh, Physica B **312**, 397 (2002).

[Chandra 2013] P. Chandra, P Coleman, and R. Flint, Nature **493**, 621 (2013).

[Correa 2012] V. F. Correa, S. Francoual, M. Jaime, N. Harrison, T. P. Murphy, E. C. Palm, S. W. Tozer, A. H. Lacerda, P. A. Sharma, and J. A. Mydosh, Phys. Rev. Lett. **109**, 246405 (2012).

[Damelin and Miller 2012] S. B. Damelin, W. Miller, Jr., *The mathematics of signal processing* (Cambridge University Press, Cambridge, U.K., 2012).

[Dawson 1989] A. LeR. Dawson, W. R. Datars, J. D. Garrett, and F. S. Razavi, J. Phys.: Condens. Matter **l**, 6817 (1989).

[de Boer 1986] F. R. de Boer, J. J. M. Franse, E. Louis, A. A. Menovsky, J. A. Mydosh, T. T. M. Palstra, U. Rauchschwalbe, W. Schlabitz, F. Steglich, and A. de Visser, Physica B **138**, 1 (1986).

[de Haas and van Alphen 1930] W. J. de Haas and P. M. van Alphen, Proc. Sect. Sci. K. ned. Akad. Wet **33**, 1106 (1930).

[de Visser 1986] A. de Visser, F. E. Kaysel, A. A. Menovsky, and J. J. M. Franse, Phys. Rev. B **34**, 8168 (1986).

[de Visser 1987] A. de Visser, F. R. de Boer, A. A. Menovsky, and J. J. M. Franse, Solid State Commun. **64**, 527 (1987).

[Doniach 1977] S. Doniach, Physica B & C, **91**, 231234 (1977).

[Dubi 2011] Y. Dubi and A. V. Balatsky, Phys. Rev. Lett. **106**, 086401 (2011).

[Elgazzar 2009] S. Elgazzar, J. Rusz, M. Amft, P. M. Oppeneer, and J. A. Mydosh: Nature Mater. **8**, 337 (2009).

[Enss and Hunklinger 2005] C. Enss and S. Hunklinger, *Low Temperature Physics* (Springer Verlag, Heidelberg, DE 2005).

[Fak 1996] B. Fak, C. Vettier, J. Flouquet, F. Bourdarot, S. Raymond, A. Verniere, P. Lejay, P. Boutrouille, N. R. Bernhoeft, S. T. Bramwell, R. A. Fisher, and N. E. Phillips, J. Magn. Magn. Mater. **154**, 339350 (1996).

[Flouquet 2004] J. Flouquet, Y. Haga, P. Haen, D. Braithwaite, G. Knebel, S. Raymond, S. Kambe, J. Magn. Magn. Mater. **272-276**, 27 (2004).

[Flouquet 2005] J. Flouquet, Prog. Low Temp. Phys. **15**, Chapter 2 (2005).

[Flouquet 2011] J. Flouquet, D. Aoki, F. Bourdarot, F. Hardy, E. Hassinger, G. Knebel, T. D. Matsuda, C. Meingast, C. Paulsen, and V. Taufour, J. Phys.: Conf. Ser. **273**, 012001 (2011).

[Grosso and Parravicini 2000] G. Grosso and G. P. Parravicini, *Solid State Physics* (Academic Press, London, U.K., 2000).

[Hassinger 2008] E. Hassinger, G. Knebel, K. Izawa, P. Lejay, B. Salce, and J. Flouquet, Phys. Rev. B **77**, 115117 (2008).

[Hassinger 2010] E. Hassinger, G. Knebel, T. D. Matsuda, D. Aoki, V. Taufour, and J. Flouquet, Phys. Rev. Lett. **105**, 216409 (2010).

[Harima 2010] H. Harima, J. Flouquet, and K. Miyake, J. Phys. Soc. Jpn. **79**, 033705 (2010).

[Kusunose 2011] H. Kusunose, H. Harima, J. Phys. Soc. Jpn. **80**, 084702 (2011).

[Harrison 2003] N. Harrison, M. Jaime, and J. A. Mydosh, Phys. Rev. Lett. **90** (9), 096402 (2003).

[Haule and Kotliar 2009] K. Haule and G. Kotliar, Nat. Phys. **5**, 796 (2009).

[Hewson 1993] A.C. Hewson, *The Kondo Problem to Heavy Fermions* (Cambridge University Press, Cambridge, U.K., 1993).

[Höfner 2010] K. Höfner, Master report, Université Paul Sabatier, Toulouse, France (2010).

[Ikeda 2012] H. Ikeda, M.-T. Suzuki, R. Arita, T. Takimoto, T. Shibauchi, and Y. Matsuda, Nat. Phys. **8**, 528 (2012).

[Inoue 2001] T. Inoue, K. Kindo, H. Okhuni, H. Sugiyama, Y. Haga, E. Yamamoto, T.C. Kobayashi, Y. Uwatoko, and Y. Ōnuki, Physica B **294-295**, 271 (2001).

[Ishida 1998] K. Ishida, Y. Kawasaki, Y. Kitaoka, K. Asayama, H. Nakamura, and J. Flouquet, Phys. Rev. B **57**, R11054 (1998).

[Jaime 2002] M. Jaime, K.H. Kim, G.A. Jorge, S. McCall, and J.A. Mydosh, Phys. Rev. Lett. **89**, 287201 (2002).

[Janik 2009] J. A. Janik, H. D. Zhou, Y.-J. Jo, L. Balicas, G. J. MacDougall, G. M. Luke, J. D. Garrett, K. J. McClellan, E. D. Bauer, J. L. Sarrao, Y. Qiu, J. R. D. Copley, Z. Yamanin, W. J. L. Buyers, and C. R. Wiebe, J. Phys.: Condens. Matter **21**, 192202 (2009).

[Jo 2007] Y. J. Jo, L. Balicas, C. Capan, K. Behnia, P. Lejay, J. Flouquet, J. A. Mydosh, and P. Schlottermann, Phys. Rev. Lett. **98**, 166404 (2007).

[Kadowaki and Woods 1986] K. Kadowaki and S. B. Woods, Solid State Commun. **58**, 507509 (1986).

[Kapitza 1941] P. L. Kapitza, J. Phys (USSR) **4** (1941).

[Kasahara 2007] Y. Kasahara, T. Iwasawa, H. Shishido, T. Shibauchi, K. Behnia, Y. Haga, T. D. Matsuda, Y. Ōnuki, M. Sigrist, and Y. Matsuda, Phys. Rev. Lett. **99**, 116402 (2007).

[Kasuya 1956] T. Kasuya, Prog. Theor. Phys. **16**, 45 (1956).

[Kawasaki 2011a] I. Kawasaki, S.-i. Fujimori, Y. Takeda, T. Okane, A. Yasui, Y. Saitoh, H. Yamagami, Y. Haga, E. Yamamoto, and Y. Ōnuki, Phys. Rev. B **83**, 235121 (2011).

[Kawasaki 2011b] I. Kawasaki, S.-i. Fujimori, T. Okane, A. Yasui, Y. Saitoh, H. Yamagami, Y. Haga, E. Yamamoto, and Y. Ōnuki, J. Phys. Soc. Jpn. **80**, 124710 (2011).

[Keller 1998] N. Keller, S. A. J. Wiegers, J. A. A. J. Perenboom, A. de Visser, A. A. Menovsky, and J. J. M. Franse, J. Magn. Magn. Mater. **177-181**, 298 (1998).

[Kim 2003a] J. S. Kim, D. Hall, P. Kumar, and G. R. Stewart, Phys. Rev. B **67**, 014404 (2003).

[Kim 2003b] K. H. Kim, N. Harrison, M. Jaime, G. S. Boebinger, and J. A. Mydosh, Phys. Rev. Lett. **91**, 25 (2003).

[Kim 2004] K.H. Kim, N. Harrison, H. Amitsuka, G.A. Jorge, M. Jaime, and J.A. Mydosch, Phys. Rev. Lett. **93**, 206402 (2004).

[Kiss 2005] A. Kiss and P. Fazekas, Phys. Rev. B **71**, 054415 (2005).

[Knafo 2004] W. Knafo, S. Raymond, B. Fåk, J. Flouquet, M.A. Adams, P. Haen, F. Lapierre, S. Yates, P. Lejay, Phys. Rev. B **70**, 174401 (2004).

[Knafo 2009] W. Knafo, S. Raymond, P. Lejay, and J. Flouquet, Nat. Phys. **5**, 753 (2009).

[Kohler 1938] M. Kohler, Ann. Phys. **32**, 211 (1938)

[Kondo 1964] J. Kondo, Prog. Theor. Phys. **32** (1), 37-49 (1964).

[Kusunose and Harima 2011] H. Kusunose and H. Harima, J. Phys. Soc. Jpn. **80**, 084702 (2011).

[Kuwahara 2013] K. Kuwahara, S. Yoshii, H. Nojiri, D. Aoki, W. Knafo, F. Duc, X. Fabrèges, G. W. Scheerer, P. Frings, G. L. J. A. Rikken, F. Bourdarot, L. P. Regnault, and J. Flouquet, Phys. Rev. Lett. **110**, 216406 (2013).

[Kwok 1990] W. K. Kwok, L. E. DeLong, G. W. Crabtree, and D. G. Hinks, Phys. Rev. B **41**, 11649 (1990).

[Landau 1930] L. D. Landau, Z. Phys. **64**, 629 (1930).

[Landau 1957] L. D. Landau, Sov. Phys. JETP **3**, 920925 (1957).

[Leggett 1975] A. J. Leggett, Rev. Mod. Phys. **47**, 331 (1975).

[Lerdawson 1989] A. LeR Dawson, W.R. Datars, J.D. Garrett, and F.R. Razavi, J. Phys.: Condens. Matter **1**, 6817 (1989).

[Levallois 2009] J. Levallois, K. Behnia, J. Flouquet, P. Lejay, and C. Proust, EPL **85**, 27003 (2009).

[Lifshitz 1960] I. M. Lifshitz, Sov. Phys. JETP **11**, 1130 (1960).

[Lifshitz and Kosevich 1955] I. M. Lifshitz and A. M. Kosevich, Zh. eksp. teor. Fiz. **29**, 730 (1955).

[Lonzarich 1997] G. G. Lonzarich, *The Electron* (Cambridge University Press, Cambridge, UK, 1997), Chap. 6.

[Malone 2011] L. Malone, T. D. Mastuda, A. Antunes, G. Knebel, V. Taufour, D. Aoki, K. Behnia, C. Proust, and J. Flouquet, Phys. Rev. B **83**, 245117 (2011).

[Maple 1986] M. B. Maple, J. W. Chen, Y. Dalichauch, T. Kohara, C. Rossel, M. S. Torikachvili, M. W. McElfresh, and J. D. Thompson, Phys. Rev. Lett. **56**, 185 (1986).

[Mason 1990] T. E. Mason, H. Lin, M. F. Collins, W. J. L. Buyers, A. A. Menovsky, and J. A. Mydosh, Physica B **163**, 45 (1990).

[Mason 1995] T. E. Mason, W. J. L. Buyers, T. Petersen, A. A. Menovsky, and J. D. Garrett, J. Phys.: Condens. Matter **7**, 5089 (1995).

[Matsuda 2001] K. Matsuda, Y. Kohori, T. Kohara, K. Kuwahara, and H. Amitsuka, Phys. Rev. Lett. **87** (8), 087203 (2001).

[Matsuda private com.] T. D. Matsuda, private communication.

[Matsuda 2011] T. D. Matsuda, E. Hassinger, D. Aoki, V. Taufour, G. Knebel, N. Tateiwa, E. Yamamoto, Y. Haga, Y. Ōnuki, Z. Fisk, and J. Flouquet, J. Phys. Soc. Jpn. **80**, 114710 (2011).

[Millis 1993] A. J. Millis, Phys. Rev. B **48**, 7183 (1993).

[Mineev 2005] V. P. Mineev and M. E. Zhitomirsky, Phys. Rev. B **72**, 014432 (2005).

[Moriya 1985] T. Moriya, *Spin Fluctuations in Itinerant Electron Magntism* (Springer-Verlag, Heidelberg, Germany, 1985).

[Motoyama 2003] G. Motoyama, T. Nishioka, and N. K. Sato, Phys. Rev. Lett. **90**, 166402 (2003).

[Mydosh and Oppeneer 2011] J. A. Mydosh and P. M. Oppeneer, Rev. Mod. Phys. **83**, 1301 (2011).

[Nakashima 2003] M. Nakashima, H. Ohkuni, Y. Inada, R. Settai, Y. Haga, E. Yamamoto, and Y Ōnuki, J. Phys.: Condens. Matter **15**, S2011-S2014 (2003).

[Nardone private com.] M. Nardone, private communication.

[Ohkuni 1997] H. Ohkuni, T. Ishida, Y. Inada, Y. Hagam E. Yamamoto, Y. Ōnuki, and S. Takahasi, J. Phys. Soc. Jpn. **66**, 4 (1997).

[Ohkuni 1999] H. Ohkuni, Y. Inada, Y. Tokiwa, K. Sakurai, R. Settai, T. Honma, Y. Haga, E. Yamamoto, Y. Ōnuki, H. Yamagami, S. Takahashi, and T. Yanagisawa, Philos. Mag. B **79**, 1045 (1999).

[Okazaki 2011] R. Okazaki, T. Shibauchi, H. J. Shi, Y. Haga, T. D. Matsuda, E. Yamamoto, Y. Ōnuki, H. Ikeda, and Y. Matsuda, Science **331**, 439 (2011).

[Onsager 1952] L. Onsager, Philos. Mag **43**, 1006 (1952).

[Oppeneer 2010] P. M. Oppeneer, J. Rusz, S. Elgazzar, M.-T. Suzuki, T. Durakiewicz, and J. A. Mydosh, Phys. Rev. B **82**, 205103 (2010).

[Palstra 1985] T. T. Palstra, A. A. Menovsky, J. van den Berg, A. J. Dirkmaat, P. H. Kes, G. J. Nieuwenhuys, and J. A. Mydosh, Phys. Rev. Lett **55**, 2727 (1985).

[Palstra 1986] T. T. Palstra, A. A. Menovsky, and J. A. Mydosh, Phys. Rev. B **33**, 6527 (1986).

[Paulsen 1990] Paulsen, A. Lacerda, L. Puech, P. Haen, P. Lejay, J. L. Tholence, J. Flouquet, and A. de Visser, J. Low Temp. Phys. **81**, 317 (1990).

[Pépin 2011] C. Pépin, M. R. Norman, S. Burdin, and A. Ferraz, Phys. Rev. Lett. **106**, 106601 (2011).

[Pippard 1989] A. B. Pippard, *Magnetoresistance in Metals* (Cambridge University Press, Cambridge, U.K., 1989).

[Pobell 1992] F. Pobell, *Matter and Methods at Low Temperatures* (Springer-Verlag, Berlin-Heidelberg, Germany, 1992).

[Pourret 2013] A. Pourret, A. Palacio-Morales, S. Krämer, L. Malone, M. Nardonne, D. Aoki, G. Knebel, and Jacques Flouquet, J. Phys. Soc. Jpn **82**, 034706 (2013).

[Ramirez 1992] A. P. Ramirez, P. Coleman, P. Chandra, E. Brück, A. A. Menovsky, Z. Fisk, and E. Bucher, Phys. Rev. Lett. **68**, 2680 (1992).

[Ruderman and Kittel 1954] M. A. Rudermann and C. Kittel, Phys. Rev. **96**, 99 (1954).

[Sachdev 1999] S. Sachdev, *Quantum Phase Transitions* (Cambridge Univ. Press, Cambridge, U.K., 1999).

[Santander 2009] F. Santander-Syro, M. Klein, F. L. Boariu, A. Nuber, P. Lejay, and F. Reinert, Nat. Phys. **5**, 637 (2009).

[Schablitz 1986] W. Schlabitz, J. Baumann, B. Pollit, U. Rauchschwalbe, H. M. Mayer, U. Ahlheim, and C.D. Bredl, Z. Phys. B **62**, 171 (1986).

[Scheerer 2012] G. W. Scheerer, W. Knafo, D. Aoki, G. Ballon, A. Mari, D. Vignolles, and J. Flouquet, Phys. Rev. B **85**, 094402 (2012).

[Schmidt 2010] A.R. Schmidt, M.H. Hamidian, P. Wahl, F. Meier, A.V. Balatsky, J.D. Garrett, T.J. Williams, G.M. Luke, and J.C. Davis, Nature **465**, 570 (2010).

[Schoenes 1987] J. Schoenes, and C. Schonenberger, Phys. Rev. B **35**, 5375 (1987).

[Sharma 2006] P. A. Sharma, N. Harrison, M. Jaime, Y. S. Oh, K. H. Kim, C. D. Batista, H. Amitsuka, and J. A. Mydosh, Phys. Rev. Lett. **97**, 156401 (2006).

[Shishido 2009] H. Shishido, K. Hashimoto, T. Shibauchi, T. Sasaki, H. Oizumi, N. Kobayashi, T. Takamasu, K. Takehana, Y. Imanaka, T. D. Matsuda, Y. Haga, Y. Ōnuki, and Y. Matsuda, Phys. Rev. Lett. **102**, 156403 (2009).

[Shoenberg 1984] D. Shoenberg, *Magnetic Oscillations in Metals* (Cambridge Univ. Press, Cambridge, U.K., 1984).

[Shubnikov and de Haas 1930] L. W. Schubnikov, W. J. de Haas, Proc. R. Neth. Acad. Arts Sci. **33**, 130 (1930).

[Stewart 2001] G.R. Stewart, Rev. Mod. Phys. 73, 797 (2001).

[Stoner 1938] E. C. Stoner, Proc. R. Soc. **A 165**, 372 (1938).

[Stryjewski 1977] E. Stryjewski, N. Giordano, Adv. Phys. **26** (5), 487650 (1977).

[Sugiyama 1990] K. Sugiyama, H. Fuke, K. Kindo, K. Shimohata, A. A. Menovsky, J. A. Mydosh, and M. Muneyuki Date, J. Phys. Soc. Jpn. **59**, 9 (1990).

[Sugiyama 1999] K. Sugiyama, M. Nakashima, H. Ohkuni, K. Kindo, Y. Haga, T. Honma, E. Yamamoto, and Y. Ōnuki, J. Phys. Soc. Jpn. **68**, 10 (1999).

[Sumiyama 1986] A. Sumiyama, Y. Oda, H. Nagano, Y. Ōnuki, K. Shibutani, and T. Komatsubara, J. Phys. Soc. Jpn. **55**, 1294-1304 (1986).

[Suslov 2003] A. Suslov, J. B. Ketterson, D. G. Hinks, D. F. Agterberg, and B. K. Sarma, Phys. Rev. B **68**, 020406 (2003).

[Takagi 2007] S. Takagi, S. Ishihara, S. Saitoh, H. I. Sasaki, H. Tanida, M. Yokoyama, and H. Amitsuka, J. Phys. Soc. Jpn. **76**, 033708 (2007).

[Tonegawa 2012] S. Tonegawa, K. Hashimoto, K. Ikada, Y.-H. Lin, H. Shishido, Y. Haga, T. D. Matsuda, E. Yamamoto, Y. Ōnuki, H. Ikeda, Y. Matsuda, and T. Shibauchi, Phys. Rev. Lett. **109**, 036401 (2012).

[Uhlig 1987] K. Uhlig, Cryogenics **27**, 8 (1987).

[Varma 2006] C. M. Varma and L. J. Zhu, Phys. Rev. Lett **96**, 036405 (2006).

[Villaume 2008] A. Villaume, F. Bourdarot, E. Hassinger, S. Raymond, V. Taufour, D. Aoki, and J. Flouquet, Phys. Rev. B **78**, 012504 (2008).

[Wiebe 2007] C. R. Wiebe, J. A. Janik, G. J. MacDougall, G. M. Luke, J. D. Garrett, H. D. Zhou, Y.-J. Jo, L. Balicas, Y. Qiu, J. R. D. Copley, Z. Yamanin, and W. J. L. Buyers, Nat. Phys. **3**, 96 (2007).

[Yanagisawa 2013] T. Yanagisawa, S Mombetsui, H Hidaka, H Amitsuka, M Akatsu, S Yasin, S Zherlitsyn, J Wosnitza, K Huang, and M. B Maple, J. Phys. Soc. Jpn. **82**, 013601 (2013).

[Yokoyama 2004] M. Yokoyama, H. Amitsuka, S. Itoh, I. Kawasaki, K. Tenya, and H. Yoshizawa, J. Phys. Soc. Jpn. **73**, 545 (2004).

[Yokoyama 2005] M. Yokoyama, H. Amitsuka, K. Tenya, K. Watanabe, S. Kawarazaki, H. Yoshizawa, and J. A. Mydosh, Phys. Rev. B **72**, 214419 (2005).

[Yosida 1957] K. Yosida, Phys. Rev. **106**, 893 (1957).

[Yoshida 2010] R. Yoshida, Y. Nakamura, M. Fukui, Y. Haga, E. Yamamoto, Y. Ōnuki, M. Okawa, S. Shin, M. Hirai, Y. Muraoka, and T. Yokoya, Phys. Rev. B **82**, 205108 (2010).